이학박사 학위논문

Life of the Most Massive Black Holes

가장 무거운 블랙홀의 일생

2014년 8월

서울대학교 대학원

물리·천문학부 천문학 전공

전 현 성

Life of the Most Massive Black Holes

by

Hyunsung Jun
(hsjun@astro.snu.ac.kr)

A thesis submitted in partial fulfillment of the final requirement for the degree of

Doctor of Philosophy

in

Astronomy

in

Astronomy Program, Department of Physics and Astronomy
Seoul National University

Committee:

Professor	Hyung Mok Lee
Professor	Myungshin Im
Professor	Myung Gyoon Lee
Professor	Jong-Hak Woo
Professor	Sukyoung Yi

ABSTRACT

Supermassive black holes (BHs) are mostly found in the center of galaxy bulges, growing in mass during the active galactic nucleus (AGN) phase. The most massive limit is identified as present day ten billion solar mass BHs, in massive quiescent galaxies. We search for observational signatures to investigate the physical evolution of extremely massive BHs (EMBHs, $>10^{9.5}M_{\odot}$). We aim to constrain the massive limit of AGNs, probe the massive end evolution of BH mass ($M_{\rm BH}$), search for evolution in the AGN dusty structure, and establish the mid-infrared fundamental scaling relation of massive BH host galaxies.

First, we examine the reliability of the $M_{\rm BH}$ for the most massive AGNs by estimating their mass using optical mass estimators, and comparing them to the previous rest-frame UV mass estimations of $\sim 10^{10}M_{\odot}$ for 27 AGNs at $0.7<z<2.5$. We find that the Balmer $M_{\rm BH}$'s are overall consistent with the Mg II masses up to $\sim 10^{10}M_{\odot}$, although a fraction of the $>10^{10}M_{\odot}$ AGN spectra suffer from disk emitter features on top of the broad Hα emission, which are weakly noticed near the UV broad line emission. On the other hand, the C IV-based $M_{\rm BH}$'s show a large scatter with respect to the Hα based, with 4 out of 8 quasars with $M_{\rm BH,C_{IV}}>10^{10}M_{\odot}$ having $M_{\rm BH,H\alpha}$ less than $10^{10}M_{\odot}$. These results suggest that previously reported rest-UV $M_{\rm BH}$ of $>10^{10}M_{\odot}$ should be carefully interpreted. We test for the biases in the $M_{\rm BH}$ from systematic uncertainty in the $M_{\rm BH}$ estimator, but find that our $M_{\rm BH,H\alpha}$ measurements will likely stay at $\sim 10^{10}M_{\odot}$.

Second, we study the rest-frame optical spectra of 155 luminous quasars at $3.3<z<6.4$ taken with the *AKARI* space telescope. We extend the scaling relation between 5100 $\mathring{A}$ and Hα luminosities of AGNs to the high luminosity, high redshift regime. Remarkably, a single linear relation can be applied to the AGN luminosities suggesting that the physical mechanism governing the relation does not evolve with redshift ($z=0$–6), over five decades in luminosity

($10^{43} < L_{\rm bol} < 10^{48}\,{\rm ergs\,s^{-1}}$). Similar scaling relations are found between the optical and the UV continuum luminosities and line widths. Applying the scaling relations to the Hβ $M_{\rm BH}$ estimator of local AGNs, we derive the $M_{\rm BH}$ estimators based on Hα, Mg II, and C IV lines finding that the UV-line based masses are overall consistent with the Balmer-line based, but with a large intrinsic scatter for the C IV estimates. Our 43 $M_{\rm BH}$ estimates from Hα confirm the existence of BHs as massive as $\sim 10^{10}$ and $10^9 M_\odot$ out to $z \sim 5$ and 6, respectively, and provide a secure footing for previous UV-line based studies that a rapid $M_{\rm BH}$ growth has occurred in the early universe.

Next, as a possible sign of AGN structure formation and evolution on the way of becoming EMBHs, we identify and characterize a population of luminous, dust-poor quasars at $z < 5$ that is photometrically similar to dust-poor quasars found at $z > 6$ previously. We fit the rest-frame UV-to-IR spectral energy distribution (SED) of 41,000 optically selected type 1 quasars with $L_{\rm bol} > 10^{45.7}\,{\rm ergs\,s^{-1}}$, to find 0.6% of the sample to be hot dust-poor, with rest-frame 2.3 μm-to-0.51 μm flux density ratios of -0.5 dex or less. The dust-poor SEDs are blue in the UV–optical and weak in the mid-IR, such that their accretion disks are relatively unobscured and the hot dust emission traces that of warm dust down to the dust-poor regime. At a given bolometric luminosity, dust-poor quasars are lower in black hole mass, higher in Eddington ratio, and higher in redshift than general luminous quasars, suggesting that they are in a rapidly growing evolutionary state in which the dust-poor phase appears as a short or rare phenomenon.

Lastly, we study the local fundamental plane (FP) relation of early-type galaxies in the mid-infrared (MIR), the final evolutionary stage of massive BH hosts. The scaling relation between size, surface brightness, and velocity dispersion of early-type galaxies has been found to be tilted against the simple virial expectation, prompting debates on its origin. In order to investigate the contribution of systematic stellar population variation to the FP tilt, we used

a sample of 56 early-type galaxies for which visible, near-infrared, and MIR (*Spitzer* IRAC) data are available. The derived slope of the FP in the MIR suggests that the stellar population effect can explain more than half of the FP suggesting that the MIR light better represents mass than the shorter wavelengths.

Through the study of the rest-frame optical spectra of high redshift AGNs, we find that the governing physics in AGNs appear to be unchanging at $z = 0$–6, and provide further support that the EMBHs in AGNs appear at $z = 5$ with a vigorous growth happening at $z = 6$ involving a dust-poor phase. When EMBHs settle in at quiescent, massive galaxies today, the host galaxies possess the infrared fundamental plane relation only slightly off from a simple virial expectation when using the MIR luminosity as a proxy of mass.

Keywords: galaxies: active – galaxies: evolution – galaxies: fundamental parameters – infrared: galaxies

Student Number: 2006 − 22963

Contents

Chapter 1

Introduction

Supermassive black holes are found to live mostly in the center of galaxy bulges, having typical masses in the $10^{6-9}M_{\odot}$ range (e.g., Kormendy & Richstone 1995). The recent discovery of $\sim 10^{10}M_{\odot}$ black holes (McConnell et al., 2011) further identified the massive limit, pushing the previous $\sim 10^{9}M_{\odot}$ order limit into heavier regimes. These extremely massive black holes ($>10^{9.5}M_{\odot}$, EMBHs) together with their giant elliptical host galaxies ($\sim 10^{12}M_{\odot}$) from the present day $M_{\rm BH}$–σ relation (e.g., Ferrarese & Merritt 2000; Gebhardt et al. 2000), are likely to be the most massive systems out of BH-host galaxy growth. On the way of understanding when, how, and why there should be a tight correlation between the BH-host properties, numerous studies have been accumulated on the slope, scatter, and redshift evolution of the scaling relations (e.g., Shen et al. 2008a; Woo et al. 2008; Bennert et al. 2010; McConnell & Ma 2013; Woo et al. 2013). However, the massive end BH-host scaling relations are yet constrained well, where overmassive BHs lying significantly above the relations are found (McConnell et al. 2011; van den Bosch et al. 2012).

Among the efforts to understand the formation and evolution of EMBHs, the BH mass measurement itself is of great importance. It is reported that there are $\sim 10^{10}M_{\odot}$ black holes in distant active galactic nuclei (AGNs), even

up to $z = 5$ (e.g., Shen et al. 2011, but see also Park et al. 2013). A BH to have already grown into such EMBH at high redshift may suggest an early, rapid mass growth rate reaching to its Eddington limit or even beyond (e.g., Volonteri & Rees 2005), and further hints that the growth of the most massive BHs may have preceded that of the galaxy bulge (e.g., Peng et al. 2006). Nevertheless, such early and intense growth of the most massive BHs seems to be at odds with the co-evolution of its host galaxy, as the formation model of EMBHs through galaxy merging (e.g., Jahnke & Macciò 2011; Volonteri & Ciotti 2013) does not necessarily induce strong active galactic nucleus (AGN) activity of EMBHs at high redshift for which $M_{\rm BH}$ of $10^{10} M_{\odot}$ are often found. Therefore, constraining the massive limit of BHs through observations of AGNs (e.g., Shen & Liu 2012), and probing the redshift evolution of the massive end BH masses (e.g., Trakhtenbrot et al. 2011) is important in quantifying how much a BH can grow within a given amount of cosmic age. Previous studies on the BH mass of distant, massive AGNs usually relied on the rest-frame UV spectral measurements of AGN emission due to the limited number of ground based infrared spectroscopy, where the UV mass estimators are secondarily calibrated to the optical mass estimation technique. Therefore, rest-frame optical spectral coverage could help check the BH masses of $10^{10} M_{\odot}$ from UV measurements. Also, the systematic biases in BH masses involved in using the mass estimators should be carefully considered to the measurements.

Next, massive BHs would have gone through extensive mass growth during the AGN phase, where according the unification model of AGNs (e.g., Krolik & Begelman 1988; Antonucci 1993; Urry & Padovai 1995) the infrared radiation originate from a dusty surrounding torus. Jiang et al. (2010) however, discovered a population of dust-poor quasars at $z > 6$ showing weak rest-frame near-infrared emission from the hot, inner dusty torus. They are relatively high in accretion rate and low in BH mass ($\sim 10^8 M_{\odot}$, compared to the $\sim 10^9 M_{\odot}$ BHs for the rest of their sample), which suggests that these quasars could be

in a stage of dusty structure formation during the onset of rapid BH mass growth, on their way to becoming EMBHs. Following studies however, do not have a consensus on the evolutionary properties such as redshift, BH mass, or accretion rate (Hao et al. 2010; Mor & Trakhtenbrot 2011). In order to better identify and characterize the dust-poor population, a larger sample covering a wide range of observed AGN properties would help.

Third, when BHs co-evolve with their host galaxies they would at some point, become quiescent early-type galaxies in the local universe. We expect these galaxies to be in a virialized, quiescent phase, which could be hinted from galaxy scaling relations. One of the correlations among galaxy parameters, is the Fundamental Plane (e.g., Dressler et al. 1987; Djorgovski & Davis 1987) concerning the size, surface brightness, and velocity dispersion of early-type galaxies. This planar relation has a virial expectation slope, but has been found tilted in the optical wavelength. Pahre et al. (1998a) used the near-infrared luminosity to construct the Fundamental Plane, and found its tilt to be smaller, from the reduced effect (e.g., Bell & de Jong 2001) of stellar populations acting on the M_*/L variation with stellar mass, M_*. Further extending this planar relation using mid-infrared wavelengths as a probe of M_*, could help constrain the stellar population effect on the systematic variation in the mass-to-light ratio.

In this thesis we follow the evolutionary timeline of the most massive black holes and their host galaxies, to understand their formation and evolution through observational signatures. In Chapter 2, we investigate the massive limit of AGNs through IRTF spectroscopy. In Chapter 3, we present the rest-frame optical spectral properties of luminous and distant quasars from *AKARI* observations, and examine the massive end growth of BH mass in the early universe. In Chapter 4, we study the evolution in the AGN dusty structure through spectral energy distribution fitting and identification of luminous dust-poor quasars. In Chapter 5, we construct the mid-infrared fundamental

plane of local early-type galaxies. Finally, in Chapter 6, we summarize our results and place them along previous works.

Chapter 2

Rest-frame Optical Black Hole Masses of Extremely Massive $1<z<2$ Quasars

2.1 Introduction

Since the identification of supermassive black holes (BHs) in galactic centers, it has been known that the typical BH masses ($M_{\rm BH}$'s) are in the $10^{6-9}M_{\odot}$ range for such galactic scale BHs (e.g., Kormendy & Richstone 1995). The recent discovery of $\sim10^{10}M_{\odot}$ BHs (McConnell et al., 2011) in quiescent galaxies further extended the massive limit, pushing the previous $\sim10^{9}M_{\odot}$ boundary to heavier regimes. These extremely massive black holes ($>10^{9.5}M_{\odot}$, hereafter EMBHs) residing in giant elliptical host galaxies in the mass range of $\sim10^{12}M_{\odot}$ estimated from the present day $M_{\rm BH}$–σ relation (e.g., Ferrarese & Merritt 2000; Gebhardt et al. 2000), are likely to be the most massive systems out of BH-host galaxy growth, although there are exceptions to this expectation (e.g., van den Bosch et al. 2012).

However, direct evidence for the existence of $10^{10}M_{\odot}$ BHs has been found

only in a handful of nearby quiescent galaxies (NGC 3842 and NGC 4889, McConnell et al. 2011; NGC 1277 in van den Bosch et al. 2012), with the validity for some of the measurements being questioned (Emsellem, 2013). Even if we consider that the measured values are acceptable, it gives rise to another question. The EMBHs deviate significantly above the $M_{\rm BH}$–σ or $M_{\rm BH}$–$L_{\rm bulge}$ relation in such a way that they are overmassive in comparison to the extrapolation of the relations to the massive end established from lower mass BHs. To explain the rather too heavy mass of EMBHs with respect to the host galaxy, Volonteri & Ciotti (2013) suggest that EMBHs are formed through frequent dry mergers, but this does not solve the problem entirely since such mergers do not necessarily induce strong active galactic nucleus (AGN) activity of EMBHs at high redshift for which $M_{\rm BH}$ of $10^{10}M_{\odot}$ are often found.

These observational and theoretical considerations lead to a question if the $M_{\rm BH}$ estimated of $10^{10}M_{\odot}$ for quasars at high redshift are correct. The $M_{\rm BH}$ estimators used for high redshift quasars are based mainly on UV-based spectral features that are secondary product from Hydrogen Balmer line based estimators, so one possibility is that the UV-based $M_{\rm BH}$'s are overestimated somehow. An independent $M_{\rm BH}$ estimates from Balmer-line based estimators should enhance the reliability of $10^{10}M_{\odot}$ BHs in distant quasars. Unfortunately, direct comparison between the UV-based versus Balmer-based $M_{\rm BH}$ estimates has been scarce for EMBHs. Previous studies have been largely limited to $M_{\rm BH}$ $<10^{9.5}M_{\odot}$ (e.g., Netzer et al. 2007; Shang et al. 2007; Dietrich et al. 2009; Greene et al. 2010; Ho et al. 2012; Park et al. 2013), and such studies find that C IV and Balmer-based estimators show a large scatter while the Mg II and Balmer based $M_{\rm BH}$'s agree better. The most extensive study in this respect is done by Shen & Liu (2012) where the sample covers dozens of EMBHs, but only with a few $\sim 10^{10}M_{\odot}$ BHs included in their study.

In order to understand the mass growth of EMBHs along redshift, accu-

rate $M_{\rm BH}$ measurement is of great importance. However, in the distant universe where it is difficult to resolve the gravitational sphere of influence from the BH, stellar or gas dynamical measurement of $M_{\rm BH}$ in quiescent galaxies becomes hardly possible. Instead, the estimation of $M_{\rm BH}$ of AGNs through broad line gas kinematics are utilized, where this method gives rather uncertain results. $M_{\rm BH}$ measurements for AGNs utilize the reverberation mapping technique (Blandford & Payne 1982; Peterson 1993) to estimate the size of the broad line region (BLR) from time delays of the broad line emission to the incident continuum. The BLR size measurements of Hβ, are further calibrated as a radius-luminosity ($R_{\rm BLR}$–L) relationship (Kaspi et al. 2000; Bentz et al. 2006), which allows the estimation of $M_{\rm BH}$ from a single measurement of optical continuum/line luminosity and broad line width of the hydrogen Balmer emission, through single epoch mass estimators.

Of the natural consequences of observing high redshift AGNs with optical spectroscopy is that the rest-frame optical (rest-optical) wavelength is redshifted to the infrared, and rest-frame ultraviolet (rest-UV) emission comes into the observed optical. The single epoch mass estimators are then, secondarily calibrated in the UV assuming that the UV continuum luminosity and broad emission line (C IV or Mg II) widths follow the optical $R_{\rm BLR}$–L relation and optical line widths respectively, as a constant or power law relation. Where there are ongoing, if not complete, studies that the slope of the C IV $R_{\rm BLR}$–L relation follows that of the optical relation, and extends up to the most luminous quasars (Kaspi et al. 2007; Sluse et al. 2011; Chelouche et al. 2012; Bentz et al. 2013), the UV continuum luminosities or line widths are yet well understood if they tightly follow the optical line widths, possibly introducing additional irreducible scatter of up to 0.24–0.39 dex (Shen & Liu 2012; Chapter 3, but see also Assef et al. 2011) when using the C IV over the Balmer $M_{\rm BH}$.

In addition to the issues on the reliability of rest-UV $M_{\rm BH}$ measurements,

the rest-optical $M_{\rm BH}$ from single epoch spectroscopy itself has limitations on its accuracy due to the systematic errors in deriving the mass equation. Bearing in mind that the single epoch $M_{\rm BH}$'s have sizable uncertainties from the constant (f-factor) in the mass equation ($\lesssim 0.4$ dex intrinsic scatter, Woo et al. 2013) and the $R_{\rm BLR}$–L relation (~ 0.1–0.2 dex intrinsic scatter, Bentz et al. 2013), it is possible that the $M_{\rm BH}$ of the most massive AGNs could be biased to high values if they are from the outlying f-factor or $R_{\rm BLR}$ values with respect to the calibrations. Therefore, we test if the UV-based $\sim 10^{10} M_{\odot}$ $M_{\rm BH}$ measurements are consistent to the rest-optical masses, through NASA Infrared Telescope Facility (IRTF), near-infrared (NIR) spectroscopy of 27 quasars at $0.7 < z < 2.5$. Comparing the massive end UV and optical $M_{\rm BH}$ estimates, we aim to double check the consistency of UV-optical mass measurements, and examine if the measurements could be systematically biased to unusually high masses from the mass estimation steps or from statistical errors. We describe the sample selection and data acquisition of extremely massive AGNs (Section 2.2), the spectral analysis in determining the $M_{\rm BH}$ (Section 2.3), and the results together with implications on the measured $M_{\rm BH}$'s (Section 2.4). Throughout, we adopt a flat ΛCDM cosmology with $H_0 = 70\,{\rm km\,s^{-1}\,Mpc^{-1}}$, $\Omega_m = 0.3$, and $\Omega_\Lambda = 0.7$. For the virial factor in the $M_{\rm BH}$ estimator, $M_{\rm BH} = \frac{f}{G} R_{\rm BLR} (\frac{\rm FWHM_{BLR}}{2})^2$, we assume $f = 5.1 \pm 1.3$ from Woo et al. (2013).

2.2 Data

2.2.1 Sample description and observations

We selected the extremely massive AGN sample from the Sloan Digital Sky Survey (SDSS) type-1 quasar catalog (DR7, Schneider et al. 2010). The spectral fitting measurement and the $M_{\rm BH}$ estimators in Shen et al. (2011) were adopted. We identified the sample by applying a mass selection of $M_{\rm BH} >$

$10^{9.5} M_{\odot}$ and signal-to-noise ratio (S/N) cut of 10 or higher. Constraining the redshift range of $0.7 < z < 2.5$ to place the broad Hα, Hβ lines within the NIR spectroscopic coverage, and further avoiding the redshifts where the broad emission are affected by the NIR telluric absorption bands, 27 SDSS quasars were randomly chosen in coordinates and bolometric luminosity within $L_{\rm bol} = 10^{46.6-48.2} {\rm ergs\,s^{-1}}$ for observations at IRTF.

We used the SpeX instrument (Rayner et al., 2003) at IRTF to obtain the NIR spectra of our targets. The 0.8–2.4 μm cross-dispersed mode (SXD) was adopted, with the slit width of $0.8''$ or $1.6''$ depending on the seeing conditions. This yields a spectral resolution of R=750 or 375 throughout the observed wavelengths, which is tuned for sensitivity over resolution for our main spectral features of interest are the broad AGN emission. The exposure time for the targets were determined to yield a spectral S/N per resolution element of 10 for the detection of Mg II or Hβ, and 5 for Hα. We carefully checked each field around the target to be safe from neighbor source contamination when nodding the spectrum along its $15''$ slit length. The observations were performed through 2011B099, 2012A040, and 2012B090 proposals in 2011 December and 2012 February/December respectively, summing to a total on-target integration of 9.7 hours within a total three full and three half night runs including observations of other targets. The weather conditions were overall photometric but somewhat varying in atmospheric seeing from 0.6–$2''$. We nodded the spectra in AB mode with a 90–180s frame time for good dark and sky subtraction, while observing the A0 V type standard stars for correction of telluric absorption (Vacca et al., 2003) and flux calibration. Also, a set of flat-field and argon arc calibrations were executed for flat-fielding and wavelength calibration.

In addition to the NIR spectroscopy, we compiled the optical spectra of quasars from the Sloan database (DR10 including both the SDSS-I/SDSS-II and the SDSS-III BOSS data, Ahn et al. 2014), in order to estimate the C IV and Mg II line based $M_{\rm BH}$ and to compare them with rest-optical masses

or previous rest-UV measurements. Also, broad-band photometric data from GALEX GR7, SDSS DR10, 2MASS PSC, and UKIDSS DR10 releases (Martin et al. 2005; Ahn et al. 2014; Skrutskie et al. 2006; Lawrence et al. 2007) were collected to supplement the spectra with rest-frame UV–optical monochromatic continuum luminosities. The latest spectra and photometry were used when the target had overlapping data (SDSS-III BOSS over SDSS-I/SDSS-II, UKIDSS over 2MASS), while multiple spectra from the same instrument were averaged.

2.2.2 Data reduction

The reduction of the IRTF spectra were done using the IDL-based package Spextool (version 3.4, Cushing et al. 2004). It involves pre-processing (linearity, flat correction), spectral extraction, wavelength and flux calibration, combining multiply observed spectra, telluric correction, order merging, and spectrum cleaning. The standard package configuration was adopted, with a seeing dependent, 0.7–1.2″ Gaussian spatial extraction radius set identical for the target and standard star spectra. We found up to a ∼10–20% level of flux difference between different orders of the cross-dispersed spectra, which were leveled using the Spextool package. Moreover, we checked for the accuracy of standard star flux calibration by convolving each flux calibrated spectrum by the broad SDSS/UKIRT filter response curves, and comparing the spectroscopic flux to that from the photometry. Overall, we find the mean and rms scatter of the spectroscopic to photometric flux ratio, to be 0.94 ± 0.15 when averaged through the set of $griz$ filters, and 0.93 ± 0.39 through the $YJHK$ filters. Indeed, the large scatter in the IRTF spectral to photometric flux ratios suggest that the standard star flux calibration could become inaccurate for targets observed in variable seeing, airmass, or guiding conditions to when observing the standard stars. Thus, we give a constant multiplicative correction to the flux calibrated SDSS/IRTF spectrum separately, for the spectroscopic

Table 2.1. Summary of IRTF observations

Name	Coordinates	z	H	$t_{\rm exp}$	S/N
J01	J010205.89+001157.0	0.725	16.85	30	17
J02	J225631.30–102228.4	0.876	17.41	24	2
J03	J100943.56+052953.9	0.942	17.07	9	16
J04	J074815.44+220059.5	1.059	16.10	24	28
J05	J083937.85+223940.7	1.315	16.25	18	25
J06	J105705.16+311907.9	1.328	17.30	24	9
J07	J020256.11+124928.0	1.339	17.49	30	3
J08	J031926.24–072808.8	1.394	16.78	30	19
J09	J105250.06+335504.9	1.408	16.40	12	23
J10	J103453.06+445723.2	1.418	15.25	9	41
J11	J105440.84+273306.4	1.452	17.12	18	11
J12	J014542.78–100807.7	1.458	16.76	24	20
J13	J040022.40–064928.6	1.516	16.58	30	25
J14	J085515.59+045232.8	1.538	17.08	18	12
J15	J074043.47+314201.2	1.544	17.70	24	7
J16	J152156.48+520238.6	2.208	15.44	6	30
J17	J133928.39+105503.2	2.243	17.18	12	14
J18	J025644.69+001246.0	2.251	17.78	30	2
J19	J090444.34+233354.1	2.257	16.62	30	53
J20	J212329.47–005053.0	2.262	15.90	12	13
J21	J005202.40+010129.3	2.271	17.07	18	5
J22	J065101.23+380759.6	2.323	17.64	30	6
J23	J211157.78+002457.6	2.325	17.58	36	13
J24	J102648.16+295410.9	2.330	16.92	24	8
J25	J103546.03+110546.5	2.361	16.45	18	21
J26	J075158.65+424522.9	2.453	17.64	24	12
J27	J094602.31+274407.1	2.481	16.66	18	34

Note. — z is the redshift from S11, H is the H-band AB magnitude, $t_{\rm exp}$ is the exposure time in minutes, and S/N is the median signal to noise ratio at rest-frame 5500–7500$\AA$.

fluxes to be consistent to that from photometry.

We summarize the IRTF observations in Table 2.1, while we plot the flux calibrated spectra together with the photometric data points in Figure 2.1. The SDSS and IRTF spectra meet fairly well at their boundaries whereas the short wavelength ($\sim 1\,\mu$m) IRTF data are noisy due to some of the data taken in bright lunar phases and the weaker throughput of higher order spectra. The average continuum S/N around the Hα line is 17, which is suitable for measuring the black hole mass of most of the targets. Still, there are three tar-

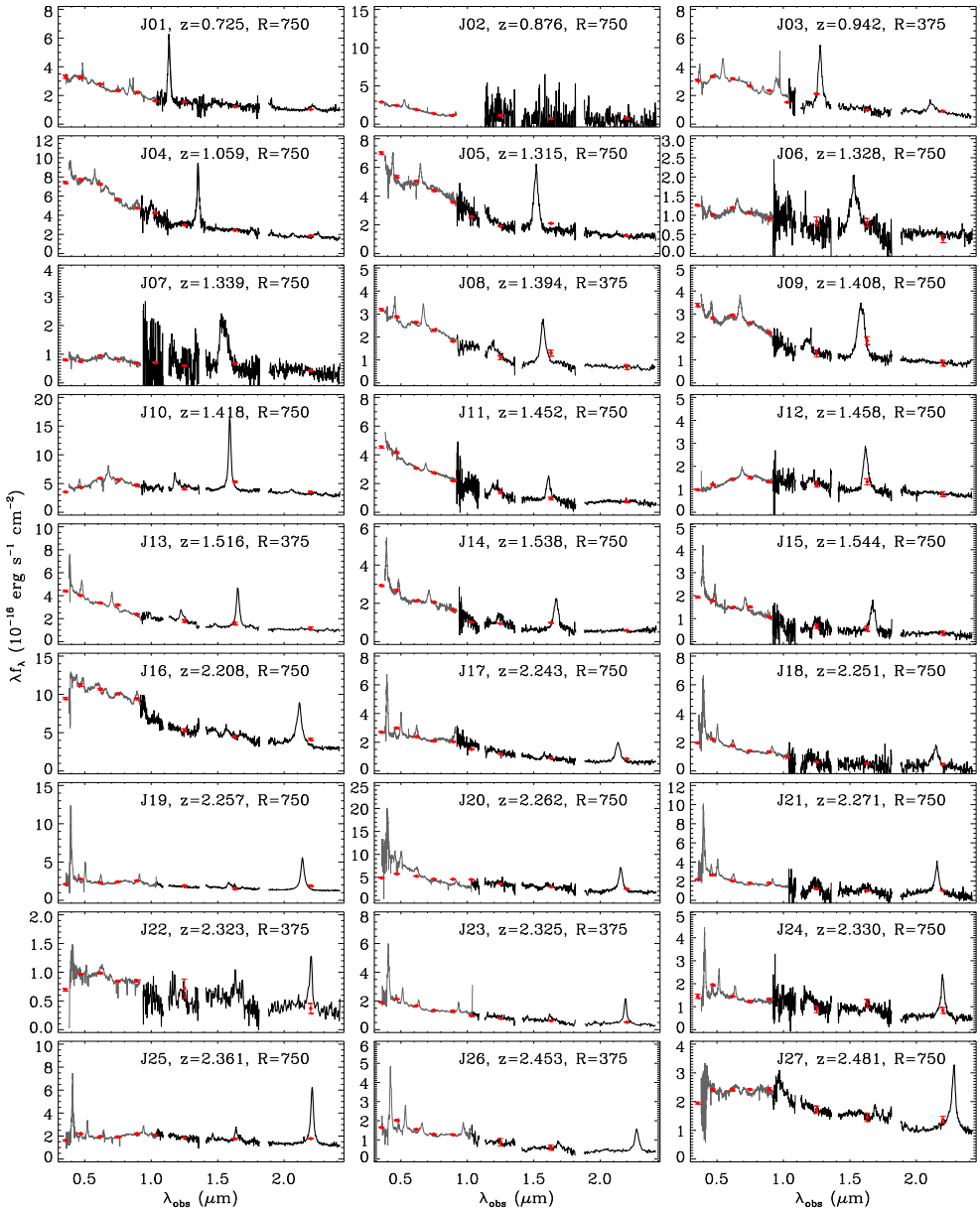

Figure 2.1: The observed-frame SDSS (gray) and IRTF (black) spectra of the sample. Wavelengths with strong NIR telluric absorption are not shown. Overplotted dots are the photometric data points from SDSS, 2MASS, or UKIDSS (red).

gets with median S/N < 5 at 5500–7500$\AA$, and we reject the target J02 from further analysis as even the Hα line strongest in the NIR spectra is too noisy. After all, we are left with 26 reduced spectra for $M_{\rm BH}$ estimation. Meanwhile, we further compiled the spectral fitting results of the $M_{\rm BH} > 10^{9.5} M_{\odot}$ SDSS quasars from Shen et al. (2011), in order to check the quality of the automated spectral fitting. All the compiled data were applied with galactic extinction correction, assuming the total-to-selective extinction ratio of R_V=3.1 and using the corrected form (Bonifacio et al., 2000) to the extinction map values of Schlegel et al. (1998).

2.3 Analysis

In order to estimate the $M_{\rm BH}$ of quasars through single epoch spectroscopy, we fit the Hα and Mg II line regions from the joint SDSS-IRTF spectra. We start from the rest-frame 4200–5600 $\AA$ fitting of the Hβ region. After subtracting the power-law continuum through 4100–4300 and 5500–5700 $\AA$ windows, we fit the Hβ emission by a single narrow (FWHM < 1200 km s^{-1}) gaussian and double broad (FWHM = 2000–12000 km s^{-1}) gaussian components, the [O III] doublet by double gaussians each, and the Hγ by a single narrow and single broad gaussian. During this process we iteratively determined the width and height of the Fe II complex from the least chi-square solution and subtracted it before the gaussian fit, using the Boroson & Green (1992) template for 4450–4650 and 5150–5350 $\AA$ regions. Once the width of the [O III]λ5007 was determined, we used it to fix the width of the various narrow emission lines near the Hα, since the narrow emission near the Hα are crowded and thus relatively complicated to model. We do not use the Hβ broad line luminosities or widths since the line sensitivity is relatively weaker than that of Hα.

Next, we fit the rest-frame 6000–7100 $\AA$ region including the Hα emission. We did not subtract the Fe II complex since they are weak and detached

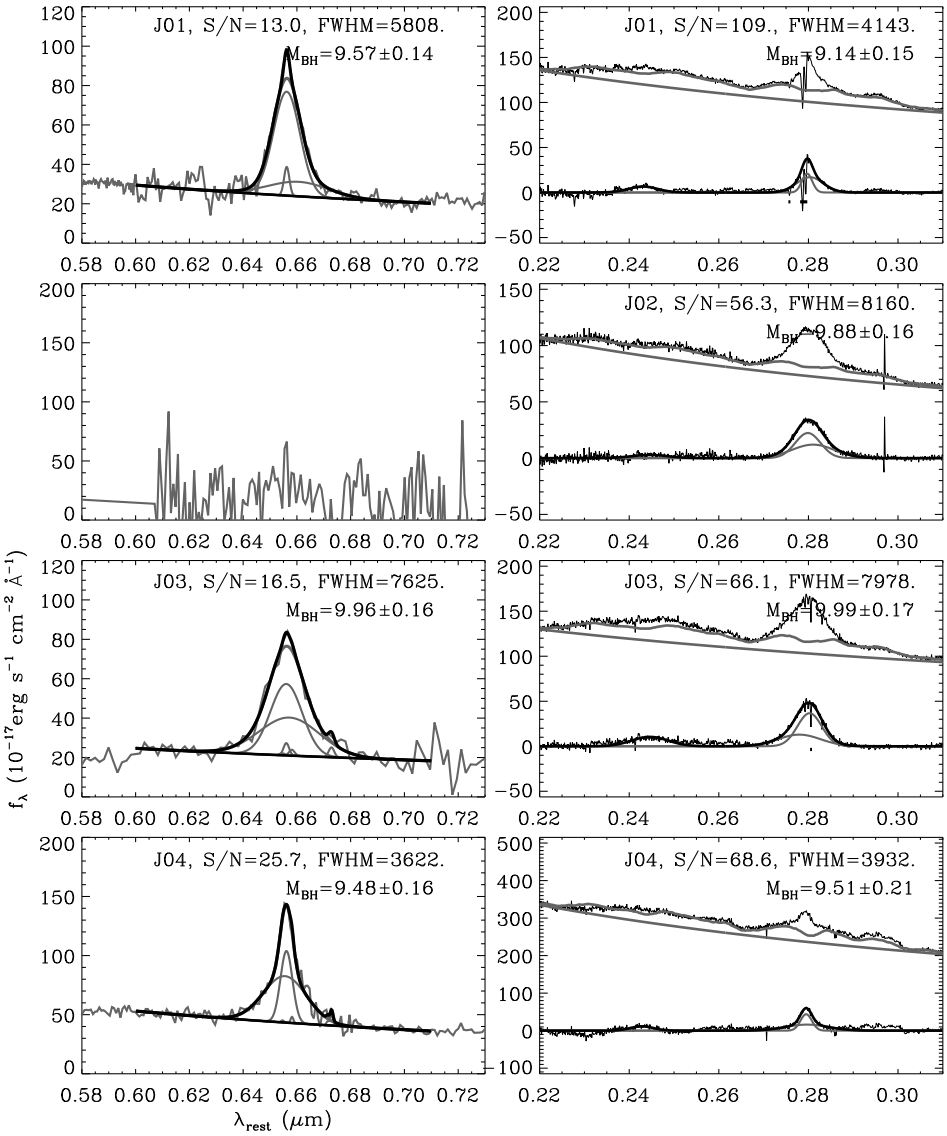

Figure 2.2: The spectral fitting of Hα (left) and Mg II (right) line regions, of the entire sample. On top of the resolution matched spectra are the narrow Hα, [N II], and [S II], broad Hα components (left, gray), the continuum and Fe II complex (right, gray), the broad Mg II components and the Fe III over the continuum/Fe II subtracted spectra (right, gray), and the sum of the total line and continuum components (left and right, black). We do not fit the spectra with too low S/N.

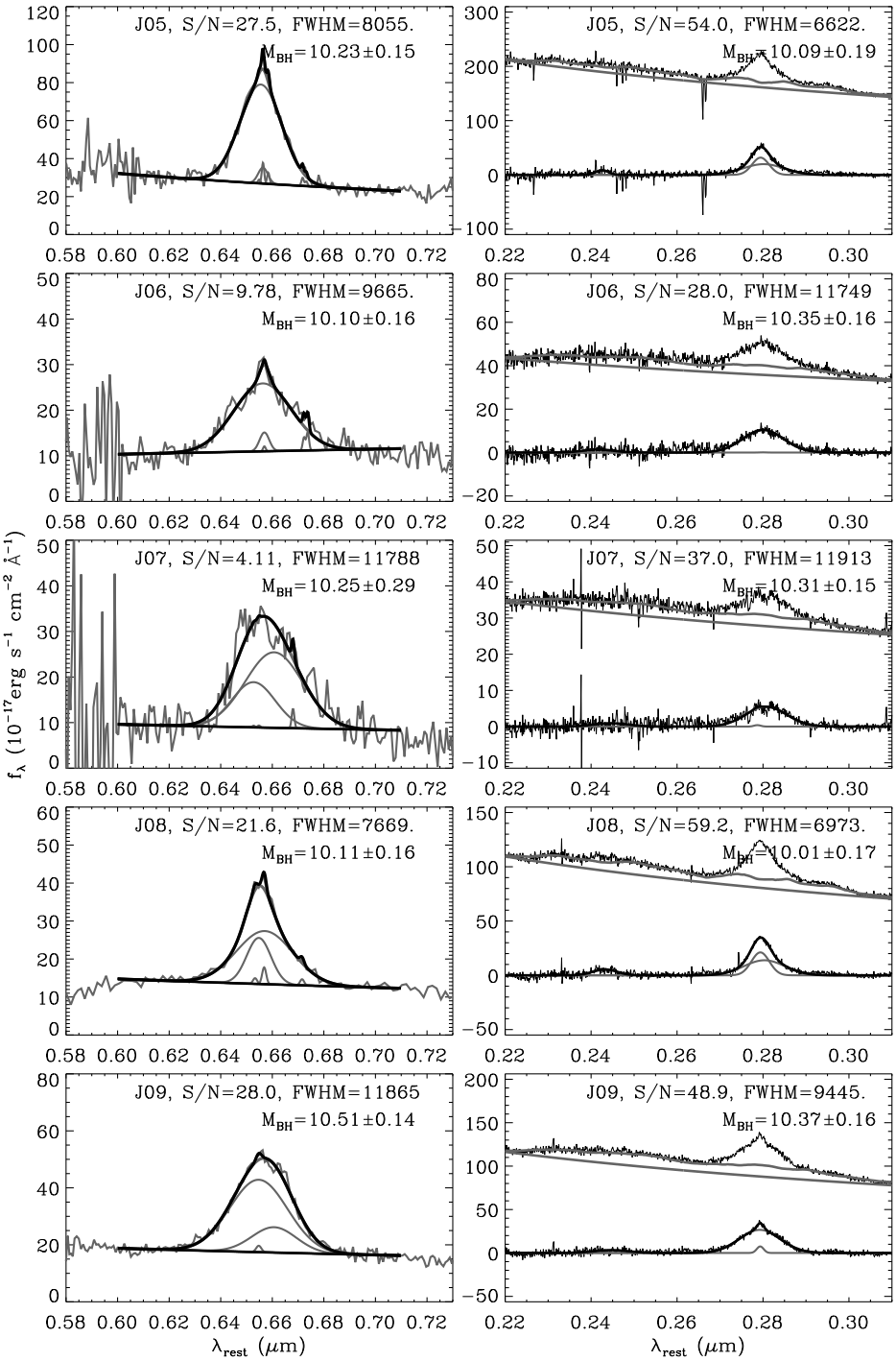

Figure 2.2: Continued.

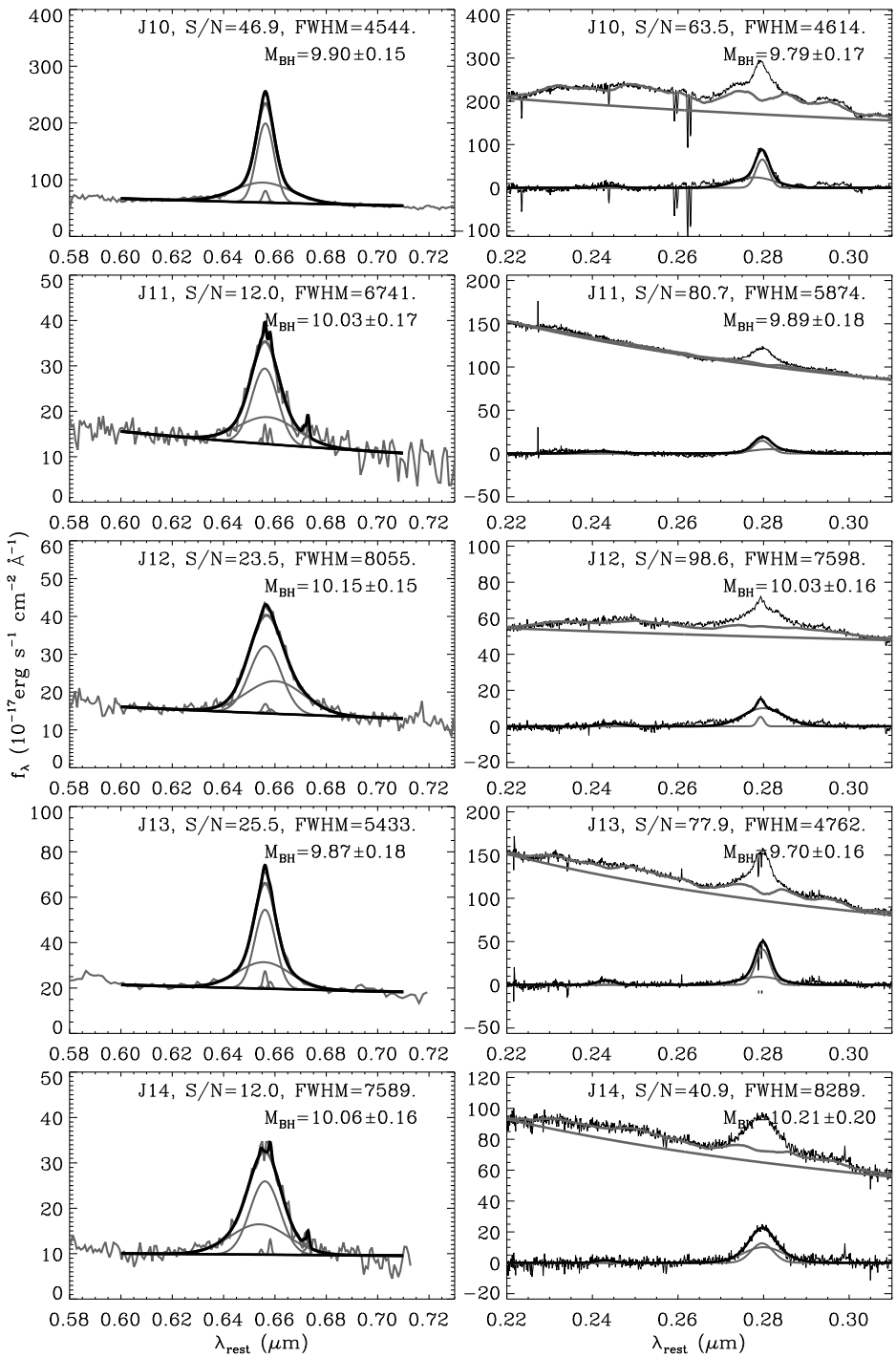

Figure 2.2: Continued.

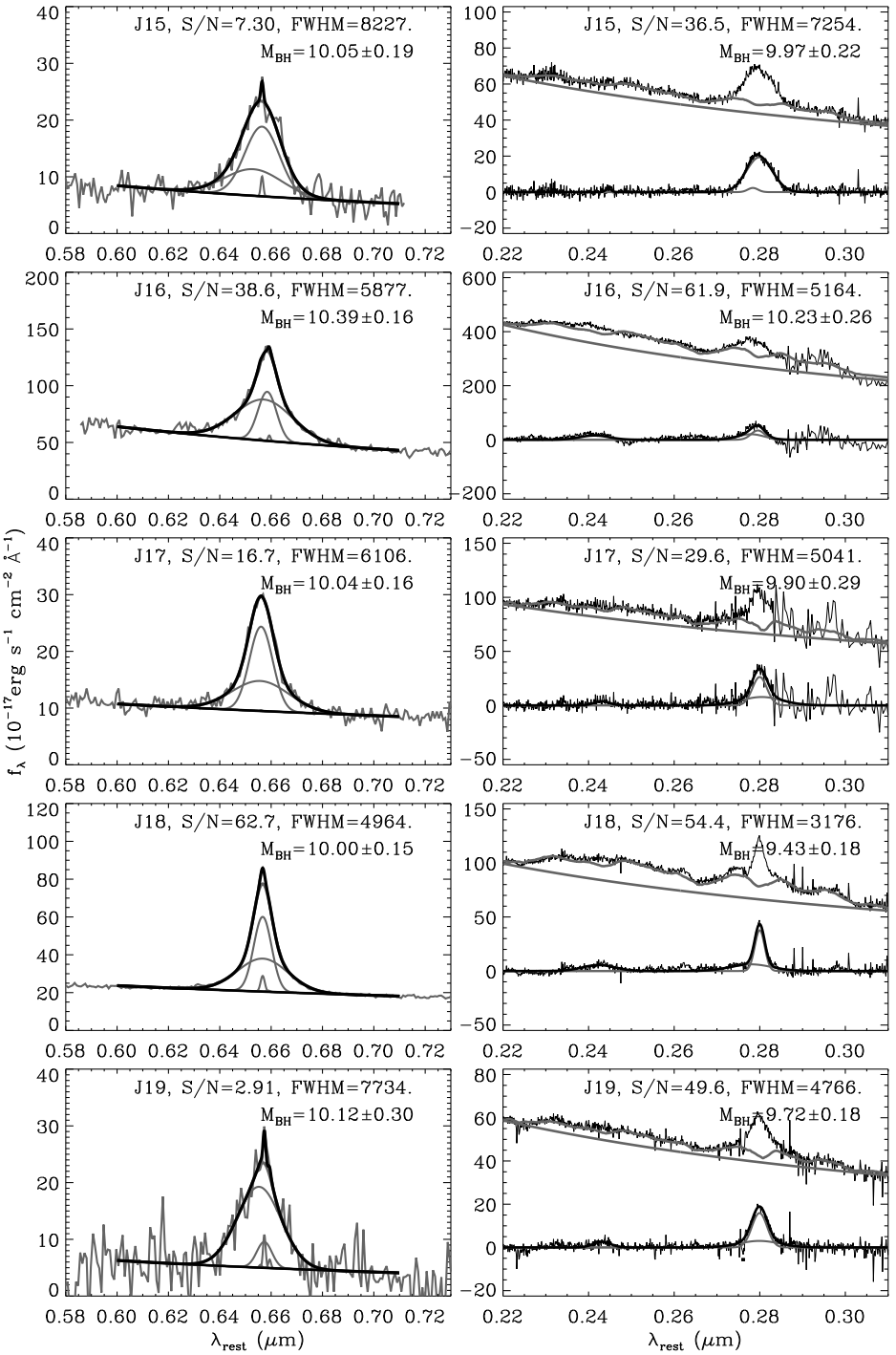

Figure 2.2: Continued.

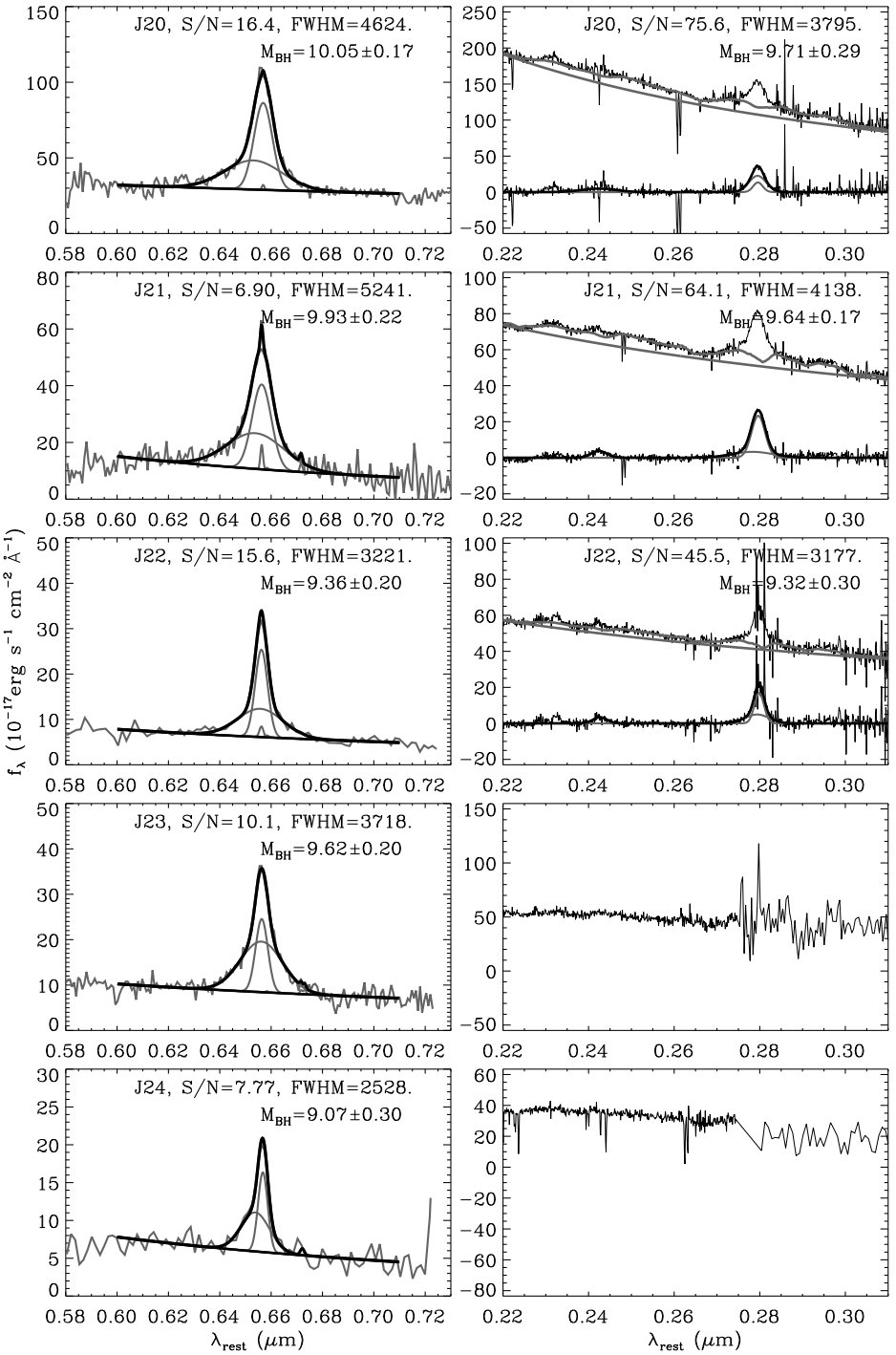

Figure 2.2: Continued.

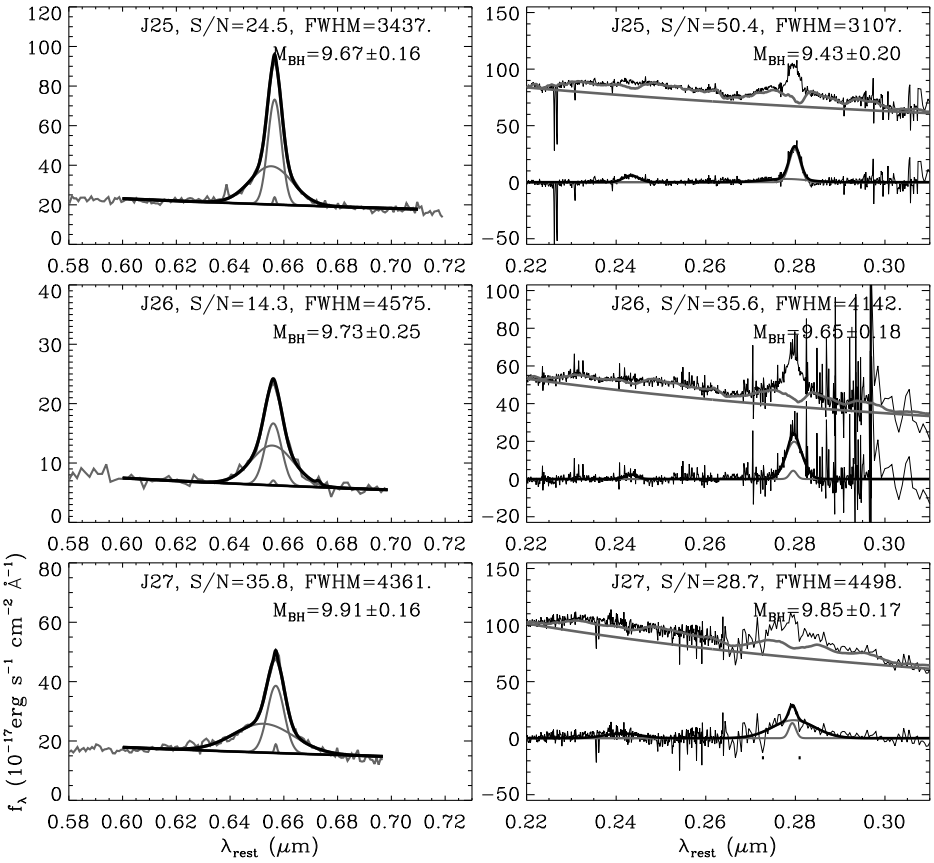

Figure 2.2: Continued.

from the Hα emission. A power-law continuum, single narrow gaussian and double broad gaussians for the Hα, two narrow gaussians for each [N II] and [S II] doublet, were simultaneously fitted with the narrow line width fixed as that of the [O III]. When the [O III] widths were not reliably measured due to poor resolution/sensitivity or strong broadening (FWHM $> 1200\,\mathrm{km\,s^{-1}}$), we fixed the narrow emission line widths to $400\,\mathrm{km\,s^{-1}}$, which is the mean FWHM of the narrow Hα out of $z < 0.37$, S/N > 20 SDSS quasars from Shen et al. (2011). Accounting for the instrumental resolution of SDSS ($R \sim 2000$) and IRTF ($R = 750$ or 375) spectra, we determined the intrinsic FWHM of the broad Hα after subtracting the instrumental FWHM from the observed FWHM in quadrature, and complied the continuum luminosity at 5100 $\mathring{A}$, L_{5100} that go into the mass estimator.

Lastly, we fit the rest-frame 2200–3100 $\mathring{A}$ region surrounding the Mg II emission. We used the Fe II template from Tsuzuki et al. (2006) since it provides the data close to the Mg II emission, compared to Vestergaard & Wilkes (2001). Following a similar methodology to the Hβ fitting, we iteratively subtracted the continuum and Fe II complex before fitting the Mg II, determined through 2150–2250 and 3050–3150 $\mathring{A}$ windows for the continuum and 2150–2410, 2460–2700, 2900–3150 $\mathring{A}$ windows for the Fe II. Afterward, we fitted the Mg II emission as double broad gaussians and the Fe III near 2420$\mathring{A}$ as a single gaussian. We note that the least chi-square solution for the width of the Fe II complex does not converge within our maximum threshold of three times the broad FWHM$_{\mathrm{H}\alpha}$, for 7 out of 25 objects. Examples of the Hα and Mg II fitting are given in Figure 2.2, with fitted parameters shown on each panel. We do not fit the C IV region, but use the fitted results of Shen et al. (2011), since the C IV emission are relatively straightforward to fit with weak Fe II nearby and without blending from other broad emission lines. The continuum luminosities and broad line widths are plugged into single epoch M_{BH} estimators for AGNs from Jun et al. (in prep., see Chapter 3) for each Hα, Mg II, and C IV emission

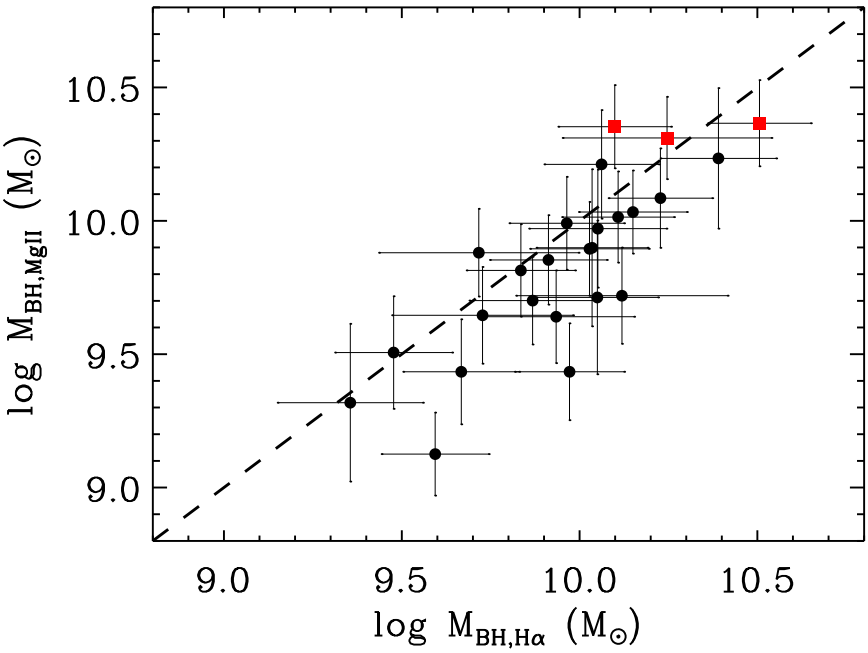

Figure 2.3: The comparison of Hα BH masses measured from IRTF spectroscopy, and Mg II masses from our fit to the SDSS-IRTF spectra. The objects with disk emitter features around the Hα are marked in red squares.

line measurements. The estimators are calibrated to yield consistent rest-UV to rest-optical $M_{\rm BH}$'s over a wide range of luminosity and redshift, suitable for this study.

2.4 Results

In Figure 2.3, we plot our measured $M_{\rm BH,H\alpha}$ and $M_{\rm BH,Mg_{II}}$. We find an overall agreement between the Hα, Mg II masses within measurement error up to $\sim 10^{10} M_\odot$, further supporting earlier results from relatively less massive regimes (e.g., Ho et al. 2012; Shen & Liu 2012; Matsuoka et al. 2013). Notice that our objects J06, J07, and J09 (possibly J19 but under a too low S/N), with asymmetric double peak or wing structures in addition to the smooth, broad Hα, all exceed $10^{10} M_\odot$ from both Hα and Mg II estimators. Because

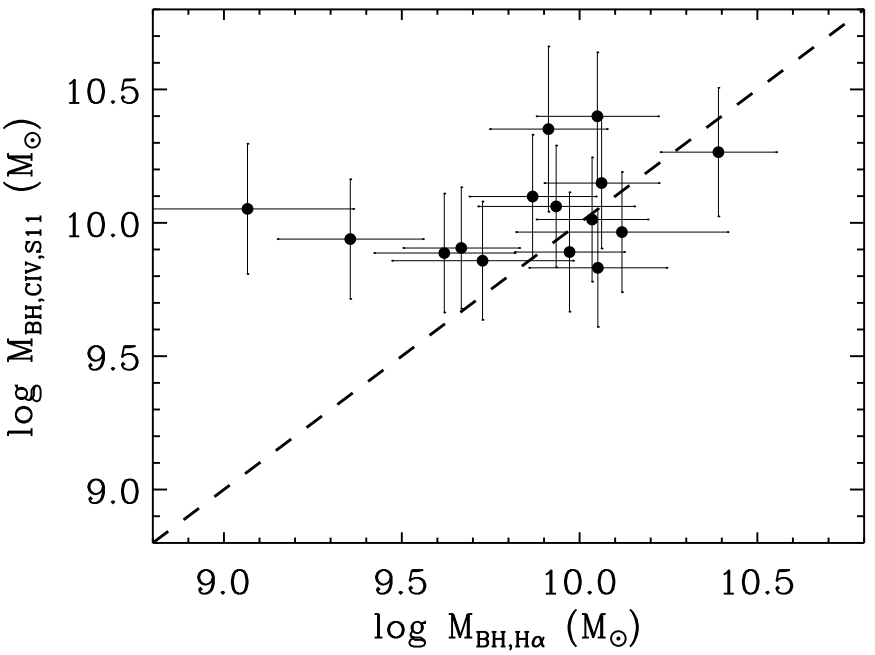

Figure 2.4: The comparison of Hα BH masses measured from IRTF spectroscopy, and C IV masses from SDSS spectral fitting of Shen et al. (2011).

these features resemble the disk emitters that are modeled by an accretion disk source (Chen & Halpern 1989; Eracleous & Halpern 1994), the single epoch mass estimation of AGNs from BLR kinematics may not hold when using the line width containing the disk emitter like features.

Figure 2.4 shows the comparison of our $M_{\rm BH,H\alpha}$, and $M_{\rm BH,C_{IV}}$ derived from the fitted quantities of Shen et al. (2011). The Hα and C IV masses are overall consistent at $\sim 10^{10} M_\odot$, but now there are outliers that are inconsistent as much as an order of magnitude, and 4 out of 8 quasars with $M_{\rm BH,C_{IV}} > 10^{10} M_\odot$ have $M_{\rm BH,H\alpha} < 10^{10} M_\odot$. This is in accord to previous studies that report a large scatter in between the Balmer and C IV BH masses (e.g., Netzer et al. 2007; Shen & Liu 2012).

2.5 Discussion

In Figure 2.5, we compare the $M_{\rm BH,Mg_{II}}$ derived from our spectral fitting and from Shen et al. (2011). Although the masses are mutually consistent, we noted in Section 2.3 that there are objects where the width of the Fe II complex did not converge within $3\,{\rm FWHM_{H\alpha}}$. Seven cases of this kind were found, where the three at $>10^{10}M_{\odot}$ sources overlap with the three objects with disk emitter features around the broad Hα (Figure 2.3). Therefore, we caution on the automated spectral fitting of Shen et al. (2011) that yields BH masses of over $10^{10}M_{\odot}$. Interestingly, these AGNs have consistent $M_{\rm BH,H\alpha}$ and $M_{\rm BH,Mg_{II}}$ although the disk emitter features are weakly found on the Mg II spectra, which indicates that disk emitters may not be easily identified out of extremely massive AGNs selected from rest-UV masses, placing negative implications on the reliability of $>10^{10}M_{\odot}$ $M_{\rm BH}$ measurements from $M_{\rm BH,Mg_{II}}$ alone.

Apart from features on the spectra that may yield spuriously large $M_{\rm BH}$'s, we consider the cases where both the rest-UV and rest-optical masses could be systematically overestimated from using single epoch estimators. One of the possibilities is the constant value of f-factor applied for all AGNs with diverse BLR motions. The upper limit in the intrinsic scatter of the f-factor comes from the intrinsic scatter of the local $M_{\rm BH}$–σ relation (~ 0.4 dex, Woo et al. 2013), which implies that some of the f-factor could be overestimated for individual AGNs. Considering a specific example of an isotropic motion of gas within the BLR (Netzer et al., 1990), it gives $f=3$ reducing 0.23 dex in BH mass to when $f=5.1$ is used in this work. Also, the $R_{\rm BLR}$–L relation has an intrinsic dispersion of 0.13–0.19 dex (Bentz et al., 2013), such that using this relation to an outlier could overestimate $R_{\rm BLR}$ from a given L. Summing these contributions together, we can expect as much as 0.36–0.42 dex of mass overestimation to our single epoch measurements. Even so, the upper envelope of $M_{\rm BH}$'s excluding the disk emitters will stay at $10^{9.8-10.0}M_{\odot}$, which supports

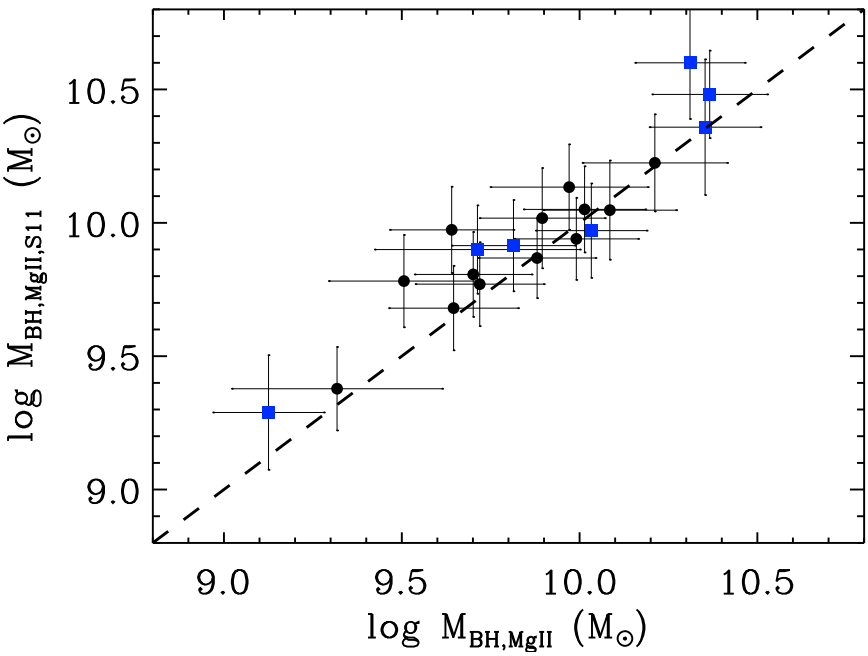

Figure 2.5: The comparison of Mg II BH masses from our fit to the SDSS spectra, and that from SDSS spectral fitting of Shen et al. (2011). The objects where the width of the Fe II complex did not converge within 3 $\mathrm{FWHM}_{\mathrm{H}\alpha}$, are marked in blue squares.

the most massive AGNs at $1 < z < 2$ indeed reach $10^{10} M_{\odot}$ unless our quasars are extreme outliers in the mass estimating recipes.

2.6 Summary

We followed up a sample of 27 extremely massive quasars at $0.7 < z < 2.5$ in order to cross check their rest-UV M_{BH} through rest-frame optical spectroscopy, and to examine possible biases to the measured M_{BH}'s. We summarize our study as follows.

1. The M_{BH} estimated for massive $\sim 10^{10} M_{\odot}$ quasars from the rest-frame UV estimators, are generally consistent to the Hα based estimates. However,

we find disk emitter like spectra for some objects measured to be $>10^{10} M_{\odot}$, which stands out more clearly on the broad Hα emission and should be carefully treated before accepting its mass.

2. We checked for systematic biases in the mass estimation recipes to calculate the possible overestimation in single epoch $M_{\rm BH}$'s. Neither the intrinsic scatter in the f-factor or $R_{\rm BLR}$–L relation rule out that there exists $\sim 10^{10} M_{\odot}$ AGNs in the intermediate redshift universe.

Chapter 3

Rest-frame Optical Spectra and Black Hole Masses of $3<z<6$ Quasars

3.1 Introduction

Quasars, galaxies that are in an active phase due to vigorous accretion of matter toward the central supermassive black hole (BH), are now vastly discovered by many surveys (e.g., Schmidt & Green 1983; Hewett et al. 1995; Boyle et al. 2000; York et al. 2000; Richards et al. 2002; Im et al. 2007; Willott et al. 2010; Wu et al. 2010). Through the discovery of quasars at high redshift (Fan et al. 2000; Cool et al. 2006; Goto 2006; Stern et al. 2007; Willott et al. 2007; Mortlock et al. 2011; Venemans et al. 2013; Bañados et al. 2014), we are witnessing the early stages of supermassive BH growth in the distant universe. At high redshift, the number density of optically luminous quasars quickly increases with cosmic time towards its maximum at $z = 2 \sim 3$ (Dunlop & Peacock 1990; Warren et al. 1994; Schmidt et al. 1995; Kennefick et al. 1995; Richards et al. 2006b; McGreer et al. 2013). Accompanied by high accretion rates among

luminous quasars at $z > 4$ (e.g., Willott et al. 2010; De Rosa et al. 2011; De Rosa et al. 2013), this suggests a rapid black hole growth of the luminous population of active galactic nuclei (AGNs) in the early universe. Also, an unusual population of AGNs known as dust-poor quasars – quasars with little infrared emission from hot and warm dust – is found to be more common at higher redshift (Jiang et al. 2010; Leipski et al. 2014). Luminous dust-poor quasars tend to have lower BH masses ($M_{\rm BH}$) or higher Eddington ratios compared to typical luminous quasars (Jiang et al. 2010; Jun & Im 2013), indicating the build-up of the AGN dusty substructure during its early mass accretion.

One of the key findings in the study of high redshift quasars is that there exist extremely massive BHs, with the mass reaching $M_{\rm BH} \sim 10^{10} M_{\odot}$ at $z = 2$–5, and $\sim 10^{9} M_{\odot}$ at $z =$6–7 (Jiang et al. 2007; Netzer et al. 2007; Kurk et al. 2007; Vestergaard et al. 2008; Shen et al. 2008b; Mortlock et al. 2011; De Rosa et al. 2013). Under the concordance cosmology, the time gap between the reionization epoch of the universe from the recent *Planck* study of the cosmic microwave background, $z \sim 11.5$ (Planck Collaboration et al., 2013), and $z = 6$ is 0.5 Gyr. Considering the case where a Population II stellar seed BH mass starts to grow at $z \sim 11.5$, the given time is too short for the seed to become an extremely massive BH at $z = 6$. Under the Eddington-limited accretion where the mass accretes at a maximal rate with the radiative acceleration and gravity in balance, we expect a BH to grow as $\exp\left(\frac{1-\epsilon}{\epsilon}\frac{t}{t_{\rm Edd}}\right)$ where $\epsilon, t, t_{\rm Edd}$ are the radiation efficiency, the duration of the mass accretion, and the Eddington limited timescale of 0.45 Gyr, respectively. Assuming a typical value of the radiation efficiency $\epsilon = 0.1$, a BH can grow by 2×10^4 times over the time span of 0.5 Gyr, without considering feedback mechanisms that could slow down the BH growth. This maximal growth factor is far too small for a stellar mass BH with a typical seed mass of $10\,M_{\odot}$, to grow into the extremely massive AGNs that have been observed recently. Consequently, BH seeds that may have started accreting prior to the reionization epoch, which are more massive

(e.g., Bromm & Loeb 2003; Begelman et al. 2006; Lodato & Natarajan 2006; Bellovary et al. 2011) or go through super-Eddington accretion (e.g., Volonteri & Rees 2005; Wyithe & Loeb 2012; Madau et al. 2014), are suggested to explain the $M_{\rm BH}$ of quasars at high redshift (also see a review on this subject by Natarajan 2014).

Obviously, accurate determination of $M_{\rm BH}$ is an important requirement for understanding of the BH growth at high redshift. This is especially true for BHs at the most massive end. A large uncertainty in $M_{\rm BH}$ can scatter the abundant low mass BHs into the high mass end of $M_{\rm BH}$ distribution, while the effect in the opposite direction is much less significant since high mass BHs are relatively rare. As a result, the number of extremely massive BHs can be easily overestimated. In principle, the correction to this effect is possible, but it requires a good knowledge on the error of $M_{\rm BH}$ measurements which is, however, rather difficult to obtain. This poses a potential challenge to the understanding of the BH growth at high redshift as described below. In most of high redshift quasar studies, BH masses are estimated using the rest-frame ultraviolet (UV)-part of spectra which is redshifted into the optical. The velocity widths of broad UV lines such as C IV and Mg II are used as measures of the gas motion of the broad line region (BLR), and the continuum or the line luminosity at the rest-frame UV (rest-UV) is used as a proxy for the size of BLR ($R_{\rm BLR}$). One gets $M_{\rm BH}$ by combining the two pieces of information through a virial mass estimator, $M_{\rm BH} \propto R_{\rm BLR} \times {\rm FWHM}^2_{\rm BLR}$ (e.g., McLure & Dunlop 2004; Vestergaard 2004; Baskin & Laor 2005; Sulentic et al. 2007; Shen et al. 2008b; Park et al. 2013).

While UV-based $M_{\rm BH}$ estimators are useful tools to measure BH masses of AGNs, they are secondary products that are derived from $M_{\rm BH}$ estimators established from the spectral properties in the optical wavelength window such as Hβ, Hα, and the continuum luminosity at 5100 $\mathring{A}$ (L_{5100}). By assuming the UV luminosity to follow the optical broad line region radius–luminosity

($R_{\rm BLR}$–L) relation with a constant factor, and the UV broad line width to follow the optical line width as a power law relation, the UV $M_{\rm BH}$ estimators are derived. Consequently, a number of studies have been carried out to justify the use of Mg II or C IV-line based $M_{\rm BH}$ estimators comparing the masses from UV $M_{\rm BH}$ estimators to those from the optical. While some studies suggest that UV-line $M_{\rm BH}$ estimators are reasonably accurate, especially for Mg II, other studies point out a large scatter between C IV-based measurements versus Hβ-based measurements which can make the C IV-based $M_{\rm BH}$ values uncertain by a factor of a few (e.g., Netzer et al. 2007; Shen & Liu 2012, hereafter S12). It has been noted that non-virialized motion (e.g., Denney 2012) or extinction (e.g., Assef et al. 2011), could severely modify the C IV line profile such that the $M_{\rm BH}$ cannot be reliably measured from a simple virial equation, although it is controversial on the exact origin of the discrepant UV-based $M_{\rm BH}$ with that of optical.

Furthermore, for the $M_{\rm BH}$ estimates to be valid, one also needs to justify the application of the low redshift $M_{\rm BH}$ estimators to high redshift, luminous quasars. Although one can expect that the $M_{\rm BH}$ estimators should not evolve in time in any significant way based on physical ingredients of AGN models, this has not been tested at the high redshift, high luminosity regime. An ultimate test would be to perform a reverberation mapping study of high luminosity quasars at high redshift, but such a study would take decades to complete, since the variability timescale is long for luminous quasars and the cosmological time dilation makes it even longer. Another way, albeit less direct than the reverberation mapping method, would be to investigate the correlation between the line luminosity and the continuum luminosity. At low redshift, the Hα or Hβ line luminosities are known to tightly correlate with the optical continuum luminosity (e.g., Greene & Ho 2005). As the radiation energy L from an accretion disk increases, the distance to the broad line region increases as $R \propto L^{0.5}$ from a simple photo-ionization argument, and this has

been confirmed observationally (Kaspi et al. 2000; Kaspi et al. 2005; Bentz et al. 2013).

Then, the energy flux of the radiation incident upon BLR clouds would be independent of the luminosity of the central power source. Yet, the observations show that the hydrogen line luminosity is proportional to the continuum luminosity from the central source. This suggests that the broad line luminosity is proportional to the amount of surrounding hydrogen gas in the BLR which in turn would be roughly proportional to the accretion rate that fuels the luminosity of the central source. A modification in the $R_{\rm BLR}$–L relation at high redshift or high luminosity for example, would result in an increase or a decrease in the incident energy flux upon the BLR, thus the correlation between the line and continuum luminosities is likely to be modified.

In order to estimate the $M_{\rm BH}$ using an optical $M_{\rm BH}$ estimator and to test the universality of the scaling relations in the rest-frame optical (rest-optical) for quasars at $z > 3.5$, spectroscopic observation is necessary at $\lambda > 2.5\,\mu$m. Spectroscopic observation of the distant and faint objects, however, is a very challenging task from the ground due to high thermal background at $\lambda > 2.5\,\mu$m and atmospheric absorptions, limiting such efforts to the study of Hβ line at $z < 3.5$ (e.g., Shemmer et al. 2004; Netzer et al. 2007; Assef et al. 2011). Recently, *AKARI* spectroscopic observations have provided a breakthrough for the study of the rest-optical spectra of distant objects, where its unique 2.5–5.0 μm coverage enables the redshifted Hα line to be probed from $z = 3$ to 6.5. With the *AKARI* spectroscopy, Oyabu et al. (2007) reported the detection of the redshifted Hα line of a quasar RX J1759.4+6638 at $z = 4.3$, and Sedgwick et al. (2013) investigated the star formation rate of submm galaxies at $z > 3.5$ based on Hα.

With one of the *AKARI* mission programs (guaranteed time) and also through several small open time programs, we performed a spectroscopic study of quasars at high and low redshifts, with the aim to obtain the rest-optical

spectra of high redshift quasars or the rest-frame 2.5–5.0 μm spectra of low redshift AGNs for the study of their properties with Brackett lines and 3.3 μm Polycyclic aromatic hydrocarbon lines. We call all these programs as QSONG (Quasar Spectroscopic Observations with NIR Grism) after the name of the mission program, and here, we present the rest-optical spectral properties of 155 type-1 quasars from QSONG, along with scaling relations and BH mass estimates based on these spectra.

The contents of the paper are constructed as the following. First, we use the spectro-photometric data including *AKARI* for $z \gtrsim 3$ AGNs (Section 3.2), and then derive the continuum and line emission properties (Section 3.3) in order to calibrate the Hα $M_{\rm BH}$ for the usage in high redshift. We check the validity of the continuum and broad line luminosity relations and line width relations with respect to the local, update the mass equations for Hα, Hβ, Mg II, and C IV, and compare the UV–optical $M_{\rm BH}$ (Section 3.4). Finally, we discuss on the reliability of single epoch $M_{\rm BH}$ estimators at high redshift, and investigate the massive end evolution of $M_{\rm BH}$ in distant AGNs (Section 3.5). Throughout this paper we adopt a flat ΛCDM cosmology with parameters of $H_0 = 70\,{\rm km\,s^{-1}\,Mpc^{-1}}$, $\Omega_m = 0.3$, and $\Omega_\Lambda = 0.7$. For the virial factor in the $M_{\rm BH}$ estimator, we adopt $f = 5.1 \pm 1.3$ based on the calibration of the $M_{\rm BH}$–σ relation using the combined sample of AGNs and quiescent galaxies by Woo et al. (2013).

3.2 Data

3.2.1 Sample

The majority of the data comes from the *AKARI* program QSONG, which is a two-year warm (phase–3) mission program consisting of $\sim$900 approved pointings, or $\sim$150 hours of observations. The program is aimed to obtain the rest-optical spectra of high redshift AGNs (Jun et al., 2012) or 2.5–5.0 μm

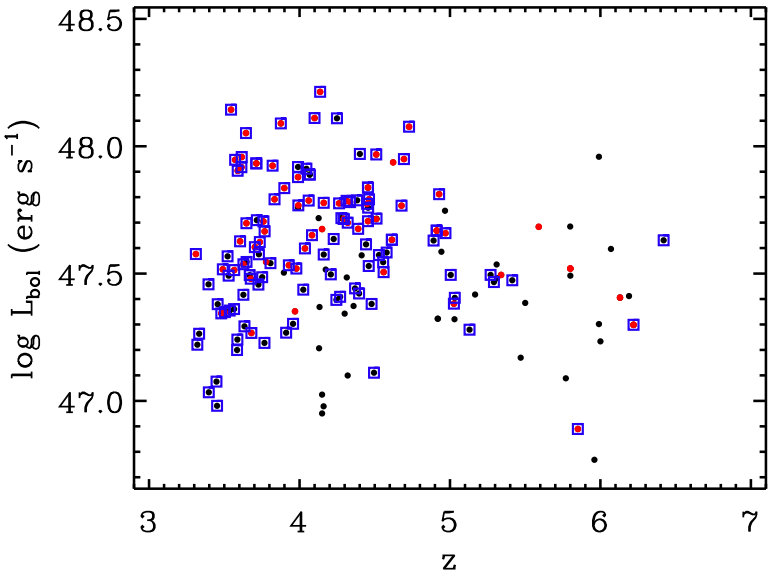

Figure 3.1: Bolometric luminosity–redshift distribution of our *AKARI* observed quasars. The subsample with $S/N_{H\alpha} > 2$ are marked in red dots, with the rest of the data in black dots. Objects with further rest-UV spectral coverage including the C IV emission are marked (blue squares).

spectra of low redshift AGNs. The sample for this high redshift study based on 65% of the entire QSONG data, is composed of optically luminous and spectroscopically confirmed type-1 quasars at $z \gtrsim 3$, mostly out of SDSS (DR5 catalog, Schneider et al. 2007; and additional discoveries from Fan et al. 2000; Fan et al. 2001; Fan et al. 2003; Fan et al. 2004; Fan et al. 2006a) and APM-UKST (Storrie-Lombardi et al. 1996; Storrie-Lombardi et al. 2001) surveys. The rest of the targets are included in Véron-Cetty & Véron (2010). We restrict the description of the sample selection and the observation to high redshift AGNs. For those who are interested in our *AKARI* observation of low redshift AGNs, please refer to another paper (Kim et al. 2014).

The targets are type-1 AGNs so that they allow the M_{BH} estimation from the broad line kinematics, through Hα/Hβ appearing within the *AKARI* near-IR (NIR) spectral coverage. In order to provide a minimal sensitivity limit to

the sample, we first considered the aperture size (68 cm) of the telescope and the restricted exposure time available at each sky position. After simulating the rest-optical spectra under the expected *AKARI* signal-to-noise ratio (S/N), the targets were chosen with z-band flux limits of ∼18.5 and 19 AB magnitudes in bright and faint subsamples, respectively, with longer exposure time assigned to fainter targets for clear line detection. Moreover, the targets were bounded for $3.3 < z < 6.4$ to place the Hα emission and the surrounding continuum within the 2.5–5.0 μm wavelength window of *AKARI* NIR spectroscopy. Without further constraints the targets were randomly selected in coordinates, redshift, and luminosity. We plot the distribution of z–$L_{\rm bol}$ in Figure 3.1, where $L_{\rm bol}$ is calculated from our 5100 $\AA$ luminosity with a bolometric correction of 9.26 (Shen et al. 2011, hereafter S11) from the spectral energy distribution (SED) of Richards et al. (2006a).

Following the Hα observations of distant AGNs through *AKARI* NIR spectroscopy (Oyabu et al. 2007; Oyabu et al. 2009), our initial Hα survey of 14 quasars at $z \sim 6$ under the Helium-cooled (phase–2) open time program HZQSO (Im, 2010), demonstrated the feasibility of *AKARI* observations in detecting the redshifted Hα emission. QSONG is essentially a phase–3 extension of the survey, for the purpose of vastly expanding the number of targets at the expense of warm phase sensitivity, therefore probing a lower redshift distribution of quasars than HZQSO, to peak at $z \sim 4$. In addition, two more phase–3 open time programs, HQSO2 and DPQSO, were aimed to either push the redshift limit of QSONG or to detect fainter optical line emission (Hβ and [O III]), from deep exposures. Unfortunately, the Helium-dry observations led to significantly higher noise levels than expected, restricting the distinct scientific goals of the phase–3 programs that required better sensitivity. Therefore, we decided to merge all open time programs listed above under the scope of QSONG.

3.2.2 Data acquisition

We mostly used the NIR grism (NG) mode of the Infrared Camera (IRC, Onaka et al. 2007; Ohyama et al. 2007) onboard the *AKARI* satellite (Murakami et al., 2007). It offers a low, wavelength dependent spectral resolution (R) from a roughly constant, ~ 3 pixels per resolution element. At 3.6 μm, $R = 120$ which corresponds to a velocity resolution of 2500 km s^{-1}, sampled by a pixel scale of 0.0097 μm in wavelength and 1.5″ in angular size. Meanwhile, a limited number of NIR prism (NP, $R = 19$ at 3.5 μm) observations were performed to better catch the fainter continuum and line luminosities. The NG targets were placed in a $1' \times 1'$ rectangular slit aperture to reduce source confusion.

The observations were performed under the Astronomical Observation Template (AOT) mode of AOT04, typical for spectroscopic observations. The number of NG pointings per target was normally 3–5 for QSONG, where one pointing observation corresponds to 355 or 400 sec on-source exposure. The number of pointings were determined based on the z-band flux, generally set to be smaller for phase–2 and larger for phase–3 open time programs. The NP observations were performed with usually 1–2 pointings. By the time of termination of the satellite mission, the QSONG program was 85% complete with 144 high redshift quasars observed. The open time programs were complete before the satellite lifetime, adding another 33 targets.

To supplement the NIR spectra, we compiled the optical spectra of the *AKARI* quasars from the Sloan Digital Sky Survey (SDSS) database (DR10 including both the SDSS-I/SDSS-II and the SDSS-III BOSS data, Ahn et al. 2014), and from observations of APM-UKST quasars (Storrie-Lombardi et al. 1996; Péroux et al. 2001) and Q0000–26 (Schneider et al., 1989), in order to estimate the C IV line based $M_{\rm BH}$. Also, we collected broad-band photometric data from optical to mid-infrared (MIR) imaging, for the calculation of the rest-frame UV–optical continuum luminosity of AGNs through SED fitting (Section 3.3.2). The data includes SDSS DR9, 2MASS PSC, UKIDSS DR10,

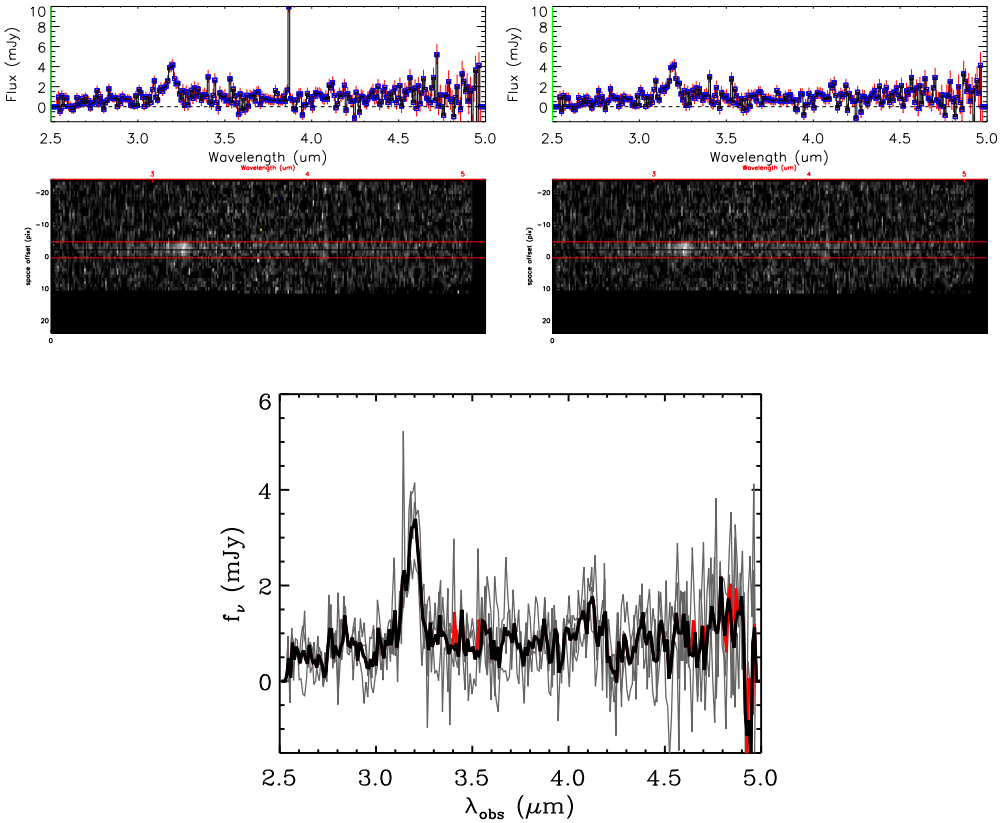

Figure 3.2: A sequential visualization of the data treatment additional to the pipeline processing. From the pipeline processed spectrum (left, 1D at top, and 2D at bottom), hot pixels were rejected (center) before the spectral extraction within the aperture mask (red lines). The multiple pointings extracted (right, gray lines) were stacked (thick black line) with sigma clipping (red line indicates clipped data).

Table 3.1. Summary of observations

Program name	Phase	Observed period	Mode	Number of targets	Observed pointings	Rejected pointings
HZQSO	2	Nov 2006–Aug 2007	NG	7	26	2
			NP	5	16	7
QSONG, HQSO2, DPQSO	3	Jun 2008–Jan 2010	NG	147	622	74
			NP	6	11	3

Note. — NG and NP stand for NIR grism and prism modes, while a pointing is about 10 minutes long. For QSONG data only the high redshift subsample are noted. The total number of targets is 165 excluding 22 rejected sources from confusion, problems in the spectra or data reduction. 10 objects are either duplicated or different in observing mode or program, yielding an effective total of 155 independent objects.

and WISE all-sky releases (Ahn et al. 2012; Skrutskie et al. 2006; Lawrence et al. 2007; Wright et al. 2010), and existing Spitzer or *AKARI* imaging (Jiang et al. 2006; Oyabu et al. 2009).

3.2.3 Data reduction

The data were reduced using the automated IDL pipeline package IRC_SPECRED (versions 20110114, 20111121 for phase–2 and 3, Ohyama et al. 2007), where pre-processing (dark, linearity, flat corrections), image registration and coaddition, flux and wavelength calibration, astrometry, spectral extraction, and aperture correction were the main tasks involved. The standard pipeline configuration was adopted, except for the usage of short exposure when the image taken for registering subframes of spectral data were contaminated by saturated stars. This procedure considerably improved the registration of 2-D spectra in both spatial and wavelength directions. In addition, astrometry of the reference image was upgraded using the 2MASS point source catalog to better extract the faint NIR spectra. Indeed, the zeroth order positions of the spectra and the 2MASS coordinates were visually well aligned for spectral extraction.

Due to the increased number of hot pixels and the background level in the phase–3 data, a non-negligible number of bad pixels remained in the reduced spectral data even after applying the IRC_SPECRED pipeline. To remove the remaining hot pixels, a further data reduction step was taken to obtain a cleaner set of spectra, as depicted in Figure 3.2. After running the spectroscopic pipeline we subtracted the remaining hot pixels using L.A.Cosmic (van Dokkum, 2001) with a threshold of $2.5\,\sigma$, and combined the 1-D spectra with a 2.5-sigma clipping. This threshold was chosen by visually inspecting the reduced spectra so that the chosen threshold removes the spiky hot pixels efficiently without affecting emission lines. Because the typical full width at half maximum (FWHM) of the broad lines in our AGNs is broader than the

spectral resolution of NG (2500 $\mathrm{km\,s^{-1}}$) but not that of NP (15,800 $\mathrm{km\,s^{-1}}$ at 3.5 μm), the hot pixel rejection and the sigma clipping were applied on the NG data only, while the undersampled NP emission spectra were kept unchanged. We clipped 2.7% and 2.9% of the NG spectral data through L.A.Cosmic and the combining process respectively.

We extracted the 1-D spectra of 3 pixel width for the phase–2 data to maximize S/N, but the width was widened to 5 pixels for the phase–3 data since the noisier spectra made it difficult to determine the center of the object spectrum. Aperture corrections were automatically carried out from the pipeline to derive the total flux, for given respective extraction widths. The pipeline did a fair job of placing the extraction aperture on the right location, but visual inspection showed it necessary to make a -1 pixel shift in spatial direction for 90% of the sample. For 10% of the cases, a bigger shift of -2 to 1 pixels was necessary. The wavelength zeropoints were determined from the pipeline taking into account the satellite attitude drift and sub-pixel coordinate rounding effects, and we did not apply any further correction as the zeropoints were confined within a 0.5 pixel scatter.

Multiple pointings of the 1-D spectra were stacked by each object, where the NG spectra were interpolated to a fixed wavelength grid, flux averaged, and error rescaled assuming Poisson error statistics. Multiple pointings of NP spectra were gathered without modifying the individual spectrum, due to their poor spectral resolution. Out of 675 pointing observations, we used 589 pointings from 165 objects, since some of the pointing observations were not usable due to contamination of the object spectrum by adjacent sources. We excluded pointing observational frame in the analysis when there was a source that is brighter than the target and its distance from the target in the spatial direction is less than the FWHM. In rare occasions, the reduction pipeline did not run properly and such data were not used. Table 3.1 summarizes the observations regarding the reduced data. The supplementary optical spectra and

the multi-wavelength imaging data are outlined in Table 3.2. In Figure 3.3, we plot the $S/N_{H\alpha}$ histogram, where the S/N is measured within $\pm$ FWHM$_{H\alpha}$ from the line center. The Galactic extinction is corrected for these spectro-photometric data, assuming the total-to-selective extinction ratio of R_V=3.1 and using the corrected form (Bonifacio et al., 2000) to the extinction map values of Schlegel et al. (1998). The photometric measurement schemes are different in each survey data, such that host galaxy contamination may not be well subtracted. We keep the diverse magnitude type and imaging resolution of each survey data however, as the high luminosity AGNs yield a compatible set of magnitudes dominated by the central AGN contribution (Jun & Im, 2013).

3.3 Analysis

3.3.1 Spectral fitting

We modeled the rest-frame 5500–7500Å spectra of our AGNs, as a sum of the power-law continuum $f_\lambda = c\,\lambda^{-(2+\alpha)}$ (where $f_\nu \propto \nu^\alpha$) and the gaussian Hα emission components. We did not attempt to fit the relatively weak emission features far (He I, [O I]), or near the Hα ([N II] and [S II] doublets, Fe II complex), as they were not detectable under the *AKARI* spectroscopic sensitivity. Likewise, the Hβ and [O III] lines were too weak to be detected in most cases and were not fitted accordingly. Examples of the fitting are given in Figure 3.4, with fitted parameters shown on each panel. We found that 23% of the sample show spiky emission/absorption features around the Hα line from low S/N spectra, which were manually masked out. The Hα line was modeled as a single broad gaussian with observed FWHMs of 2500–10,000 km s^{-1}, for the inability to clearly resolve the narrow or multiple broad components at $R \sim 120$. The Hα line center was set free within $\pm$ 2500 km s^{-1} to the UV line-based redshift from references in Table 3.2. However, we found four exceptions whose the

Table 3.2. Supplementary data

Name	Wavelength	N	Exposure	Reference
Spectra				
SDSS	3800–9200Å	111	45m	1
BOSS	3650–10400Å	98	45m	1
APM–UKST	∼3500–9000Å	16	15–60m	2,3
Hale	4500–9000Å	1	30m	4
Photometry				
SDSS	$ugriz$	134	54s	5
2MASS	JHK	73	8s	6
UKIDSS	$YJHK$	34	40s	7
WISE	$W1$–$W4$	160	124s	8
Spitzer	IRAC, MIPS 24μm	8	17–23m	9
AKARI	IRC 2–11μm	1	–	10

Note. — N is the number of matches to the 165 *AKARI* objects in Table 3.1. Exposure times are typical values. The references numbered are in the increasing order as Ahn et al. 2014; Storrie-Lombardi et al. 1996; Péroux et al. 2001; Schneider et al. 1989; Ahn et al. 2012; Skrutskie et al. 2006; Lawrence et al. 2007; Wright et al. 2010; Jiang et al. 2006; Oyabu et al. 2007.

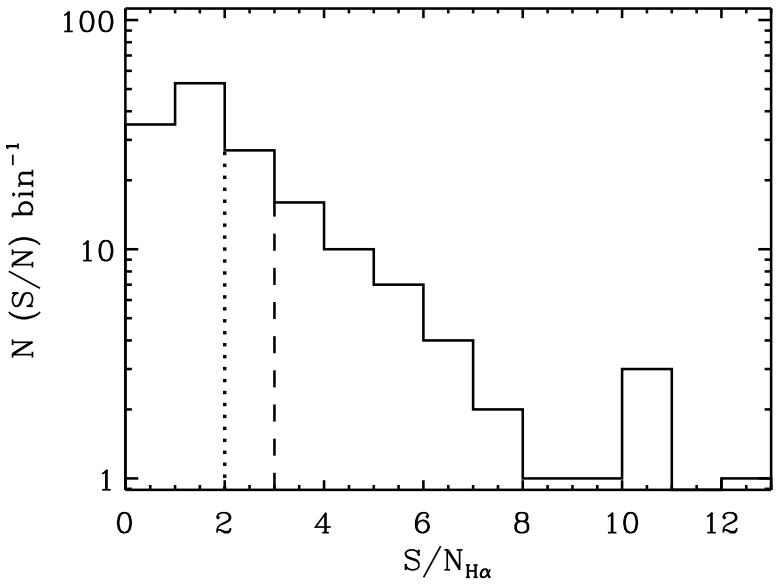

Figure 3.3: The $S/N_{H\alpha}$ distribution of our 160 *AKARI* observed quasars. The $S/N_{H\alpha} > 2$ and > 3 cuts are marked in dotted and dashed lines, which are given to limit the measurement of $L_{H\alpha}$ and $FWHM_{H\alpha}$ respectively (Figure 3.5).

Hα line centers were significantly redshifted from the UV-line based redshifts. In these cases, the velocity range was loosened to $\pm\,10{,}000\,\mathrm{km\,s^{-1}}$, where the H$\alpha$ showed velocity shifts of 3600–5600 $\mathrm{km\,s^{-1}}$. Next, the measured broad line width $FWHM_{obs}$, was subtracted by the instrumental resolution $FWHM_{ins}$ (2500 $\mathrm{km\,s^{-1}}$ for NG) in quadrature, to obtain the intrinsic line width FWHM $= \sqrt{(FWHM_{obs})^2 - (FWHM_{ins})^2}$.

Extracting the broad emission line luminosity and width is important in accurately estimating the M_{BH} of AGNs. The limited *AKARI* sensitivity (Figure 3.3) and spectral resolution could produce systematic bias in the measurement of line parameters such as the line luminosity and widths (e.g., Denney et al. 2009). Therefore, we investigated how the low resolution, low S/N spectra affect the quality of the spectral fitting. This was done by running Monte Carlo simulations on a set of luminous SDSS quasar spectra (DR7, Schneider et al. 2010) of $R \sim 2000$ to mimic the quality of *AKARI* spectra. Given that the

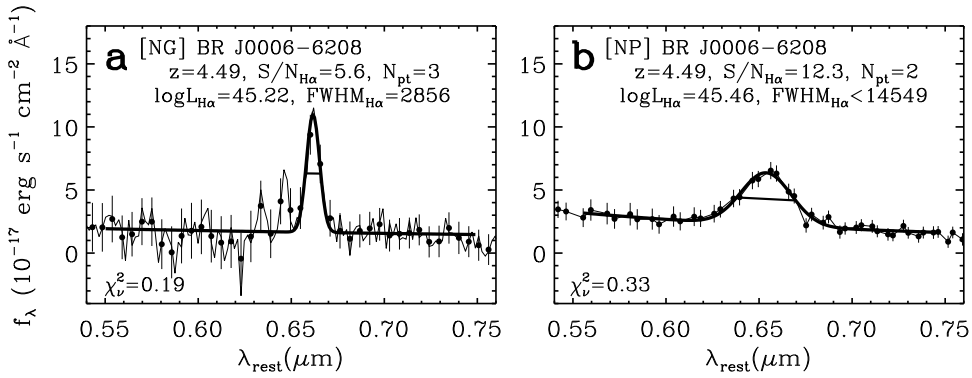

Figure 3.4: Examples of the rest-frame Hα emission fitting. On top of the spectra (thin line), the resolution (3 pixel) matched data (dots) and errors, the best-fit to the continuum and Hα line emission (thick line), and FWHM are indicated. On the figures, the observation mode, the name of object, the redshift and S/N of the Hα emission, the number of *AKARI* pointings, N_{pt}, Hα luminosity (ergs s^{-1}) and FWHM (km s^{-1}) are printed. The (a) NG and (b) NP observations performed for BR J0006–6208 gives an idea of the enhanced resolution and sensitivity of each spectroscopic mode.

host galaxy contamination to the quasar spectrum is negligible at $L_{\rm bol} > 10^{46}$ ergs s^{-1} (Shen et al. 2011, hereafter S11), we collected 15, $L_{\rm bol} > 10^{46}$ ergs s^{-1}, type-1 quasar spectra with continuum sensitivity of S/N > 20, where the Hα emission region is present ($z < 0.3$) and well fit ($\chi^2_\nu < 2$) from S11.

We smoothed the SDSS spectra with a Gaussian function to match the *AKARI* NG resolution, R=120, and rebinned the data to match the 3 pixel per resolution sampling of the *AKARI* spectra. Then, without adding extra noise, we followed the same method to measure the Hα line FWHM and luminosity as for the *AKARI* spectra (e.g., Figure 3.5a). In Figures 3.5b and 3.5c we compare the fitted parameters FWHM$_{\rm H\alpha}$ and $L_{\rm H\alpha}$ from the smoothed and binned spectra, to that of the measurement from S11. We find that the FWHM at > 2500 km s^{-1} and the line luminosity from the degraded resolution spectra, are remarkably consistent with S11 within ~ 0.04 dex offset and intrinsic scatter ($\epsilon_{\rm int}$). This could bias the $M_{\rm BH}$ measurements up to ~ 0.1 dex in offset and $\epsilon_{\rm int}$ when following the $M_{\rm BH} \sim L^{0.5} \times {\rm FWHM}^2$ behavior, but this

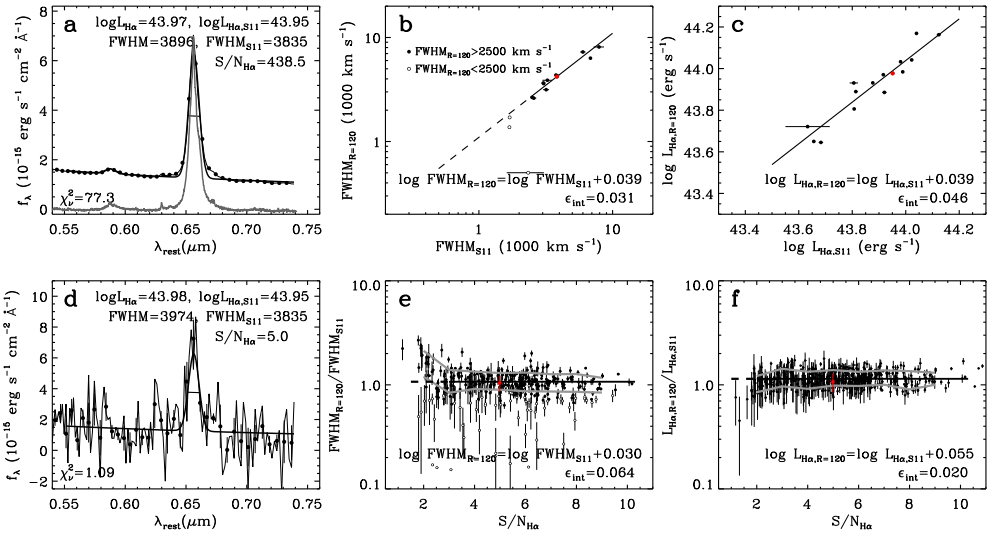

Figure 3.5: An example of fitting the resolution degraded SDSS spectrum to test the reliability of $M_{\rm BH}$ from *AKARI* observations (top left), where the continuum subtracted original SDSS spectrum (gray), and the *AKARI* resolution matched spectrum (black dots) with fit to the data (thick line) are plotted. The broad $\rm FWHM_{H\alpha}$ of $z<0.3$, $L_{\rm bol}>10^{46}$ ergs s^{-1} SDSS quasars from S11 are compared to our fit (top center) to the smoothed and binned spectra that matches the resolution and the sampling of the *AKARI* data. Offsets from a 1–1 relation and intrinsic scatter ($\epsilon_{\rm int}$) are displayed, where only the $\rm FWHM_{H\alpha}>2500$ km s^{-1} data are used for the comparison of FWHMs. Notice the red highlighted symbol to represent the example on the leftmost panel. Likewise, the Hα luminosity from S11 and our single gaussian fit to the modified spectra, are compared (top right). Further down of the figure, we also test the effect of low sensitivity to the fitting by adding a set of gaussian random noise to the resolution degraded spectrum (bottom left). The ratio of our $\rm FWHM_{H\alpha}$, $L_{\rm H\alpha}$ measurements to that from S11 are plotted along the $\rm S/N_{H\alpha}$ (bottom center and right). The range of binned average offset plus rms scatter along $\rm S/N_{H\alpha}$ are shown in gray lines. When calculating the overall offset and rms scatter of the quantities, only the $\rm S/N_{H\alpha}>3$, $\rm FWHM_{H\alpha}>2500$ km s^{-1} data are used for the comparison of $\rm FWHM_{H\alpha}$, and the $\rm S/N_{H\alpha}>2$ and any $\rm FWHM_{H\alpha}$ data for the $L_{\rm H\alpha}$.

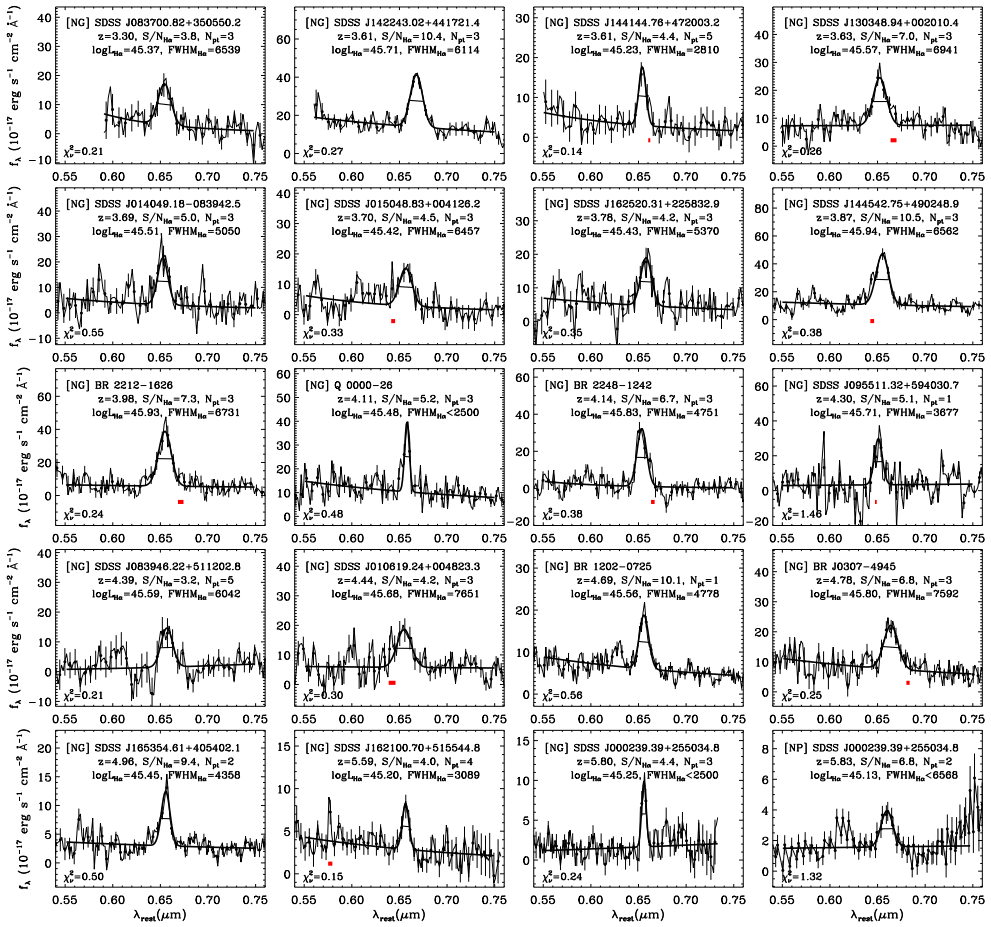

Figure 3.6: Rest-frame Hα spectral fitting of selected objects with $S/N_{H\alpha} > 3$, sorted by the Hα redshift. The data point symbols and colors follow the meaning of Figure 3.4. When there were contaminations to the Hα emission, we masked out the region (red rectangle).

is smaller than the typical $M_{\rm BH}$ measurement uncertainty (e.g., Figure 3.14c). Exceptions to the consistency between the simulated and observed parameters are the line width measurements at $\rm FWHM_{H\alpha} < 2500\ km\,s^{-1}$, where the simulated FWHM values fall below the extrapolated linear relation. Therefore, we give a $\rm FWHM_{H\alpha} > 2500\,km\,s^{-1}$ limit to our *AKARI* data to restrict the sample with less biased line width measurements. Meanwhile, the narrow Hα and [N II] doublet luminosities of the fiducial SDSS AGNs add up to the broad $L_{\rm H\alpha}$, by less than 0.01 dex altogether. The weakness of the narrow emission lines in luminous AGNs guarantees that the narrow line contaminations to the degraded resolution spectra are negligible.

Second, to investigate the effect of low S/N to the fitted results, we added a set of random gaussian noises on top of the degraded resolution spectra. Each SDSS spectrum was repeatedly simulated 30 times adding the random errors, for the $\rm S/N_{H\alpha}$ to be distributed down to the level of *AKARI* S/N. Again, we followed the same method to measure the Hα line FWHM (only for the $\rm FWHM_{H\alpha} > 2500\,km\,s^{-1}$ objects from Figure 3.5b) and luminosity as for the *AKARI* spectra (e.g., Figure 3.5d). In Figures 3.5e and 3.5f we plot the ratios of $\rm FWHM_{H\alpha}$ and $L_{\rm H\alpha}$ from the degraded resolution and sensitivity spectra, to that from S11, along $\rm S/N_{H\alpha}$. Overall, we find both $\rm FWHM_{H\alpha}$ and $L_{\rm H\alpha}$ to be similar to the values before adding the noises, at $\rm FWHM_{H\alpha} > 2500\,km\,s^{-1}$, $\rm S/N_{H\alpha} > 3$ for the $\rm FWHM_{H\alpha}$ and $\rm S/N_{H\alpha} > 2$ for the $L_{\rm H\alpha}$. Therefore, we conclude that neither the poor resolution nor sensitivity biases the fitted results by greater than ~ 0.1 dex level of systematic offset or scatter in $M_{\rm BH}$, and we give the corresponding FWHM and S/N cuts to the *AKARI* data.

Having tested the reliability of fitted quantities under possible systematic biases, we come back to the fitting of the *AKARI* data and find the fit to converge for 160 out of 165 objects. Five failures show noisy spectra near the Hα and were removed. The goodness of the spectral fitting is quantified as the reduced chi-square, and it reaches down to $\chi^2_\nu = 0.33$ in median. The fraction of

AGNs passing the reliability limit for the FWHM measurements ($S/N_{H\alpha} > 3$) are 67 % (N=8) and 25 % (N=37) for the phase–2 and 3 data respectively. Also, we flagged the five NG objects of $FWHM_{int} < 2500\,km\,s^{-1}$ with an upper limit of $2500\,km\,s^{-1}$, and put upper limits on the measured FWHM of the five NP sources (e.g., Figure 3.4b). In total, we collect 45 $FWHM_{H\alpha}$ measurements including ten upper limits, where two upper limits in NP have overlapping measurements in NG.

Next, we computed the Hα line luminosity $L_{H\alpha}$ and the 5100 $\AA$ continuum luminosity L_{5100} from the spectra, converting the measured rest-frame fluxes using the luminosity distance and assuming isotropic radiation. The $L_{H\alpha}$ was derived from the gaussian fit to the observed flux. The reliability limit for $L_{H\alpha}$ ($S/N_{H\alpha} > 2$) is satisfied for 45 % (N=72) of the data, while the rest of the sample were provided with $2\,\sigma$ upper limits from their given noise levels collected within $\pm 4000\,km\,s^{-1}$ of the Hα line center. Meanwhile, the L_{5100} was calculated from the average of rest-frame 5000–5200 $\AA$ observed fluxes to reduce the measurement uncertainty. The L_{5100} measurements were kept only when $S/N_{5100} > 2$, and the rest of the data were given with $2\,\sigma$ upper limits alike $L_{H\alpha}$. We have less L_{5100} measurements than $L_{H\alpha}$ where only 25 % (N=41) meet $S/N_{5100} > 2$, not to mention the limited number of spectra (53 %, N=88) covering the rest-frame 5100 $\AA$. Thus, we also derived the L_{5100} alternatively by the photometric SED fitting (Section 3.3.2).

In addition, we fitted the C IV region (rest-frame 1445–1705$\AA$) of 121 objects with a SED model containing a power law component and double broad Gaussians to model the C IV emission. Also, a single broad gaussian was used to fit the 1600$\AA$ feature (Laor et al., 1994), and the He II and O III] around 1650$\AA$ altogether since these emission are blended but relatively detached from the C IV. This component was not regarded as a part of the C IV, consistent with the previous studies (e.g,. prescription A of Assef et al. 2011; S12). We do not subtract the broad Fe II complex around the C IV emission, as it does not

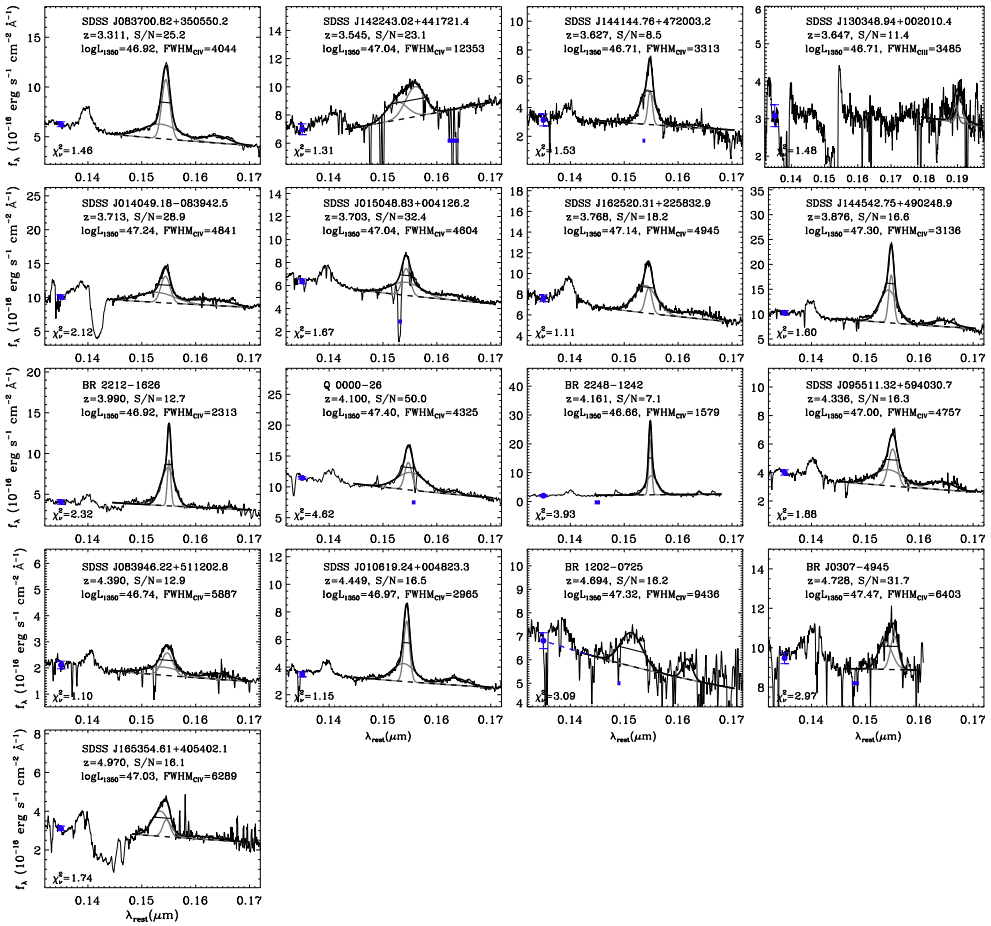

Figure 3.7: Rest-frame C IV spectral fitting of the identical objects in Figure 3.6 plotted at the same relative location, following the format of the plotted data and printed numbers. The spectra are shown when they are available from the listed references in Table 3.2. When there were contaminations around the C IV emission, we masked out the region (blue rectangle). Additionally shown are the double gaussian fit (gray) to the C IV and the continuum underneath (dashed line), together with the 1350 $\AA$ monochromatic flux marked on its wavelength. The C IV spectra displayed are smoothed down to $R = 500$, to highlight the spectral features better.

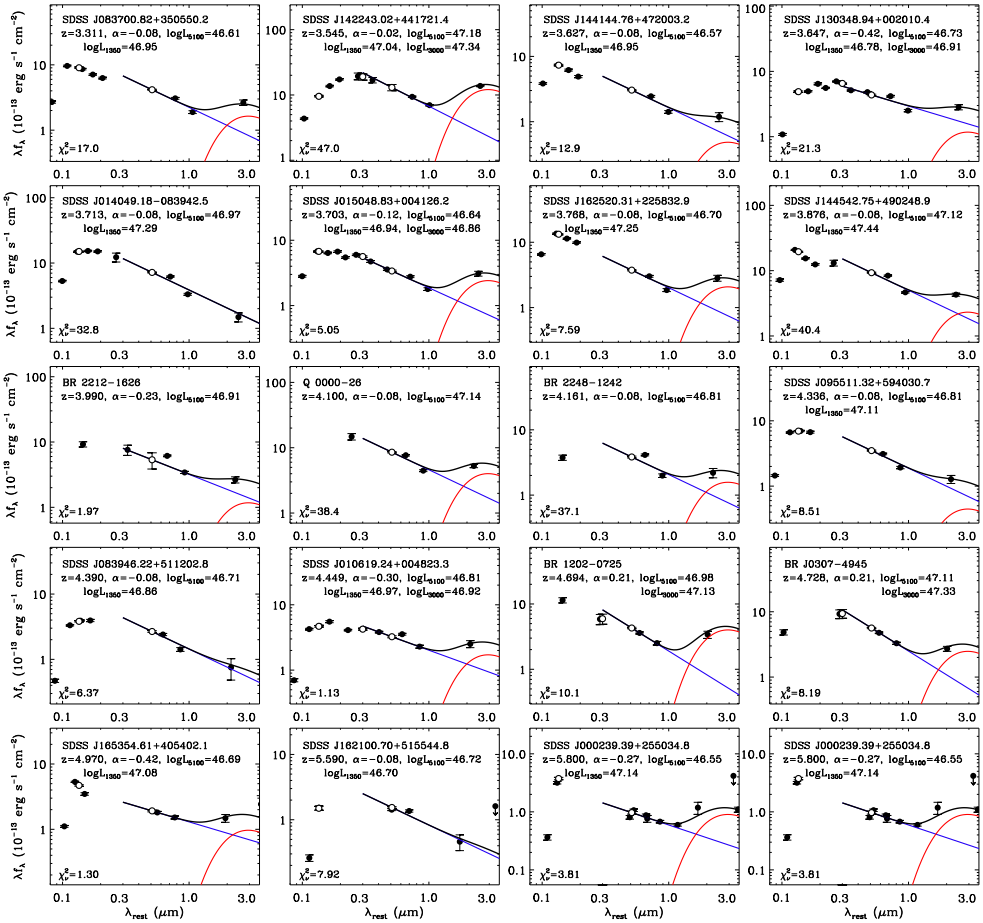

Figure 3.8: Rest-frame UV–NIR broad-band SED of the objects in Figure 3.6 plotted at the same relative location. The figure shows the observed data points (filled circles) and WISE $2\,\sigma$ upper limits (arrows), model fits of the accretion disk (blue line) and the T=1250 K dust components (red curve) together with their sum (black curve). Also, the monochromatic 1350, 3000, and 5100 $\mathring{A}$ fluxes are drawn (open circles) when available.

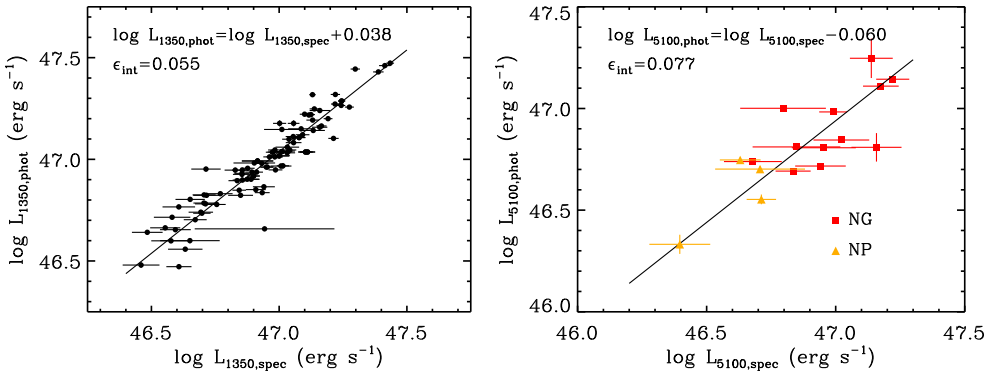

Figure 3.9: Comparison of spectroscopically and photometrically derived monochromatic luminosities, for L_{1350} (left) and L_{5100} (right). The *AKARI* NG/NP data points for the L_{5100} are highlighted with red squares and yellow triangles, respectively. Offsets to the luminosities from a 1–1 relation, and $\epsilon_{\rm int}$ from this relation are displayed.

change the $\mathrm{FWHM_{C\,IV}}$ meaningfully (S11). The optical spectra were fitted after carefully masking out the absorption features around the C IV line for 25 % of the spectra. Meanwhile, 16 spectra without error information were fitted assuming the flux error is uniform at all wavelengths, and the rms scatter of the best-fit solution is chosen to be the flux error afterward. Out of five spectra with severe broad absorption line (BAL) features, we fitted the C III]λ1908 and used its line width as an effective $\mathrm{FWHM_{C\,IV}}$ surrogate (S12) for two objects, while excluding the remaining three objects from the UV line analysis. In total, we derived $\mathrm{FWHM_{C\,IV}}$ and L_{1350} for 118 objects. The L_{1350} and its error were calculated from the average of rest-frame $1350 \pm 15\,\mathring{A}$ observed fluxes to avoid contamination from narrow absorption, while for seven BAL quasars we extrapolated the continuum around the C IV emission to $1350\,\mathring{A}$. When spectra of an object were available from both SDSS-I/SDSS-II and BOSS, we performed the fit to the spectra from each dataset separately, and took the average of the parameter values from the independent fits. We plot examples of the spectral fitting of the Hα region in Figure 3.6, and of the C IV in Figure 3.7.

3.3.2 Broad-band SED fitting

The photometry datasets in Table 3.2 covers a wide wavelength range in broad-band filters from u-band through 24 μm, thus we fitted the broad-band SEDs to provide further information on the AGN continuum luminosities. Under a photometric sensitivity limit of S/N > 5 for the observed optical–NIR, and S/N > 2 in the MIR, we modeled the SED in the rest-frame 0.3–5 μm including 4–5 data points on average, as a sum of power law continuum and black body emission from hot dust of T=1250 K (e.g., Jun & Im 2013). For 53% of the case (N=87) for which there were no rest-frame 0.3–0.6 μm data points available, we used the average continuum slope α = -0.08 of luminous SDSS quasars (Jun & Im, 2013). The uncertainty in fixing the continuum slope was tested from objects that cover the rest-frame 0.3–0.6 μm, and comparing the L_{5100} with and without fixing the α. The test yields the L_{5100} to be offset by -0.01 $\pm$ 0.07 dex when α is fixed, compared to when α is free. Since the offsets are small, we find our method to fix the α when missing the photometric coverage near the rest-5100 $\mathring{A}$, to be reliable in tracing the L_{5100}. In addition, considering the filter bandwidths and the AGN line equivalent widths from Vanden Berk et al. (2001), we find the Hα to be the only line that meaningfully contributes to the rest-optical photometry over the continuum emission (by > 0.03 dex). Thus, we removed the data point enclosing the Hα emission when the χ^2_ν containing that data point became larger than that without. Through this procedure we obtained 164 photometrically derived L_{5100}, while removing one object without any detections in the rest-frame 0.3–5 μm under our sensitivity limit. Examples of the broad-band SED fitting are shown in Figure 3.8. The reduced chi-square values have a median of $\chi^2_\nu = 3.3$, is acceptable given the simplification of the SED model that does not take into account the emission line features, and the general agreement of the fit to the data demonstrated in Figure 3.8.

Table 3.3. Continuum and line based properties of the sample

Name	$z_{\rm ref}$	$z_{\rm H\alpha}$	log L_{1350}	log L_{5100}	log $L_{\rm H\alpha}$	FWHM$_{1000}$ C$_{\rm IV}$	FWHM$_{1000}$ Hα	log $M_{\rm BH}$ C$_{\rm IV}$	log $M_{\rm BH}$ Hα
SDSS J000239.39+255034.8	5.800	5.79	99.00 ± 99.00	46.55 ± 0.02	45.14 ± 0.11	99.00 ± 99.00	2.50 ± -1.00	99.00 ± 99.00	9.24 ± -1.00
Q 0000-26	4.100	4.11	47.40 ± 0.01	47.14 ± 0.01	45.48 ± 0.13	4.33 ± 0.28	2.50 ± -1.00	9.80 ± 0.23	9.56 ± -1.00
SDSS J000552.34-000655.8	5.850	5.85	99.00 ± 99.00	45.92 ± 0.15	44.78 ± 0.31	99.00 ± 99.00	99.00 ± 99.00	99.00 ± 99.00	99.00 ± 99.00
BR J0006-6208	4.455	4.49	46.90 ± 0.02	46.74 ± 0.01	45.46 ± 0.06	11.33 ± 1.33	2.85 ± 0.85	10.42 ± 0.27	9.46 ± 0.31
SDSS J001115.23+144601.8	4.967	4.97	99.00 ± 99.00	46.78 ± 0.02	47.97 ± -1.00	99.00 ± 99.00	99.00 ± 99.00	99.00 ± 99.00	99.00 ± 99.00
BR J0018-3527	4.150	4.15	99.00 ± 99.00	46.71 ± 0.01	45.39 ± 0.29	99.00 ± 99.00	99.00 ± 99.00	99.00 ± 99.00	99.00 ± 99.00
PMN J0022-0759	3.896	3.91	99.00 ± 99.00	46.54 ± 0.01	47.97 ± -1.00	99.00 ± 99.00	99.00 ± 99.00	99.00 ± 99.00	99.00 ± 99.00
BR 0019-1522	4.528	4.49	46.95 ± 0.02	46.61 ± 0.02	47.92 ± -1.00	3.48 ± 0.33	99.00 ± 99.00	9.35 ± 0.22	99.00 ± 99.00
BR J0030-5129	4.174	4.15	99.00 ± 99.00	46.55 ± 0.01	48.02 ± -1.00	99.00 ± 99.00	99.00 ± 99.00	99.00 ± 99.00	99.00 ± 99.00
BRI J0048-2442	4.150	4.12	99.00 ± 99.00	45.98 ± 0.20	48.08 ± -1.00	99.00 ± 99.00	99.00 ± 99.00	99.00 ± 99.00	99.00 ± 99.00
BRI J0048-244	4.150	4.18	99.00 ± 99.00	46.06 ± 0.03	47.90 ± -1.00	99.00 ± 99.00	99.00 ± 99.00	99.00 ± 99.00	99.00 ± 99.00
SDSS J010619.24+004823.3	4.449	4.44	46.99 ± 0.01	46.81 ± 0.02	45.69 ± 0.19	3.00 ± 0.20	7.74 ± 2.92	9.23 ± 0.12	10.42 ± 0.38
BRI J0113-280	4.300	4.26	99.00 ± 99.00	46.38 ± 0.02	47.92 ± -1.00	99.00 ± 99.00	99.00 ± 99.00	99.00 ± 99.00	99.00 ± 99.00
SDSS J011351.96-093551.1	3.668	3.68	46.93 ± 0.03	46.53 ± 0.01	47.65 ± -1.00	8.64 ± 0.36	99.00 ± 99.00	10.19 ± 0.24	99.00 ± 99.00
SDSS J011453.81-103934.0	3.730	3.76	46.65 ± 0.12	46.61 ± 0.01	47.69 ± -1.00	5.11 ± 0.35	99.00 ± 99.00	9.54 ± 0.23	99.00 ± 99.00
SDSS J012211.11+150914.3	4.460	4.50	47.00 ± 0.04	46.56 ± 0.03	47.91 ± -1.00	7.59 ± 0.82	99.00 ± 99.00	10.10 ± 0.25	99.00 ± 99.00
SDSS J012403.77+004432.7	3.834	3.83	47.11 ± 0.01	46.83 ± 0.01	45.44 ± 0.20	8.06 ± 0.29	3.76 ± 1.69	10.22 ± 0.17	9.77 ± 0.44
SDSS J012700.68-004559.1	4.082	4.07	47.01 ± 0.01	46.68 ± 0.01	45.14 ± 0.33	6.96 ± 0.27	99.00 ± 99.00	10.03 ± 0.14	99.00 ± 99.00
BRI J0137-422	3.970	3.98	99.00 ± 99.00	46.38 ± 0.02	45.49 ± 0.22	99.00 ± 99.00	5.95 ± 2.46	99.00 ± 99.00	9.95 ± 0.41
SDSS J014049.18-083942.5	3.713	3.69	47.24 ± 0.01	46.97 ± 0.01	45.51 ± 0.12	4.84 ± 0.07	5.05 ± 1.27	9.82 ± 0.22	10.11 ± 0.28
SDSS J015048.83+004126.2	3.702	3.70	46.95 ± 0.01	46.64 ± 0.01	45.42 ± 0.17	4.14 ± 0.34	6.47 ± 2.18	9.50 ± 0.12	10.16 ± 0.34

Table 3.3 (cont'd)

Name	$z_{\rm ref}$	$z_{\rm H\alpha}$	log L_{1350}	log L_{5100}	log $L_{\rm H\alpha}$	FWHM$_{1000}$ C$_{\rm IV}$	FWHM$_{1000}$ Hα	log $M_{\rm BH}$ C$_{\rm IV}$	log $M_{\rm BH}$ Hα
SDSS J021646.94-092107.3	3.716	3.70	47.01 ± 0.01	46.74 ± 0.01	45.47 ± 0.11	9.87 ± 0.96	99.00 ± 99.00	10.35 ± 0.19	99.00 ± 99.00
SDSS J023137.65-072854.4	5.413	5.41	46.66 ± 0.07	46.51 ± 0.02	$48.20 \pm$-1.00	3.03 ± 0.33	99.00 ± 99.00	9.06 ± 0.23	99.00 ± 99.00
BR J0234-1806	4.314	4.28	99.00 ± 99.00	46.52 ± 0.01	$47.99 \pm$-1.00	99.00 ± 99.00	99.00 ± 99.00	99.00 ± 99.00	99.00 ± 99.00
SDSS J024447.79-081606.0	4.068	4.06	47.19 ± 0.02	46.94 ± 0.01	$47.96 \pm$-1.00	9.76 ± 0.54	99.00 ± 99.00	10.44 ± 0.25	99.00 ± 99.00
BR J0301-5537	4.133	4.15	99.00 ± 99.00	46.40 ± 0.01	$47.86 \pm$-1.00	99.00 ± 99.00	99.00 ± 99.00	99.00 ± 99.00	99.00 ± 99.00
BR J0307-4945	4.728	4.78	47.47 ± 0.01	47.11 ± 0.01	45.79 ± 0.11	6.40 ± 0.86	7.59 ± 1.51	10.20 ± 0.26	10.56 ± 0.24
BR J0324-2918	4.622	4.60	99.00 ± 99.00	46.97 ± 0.01	45.29 ± 0.27	99.00 ± 99.00	99.00 ± 99.00	99.00 ± 99.00	99.00 ± 99.00
SDSS J034402.85-065300.6	3.957	3.93	46.98 ± 0.02	46.34 ± 0.02	$47.83 \pm$-1.00	7.23 ± 0.24	99.00 ± 99.00	10.05 ± 0.23	99.00 ± 99.00
BR J0426-2202	4.320	4.33	47.13 ± 0.01	46.73 ± 0.01	45.46 ± 0.20	5.55 ± 1.16	4.19 ± 1.79	9.88 ± 0.29	9.81 ± 0.42
BR J0525-3343	4.383	4.40	47.01 ± 0.02	46.82 ± 0.01	$47.89 \pm$-1.00	11.23 ± 2.14	99.00 ± 99.00	10.47 ± 0.30	99.00 ± 99.00
BR J0529-3526	4.413	4.41	99.00 ± 99.00	46.60 ± 0.01	45.32 ± 0.35	99.00 ± 99.00	99.00 ± 99.00	99.00 ± 99.00	99.00 ± 99.00
BR J0714-6455	4.462	4.44	47.32 ± 0.01	46.83 ± 0.01	45.45 ± 0.23	11.42 ± 0.33	7.86 ± 3.33	10.66 ± 0.25	10.44 ± 0.42
SDSS J073149.51+285448.7	3.676	3.69	46.96 ± 0.02	46.51 ± 0.01	45.13 ± 0.28	7.08 ± 0.63	99.00 ± 99.00	10.02 ± 0.24	99.00 ± 99.00
SDSS J075303.33+423130.8	3.590	3.56	47.23 ± 0.01	46.94 ± 0.07	45.32 ± 0.19	2.93 ± 0.08	6.24 ± 2.29	9.34 ± 0.11	10.29 ± 0.37
SDSS J080430.57+542041.1	3.759	3.75	46.99 ± 0.01	46.74 ± 0.01	45.29 ± 0.24	7.13 ± 0.32	99.00 ± 99.00	10.04 ± 0.17	99.00 ± 99.00
SDSS J080849.43+521515.3	4.456	4.49	47.16 ± 0.01	46.79 ± 0.01	$47.91 \pm$-1.00	8.41 ± 0.31	99.00 ± 99.00	10.29 ± 0.14	99.00 ± 99.00
SDSS J081754.52+413225.3	3.537	3.53	46.59 ± 0.02	46.39 ± 0.01	$47.67 \pm$-1.00	4.94 ± 0.12	99.00 ± 99.00	9.48 ± 0.12	99.00 ± 99.00
SDSS J081827.40+172251.8	6.000	6.00	99.00 ± 99.00	46.27 ± 0.37	$48.40 \pm$-1.00	99.00 ± 99.00	99.00 ± 99.00	99.00 ± 99.00	99.00 ± 99.00
SDSS J083118.52+424728.8	3.321	3.32	46.58 ± 0.04	46.25 ± 0.01	$47.58 \pm$-1.00	7.21 ± 0.48	99.00 ± 99.00	9.82 ± 0.17	99.00 ± 99.00
SDSS J083700.82+350550.2	3.311	3.30	46.87 ± 0.02	46.61 ± 0.01	45.36 ± 0.19	4.03 ± 0.17	6.43 ± 2.50	9.44 ± 0.13	10.14 ± 0.39
SDSS J083946.22+511202.8	4.390	4.39	46.84 ± 0.03	46.71 ± 0.01	45.60 ± 0.21	5.78 ± 0.21	6.21 ± 2.50	9.76 ± 0.16	10.16 ± 0.40

Table 3.3 (cont'd)

Name	$z_{\rm ref}$	$z_{\rm H\alpha}$	log L_{1350}	log L_{5100}	log $L_{\rm H\alpha}$	FWHM$_{1000}$ C$_{\rm IV}$	FWHM$_{1000}$ Hα	log $M_{\rm BH}$ C$_{\rm IV}$	log $M_{\rm BH}$ Hα
SDSS J084119.52+290504.4	5.960	5.91	99.00 ± 99.00	45.80 ± 0.19	48.35 ± -1.00	99.00 ± 99.00	99.00 ± 99.00	99.00 ± 99.00	99.00 ± 99.00
SDSS J085837.95+052141.7	3.528	3.56	46.84 ± 0.03	46.53 ± 0.01	47.62 ± -1.00	6.82 ± 0.68	99.00 ± 99.00	9.91 ± 0.24	99.00 ± 99.00
87GB 090153.2+694215	5.470	5.47	99.00 ± 99.00	46.20 ± 0.05	48.11 ± -1.00	99.00 ± 99.00	99.00 ± 99.00	99.00 ± 99.00	99.00 ± 99.00
SDSS J090634.84+023433.8	4.511	4.52	47.03 ± 0.02	46.75 ± 0.02	47.99 ± -1.00	8.95 ± 1.18	99.00 ± 99.00	10.27 ± 0.21	99.00 ± 99.00
SDSS J092721.82+200123.7	5.770	5.73	99.00 ± 99.00	46.12 ± 0.09	48.32 ± -1.00	99.00 ± 99.00	99.00 ± 99.00	99.00 ± 99.00	99.00 ± 99.00
SDSS J093554.45+525616.5	4.005	3.99	46.90 ± 0.02	46.79 ± 0.01	45.43 ± 0.22	5.74 ± 0.37	3.04 ± 1.59	9.79 ± 0.23	9.55 ± 0.51
BR 0951-0450	4.369	4.35	46.71 ± 0.03	46.47 ± 0.02	48.03 ± -1.00	5.64 ± 0.60	99.00 ± 99.00	9.66 ± 0.24	99.00 ± 99.00
SDSS J095511.32+594030.7	4.336	4.30	47.03 ± 0.02	46.81 ± 0.01	45.72 ± 0.14	4.61 ± 0.26	3.70 ± 1.11	9.65 ± 0.16	9.74 ± 0.32
SDSS J095744.46+330820.7	4.227	4.21	47.17 ± 0.02	46.67 ± 0.01	48.05 ± -1.00	9.19 ± 0.67	99.00 ± 99.00	10.37 ± 0.25	99.00 ± 99.00
QUEST J101046.3-013104.1	5.090	5.05	99.00 ± 99.00	47.71 ± 0.01	48.02 ± -1.00	99.00 ± 99.00	99.00 ± 99.00	99.00 ± 99.00	99.00 ± 99.00
SDSS J101336.37+561536.4	3.633	3.64	46.95 ± 0.03	46.95 ± 0.09	45.58 ± 0.14	6.90 ± 0.91	6.66 ± 1.87	9.99 ± 0.26	10.36 ± 0.31
SDSS J102622.89+471907.0	4.943	4.91	99.00 ± 99.00	46.62 ± 0.02	47.97 ± -1.00	99.00 ± 99.00	99.00 ± 99.00	99.00 ± 99.00	99.00 ± 99.00
SDSS J103221.11+092749.0	3.997	4.02	47.02 ± 0.01	46.55 ± 0.02	45.31 ± 0.33	7.58 ± 0.43	99.00 ± 99.00	10.11 ± 0.14	99.00 ± 99.00
SDSS J103242.71+433605.4	3.456	3.45	46.50 ± 0.07	46.41 ± 0.01	47.62 ± -1.00	5.97 ± 0.19	99.00 ± 99.00	9.60 ± 0.16	99.00 ± 99.00
SDSS J104351.20+650647.6	4.471	4.51	46.85 ± 0.05	46.41 ± 0.02	47.91 ± -1.00	4.07 ± 1.14	99.00 ± 99.00	9.44 ± 0.34	99.00 ± 99.00
SDSS J104433.04-012502.2	5.800	5.80	99.00 ± 99.00	46.53 ± 0.03	48.35 ± -1.00	99.00 ± 99.00	99.00 ± 99.00	99.00 ± 99.00	99.00 ± 99.00
SDSS J104437.06+650645.0	3.648	3.67	46.88 ± 0.03	46.58 ± 0.01	47.81 ± -1.00	4.25 ± 0.23	99.00 ± 99.00	9.49 ± 0.22	99.00 ± 99.00
SDSS J104845.05+463718.3	6.190	6.19	99.00 ± 99.00	46.44 ± 0.04	48.50 ± -1.00	99.00 ± 99.00	99.00 ± 99.00	99.00 ± 99.00	99.00 ± 99.00
SDSS J105123.03+354534.3	4.913	4.91	46.86 ± 0.05	46.70 ± 0.01	45.52 ± 0.18	3.35 ± 0.17	3.93 ± -1.00	9.26 ± 0.21	9.74 ± -1.00
SDSS J105756.28+455553.0	4.138	4.13	47.43 ± 0.02	47.25 ± 0.10	45.90 ± 0.09	6.93 ± 0.25	4.22 ± 0.70	10.26 ± 0.24	10.09 ± 0.23
SDSS J110657.83+081643.3	4.268	4.27	46.79 ± 0.02	46.44 ± 0.03	47.95 ± -1.00	4.85 ± 0.35	99.00 ± 99.00	9.57 ± 0.16	99.00 ± 99.00

Table 3.3 (cont'd)

Name	$z_{\rm ref}$	$z_{\rm H\alpha}$	log L_{1350}	log L_{5100}	log $L_{\rm H\alpha}$	FWHM$_{1000}$ C$_{\rm IV}$	FWHM$_{1000}$ Hα	log $M_{\rm BH}$ C$_{\rm IV}$	log $M_{\rm BH}$ Hα
SDSS J111348.13+540940.0	3.777	3.77	99.00 ± 99.00	46.58 ± 0.01	45.12 ± 0.30	99.00 ± 99.00	99.00 ± 99.00	99.00 ± 99.00	99.00 ± 99.00
BRI 1114-0822	4.495	4.47	46.58 ± 0.03	46.14 ± 0.03	48.07 ± -1.00	6.06 ± 0.12	99.00 ± 99.00	9.66 ± 0.22	99.00 ± 99.00
SDSS J113002.35+115438.3	3.402	3.39	46.91 ± 0.02	46.49 ± 0.02	47.63 ± -1.00	6.25 ± 0.08	99.00 ± 99.00	9.87 ± 0.16	99.00 ± 99.00
SDSS J113142.31+384854.6	4.127	4.10	99.00 ± 99.00	46.75 ± 0.01	47.94 ± -1.00	99.00 ± 99.00	99.00 ± 99.00	99.00 ± 99.00	99.00 ± 99.00
SDSS J113246.50+120901.6	5.167	5.16	99.00 ± 99.00	46.45 ± 0.03	48.10 ± -1.00	99.00 ± 99.00	99.00 ± 99.00	99.00 ± 99.00	99.00 ± 99.00
SDSS J113307.63+522835.5	3.736	3.74	46.71 ± 0.04	46.66 ± 0.07	45.33 ± 0.20	7.14 ± 0.37	2.50 ± -1.00	9.88 ± 0.23	9.30 ± -1.00
SDSS J113418.96+574204.6	3.522	3.49	46.98 ± 0.03	46.60 ± 0.01	47.67 ± -1.00	7.90 ± 0.84	99.00 ± 99.00	10.13 ± 0.25	99.00 ± 99.00
SDSS J114514.18+394715.9	4.061	4.03	47.02 ± 0.02	46.82 ± 0.01	45.27 ± 0.32	7.51 ± 0.34	99.00 ± 99.00	10.10 ± 0.17	99.00 ± 99.00
SDSS J114657.79+403708.6	5.005	4.99	46.54 ± 0.08	46.53 ± 0.02	48.05 ± -1.00	4.43 ± 0.71	99.00 ± 99.00	9.35 ± 0.26	99.00 ± 99.00
SDSS J114816.64+525150.2	6.420	6.38	99.00 ± 99.00	46.66 ± 0.02	48.19 ± -1.00	99.00 ± 99.00	99.00 ± 99.00	99.00 ± 99.00	99.00 ± 99.00
SDSS J115757.96+485655.7	4.245	4.22	46.72 ± 0.05	46.43 ± 0.01	47.93 ± -1.00	4.72 ± 0.30	99.00 ± 99.00	9.50 ± 0.22	99.00 ± 99.00
SDSS J115935.63+042420.0	3.448	3.45	46.53 ± 0.04	46.11 ± 0.03	47.62 ± -1.00	4.10 ± 0.36	99.00 ± 99.00	9.27 ± 0.16	99.00 ± 99.00
SDSS J120110.31+211758.5	4.579	4.56	47.00 ± 0.04	46.62 ± 0.02	48.03 ± -1.00	12.09 ± 0.48	99.00 ± 99.00	10.54 ± 0.25	99.00 ± 99.00
SDSS J120207.78+323538.8	5.292	5.27	47.05 ± 0.03	46.50 ± 0.03	45.34 ± 0.36	10.06 ± 1.83	99.00 ± 99.00	10.39 ± 0.29	99.00 ± 99.00
SDSS J120441.71-002149.5	5.032	5.07	46.48 ± 0.07	46.44 ± 0.04	47.99 ± -1.00	5.71 ± 1.75	99.00 ± 99.00	9.55 ± 0.36	99.00 ± 99.00
SDSS J120447.15+330938.7	3.616	3.64	46.93 ± 0.15	46.99 ± 0.01	45.65 ± 0.13	8.08 ± 0.28	7.82 ± 2.01	10.11 ± 0.18	10.53 ± 0.28
BR 1202-0725	4.694	4.69	47.32 ± 0.02	46.98 ± 0.01	45.56 ± 0.07	9.44 ± 0.45	4.78 ± 0.65	10.48 ± 0.25	10.07 ± 0.20
SDSS J120934.54+553745.4	3.573	3.58	47.13 ± 0.02	46.98 ± 0.06	45.38 ± 0.14	3.77 ± 0.99	2.50 ± -1.00	9.52 ± 0.32	9.47 ± -1.00
SDSS J122738.30+572748.9	3.990	4.02	99.00 ± 99.00	46.79 ± 0.01	47.93 ± -1.00	99.00 ± 99.00	99.00 ± 99.00	99.00 ± 99.00	99.00 ± 99.00
SDSS J123239.29+525250.9	4.293	4.27	47.08 ± 0.02	46.75 ± 0.01	45.39 ± 0.28	7.71 ± 0.19	99.00 ± 99.00	10.16 ± 0.23	99.00 ± 99.00
SDSS J124306.55+530522.0	3.567	3.55	46.97 ± 0.03	46.55 ± 0.01	44.95 ± 0.35	6.65 ± 1.02	99.00 ± 99.00	9.97 ± 0.27	99.00 ± 99.00

Table 3.3 (cont'd)

Name	$z_{\rm ref}$	$z_{\rm H\alpha}$	log L_{1350}	log L_{5100}	log $L_{\rm H\alpha}$	FWHM$_{1000}$ C$_{\rm IV}$	FWHM$_{1000}$ Hα	log $M_{\rm BH}$ C$_{\rm IV}$	log $M_{\rm BH}$ Hα
SDSS J125051.93+313021.9	6.130	6.15	99.00 ± 99.00	46.44 ± 0.05	48.44 ± -1.00	99.00 ± 99.00	99.00 ± 99.00	99.00 ± 99.00	99.00 ± 99.00
SDSS J125051.93+313021.9	6.130	6.09	99.00 ± 99.00	46.44 ± 0.05	44.84 ± 0.35	99.00 ± 99.00	99.00 ± 99.00	99.00 ± 99.00	99.00 ± 99.00
SDSS J130002.16+011823.0	4.613	4.62	46.88 ± 0.04	46.67 ± 0.02	48.02 ± -1.00	5.44 ± 0.87	99.00 ± 99.00	9.73 ± 0.21	99.00 ± 99.00
SDSS J130348.94+002010.4	3.647	3.62	46.74 ± 0.01	46.73 ± 0.01	45.57 ± 0.11	2.67 ± 0.12	6.98 ± 1.56	9.46 ± 0.09	10.28 ± 0.26
SDSS J130608.26+035626.3	5.990	5.94	99.00 ± 99.00	46.33 ± 0.04	48.47 ± -1.00	99.00 ± 99.00	99.00 ± 99.00	99.00 ± 99.00	99.00 ± 99.00
SDSS J131914.20+520200.0	3.899	3.93	47.22 ± 0.02	46.87 ± 0.01	45.41 ± 0.26	4.65 ± 0.20	99.00 ± 99.00	9.77 ± 0.22	99.00 ± 99.00
SDSS J132420.83+422554.6	4.035	4.01	46.85 ± 0.04	46.63 ± 0.01	45.47 ± 0.16	6.76 ± 1.00	3.33 ± 1.22	9.92 ± 0.26	9.55 ± 0.37
SDSS J132423.26+623342.1	3.634	3.60	46.48 ± 0.06	46.33 ± 0.01	47.68 ± -1.00	5.69 ± 0.13	99.00 ± 99.00	9.55 ± 0.22	99.00 ± 99.00
SDSS J132603.00+295758.1	3.767	3.76	46.93 ± 0.03	46.26 ± 0.03	47.72 ± -1.00	7.30 ± 0.69	99.00 ± 99.00	10.03 ± 0.24	99.00 ± 99.00
SDSS J133223.26+503431.3	3.807	3.80	47.01 ± 0.02	46.57 ± 0.01	47.72 ± -1.00	6.89 ± 1.06	99.00 ± 99.00	10.02 ± 0.27	99.00 ± 99.00
SDSS J133412.56+122020.7	5.130	5.09	46.68 ± 0.06	46.31 ± 0.04	48.16 ± -1.00	4.38 ± 0.97	99.00 ± 99.00	9.41 ± 0.29	99.00 ± 99.00
SDSS J133448.70+521317.9	3.605	3.60	46.71 ± 0.05	46.66 ± 0.06	45.17 ± 0.25	3.68 ± 0.25	99.00 ± 99.00	9.27 ± 0.21	99.00 ± 99.00
SDSS J133529.45+410125.9	4.263	4.29	47.21 ± 0.01	46.81 ± 0.07	45.78 ± 0.15	6.45 ± 1.72	3.90 ± 1.21	10.06 ± 0.30	9.79 ± 0.32
BRI 1335-0417	4.396	4.40	46.81 ± 0.02	46.46 ± 0.01	48.08 ± -1.00	10.33 ± 0.29	99.00 ± 99.00	10.29 ± 0.24	99.00 ± 99.00
SDSS J134015.03+392630.7	5.026	5.05	46.68 ± 0.06	46.42 ± 0.02	45.15 ± 0.30	8.94 ± 0.53	99.00 ± 99.00	10.08 ± 0.24	99.00 ± 99.00
SDSS J134040.24+281328.1	5.340	5.38	99.00 ± 99.00	46.53 ± 0.03	45.56 ± 0.23	99.00 ± 99.00	2.94 ± 1.45	99.00 ± 99.00	9.38 ± 0.48
SDSS J134743.29+495621.3	4.510	4.53	47.39 ± 0.02	47.00 ± 0.01	45.51 ± 0.19	7.13 ± 1.63	6.78 ± 2.34	10.26 ± 0.32	10.40 ± 0.35
BRI 1346-0322	3.992	3.99	46.64 ± 0.03	46.80 ± 0.01	45.26 ± 0.16	4.77 ± 0.08	99.00 ± 99.00	9.47 ± 0.21	99.00 ± 99.00
SDSS J140132.76+411150.4	4.017	4.04	46.48 ± 0.04	46.47 ± 0.01	47.88 ± -1.00	5.49 ± 1.62	99.00 ± 99.00	9.52 ± 0.31	99.00 ± 99.00
SDSS J140146.53+024434.7	4.442	4.41	47.01 ± 0.02	46.65 ± 0.02	48.00 ± -1.00	6.37 ± 2.69	99.00 ± 99.00	9.93 ± 0.34	99.00 ± 99.00
SDSS J140248.08+014634.0	4.161	4.18	47.09 ± 0.03	46.61 ± 0.02	48.07 ± -1.00	8.11 ± 1.47	99.00 ± 99.00	10.22 ± 0.29	99.00 ± 99.00

Table 3.3 (cont'd)

Name	$z_{\rm ref}$	$z_{\rm H\alpha}$	log L_{1350}	log L_{5100}	log $L_{\rm H\alpha}$	FWHM$_{1000}$ C$_{\rm IV}$	FWHM$_{1000}$ Hα	log $M_{\rm BH}$ C$_{\rm IV}$	log $M_{\rm BH}$ Hα
SDSS J141831.70+444937.5	4.312	4.33	47.04 ± 0.02	46.82 ± 0.12	45.32 ± 0.29	6.10 ± 0.39	99.00 ± 99.00	9.92 ± 0.17	99.00 ± 99.00
SDSS J142144.98+351315.4	4.556	4.55	46.87 ± 0.05	46.58 ± 0.01	$47.88 \pm$-1.00	6.98 ± 1.33	99.00 ± 99.00	9.96 ± 0.29	99.00 ± 99.00
SDSS J142242.13+461310.2	3.726	3.71	46.98 ± 0.03	46.49 ± 0.01	$47.79 \pm$-1.00	7.76 ± 0.57	99.00 ± 99.00	10.11 ± 0.24	99.00 ± 99.00
SDSS J142243.02+441721.4	3.545	3.61	47.05 ± 0.01	47.18 ± 0.05	45.71 ± 0.07	11.87 ± 0.53	6.11 ± 0.84	10.54 ± 0.18	10.40 ± 0.21
SDSS J143835.95+431459.2	4.611	4.67	47.35 ± 0.01	99.00 ± 99.00	45.39 ± 0.20	9.84 ± 0.42	4.92 ± 1.89	10.53 ± 0.15	99.00 ± 99.00
SDSS J144144.76+472003.2	3.633	3.62	46.71 ± 0.06	46.57 ± 0.01	45.24 ± 0.18	3.31 ± 0.23	2.84 ± 1.32	9.17 ± 0.21	9.37 ± 0.45
SDSS J144213.09+391856.0	3.627	3.61	47.01 ± 0.02	46.45 ± 0.01	$47.58 \pm$-1.00	7.53 ± 0.76	99.00 ± 99.00	10.10 ± 0.19	99.00 ± 99.00
SDSS J144340.70+585653.2	4.277	4.31	47.24 ± 0.02	46.75 ± 0.10	$47.96 \pm$-1.00	9.19 ± 0.23	99.00 ± 99.00	10.41 ± 0.24	99.00 ± 99.00
SDSS J144350.66+362315.1	5.270	5.25	46.78 ± 0.03	46.53 ± 0.02	$48.08 \pm$-1.00	9.46 ± 1.49	99.00 ± 99.00	10.18 ± 0.23	99.00 ± 99.00
SDSS J144542.75+490248.9	3.875	3.87	47.30 ± 0.02	47.12 ± 0.01	45.94 ± 0.07	3.14 ± 0.12	6.57 ± 0.97	9.44 ± 0.21	10.44 ± 0.21
SDSS J144733.46+465723.6	3.587	3.61	46.59 ± 0.06	46.27 ± 0.01	$47.58 \pm$-1.00	4.79 ± 0.90	99.00 ± 99.00	9.45 ± 0.27	99.00 ± 99.00
SDSS J145408.95+511443.7	3.644	3.61	47.22 ± 0.02	47.08 ± 0.08	45.46 ± 0.16	4.64 ± 0.27	4.68 ± 1.52	9.77 ± 0.22	10.10 ± 0.34
SDSS J150620.48+460642.4	3.504	3.52	46.84 ± 0.02	46.38 ± 0.01	45.21 ± 0.22	7.21 ± 0.21	6.98 ± 3.02	9.96 ± 0.16	10.10 ± 0.42
SDSS J150654.54+522004.6	4.068	4.05	47.11 ± 0.02	46.92 ± 0.01	$47.00 \pm$-1.00	9.24 ± 1.43	99.00 ± 99.00	10.34 ± 0.22	99.00 ± 99.00
SDSS J151035.29+514841.0	5.031	5.02	99.00 ± 99.00	46.35 ± 0.02	45.27 ± 0.35	99.00 ± 99.00	99.00 ± 99.00	99.00 ± 99.00	99.00 ± 99.00
SDSS J151442.74+532412.0	3.565	3.57	46.65 ± 0.06	46.39 ± 0.01	$47.58 \pm$-1.00	5.77 ± 0.11	99.00 ± 99.00	9.66 ± 0.22	99.00 ± 99.00
SDSS J152034.53+383906.5	3.397	3.42	46.47 ± 0.05	46.07 ± 0.01	$47.46 \pm$-1.00	6.92 ± 0.46	99.00 ± 99.00	9.72 ± 0.17	99.00 ± 99.00
SDSS J152413.35+430537.4	3.929	3.95	46.83 ± 0.02	46.57 ± 0.01	45.23 ± 0.29	5.07 ± 0.89	99.00 ± 99.00	9.64 ± 0.22	99.00 ± 99.00
SDSS J153650.25+500810.3	4.927	4.92	47.01 ± 0.07	46.85 ± 0.01	45.49 ± 0.17	2.65 ± 0.65	3.49 ± 1.25	9.13 ± 0.31	9.71 ± 0.36
SDSS J153725.35-014650.3	3.452	3.43	46.55 ± 0.06	46.01 ± 0.04	$47.56 \pm$-1.00	5.62 ± 0.15	99.00 ± 99.00	9.58 ± 0.22	99.00 ± 99.00
SDSS J153825.74+420933.3	3.826	3.82	46.82 ± 0.02	46.52 ± 0.01	$47.79 \pm$-1.00	7.78 ± 0.60	99.00 ± 99.00	10.03 ± 0.18	99.00 ± 99.00

Table 3.3 (cont'd)

Name	$z_{\rm ref}$	$z_{\rm H\alpha}$	log L_{1350}	log L_{5100}	log $L_{\rm H\alpha}$	FWHM$_{1000}$ C$_{\rm IV}$	FWHM$_{1000}$ Hα	log $M_{\rm BH}$ C$_{\rm IV}$	log $M_{\rm BH}$ Hα
SDSS J154340.38+341744.4	4.414	4.39	47.15 ± 0.02	47.00 ± 0.01	$48.02 \pm$ -1.00	5.16 ± 0.15	99.00 ± 99.00	9.82 ± 0.16	99.00 ± 99.00
SDSS J154914.45+364822.0	3.585	3.60	46.59 ± 0.03	46.23 ± 0.01	44.88 ± 0.35	6.96 ± 0.51	99.00 ± 99.00	9.79 ± 0.17	99.00 ± 99.00
SDSS J160254.00+422825.0	6.070	6.09	99.00 ± 99.00	46.63 ± 0.02	$48.47 \pm$ -1.00	99.00 ± 99.00	99.00 ± 99.00	99.00 ± 99.00	99.00 ± 99.00
SDSS J161140.13+273029.6	3.333	3.33	46.70 ± 0.04	46.30 ± 0.02	$47.58 \pm$ -1.00	4.52 ± 0.38	99.00 ± 99.00	9.45 ± 0.17	99.00 ± 99.00
SDSS J161425.13+464028.9	5.310	5.31	99.00 ± 99.00	46.57 ± 0.01	$48.07 \pm$ -1.00	99.00 ± 99.00	99.00 ± 99.00	99.00 ± 99.00	99.00 ± 99.00
SDSS J162100.70+515544.8	5.590	5.59	99.00 ± 99.00	46.72 ± 0.01	45.20 ± 0.18	99.00 ± 99.00	3.09 ± 1.17	99.00 ± 99.00	9.53 ± 0.38
SDSS J162331.81+311200.5	6.220	6.23	99.00 ± 99.00	46.33 ± 0.05	44.95 ± 0.17	99.00 ± 99.00	$5.75 \pm$ -1.00	99.00 ± 99.00	$9.89 \pm$ -1.00
SDSS J162520.31+225832.9	3.768	3.78	47.11 ± 0.01	46.70 ± 0.01	45.44 ± 0.17	5.02 ± 0.18	5.37 ± 1.80	9.78 ± 0.16	10.03 ± 0.34
SDSS J162623.38+484136.4	4.891	4.85	47.09 ± 0.05	46.66 ± 0.01	$47.92 \pm$ -1.00	2.70 ± 0.20	99.00 ± 99.00	9.19 ± 0.22	99.00 ± 99.00
SDSS J162943.43+391211.4	3.912	3.92	46.71 ± 0.03	46.30 ± 0.01	$47.93 \pm$ -1.00	7.19 ± 0.44	99.00 ± 99.00	9.89 ± 0.17	99.00 ± 99.00
SDSS J163636.92+315717.0	4.559	4.57	46.95 ± 0.03	46.54 ± 0.02	45.57 ± 0.23	4.90 ± 0.85	6.66 ± 2.87	9.67 ± 0.22	10.14 ± 0.42
SDSS J163847.42+232716.4	3.820	3.84	46.88 ± 0.06	46.96 ± 0.01	45.28 ± 0.27	5.09 ± 0.45	99.00 ± 99.00	9.66 ± 0.17	99.00 ± 99.00
SDSS J163950.52+434003.7	3.990	3.97	47.28 ± 0.01	46.95 ± 0.01	$47.87 \pm$ -1.00	11.53 ± 0.74	99.00 ± 99.00	10.65 ± 0.19	99.00 ± 99.00
SDSS J164248.71+240303.3	3.480	3.48	46.96 ± 0.02	46.38 ± 0.01	45.12 ± 0.22	6.53 ± 0.45	$2.50 \pm$ -1.00	9.94 ± 0.17	$9.15 \pm$ -1.00
SDSS J165354.61+405402.1	4.977	4.97	47.05 ± 0.01	46.69 ± 0.01	45.45 ± 0.08	6.60 ± 0.34	4.36 ± 0.66	10.00 ± 0.14	9.83 ± 0.20
SDSS J165436.85+222733.7	4.698	4.68	47.09 ± 0.02	46.80 ± 0.01	45.48 ± 0.24	6.51 ± 0.61	99.00 ± 99.00	10.01 ± 0.18	99.00 ± 99.00
SDSS J165902.11+270935.1	5.312	5.33	99.00 ± 99.00	46.51 ± 0.02	$48.04 \pm$ -1.00	99.00 ± 99.00	99.00 ± 99.00	99.00 ± 99.00	99.00 ± 99.00
SDSS J172100.76+601721.0	5.799	5.79	99.00 ± 99.00	46.72 ± 0.02	$47.81 \pm$ -1.00	99.00 ± 99.00	99.00 ± 99.00	99.00 ± 99.00	99.00 ± 99.00
SDSS J173744.87+582829.5	4.916	4.90	99.00 ± 99.00	46.36 ± 0.02	$48.07 \pm$ -1.00	99.00 ± 99.00	99.00 ± 99.00	99.00 ± 99.00	99.00 ± 99.00
PSS J1745+6848	4.130	4.13	99.00 ± 99.00	46.24 ± 0.01	$47.99 \pm$ -1.00	99.00 ± 99.00	99.00 ± 99.00	99.00 ± 99.00	99.00 ± 99.00
RX J1759.4+6638	4.320	4.30	99.00 ± 99.00	46.13 ± 0.03	$47.96 \pm$ -1.00	99.00 ± 99.00	99.00 ± 99.00	99.00 ± 99.00	99.00 ± 99.00

Table 3.3 (cont'd)

Name	$z_{\rm ref}$	$z_{\rm H\alpha}$	log L_{1350}	log L_{5100}	log $L_{\rm H\alpha}$	FWHM$_{1000}$ C$_{\rm IV}$	FWHM$_{1000}$ Hα	log $M_{\rm BH}$ C$_{\rm IV}$	log $M_{\rm BH}$ Hα
PSS J1802+5616	4.160	4.16	99.00 ± 99.00	46.01 ± 0.02	$48.17 \pm$-1.00	99.00 ± 99.00	99.00 ± 99.00	99.00 ± 99.00	99.00 ± 99.00
BR 2212-1626	3.990	3.98	46.92 ± 0.03	46.91 ± 0.12	45.93 ± 0.10	2.31 ± 0.10	6.73 ± 1.26	8.95 ± 0.20	10.35 ± 0.24
BRI 2235-0301	4.249	4.28	47.02 ± 0.02	47.14 ± 0.01	$47.92 \pm$-1.00	10.29 ± 0.39	99.00 ± 99.00	10.40 ± 0.24	99.00 ± 99.00
SDSS J223841.81-000105.2	3.490	3.49	46.86 ± 0.02	46.55 ± 0.02	44.97 ± 0.33	6.10 ± 0.36	99.00 ± 99.00	9.82 ± 0.17	99.00 ± 99.00
BR 2248-1242	4.161	4.14	46.66 ± 0.07	46.81 ± 0.01	45.82 ± 0.10	1.58 ± 0.07	4.74 ± 0.96	8.46 ± 0.19	9.97 ± 0.24
BR J2328-4513	4.359	4.32	99.00 ± 99.00	46.41 ± 0.02	$47.92 \pm$-1.00	99.00 ± 99.00	99.00 ± 99.00	99.00 ± 99.00	99.00 ± 99.00
SDSS J233330.17+152538.7	3.680	3.68	46.61 ± 0.06	46.30 ± 0.02	45.19 ± 0.26	6.07 ± 0.88	99.00 ± 99.00	9.68 ± 0.26	99.00 ± 99.00
BR J2349-3712	4.208	4.22	46.86 ± 0.02	46.53 ± 0.01	$47.95 \pm$-1.00	5.73 ± 0.37	99.00 ± 99.00	9.77 ± 0.23	99.00 ± 99.00

Note. — Catalog of the properties derived for the *AKARI* quasars, sorted by right ascension. Most of the $z_{\rm ref}$ at ~ 6 are rounded to hundredths. The units for L, FWHM, and $M_{\rm BH}$ are ergs s^{-1}, 1000 km s^{-1}, and $M_{\odot}$. Columns 9 and 10 are from equations 3.9 and 3.6, respectively. Empty parameters are entered as 99 and upper limits are given with errors of -1.

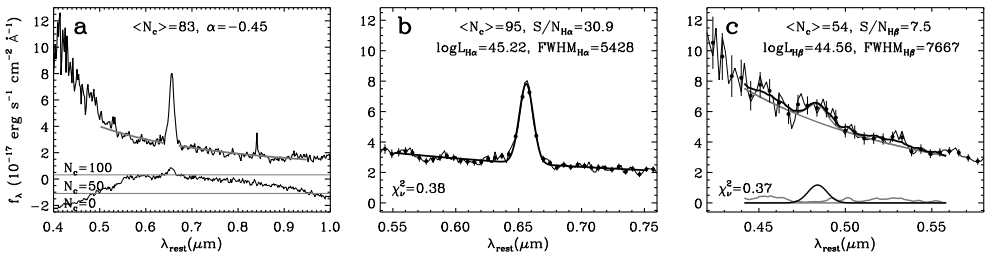

Figure 3.10: Composite spectra from *AKARI* observations. (a) The spectra within 0.4–1 μm (top), and the number of spectra used to construct the composite, N_c, plotted against wavelength (bottom). The mean N_c and the continuum slope from the 0.5–0.95 μm region are printed. (b) Hα region fit of the composite spectra. (c) Hβ region fit of the composite spectra. The sum of the continuum, Hβ emission, and the Fe II complex (thick black line), and the continuum (gray line) are overplotted on the data, while the Hβ and the Fe II emission components are separately plotted below the spectrum in black and gray lines.

Meanwhile, we interpolated the broad-band SED around the rest-frame 1350 and 3000 $\AA$ to obtain L_{1350} and L_{3000}. For this, we used objects with more than two data points in the rest-frame 500–2500 $\AA$ for L_{1350} or 2000–6000 $\AA$ for L_{3000}. The interpolation is done linearly to the data points, and we obtain 133 L_{1350} and 47 L_{3000} values. The L_{1350} and L_{5100} continuum luminosities derived by photometric and spectroscopic methods roughly agree with each other as shown in Figure 3.9. Likewise to L_{5100}, we calculated the level of C IV or Mg II line contamination to the L_{1350} and L_{5100} from broad-band photometry. The C IV and Mg II elevates the observed broad-band flux by up to 0.06 and 0.04 dex. Thus, it is possible that the photometry embracing the broad UV emission is boosted by more than the typical measurement error in L_{1350} and L_{3000}, which are 0.01 and 0.03 dex, respectively. Between the spectroscopically and photometrically derived continuum luminosities, we will use in the following discussion the spectroscopically derived L_{1350} and the photometrically derived L_{3000} and L_{5100}. We do so because the line contaminations near 1350 $\AA$ through the broad-band photometry can be significantly larger

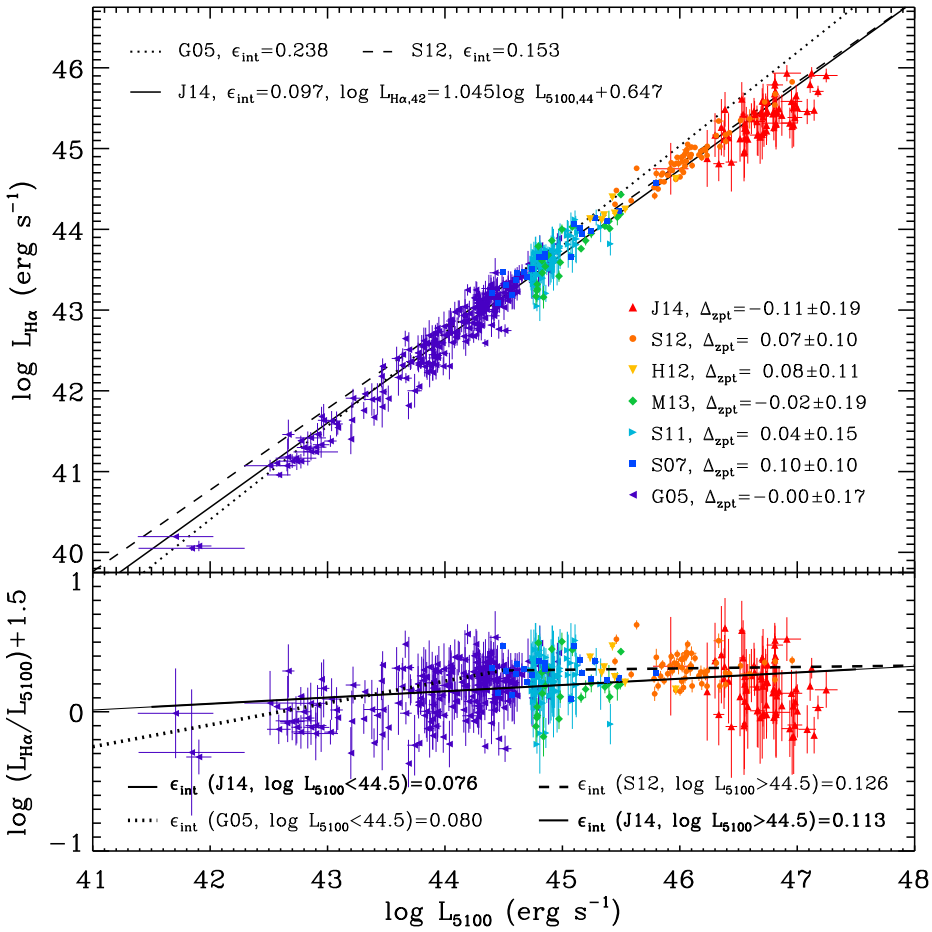

Figure 3.11: The L_{5100}–$L_{H\alpha}$ relation of AGNs (top), and its projection on the L_{5100}–$L_{H\alpha}/L_{5100}$ (bottom), from combined references. The references abbreviated on the plot are summarized in Table 3.4, where all measurements from references are converted to our adopted cosmology. We limited the G05 data with $L_{5100} < 10^{44.73}\,\mathrm{ergs\,s^{-1}}$ to avoid overlap with the S11 data. The L_{5100}–$L_{H\alpha}$ relation from G05, S12, and J14 are shown in dotted, dashed, and solid lines respectively. The zeropoint offset and rms scatter of each literature data with respect to our relation are denoted as Δ_{zpt}. The intrinsic scatter (ϵ_{int}, dex) of the entire data with respect to the G05, S12, and J14 relations (top), and of the data divided by $L_{5100} = 10^{44.5}\,\mathrm{ergs\,s^{-1}}$ (bottom), are shown. The L_{5100} in M13 and J14 are from photometric SED fitting (Section 3.3.2), while the rest are spectroscopically derived from each reference. The $L_{H\alpha}$ are from broad emission for all references but for the G05, S07, and S11 data, where the narrow component is included.

than the measurement uncertainty, while it is not so around the Mg II and Hα lines. The large error in L_{5100} from *AKARI* spectra is also another reason why we opt to use L_{5100} from the broad-band SED fitting. The fitted properties from this section, and the $M_{\rm BH}$ to appear in Section 3.4, are listed in Table 3.3. For objects with both NG and NP observations and $\rm S/N_{H\alpha} > 3$, we use the $z_{\rm H\alpha}$ and $\rm FWHM_{H\alpha}$ from the NG, and the $L_{\rm H\alpha}$ from the NP, while we list only the values from the NG mode otherwise.

3.4 Results

3.4.1 Composite spectra

To investigate the overall rest-optical spectral properties of the sample, we construct the composite *AKARI* spectra. Out of 154 objects observed with NG, 128 are used for the composite construction after removing 26 spectra due to a mild level of confusion from neighbor source spectra, negative continuum levels, or strong fluctuations near the Hα due to warm pixels. The composite is constructed by normalizing the spectra at 5100 $\mathring{A}$ and taking their error weighted mean to maximize the S/N. Each spectral flux and error were de-redshifted, and rebinned to a common wavelength scale of 18 $\mathring{A}$ per bin which is equal to that of the *AKARI* at rest-frame Hα. In Figures 3.10a–3.10c, we plot the composite spectrum, and zoomed-in fit to the Hα and Hβ regions, respectively.

We determine the continuum slope from the 0.5–0.95 μm region from Figure 3.10a, where the number of spectra used to construct the composite exceeds 50. The slope $\alpha = -0.45$ (where $f_\nu \propto \nu^\alpha$) is close to $\alpha = -(0.37\text{–}0.48)$ of Glikman et al. (2006) determined through the composite of local luminous quasars at similar wavelengths, indicating a similarity in the rest-optical continuum shape of luminous type-1 quasars with respect to redshift. Interestingly, we detect a sign of the Hβ and Fe II complex emissions from Figure 3.10c.

The Hβ region was fitted with the Boroson & Green (1992) Fe II template, following the method of Shen et al. (2008b). We find $L_{\mathrm{H}\alpha}/L_{\mathrm{H}\beta} = 4.5 \pm 1.9$, which is marginally consistent to 3.6 ± 1.4 from luminous $z \sim 2$ quasars (S12) or the model broad Balmer line decrement of AGNs at T=10,000–12,000 K, $L_{\mathrm{H}\alpha}/L_{\mathrm{H}\beta} = 3.6$–$8.8$ (Osterbrock, 1989), but with a large uncertainty. Since the Balmer decrement value and the $\mathrm{S/N}_{\mathrm{H}\alpha}$ of each *AKARI* spectrum suggest that the strongest Hβ in our individual spectrum would appear as $\mathrm{S/N}_{\mathrm{H}\beta}$=1–2, we do not expect the Hβ emission to be individually detected, consistent with the visual inspection in Section 3.3.1. Apart from this, we do not find hint of other emission lines in the composite spectra.

3.4.2 Luminosity and line width scaling relations

The derivation of continuum and line luminosities for distant, luminous quasars allows us to examine the universality of the luminosity scaling relations over a wide range of redshifts and luminosities. Starting from the L_{5100}–$L_{\mathrm{H}\alpha}$ relation, we plot in Figure 3.11 our derived data points and the data taken from literatures (Greene & Ho 2005, hereafter G05; Shang et al. 2007, hereafter S07; S11; Ho et al. 2012; Matsuoka et al. 2013; S12) that cover a range of L_{5100} and z, as summarized in Table 3.4. Our *AKARI* data extends the relation at the high redshift ($z > 3.3$) and high luminosity end ($L_{5100} > 10^{46}\,\mathrm{ergs\,s^{-1}}$). To minimize the host galaxy contribution to the AGN luminosities, we chose AGNs with host contamination <20% in L_{5100}, $L_{\mathrm{H}\alpha}$ for some datasets (G05; S07), while we plotted only the $L_{5100} > 10^{44.73}\,\mathrm{ergs\,s^{-1}}$ data for the rest of references to meet <10% in host contamination (S11). Meanwhile, the broad $L_{\mathrm{H}\alpha}$ could contain the narrow component for *AKARI* data, while the broad and narrow line luminosities are combined for the G05, S07, and S11 data too. We find that the contribution from the narrow component to $L_{\mathrm{H}\alpha}$ estimated from Section 3.3.1 and the references, is negligible (2% and $< 10\%$, respectively), allowing us to consider $L_{\mathrm{H}\alpha}$ to be approximately the line luminosity of the

broad line component.

Figure 3.11 shows a remarkable correlation between L_{5100} and $L_{\mathrm{H}\alpha}$ even when AGNs are drawn from various samples covering a wide range of redshifts and luminosities. This strongly suggests that the physics governing the correlation is the same for low and high luminosity AGNs, and there is no strong evolution in the relation from $z=0$ to $z=6$ over the range explored here. The *AKARI* data points are mildly below the relation where the offset could indicate a growing population of weak emission line quasars at high redshift (Fan et al. 1999; Diamond-Stanic et al. 2009), but the overall deviations are within the scatter of the data. We fitted the relation using the linear regression with bivariate correlated errors and intrinsic scatter (BCES, Akritas & Bershady 1996)[1], to find the following result,[2]

$$\begin{aligned}\log L_{\mathrm{H}\alpha,42} = (1.046 \pm 0.008)\ \log L_{5100,44} \\ +(0.645 \pm 0.010).\end{aligned} \tag{3.1}$$

The best-fit relation fits the entire data with an intrinsic rms scatter of 0.10 dex.

To examine the universality of the relation further, we discuss how the L_{5100}–$L_{\mathrm{H}\alpha}$ relation of G05 at $z\sim0$ of lower luminosity AGNs and S12 at $z\sim2$ of higher luminosity AGNs fare with each literature values. First, the G05 relation can describe the L_{5100}–$L_{\mathrm{H}\alpha}$ relation of S07, S11, and M13 AGNs over the overlapping luminosity interval ($L_{5100}\lesssim10^{45}\,\mathrm{ergs\,s^{-1}}$). When extrapolated to higher luminosity, it starts to deviate from the data points regardless of redshift. Likewise, the S12 relation can describe the L_{5100}–$L_{\mathrm{H}\alpha}$ relation down to $L_{5100}\lesssim10^{44.5}\,\mathrm{ergs\,s^{-1}}$ including the S07 data at $z<0.4$ and our AGNs at $z>3.3$. However, when applied to the entire datasets, the G05 and S12 relations show deviations from the data at high and low lumnosity regions,

[1] Throughout this paper we use the BCES fit to derive the linear relations.

[2] Throughout this paper we use subscript numbers to the luminosity to indicate its wavelength and unit, such as $L_{5100,44}=L_{5100\,\mathring{A}}/10^{44}\,\mathrm{ergs\,s^{-1}}$.

respectively. Consequently, both relations produce $\epsilon_{\rm int} = 0.15$–$0.24$ dex against the data which is worse than 0.10 dex of our L_{5100}–$L_{\rm H\alpha}$ relation of Equation (3.1).

To check if the inconsistency in the G05 and S12 relations at the faint and luminous end arises from a possible break in the relation itself, we considered the case where the slope changes at $L_{5100} \sim 10^{44.5}\,{\rm erg\,s^{-1}}$, where the G05 and S12 relations meet. For this, we computed the $\epsilon_{\rm int}$ of the $L_{5100} < 10^{44.5}\,{\rm erg\,s^{-1}}$ and $L_{5100} > 10^{44.5}\,{\rm erg\,s^{-1}}$ data against the G05, S12, and our relation in Equation (3.1), and examined if our simple relation is any worse than the combination of G05 and S12 relations with a break at $L_{5100} = 10^{44.5}\,{\rm erg\,s^{-1}}$. As indicated in the lower panel of Figure 3.11, the $\epsilon_{\rm int}$ values against our relation is comparable to or slightly smaller than the $\epsilon_{\rm int}$ against the G05 or S12 relations at low and high luminosities respectively. This suggests that there is no strong need for a broken power-law form of the L_{5100}–$L_{\rm H\alpha}$ relation, and a simple relation of Equation (3.1) can be employed to describe the response of broad line region to the incident continuum emission over the covered redshift and luminosity ranges in Figure 3.11 and Table 3.4.

Likewise, we plot in Figure 3.12 the L_{5100}–L_{1350} and L_{5100}–L_{3000} relations from the luminosities derived in Section 3.3 and taken from references. Apart from the literature data where the host contamination in L_{5100} is estimated to be <20% (S07), or minimized by Hubble Space Telescope (HST) observations (Bentz et al. 2013, and a part of Park et al. 2013), we limit the literature sample with $L_{5100} > 10^{44.73}\,{\rm erg\,s^{-1}}$ to keep the host galaxy contamination below 10% (S11). Meanwhile, the McLure & Jarvis (2002) data are cross checked with Bentz et al. (2013), to include only the AGNs with <20% host contamination in L_{5100}. Similarly to the L_{5100}–$L_{\rm H\alpha}$ relation, we do not find any evolution in the L_{5100}–L_{1350} and L_{5100}–L_{3000} relations for a particular set of data, and we

Table 3.4. Dynamical range of references

Reference	z	L_{5100} (ergs s^{-1})
M02	0.02–0.29	43.7–46.0
G05	<0.35	41.7–45.0
N07	2.3–3.5	45.2–46.3
S07	0.08–0.40	44.4–45.8
M08	0.35–0.37	43.6–44.4
D09	1.1–2.2	46.1–46.7
A11	1.4–3.6	44.8–46.5
S11	0.08–0.80	43.8–46.4
H12	1.4–1.5	45.2–46.0
S12	1.5–2.2	45.4–47.0
M13	0.7–1.7	44.8–45.5
P13	<0.23	42.6–45.9
J14	3.3–6.2	45.9–47.2

Note. — The abbreviated references are McLure & Jarvis 2002; Greene & Ho 2005; Netzer et al. 2007; Shang et al. 2007; McGill et al. 2008; Dietrich et al. 2009; Assef et al. 2011; Shen et al. 2011; Ho et al. 2012; Shen & Liu 2012; Matsuoka et al. 2013; Park et al. 2013; and this work.

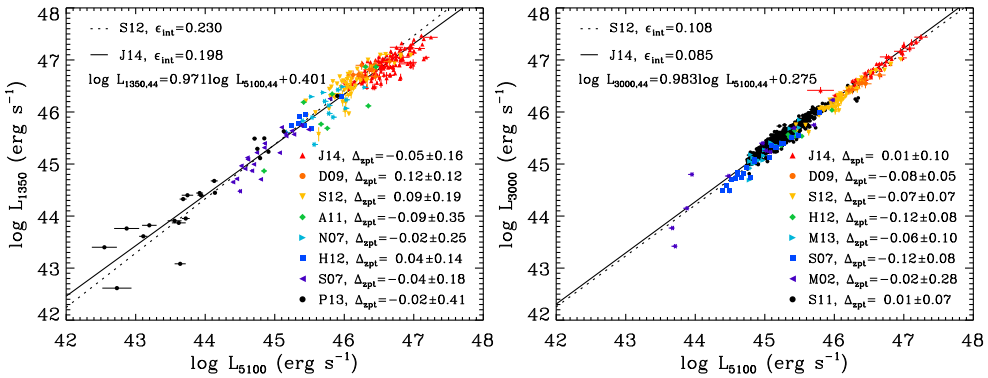

Figure 3.12: The L_{5100}–L_{1350} and L_{5100}–L_{3000} relations of AGNs from combined references. The references abbreviated on the plot are summarized in Table 3.4, where all measurements from references are converted to our adopted cosmology. The L_{1350} of the N07 sample are searched from S11. The L_{5100}, L_{3000}, and L_{1350} are spectroscopically derived, except for the L_{5100}, L_{3000} from J14 where they are from photometric SED fitting (Section 3.3.2). We assign a modest 10% error for L_{5100} of the N07 data and L_{1350}, L_{5100} of the A11 data, and 20% error for the L_{1350}, L_{3000}, and L_{5100} from D09 data, from visual inspection of their spectra. The L_{5100}–L_{1350}, L_{5100}–L_{3000} relations from S12 and J14 are shown in dotted and solid lines respectively. The zeropoint offset and rms scatter of each literature data with respect to our relations, are indicated.

find the best-fit correlation to be,

$$\begin{aligned} \log L_{1350,44} &= (0.971 \pm 0.022)\ \log L_{5100,44} \\ &\quad +(0.401 \pm 0.051) \\ \log L_{3000,44} &= (0.983 \pm 0.009)\ \log L_{5100,44} \\ &\quad +(0.275 \pm 0.013). \end{aligned} \tag{3.2}$$

The $\epsilon_{\rm int}$ values (dex) to these best-fit relation, as well as the relation with respect to S12 are presented in Figure 3.12.

Finally, we compare the broad line FWHM of Hβ, Hα, Mg II, and C IV in Figure 3.13 in order to calibrate the $M_{\rm BH}$ from multiple line based recipes and to check for any evolution in the FWHM relations. For good comparison of FWHMs, we restricted the mixed samples to have the fractional errors of

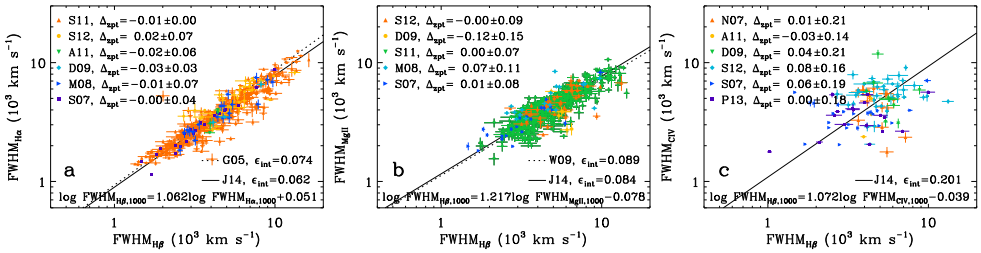

Figure 3.13: The $\mathrm{FWHM}_{\mathrm{H}\beta}$–$\mathrm{FWHM}_{\mathrm{H}\alpha}$, $\mathrm{FWHM}_{\mathrm{H}\beta}$–$\mathrm{FWHM}_{\mathrm{Mg\,II}}$, and $\mathrm{FWHM}_{\mathrm{H}\beta}$–$\mathrm{FWHM}_{\mathrm{C\,IV}}$ relations of AGNs from combined references. The references abbreviated on the plot are summarized in Table 3.4, with W09 additionally from Wang et al. (2009). The *AKARI* data are not present since the sample do not have simultaneous coverage of the FWHMs plotted. We limited the G05 data with a $L_{5100} < 10^{44.73}\,\mathrm{ergs\,s^{-1}}$ limit to avoid overlap with the S11 data. We assign a 10% error for $\mathrm{FWHM}_{\mathrm{H}\beta}$, $\mathrm{FWHM}_{\mathrm{C\,IV}}$ of the N07 data, following their argument. The $\mathrm{FWHM}_{\mathrm{H}\beta}$–$\mathrm{FWHM}_{\mathrm{H}\alpha}$ relation of G05, and $\mathrm{FWHM}_{\mathrm{H}\beta}$–$\mathrm{FWHM}_{\mathrm{Mg\,II}}$ relation of W09 are shown in dotted lines, while the relations from this work are shown as solid lines. The zeropoint offset and rms scatter of each literature data with respect to our relations, are indicated. The FWHMs are of the broad emission line.

FWHM less than 15%, while additionally limiting the S/N and reduced chi-square of the SDSS spectra to be S/N>20 and $\chi^2_\nu < 2$. In Figure 3.13a, we fit the $\mathrm{FWHM}_{\mathrm{H}\beta}$–$\mathrm{FWHM}_{\mathrm{H}\alpha}$ relation from the collected data, where we find the offset of each reference data to this relation to fall within each scatter. The ϵ_{int} of all the data to our relation, 0.062 dex, is smaller than when using the relation from G05.

Second, we derive the $\mathrm{FWHM}_{\mathrm{H}\beta}$–$\mathrm{FWHM}_{\mathrm{Mg\,II}}$ relation. Since it is debatable whether to subtract the narrow component for the Mg II line width measurement (e.g., S11), we compared the $\mathrm{FWHM}_{\mathrm{H}\beta}$ to the $\mathrm{FWHM}_{\mathrm{Mg\,II}}$ with and without the narrow component subtraction, from the S11 data at $0.45 < z < 0.8$. We find the least ϵ_{int} to the $\mathrm{FWHM}_{\mathrm{H}\beta}$ when averaging the line widths derived with and without the subtraction of the narrow component (0.078 dex), than to use each method (0.084 and 0.080 dex respectively), consistent with Jun & Im (2013). Also, the slope and constant of the relation are consistent within

uncertainty with those derived with and without the subtraction of the narrow $\mathrm{FWHM_{Mg\,II}}$ component. Therefore, we use the averaged $\mathrm{FWHM_{Mg\,II}}$ with and without narrow component subtraction in S11, and each method used for the literature data, to derive the $\mathrm{FWHM_{H\beta}}$–$\mathrm{FWHM_{Mg\,II}}$ relation altogether. We note that the relative FWHM offset of the literature data to our relation shown in Figure 3.13b are within the scatter of data points, indicating that the details of fitting to exclude the narrow Mg II component (S07; McGill et al. 2008; Dietrich et al. 2009) or to include but subtract it (S12) does not affect the line widths significantly overall. The rms of all the data to our relation, 0.084 dex, is smaller than that from W09, and small enough to regard the $\mathrm{FWHM_{Mg\,II}}$ as a marginally good substitute of $\mathrm{FWHM_{H\beta}}$ as much as $\mathrm{FWHM_{H\alpha}}$.

Third, we derive the $\mathrm{FWHM_{H\beta}}$–$\mathrm{FWHM_{C\,IV}}$ relation in Figure 3.13c. The data can be fitted altogether with a log-linear relation, but the $\epsilon_{\rm int}$ of the data to the relation, 0.201 dex, is large and comparable to the systematic uncertainty of single-epoch BH mass estimators when scaled as the FWHM squared. Overall, we find the relations of $\mathrm{FWHM_{H\alpha}}$, $\mathrm{FWHM_{Mg\,II}}$ and $\mathrm{FWHM_{C\,IV}}$ against the $\mathrm{FWHM_{H\beta}}$ without any noticeable evolution for the samples considered, covering a wide range of luminosity or redshift. Therefore, although the data is missing at $z \gtrsim 3$, we use our FWHM relations to calibrate the $M_{\rm BH}$ estimators for general usage in terms of redshift. Our derived FWHM relations are as follows,[3]

$$\begin{aligned}
&\log \mathrm{FWHM_{H\beta,1000}} \\
&= (1.062 \pm 0.015)\ \log \mathrm{FWHM_{H\alpha,1000}} + (0.051 \pm 0.009) \\
&= (1.217 \pm 0.029)\ \log \mathrm{FWHM_{Mg\,II,1000}} - (0.078 \pm 0.019) \\
&= (1.072 \pm 0.071)\ \log \mathrm{FWHM_{C\,IV,1000}} - (0.039 \pm 0.053).
\end{aligned} \tag{3.3}$$

[3]Throughout this paper we use subscript numbers to the line width to indicate its unit, such as $\mathrm{FWHM_{H\beta,1000}} = \mathrm{FWHM_{H\beta}}/10^3\,\mathrm{km\,s^{-1}}$.

3.4.3 Updated $M_{\rm BH}$ estimators

Using the scaling relations obtained above, we now present an updated set of $M_{\rm BH}$ estimators based on various lines. Since the reverberation mapping of Hβ and L_{5100} forms the basis of mass estimation for AGNs, we start from the $M_{\rm BH}$ estimator that uses the 5100Å luminosity and Hβ line width to take the following form and derive other estimators using scaling relations discussed above:

$$M_{\rm BH} = \frac{f}{G} R_{\rm BLR}(L_{5100}) \Big(\frac{\rm FWHM_{H\beta}}{2}\Big)^2. \tag{3.4}$$

Previous secondary calibrations to the $M_{\rm BH}$ were performed through replacing the (L_{5100}, FWHM$_{\rm H\beta}$) of the local reverberation mapped sample or SDSS AGNs, by ($L_{\rm H\alpha}$, FWHM$_{\rm H\alpha}$) (e.g., Greene & Ho 2005), (L_{3000}, FWHM$_{\rm MgII}$) (e.g., McLure & Jarvis 2002), or (L_{1350}, FWHM$_{\rm C_{IV}}$) (e.g., Vestergaard & Peterson 2006). Using the latest R–L relation from Bentz et al. (2013)[4] and the constant for the mass equation (f–factor, $f = 5.1 \pm 1.3$) from Woo et al. (2013), we derive first the Hβ $M_{\rm BH}$ estimator as,

$$\begin{aligned} &R_{\rm BLR} = (34.7 \pm 2.5)\, {L_{5100,44}}^{(0.533\pm0.034)}\, {\rm lt-day} \\ &M_{\rm BH}(L_{5100}, {\rm FWHM_{H\beta}}) = (8.63 \pm 2.29) \times 10^6 \\ &\times {L_{5100,44}}^{(0.533\pm0.034)}\, {\rm FWHM_{H\beta,1000}}^2 M_\odot. \end{aligned} \tag{3.5}$$

Replacing the Hβ line width through the FWHM$_{\rm H\beta}$–FWHM$_{\rm H\alpha}$ relation from Equation (3.3) we get the $M_{\rm BH}$ from (L_{5100}, FWHM$_{\rm H\alpha}$),

$$\begin{aligned} &M_{\rm BH}(L_{5100}, {\rm FWHM_{H\alpha}}) = (1.09 \pm 0.29) \times 10^7 \\ &\times {L_{5100,44}}^{(0.533\pm0.034)}\, {\rm FWHM_{H\alpha,1000}}^{(2.12\pm0.03)} M_\odot. \end{aligned} \tag{3.6}$$

[4]We shifted the relation to Hubble parameter of $H_0 = 70\,{\rm km\,s^{-1}\,Mpc^{-1}}$ which is our adopted value throughout this work.

Finally, the application of Equation (3.1) yields the $M_{\rm BH}$ from ($L_{\rm H\alpha}$, FWHM$_{\rm H\alpha}$),

$$M_{\rm BH}(L_{\rm H\alpha}, {\rm FWHM}_{\rm H\alpha}) = (5.11 \pm 1.39) \times 10^6 \times L_{\rm H\alpha,42}{}^{(0.510\pm0.033)}\, {\rm FWHM}_{\rm H\alpha,1000}{}^{(2.12\pm0.03)} M_\odot. \quad (3.7)$$

Likewise, using Equations (3.2) and (3.3) to replace the continuum luminosity and line width in Equation (3.5) to those of Mg II and C IV yields,

$$M_{\rm BH}(L_{3000}, {\rm FWHM}_{\rm MgII}) = (4.28 \pm 1.20) \times 10^6 \times L_{3000,44}{}^{(0.542\pm0.035)}\, {\rm FWHM}_{\rm MgII,1000}{}^{(2.43\pm0.06)} M_\odot \quad (3.8)$$

$$M_{\rm BH}(L_{1350}, {\rm FWHM}_{\rm CIV}) = (4.35 \pm 1.60) \times 10^6 \times L_{1350,44}{}^{(0.549\pm0.037)}\, {\rm FWHM}_{\rm CIV,1000}{}^{(2.14\pm0.14)} M_\odot. \quad (3.9)$$

The $M_{\rm BH}$ based on Hα and C IV from our estimators for the *AKARI* sample are given in Table 3.3. It is worth noting that Equation (3.4) may not hold if the FWHM$_{\rm H\beta}$ is not exactly proportional to the velocity dispersion, σ (Peterson et al. 2004; Collin et al. 2006), or if the *R*–*L* relation breaks down at high luminosity where the relation has not been tested extensively with the reverberation technique ($L_{5100} > 10^{46}$ergs s^{-1}, Bentz et al. 2013). Nevertheless, considering the advantages of using the FWHM (to be robust under poor sensitivity, wings in the line profile, or deblending, see S12) for the single epoch mass estimation, and the current expectations in the high luminosity *R*–*L* relation (see Section 3.5.1), our set of calibrations have the merit where the rest-UV to optical $M_{\rm BH}$ estimations are mutually consistent through a wide range of redshifts, luminosities, and fitting methodologies.

To check the consistency between our $M_{\rm BH}$ estimators, we first compare the Balmer $M_{\rm BH}$ using the estimator in this work and existing estimators in Figure 3.14. The $M_{\rm BH,H\beta}$ and $M_{\rm BH,H\alpha}$ are compared, where a $\Delta M_{\rm BH} < 0.3$ dex

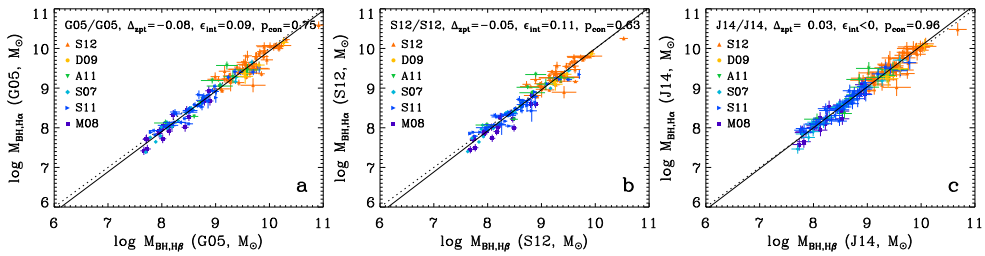

Figure 3.14: The comparison of Balmer $M_{\rm BH}$ relations of AGNs, from combined references. The references abbreviated on the plot are summarized in Table 3.4. All measurements are converted to our adopted cosmology and f–factor. The linear fit to the $M_{\rm BH}$ relation and a 1–1 relation are represented by solid and dotted lines respectively, while the zeropoint offset between the masses ($\Delta_{\rm zpt}$), intrinsic scatter with respect to a 1-1 relation ($\epsilon_{\rm int}$), and the fraction where the masses are consistent within error ($\rm p_{con}$) are printed.

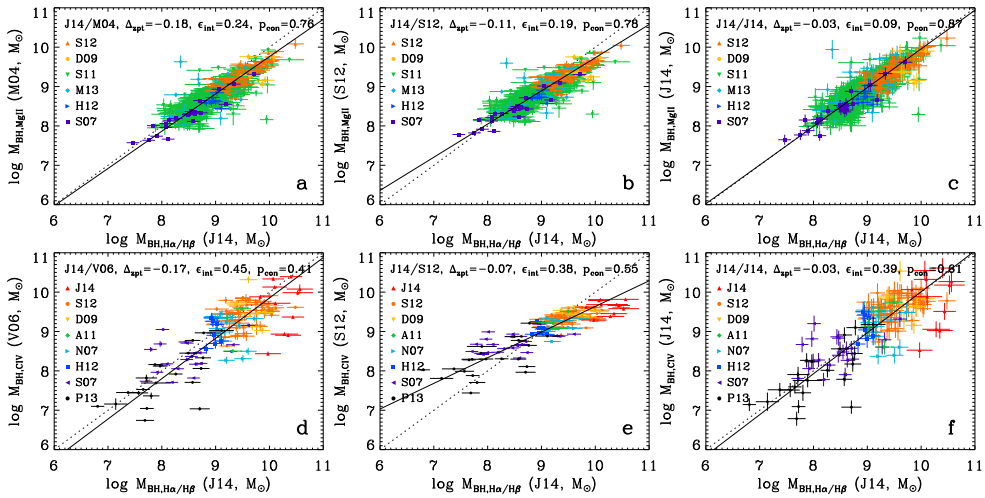

Figure 3.15: The comparison of Balmer $M_{\rm BH}$ to the UV $M_{\rm BH}$ of AGNs, from combined references. The references abbreviated on the plot are summarized in Table 3.4, with M04, V06 estimators from McLure & Dunlop (2004) and Vestergaard & Peterson (2006). All measurements are converted to our adopted cosmology and f–factor. We use the $M_{\rm BH}(L_{5100}, {\rm FWHM_{H\alpha}})$ for the Balmer masses, unless when the Hα line was uncovered and the $M_{\rm BH}(L_{5100}, {\rm FWHM_{H\beta}})$ was used. The rest of the figure format follows that of Figure 3.14.

error cut is applied to the data out of various references. The $M_{\rm BH}$'s are derived from the G05, S11 estimators and from this work (Equations 3.5, 3.6) in Figures 3.14a–3.14c respectively, where the zeropoint offset between the masses ($\Delta_{\rm zpt}$), intrinsic scatter with respect to a 1-1 relation ($\epsilon_{\rm int}$), and the fraction where the masses are consistent within error ($\rm p_{con}$) are shown. We find that the masses from our estimators are closer to a 1–1 relation than of G05 or S11, throughout the range $10^{7-10}M_{\odot}$. Also, fully considering the propagated errors in the mass equation, our estimators may overestimate the $M_{\rm BH}$ uncertainty when comparing the Hβ and Hα masses as reflected from the negative $\epsilon_{\rm int}$, which suggests that the difference in the f–factor or $R_{\rm BLR}$ for the Hβ and Hα line emitting regions are likely to be smaller than their uncertainty. Therefore, we regard the Hβ and Hα $M_{\rm BH}$'s from our estimators to be indistinguishable, which is supported by the high fraction (96 %) of Hβ/Hα masses to be consistent within measurement error.

With the Balmer $M_{\rm BH}$ recipes checked to be mutually consistent, we further compare the Balmer to the UV-based $M_{\rm BH}$'s with $\Delta M_{\rm BH} < 0.3$ dex, in Figure 3.15. We use $M_{\rm BH,H\alpha}$ as the Balmer mass due to the stronger Hα emission than Hβ, unless when only the Hβ line is observed and the $M_{\rm BH,H\beta}$ is used. Compared to the conventional estimators calibrated at relatively low luminosity and redshift (McLure & Dunlop 2004; Vestergaard & Peterson 2006) or relatively high luminosity and redshift (S12), our calibrations (Equation 3.5, 3.6, 3.8, 3.9) bring the rest-UV (Mg II in Figure 3.15a–3.15c, C IV in Figure 3.15d–3.15f) and Balmer $M_{\rm BH}$ to be closer to a 1–1 relation in the range $10^{7-10}M_{\odot}$ in terms of both zeropoint offset and intrinsic scatter. Especially, we find the McLure & Dunlop (2004) and S12 estimators to bring a systematic offset in the $M_{\rm BH,MgII}$ or $M_{\rm BH,CIV}$ with the Balmer $M_{\rm BH}$, which is largely from the different slope of the FWHM term to that of our estimator, checked by fixing the slope of the FWHM term to that of our estimators. This effect is the most pronounced when comparing the C IV and Balmer $M_{\rm BH}$ in Figure

3.15e, where the $M_{\rm BH,C_{IV}}$ calibrated with a shallow $\rm FWHM_{C_{IV}}$ slope (S12; see also, Park et al. 2013) makes its intrinsic scatter to the Balmer $M_{\rm BH}$ as small as our estimator, and may even place the C IV and Balmer masses to be consistent when calibrated within a narrow range of masses, but shows a severe systematic offset to the Balmer $M_{\rm BH}$ over a wide dynamic range. Thus, we caution on the usage of conventional estimators when extensively comparing the rest-optical and UV $M_{\rm BH}$'s.

Even when using our rest-UV mass equations with minimized zeropoint and systematic offsets, the intrinsic scatter is another issue. Although our $\epsilon_{\rm int}$ of the $M_{\rm BH,Mg_{II}}$ to the Balmer $M_{\rm BH}$ is relatively small (0.09 dex), the $\epsilon_{\rm int}$ of the $M_{\rm BH,C_{IV}}$ to the Balmer $M_{\rm BH}$ (0.39 dex) is comparable to the systematic uncertainty of the single epoch mass estimator itself (Bentz et al. 2013; Woo et al. 2013). Moreover, since our estimators take into account the error of f–factor, $R-L$ relation, scatter in the UV–optical luminosity and line width relations, the rest-UV masses that deviate more than its error from the Balmer masses (13% of the $M_{\rm BH,Mg_{II}}$ and 39% of the $M_{\rm BH,C_{IV}}$) indicate a serious flaw in the rest-UV calibration steps, such that the $M_{\rm BH,C_{IV}}$ may not be generally used to yield consistent $M_{\rm BH}$ to the Balmer masses. Indeed, we find 4 out of 11 $M_{\rm BH,C_{IV}}$'s of *AKARI* quasars on Figure 3.15f to be scattered to the $M_{\rm BH,H\alpha}$ by an order of magnitude or larger, such that the use of C IV masses is doubtful up to the highest redshifts even when considering the additional uncertainties in the *AKARI* $M_{\rm BH,H\alpha}$ tested in Figure 3.5.

3.5 Discussion

3.5.1 Reliability of single-epoch AGN black hole masses

Does the relations between continuum and line luminosities, and the FWHM relations that hold up to the highest luminosity AGNs, guarantee the mass estimation of the most luminous AGNs? Unfortunately the answer is not

clear yet, since the $R_{\rm BLR,H\beta}$–L_{5100} relation is not observationally probed for $L_{5100} > 10^{46}\,{\rm ergs\,s^{-1}}$ (Bentz et al., 2013). A hint to estimate the high luminosity end behavior of the optical R–L relation is to look at the $R_{\rm BLR,C_{IV}}$–L_{1350} relation, where the $R_{\rm BLR,C_{IV}}$ traces the inner part to the Hβ line region. Although the current number of C IV reverberation measurements is small (Kaspi et al. 2007, Sluse et al. 2011, Chelouche et al. 2012), they cover up to luminosities of $L_{1350} = 10^{47.0}\,{\rm ergs\,s^{-1}}$ and $L_{5100} = 10^{46.8}\,{\rm ergs\,s^{-1}}$. The slope of the relation in Kaspi et al. (2007), (0.52–0.55)$\pm$0.04, is within the uncertainty to the slope of the $R_{\rm BLR,H\beta}$–L_{5100} relation (Bentz et al., 2013), 0.533 ± 0.034. This suggests that the ratio of $R_{\rm BLR,H\beta}$-to-$R_{\rm BLR,C_{IV}}$ is nearly a constant at 2-4 over $L_{5100} < 10^{46}\,{\rm ergs\,s^{-1}}$, where the proportionality of L_{5100} and L_{1350} suggests that it is likely so at a higher luminosity range. Therefore, we do not expect a break in the luminous end optical R–L relation unless the optical data will somehow fail to form a simple relation at high luminosity where the current UV relation holds. Future compilations of both the C IV and Hβ broad line region sizes will help to better constrain the luminous end R–L relation.

Even if we find it plausible to assume that the $R_{\rm BLR,H\beta}$–L_{5100} relation does not change its slope in the luminous end, the large scatter in between the Balmer and rest-UV BH masses imposes further limitations on the usage of UV $M_{\rm BH}$ estimators. The greatest uncertainties when calibrating the UV $M_{\rm BH}$ estimators in this work ($\epsilon_{\rm int} > 0.1$ dex), come from the scatter in the L_{5100}–L_{1350} and ${\rm FWHM_{H\beta}}$–${\rm FWHM_{C_{IV}}}$ relations. Since a variety of obscuration in the rest-UV continuum of quasars may result in a scattered L_{5100}–L_{1350} relation, we suggest to take into account the level of obscuration when establishing the $M_{\rm BH,C_{IV}}$ estimator, although careful treatment is required as it is controversial whether the color correction into the $M_{\rm BH}$ works to reduce the scatter between the C IV and Balmer masses (Assef et al. 2011; S12). Meanwhile, the scatter in the FWHM relations which is the largest for the ${\rm FWHM_{H\beta}}$–${\rm FWHM_{C_{IV}}}$ relation, could arise from broad absorption features or a non-reverberating

component of the C IV broad emission (Denney, 2012), where future reverberation mapping will further enable us to test. Without detailed analysis on the origin of the scatter in between the Balmer and rest-UV BH masses, we caution on the individual measurement of BH masses from UV, especially the one using C IV.

3.5.2 On the massive end black hole mass evolution

Having cross-calibrated the $M_{\rm BH}$ estimators, we plot the distant Balmer and Mg II BH masses along redshift and the $M_{\rm BH}$ histogram in Figure 3.16, from our *AKARI* observations and the literature. First of all, we notice that the most massive envelope that stays at $\sim 10^{10} M_{\odot}$ up to $z \sim 5$, starts to disappear at higher redshift. To quantify how significant the massive end $z > 5$ quasars are smaller in BH mass, we performed the Kolmogorov–Smirnov (K–S) test by comparing the mass distribution at above $z = 5$ and below, and for $M_{\rm BH} > 2 \times 10^9 M_{\odot}$. This threshold mass for completeness, is governed by the shallow *AKARI* data and is determined through the L_{5100} limit at $\mathrm{S/N_{H\alpha}} = 3$ and the FWHM limit of $2500\,\mathrm{km\,s^{-1}}$ from Section 3.3.1. The K–S probability $p_{KS} = 1.0\%$ turns out to be meaningfully small, supporting the massive end BHs at $z < 5$ to be heavier than at $z > 5$.

This evolution is also reflected through the $M_{\rm BH}$ histogram in Figure 3.16. When comparing the $M_{\rm BH} > 2 \times 10^9 M_{\odot}$ data at above $z = 5$ and below, we find that the functional form of the $z = 6$ BH mass function from Willott et al. (2010) fits the $z > 5$ histogram well, but cannot fit the $z < 5$ histogram for any normalization such that it shows an excess of $\sim 10^{10} M_{\odot}$ BHs. Overall, we find that the $z > 5$, $\sim 10^9 M_{\odot}$ AGNs are likely to be in a rapidly growing state such that their masses will become $\sim 10^{10} M_{\odot}$ at $z < 5$, consistent with the higher Eddington ratio trend found in distant, luminous AGNs (De Rosa et al. 2011; Willott et al. 2010). We checked our results to be unchanged by the inclusion of *AKARI* data with poor resolution/sensitivity that could bias the masses

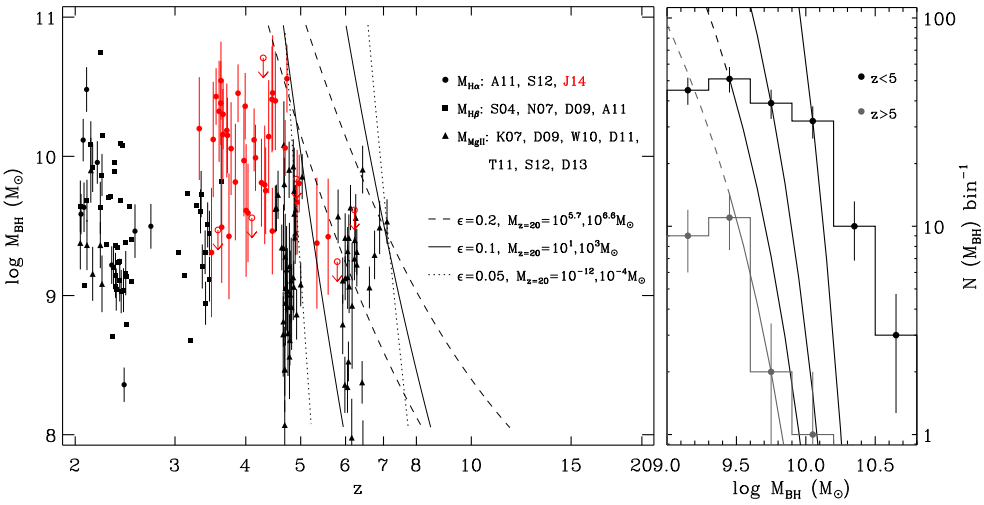

Figure 3.16: The $M_{\rm BH}$ of AGNs along redshift (left). The $M_{\rm BH}$ from Hα are in circles, Hβ in squares, and Mg II in triangles, while our *AKARI* data points are in red circles. For multiple line based masses for an object we choose the Hα over Hβ, and Hβ over Mg II, while for repeated measurements of an object we used the latest results. Most of the references abbreviated on the plot are summarized in Table 3.4, with S04, K07, W10, D11, T11, D13 additionally from Shemmer et al. (2004), Kurk et al. (2007), Willott et al. (2010), De Rosa et al. (2011), Trakhtenbrot et al. (2011), and De Rosa et al. (2013). We do not plot the error for the S04 data as they are not available, and do not use a part of the T11 data with poor quality (flagged "3"). The model tracks of exponential black hole growth that matches the massive envelope of AGNs at $z \sim 5$ and 7 are plotted, with each set of parameters describing the curve shown. On the right panel, we plot the histogram of $M_{\rm BH}$ at $z < 5$ (black) and $z > 5$ (gray) respectively, with errors determined through Poisson statistics. The BH mass function of Willott et al. (2010) is overplotted on the $M_{\rm BH}$ histograms with a varying normalization for comparison to the data.

by up to ~ 0.1 dex (Section 3.3.1), by performing the entire analysis in Figure 3.16 making a -0.1 dex correction to the *AKARI* datapoints, only to find the trend to be mildly weaker ($p_{KS} = 2.5\%$).

We further investigate the upper mass envelope of $z > 5$ AGNs to check if their extremely high masses can be explained by the earliest BH growth from model seed masses. For this we follow Volonteri & Rees (2005) to assume a continuous, Eddington limited accretion of matter to the BH seed at $z = 20$, where the BH will grow with time as,

$$M(t) = M_{20} \exp\Big(\frac{1-\epsilon}{\epsilon}\frac{t-t_{20}}{t_{\rm Edd}}\Big), \tag{3.10}$$

where $t_{20}, M_{20}, \epsilon, t_{\rm Edd}$ are the age of the universe and seed BH mass at $z = 20$, radiative efficiency, and Eddington limited timescale of 0.45 Gyr, respectively. For each given $\epsilon = 0.05, 0.1, 0.2$ we determined a pair of seed masses M_{20} such that the growth curve reaches the observed massive limit at $z \sim 5$ and $z \sim 7$ respectively, shown in Figure 3.16. When $\epsilon = 0.05$, the seed masses to explain the most massive BHs at $z \sim 5$ and 7 are $M_{20} \sim 10^{-12} M_\odot$ and $10^{-4} M_\odot$ respectively, which in other words, gives plenty of time for seed BHs of any meaningful mass to grow up to $> 10^9 M_\odot$ below $z \sim 7$ without a strictly continuous, Eddington limited accretion. If $\epsilon = 0.1$ that is roughly consistent with Soltan argument measurements (Soltan 1982; Yu & Tremaine 2002; Marconi et al. 2004), it predicts $M_{20} \sim 10^{1-3} M_\odot$ which gives a reasonable estimate of the seed mass to be Population III stars. However, it may be difficult for stellar seed BHs to keep its Eddington limited accretion from $z = 20$ to 7–5, which is 0.6–1.0 Gyrs in duration and is longer than the typical quasar lifetime. Lastly, the $\epsilon = 0.2$ model only accepts very heavy seed BHs at $M_{20} \sim 10^{5.7-6.6} M_\odot$, which requires supercritical accretion from lighter seed masses (Volonteri & Rees, 2005) or supports direct collapse of massive primordial gas (Volonteri et al., 2008).

3.6 Summary

We measured the redshifted Hα emission and rest-UV to rest-optical continuum properties of 155 luminous quasars at $3 \lesssim z \lesssim 6$ from *AKARI* spectroscopy and photometry to literature data, to estimate their $M_{\rm BH}$. We summarize our findings as the following.

1. The L_{5100}–$L_{\rm H\alpha}$ relation holds up to the most luminous quasars ($L_{5100} \sim 10^{47}\,{\rm ergs\,s^{-1}}$) with a single slope unchanging up to $z \sim 6$, suggesting a consistent response of the broad line region to the incident continuum irrespective of AGN luminosity and redshift.

2. The relations between rest-optical and UV continuum and line luminosities, and the FWHM relations hold up to the highest luminosity AGNs. Together with predictions of an extended optical R–L relation to the highest luminosities, it enables us to calibrate the rest-UV $M_{\rm BH}$ estimators to be consistent to the Balmer masses overall. However, some of the rest-UV and optical $M_{\rm BH}$ are scattered more than their uncertainties including the errors from the recipe, for only 13% of Mg II masses but for 39% of the C IV estimation.

3. The massive end envelope of $M_{\rm BH}$ steeply evolves at $z > 5$, suggesting they are in a rapidly growing state from given seed masses. The most massive BHs at $z = 5$–7 can be explained by the Eddington limited, continuous accretion onto $\sim 10^{1-3} M_{\odot}$ seed masses at $z = 20$ if $\epsilon = 0.1$, while there are a range of viable accretion rates and seed masses if ϵ is different.

We expect future observations to compile sensitive measurements of (L_{5100}, $L_{\rm H\alpha}$) to better identify the outliers in the L_{5100}–$L_{\rm H\alpha}$ relation, where an example would be a small population of weak emission line quasars. Also, future rest-optical reverberation mapping of high luminosity AGNs will verify if the prediction on the R–L relation to extend with a single slope will hold. Most importantly, the discovery of the highest redshift quasars will further uncover the evolutionary tracks of the earliest BH growth, also improving the current

understanding of $M_{\rm BH}$ growth at $z > 5$ from small number statistics.

Chapter 4

Physical Properties of Luminous Dust-poor Quasars

4.1 Introduction

Active galactic nuclei (AGNs) are known to radiate over a wide range of wavelengths. The unified model (e.g., Krolik & Begelman 1988; Antonucci 1993; Urry & Padovai 1995) postulates that dusty structures surrounding the central black hole are responsible for the infrared emission. Thermally reprocessed emission from heated dust is prominent in the infrared spectral energy distribution (SED) of AGNs. The hottest dust reaches temperatures up to 1500 K and gives off near-infrared (NIR) radiation in excess of the light from the accretion disk and the host galaxy, but it does not get much hotter, because of the sublimation of dust grains (e.g., Barvainis 1987). Hot dust in AGNs is common (e.g., Glikman et al. 2006) and is often modeled as lying in the inner dust torus (e.g., Barvainis 1987).

Recently, this common feature of NIR excess due to hot dust emission was found to be missing for a few quasars at $z \sim 6$ (Jiang et al. 2010, hereafter

J10). Based on the rest-frame NIR-to-optical flux ratios[1], $\log(L_{3.5}/L_{0.51})$, J10 found two quasars (out of 21 at $z\sim6$) with exceptionally small flux ratios, such that the hot dust emission component was almost absent, while no such AGNs were found at lower redshifts. These particular examples were interpreted as representing the existence of quasars before the formation of dusty structure, observed early in their lifetimes. Hao et al. (2010, hereafter H10) then selected hot dust-poor quasars showing weak NIR versus optical slope and reported that $\gtrsim$10% of quasars were hot dust-poor even at low redshifts, although their definition of "hot dust-poor" is different from that of J10. H10 provided wider possibilities in explaining the deficiency of hot dust radiation, raising dust destruction models as the origin. Meanwhile, Mor & Trakhtenbrot (2011, hereafter M11) found 1.7% of their quasars at redshifts of $0.75<z<2$ to be hot-dust-free[2], having zero hot dust covering factors ($\mathrm{CF_{hd}}$=$L_{\mathrm{hd}}/L_{\mathrm{bol}}$), and $\gtrsim$ 16% to be hot dust-poor, lying below the lower $\sim3\,\sigma$ distribution of $\mathrm{CF_{hd}}$. Still contrary to J10, they could not find a redshift dependence on the distribution of $\mathrm{CF_{hd}}$ or on the fraction of their hot dust-poor quasars.

Not only the number evolution but also the origin of hot dust-poor quasars remains controversial. Although J10 found hot dust-poor quasars to have lower black hole masses (M_{BH}) and higher Eddington ratios (f_{Edd}), H10 did not find their hot dust-poor quasars to be clustered in any specific range of M_{BH}, f_{Edd}, or bolometric luminosity (L_{bol}). Since both studies suffered from relatively small sample sizes of a few hundred, a larger parent sample might help clarify the properties of dust-poor quasars. Based on 15,000 quasars with Sloan Digital Sky Survey (SDSS) and Wide-Field Infrared Survey Explorer (*WISE*) coverage, M11 still failed to find a meaningful link between the hot dust covering factor with M_{BH} or f_{Edd} and, from the scatter in the correlations, suggested

[1] We define $L_\lambda = L_{\lambda(\mu\mathrm{m})} = 4\pi d_L^2\,\lambda F_\lambda$ as the rest-frame monochromatic luminosity, where d_L is the luminosity distance and F_λ is the rest-frame specific flux.

[2] Throughout this chapter we use the term "dust-poor" to indicate weak IR dust emission below a certain threshold and "dust-free" for completely absent of dust emission.

that CF_{hd} is independent of the evolutionary stage of the black hole. The latest study, by Ma & Wang (2013), of the properties of the warm dust covering factors (CF_{wd}) of 12,000 quasars agrees with M11 on the anticorrelation between CF_{wd} and L_{bol} but disagrees on the anticorrelation in CF_{wd} and M_{BH}, further complicating the case.

Previous studies of dust-poor quasars have followed mutually different definitions of being hot dust-poor or hot-dust-free, thus adding an uncertainty when trying to compare the results of each for selected dust-poor populations. For luminous quasars, the selection criterion of J10 based on the NIR-to-optical flux ratio, picks out SEDs with an apparently weak NIR bump originating from the hot dust radiation. On the other hand, for less luminous ($L_{bol} \lesssim 10^{46}\,\mathrm{ergs\,s^{-1}}$) quasars, where host galaxy contamination of the SED becomes meaningful, it would be better to use dust emission strength indicators that take into account the fraction of host galaxy light (H10), or to apply a luminosity-dependent average galaxy contamination correction to the observed fluxes (e.g., Shen et al. 2011, hereafter S11). Moreover, selection of hot dust-poor quasars to date has relied on the weak NIR emission, and it is unclear whether hot dust-poor quasars are also dust-poor in warmer phases, where the mid-infrared (MIR) is thought to be the peak wavelength of AGN dust emission (e.g., Richards et al. 2006a). Finally, all previous studies lack either the sample size (J10; H10) or redshift coverage (M11; Ma & Wang 2013) to meaningfully disentangle number evolution and characteristics of the physical parameters of dust-poor quasars.

In this study, we aim to identify the lower redshift counterparts of the high-redshift, hot dust-poor quasars of J10, to compare and understand the observational features of local with high-redshift populations. Where our sample quasars are defined to be luminous enough to have almost negligible host contamination (Section 4.2), we choose NIR-to-optical flux ratios to find weak hot dust emission sources matching those in J10. Our spectrophotometric data

(Section 4.2), encompassing 41,000 quasars at $0 < z < 5$ with contiguous wavelength coverage from the UV to the IR, enables reliable modeling of the SED and measurement of both hot and warm dust emission strengths (Section 4.3). With the help of large number statistics and multiwavelength data, we are able to better identify dust-poor quasars, constrain their evolution in redshift space, and understand their nature as reflected through key physical parameters (Sections 4 and 5). Throughout, we adopt a flat ΛCDM cosmology with $H_0 = 70\,\mathrm{km\,s^{-1}\,Mpc^{-1}}$, $\Omega_m = 0.3$, and $\Omega_\Lambda = 0.7$.

4.2 Sample definition and AGN data set

For the selection of hot dust-poor quasars we follow J10 and use NIR-to-optical flux ratios to indicate the relative strength of the dust emission. Defining f_λ as the $\lambda\,\mu$m–to–optical flux ratio[3],

$$f_\lambda \;=\; \log\left(\lambda F_\lambda / 0.51 F_{0.51}\right) \;=\; \log\left(L_\lambda / L_{0.51}\right), \tag{4.1}$$

we categorize "hot dust-poor" quasars as those with $f_{2.3} < -0.5$, where $f_{2.3}$ is chosen for the 2.3 μm data to be effective in constraining the hot dust emission, as it is the wavelength where the 1250 K blackbody component for the SED fitting (Section 4.3) peaks in F_λ-space. In addition, the hot dust-poor criterion is set to select objects with a weak NIR bump at 2.3 μm, equivalent to the objects from J10 that are below the lower $3\,\sigma$ distribution in $f_{3.5}$ ($\lesssim -0.5$). In Figure 4.1, our selection criterion is compared with the SEDs of quasars from J10. Because of the variety of quasar optical continuum slopes, a single value of $f_{2.3}$ can be derived from a range of α, where $F_\nu \propto \nu^\alpha$. In this figure, we show two example SEDs with different continuum slopes that satisfy $f_{2.3} = -0.5$, with α lying within 1σ of the average of all quasars in this work. If

[3] We use rest-frame flux for F_λ, F_ν throughout the paper, in uppercase to prevent confusion with the rest-frame flux ratio f_λ.

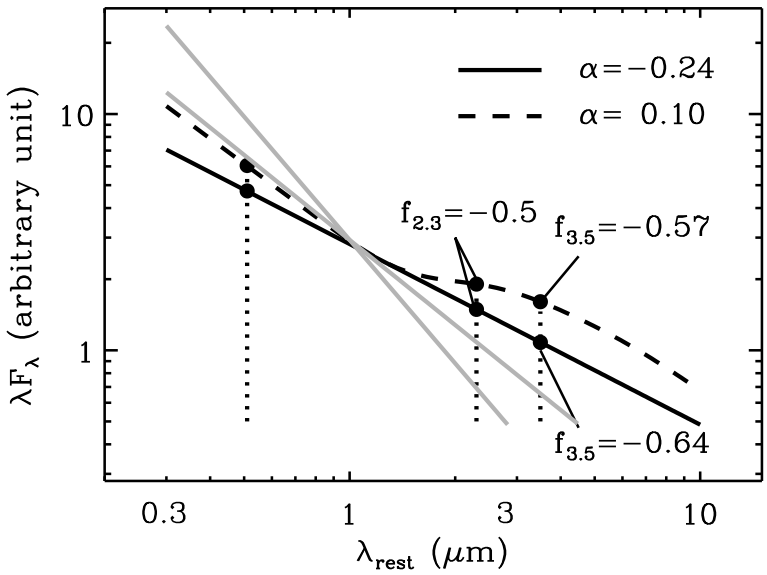

Figure 4.1: Graphical examples of two hot dust-poor quasar SEDs (black lines) with $f_{2.3} = -0.5$ from Equation (4.1), where the $f_{2.3}$ are calculated from the logarithmic ratio of 2.3 μm to 0.51 μm flux in λf_λ-space. The cases falling on the marginal limit of hot dust-poor quasar selection correspond to SEDs that are either purely power-law (black solid line) or power-law plus weak hot dust emission (dashed line), with both $f_{3.5}$-values lying below $3\,\sigma$ of the distribution in J10. Overplotted are two extreme SEDs comparable in $f_{3.5}$ to the dust-free quasars from J10 (gray lines).

$\alpha = -0.24$, the SED is purely a power law in the optical–NIR (black solid line); when $\alpha = 0.10$, the SED is the sum of a power law and a weak hot dust emission component similar in strength to that of J1411+1217 from J10 (dashed line). The $f_{3.5}$ for both examples are -0.64 and -0.57, which are higher than $f_{3.5} \lesssim -1$ for the two hot-dust-free quasars in J10 but still below the lower 3σ range of $f_{3.5}$ in Figure 2 of J10, separating weak hot-dust-radiating AGNs from the rest of the distribution.

The search for hot dust-poor quasars is based on the SDSS Quasar Catalog (DR9 edition; Schneider et al. 2010; Pâris et al. 2012), which provides the largest number (185,801) of optically selected type 1 AGNs together with

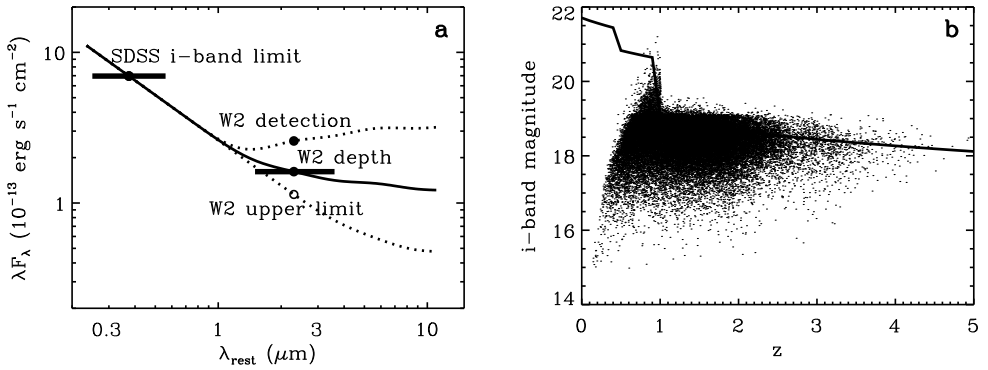

Figure 4.2: (a) Illustration of the SDSS i-band limit for a marginal hot dust-poor quasar with $f_{2.3} = -0.5$ at $z = 1$, set for the rest-frame 2.3 μm to fall on the *WISE* (in this case W2) S/N=2 detection limit. Under the i-band flux limit, not only are hot-dust-rich ($f_{2.3} > -0.5$) objects detected at 2.3 μm, but hot dust-poor ($f_{2.3} < -0.5$) objects are either detected or given with upper limits deeper than the 2.3 μm flux meeting $f_{2.3} = -0.5$, such that the classification of hot dust-poor/-rich quasars becomes more complete under the given *WISE* sensitivity. (b) SDSS i-magnitude cut (solid line) as a function of redshift. The $f_{2.3} = -0.5$ quasars on this line will fall on the *WISE* rest-frame 2.3 μm detection limit for $t_{\rm exp} = 97$ s. Dots represent objects satisfying the i-band sensitivity limit for their respective *WISE* limits, mostly preserving the main magnitude limit ($i < 19.1$) for SDSS quasar selection. Objects above the solid line remain in the sample, since their *WISE* image depths are deeper than the fiducial *WISE* limit.

ancillary AGN properties (S11), from a survey area of 14,555 $\deg^2$. In addition to the SDSS optical imaging and spectroscopic data, we gathered UV through MIR imaging data from the *Galaxy Evolution Explorer (GALEX)*, the Two Micron All Sky Survey (2MASS), the UKIRT Infrared Deep Sky Survey (UKIDSS), and *WISE* (Martin et al. 2005; Skrutskie et al. 2006; Lawrence et al. 2007; Wright et al. 2010), covering $\sim 26{,}000\,\deg^2$, the full sky, $\sim 4000\,\deg^2$, and the full sky, respectively. This multiwavelength data set enables the measurement of hot and warm dust emission strengths $f_{2.3}$ and f_{10}, where f_{10} will be used to probe the warm dust emission of hot dust-poor quasars in comparison with $f_{2.3}$. Also, additional NIR data were obtained from our own UKIRT imaging observations, to improve the photometric accuracy of 113 type 1 AGNs that have low signal-to-noise ratio (S/N) in the 2MASS data, including 32 hot dust-poor objects at $z \gtrsim 2$. Of the hot dust-poor quasars observed by UKIRT, 19 satisfied the $f_{2.3} < -0.5$ criterion, while 13 did not.

Objects in the SDSS Quasar Catalog were matched within radii of $2''$, with multiwavelength data from the UV through the MIR: *GALEX* GR7 for UV, 2MASS and UKIDSS DR10 for NIR, and *WISE* all-sky for MIR. Since the *GALEX* and UKIDSS data consist of several separate surveys (AIS, MIS, DIS, NGS, GII, and CAI for *GALEX* , and LAS, GCS, and DXS for UKIDSS), we merged each catalog containing the UV and NIR survey data, respectively, with overlapping sources to have single photometry of better quality. The matching was performed for all the UV–MIR data, but for the 2MASS data we instead took the matched catalog of Schneider et al. (2010), which adopts the closest neighbor for multiple matches of 1.5% occurrence. On the other hand, multiple SDSS-to-UKIDSS NIR matches of 0.72% occurrence were removed instead of keeping the closest pair, to prevent source confusion in UV/MIR data under poor seeing, as UKIDSS data have the best seeing to tell whether or not there is confusion. In the absence of UKIDSS coverage the number of multiple SDSS–2MASS matches could not be fully trusted, because of the

higher incidence of multiple matching than for SDSS–UKIDSS at an identical $2''$ matching radius. For this reason, we did not reject the multiple SDSS–2MASS matched objects without UKIDSS coverage in principle but visually reexamined the SDSS images of the vicinity of hot dust-poor quasars (Section 4.4.1) to remove those with definite source confusion within the angular resolution of the SDSS imaging. Meanwhile, hot dust rich ($f_{2.3} > -0.5$) objects without UKIDSS data are revealed to have a mild level of confusion, expected to be 0.72% from the SDSS–UKIDSS matching, although we regard this fraction to be negligible in counting the number of hot-dust-rich quasars later on. Finally, objects undetected or blended in *WISE* are given with upper flux limits, while those undetected in the NIR were removed, in order to provide careful constraints on the dust emission strength.

Photometric data collected from multiwavelength catalogs can potentially suffer from several problems: First, the photometry of AGNs includes contributions from the host galaxy that needs to be minimized or subtracted somehow. Second, the mixture of different definitions of Kron, point-spread function (PSF), aperture, and profile-fit magnitudes for UV, optical, NIR, and MIR data brings in, inaccurate photometry of extended objects from PSF or aperture magnitudes. Both of these potential problems can be avoided by minimizing the host galaxy contamination. Thus, we limited our sample with a bolometric luminosity cut of $L_{\rm bol} > 10^{45.70}\,{\rm ergs\,s^{-1}}$, derived from $L_{0.51} > 10^{44.73}\,{\rm ergs\,s^{-1}}$ (Section 4.3) using an optical-to-bolometric correction of 9.26 (S11). By doing so, host contamination is limited to less than 10% in 5100 $\mathring{A}$ (S11). After applying the luminosity cut, we double-checked whether fixed-aperture (PSF or aperture) magnitudes were consistent with total magnitudes by comparing PSF versus Petrosian magnitudes for the SDSS *ugriz* filters, and aperture versus Petrosian magnitudes for 2MASS or UKIDSS *JHK* filters. We found the median difference between the magnitude systems to be at most 0.03 mag at all filters, with the rms scatter falling within 0.1 mag for

SDSS or UKIDSS data and within 0.2 mag for 2MASS. Therefore, we consider our luminosity-cut sample to have a compatible set of magnitudes dominated by the central AGN contribution.

As a next step, we imposed an i-band flux limit that varies with redshift and the *WISE* depth for each object. This is necessary because the *WISE* flux limits are not deep enough for some of the SDSS quasars to determine whether the object has $f_{2.3} < -0.5$. In other words, we selected objects that are bright enough in both observed-frame i and *WISE* bands to allow us to determine whether the object is dust-poor or not. Since each observed band traces different rest-frame wavelengths at different redshifts, the i-band cut changes as a function of redshift. Furthermore, the *WISE* depths are not uniform over the entire sky, so the i-band depth needs to be different at each location on the sky. The i-band flux limits were determined by requiring a quasar with $f_{2.3} = -0.5$ at the i magnitude to have 2σ detection in the *WISE* band covering rest-frame $2.3\,\mu$m. Figure 4.2(a) shows a fiducial i-band magnitude limit, which assumes the typical *WISE* limit with 97 s exposure (11 frames; Wright et al. 2010). When the exposure time, $t_{\rm exp}$, was different at the position of another quasar, we adjusted the fiducial i-band limit by adding $1.25\log(t_{\rm exp}/97\,{\rm s})$. The objects passing the i-band limit are depicted in Figure 4.2(b).

Last, we required at least two data points to lie in the rest-frame 0.3–1 μm with one of the points at shortward of $0.6\,\mu$m, so that the optical continuum slope could be reliably measured from the SED fitting. In short, going over the number of matches through the sample selection process, 100% and 54% of SDSS quasars have NIR coverage and detection, respectively, where almost all the nondetections come from the shallow 2MASS data. From the NIR-detected data 100% and 91% are covered and detected in the *WISE* MIR, yielding 49% of the initial catalog to be matched with contiguous rest-frame UV–NIR information, of which 82% are matched in the *GALEX* UV. The bolometric luminosity cut passes through 81% of the multiwavelength data,

while the i-band limit leaves a further 56% of the remaining sample. Finally, the constraints on the shallow *WISE* upper limits and the number of optical data points sum to a 2% rejection, leaving 22% of the initial SDSS sample, or 40,825 objects, for the SED fitting analysis. We summarize the final data set and observations in Table 4.1.

4.3 Fitting of broad-band SED and spectra

We modeled individual quasar SEDs within rest-frame 0.3–20 μm boundaries as a combination of a power-law continuum from the accretion disk and blackbody emission from heated dust in hot and warm phases. For all quasars, a default 1250 K hot dust emission was considered, because it well describes the NIR part of the SED (Glikman et al., 2006). In cases where rest-frame 3.5 and 9 μm data were available, 500 and 200 K blackbodies were added respectively to model the MIR continuum emission of AGNs through warm dust phases, where the combination of warm dust temperatures is found to fit the observed SEDs of AGNs well (e.g., Barvainis 1987; Hao et al. 2005). Quantitatively expressing the model SED as

$$F_\lambda = F_{\lambda,\mathrm{disk}} + F_{\lambda,\mathrm{dust}}, \tag{4.2}$$

it consists of an accretion disk component, $F_{\lambda,\mathrm{disk}} = c_{\mathrm{disk}}\,\lambda^{-(2+\alpha)}$ and a combination of dust emission components, $F_{\lambda,\mathrm{dust}} = c_{\mathrm{hd}}\,B_\lambda(1250\,\mathrm{K}) + c_{\mathrm{id}}\,B_\lambda(500\,\mathrm{K}) + c_{\mathrm{wd}}\,B_\lambda(200\,\mathrm{K})$, where α is the power-law continuum slope in $F_\nu \propto \nu^\alpha$ and $c_{\mathrm{hd}}, c_{\mathrm{id}}, c_{\mathrm{wd}}$ are contributions from the hot (1250 K), intermediate (500 K), and warm (200 K) dust blackbodies. The $c_{\mathrm{id}}, c_{\mathrm{wd}}$ were used when the rest-frame IR data included 3.5 μm/9 μm, the geometric mean of the peak wavelengths out of hot–intermediate/intermediate–warm components, and were fixed to zero otherwise. The peaks of the blackbody radiation from hot- and warm-dust models in F_λ-space are at 2.3 and 14 μm, which means that *WISE* covers hot

Table 4.1. Summary of imaging data

Name	Filters	N	$t_{\rm exp}$ (s)
Cataloged data			
GALEX	FUV/NUV	17797/33741	368/1504
SDSS	$ugriz$	40825	54
2MASS	JHK	33725	8
UKIDSS	$YJHK$	18698	40
WISE	$W1$–$W4$	40825	123
Newly acquired data			
UKIRT	$YJHK$	113	100

Note. — N is the number of objects detected in at least one filter within the corresponding data set, out of the N=40,825 final multi-wavelength matched sample limited in bolometric luminosity, i-band flux, and the number of optical data points, from the initial N=185,801 SDSS quasars. $t_{\rm exp}$ is the median exposure time of a single-band image in the corresponding data set.

dust emission mostly within the W1–W3 bands over $z = 0$–4, while warm dust emission is usually probed under the inclusion of W4 at $z \lesssim 0.5$.

The SED fitting was performed over the entire sample of 40,825 objects, which excludes 139 and 895 quasars that were rejected (Section 4.2) because of shallow *WISE* upper limits and insufficient rest-frame optical coverage, respectively. The median reduced chi-squared values, χ^2_ν, are not the best, at 5.4 and 3.0, for all and for hot dust-poor objects separately. Still, we find the high-χ^2_ν sources (e.g., in Figure 4.5) to show acceptable fits to the data, while there are no cases without a fit solution in the entire sample. Rather large χ^2_ν-

values do not indicate a poor determination of the continuum slope, since they are caused by wiggly features in the continuum such as broad emission lines or the Fe_{II} complex and photometric variabilities between different-wavelength data sets. A further test of the accuracy of the SED fitting under special conditions, when the gap between the *WISE* $W2$ and $W3$ bands becomes problematic in constraining the $f_{2.3}$, is described in Section 4.4.2.

Having gone through the SED fitting, we used IR-to-optical flux ratios $f_{2.3}$ and f_{10} to quantify hot/warm dust emission strengths over that of the optical continuum. We measured the $f_{2.3}$ and f_{10} from the fluxes on the fitted SED curve at the corresponding rest-frame wavelengths, while f_{10} was computed only when the warm (200 K) dust component was used for the SED fit. Upper limits for $f_{2.3}$ and f_{10} were provided from the upper flux limits in the case of *WISE* nondetections, taking the upper flux limits as detections. The use of $f_{2.3}$ and f_{10} instead of $\alpha, c_{\rm disk}, c_{\rm hd}, c_{\rm id}$, and $c_{\rm wd}$ is more straightforward for selecting quasars with weak dust emission, as $c_{\rm hd}, c_{\rm id}$, and $c_{\rm wd}$ are easily coupled with α, which varies by object. An example is a red quasar with low α due to optical extinction and high $f_{2.3}$ and f_{10} from strong hot–warm dust emission. Because the extrapolated red power-law component could take care of the NIR–MIR emission, the resultant small $c_{\rm hd}, c_{\rm id}$, and $c_{\rm wd}$ for instance, are not necessarily good indicators of little dust emission.

We wanted to pay careful attention for the modeling to be robust against systematic effects. First, broad emission lines could disturb the optical broad-band fluxes from a simple power-law continuum model, where Hα is the strongest and the only meaningful (>0.02 dex) line contamination within our wavelength of interest (Hao et al., 2011). Therefore, we removed the broad-band point enclosing rest-frame Hα if the χ^2_ν containing that data point was larger than that without. We additionally note that although the rest-frame 10 μm is often surrounded by polycyclic aromatic hydrocarbon emission and silicate absorption features, we expect the line contamination to be negligible

considering the very wide filter transmission of W3 and W4. Second, variability can be a problem with multiwavelength data taken at different epochs, because it could bring flux offsets. As a sanity check, we computed the scatter in the magnitude difference between the 2MASS and UKIDSS J and K AB magnitudes, finding the median rms of the magnitude difference to be ~ 0.1 mag after subtracting the magnitude measurement error in quadrature. Because this level of variability is limited, and indistinguishable from that derived from hot dust-poor quasars alone, we consider the variability issue to be tolerable for the selection of hot dust-poor SEDs.

To supplement the photometric products with spectroscopy, we compiled black hole masses based on the UV/optical line and continuum fitting (of both DR7 and DR9 data) by S11, adopting $M_{\rm BH}$ estimators in the form

$$\log\left(\frac{M_{\rm BH}}{M_\odot}\right) = a + b\log\left(\frac{L_\lambda}{10^{44}\,{\rm erg\,s^{-1}}}\right) + c\log\left(\frac{\rm FWHM}{10^3\,{\rm km\,s^{-1}}}\right), \qquad (4.3)$$

with $L_\lambda = (L_{0.51}, L_{0.51}, L_{0.135})$ and $(a, b, c) = \{(6.99,\ 0.50,\ 2.1),\ (6.91,\ 0.50,\ 2),\ (6.66,\ 0.53,\ 2)\}$, for spectral regions around Hα, Hβ, and C$_{\rm IV}$ respectively. For the Mg$_{\rm II}$ estimator, $L_\lambda = L_{0.3}$ and $(b, c) = (0.62,\ 2)$, while $a = (6.75,\ 6.81,\ 6.79)$ depending on the narrow line to be subtracted or included (DR7), or unused in the fitting (DR9), individually. The Hα, Hβ, Mg$_{\rm II}$, and C$_{\rm IV}$) recipes were originally from Greene & Ho (2005), Vestergaard & Peterson (2006), McLure & Dunlop (2004), and Vestergaard & Peterson (2006), respectively, but we primarily followed the cross-calibrated form of (a, b) from S11 to provide consistency between $M_{\rm BH}$ from different lines. Within the following redshift intervals, we used the black hole mass estimator from Hα ($z < 0.37$), Hβ ($z < 0.84$), Mg$_{\rm II}$ ($0.7 < z < 2.1$), and C$_{\rm IV}$ ($z > 2.1$), while masses from different estimators were averaged for overlapping redshifts.

Because of the automatic nature of the spectral fitting in S11, we visually inspected the fits for hot dust-poor quasars as a sanity check, tried direct

fitting by ourselves, and compared with the $M_{\rm BH}$ in S11 from different methodologies. The continuum and line fits by S11 were reproducible overall, but with cases of problematic fitted results. First of all, we checked the Hβ fits by following the method of S11 except for using the Fe$_{\rm II}$ template of Tsuzuki et al. (2006) to fit the spectra around the Hβ region. For a total of nine quasars at $z<0.84$, we found good agreement in our Hβ $M_{\rm BH}$ with S11 values, with -0.09 ± 0.08 dex relative offset and scatter. Thus, we trust and keep the Hβ $M_{\rm BH}$ of S11. Likewise, we performed C$_{\rm IV}$ fits for 92 hot dust-poor quasars at $z>2.1$ with similar methodology to S11, but carefully masking out the absorption features. We found 20 spectra with strong absorption, including broad absorption line (BAL) systems, such that the fitting would be meaningless. Hence, for the spectra with severe C$_{\rm IV}$ absorption but good quality in C$_{\rm III]}\lambda$1908 (see, e.g., Figure 4.3), we fitted the C$_{\rm III]}$ and used the line width as an effective surrogate for the C$_{\rm IV}$ full width at half-maximum (FWHM) (Shen & Liu, 2012) for nine objects, while we dropped the $M_{\rm BH}$ for the remaining 11 objects. The C$_{\rm IV}$ $M_{\rm BH}$ without absorption spectra are offset by -0.05 ± 0.22 dex relative to S11's values, where we keep our C$_{\rm IV}$– and C$_{\rm III]}$–based $M_{\rm BH}$ for the better treatment of absorption features.

For the Mg$_{\rm II}$ fitting, we note that the DR7 and DR9 spectra are treated differently in S11, such that the DR7 broad Mg$_{\rm II}$ FWHMs are measured with and without subtracting the narrow (<1200 km s^{-1}) component whereas the narrow-line component itself is not used for the DR9 fitting. In order to shift each Mg$_{\rm II}$ mass estimator to be mutually consistent, we followed the argument of S11 to normalize each Mg$_{\rm II}$ $M_{\rm BH}$ recipe to the Hβ $M_{\rm BH}$ of Vestergaard & Peterson (2006), obtaining the coefficient a in Equation (4.3), while keeping b and c fixed. This process was performed for all 2489 objects covering both Hβ and Mg$_{\rm II}$ emission lines at $0.7<z<0.8$ with continuum S/N>5. We find $a=6.75$ when using the Mg$_{\rm II}$ line width measured when subtracting the narrow component, consistent with 6.74 in S11, and $a=6.81$ when the narrow

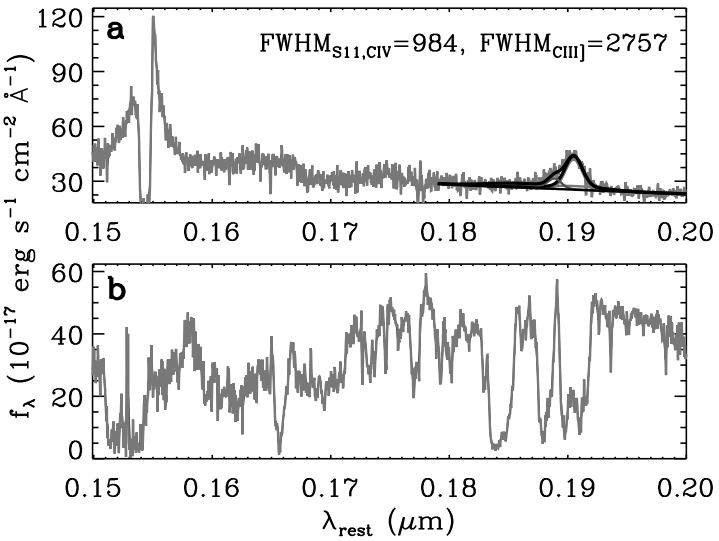

Figure 4.3: (a) Example $C_{IV}\lambda1549$ broad line suffering from an absorption feature, with the $C_{III]}\lambda1908$ spectral region with emission-line fits around the $C_{III]}$ overplotted. In this case, where the $C_{III]}$ is well identified from neighboring lines, the C_{IV} FWHM is replaced with that of $C_{III]}$. The broad-line FWHMs (in km s^{-1}) from S11 and from our fits are shown. (b) Examples of C_{IV} and $C_{III]}$ both showing BAL features, in which case the M_{BH} information was dropped.

component is included. Next, we normalized the DR9 Mg_{II} M_{BH} with that of 1125 overlapping DR7 objects at $0.7 < z < 2.1$ to find $a = 6.79$, irrespective of whether the narrow Mg_{II} lines of DR7 quasars are subtracted or not, and even when these two DR7 masses are averaged. Since it is still debatable whether the narrow component should be subtracted for the Mg_{II} line width measurement (e.g., S11), we averaged the M_{BH}'s with the narrow component subtracted or included for the DR7 sample that gave the least scatter with the overlapping DR9 M_{BH}; at the same time, caution regarding the accuracy of S11's Mg_{II} M_{BH}'s is called for until the fitting-dependent systematic uncertainties are clarified in the future. Last, we replaced seven Mg_{II} M_{BH}'s at $z < 2.1$ with low S/N with those from C_{IV}.

In addition to the black hole mass estimates, we computed the bolometric

luminosities from the 5100 $\AA$ monochromatic luminosity, L_{5100}, derived from our own broadband SED fit. This approach may reduce the systematic uncertainties from extinction or BAL features compared with converting the rest-frame UV into bolometric luminosity. We used a constant bolometric correction of 9.26 (S11), derived from the composite quasar SED of Richards et al. (2006a). To check whether our photometrically determined 5100 $\AA$ luminosities are reliable, we compared our values with that from the spectral fitting in S11, finding good agreement, with a difference $L_{5100} - L_{5100,S11} = 0.06 \pm 0.16$ dex.

4.4 Results

4.4.1 Number Counts and SEDs of Dust-poor Quasars

There are 253 objects that met the hot dust-poor quasar criterion $f_{2.3} < -0.5$. By visually inspecting individual images and spectra, we find 17 blended images in SDSS and three stellar spectra, which are rejected. After all this, we keep 233 hot dust-poor quasars from a total of 40,805, or 0.6%. Figure 4.4 shows the composite SED of hot dust-poor quasars together with that of the whole sample. Both composites were constructed by the geometric mean so as to preserve the global continuum shape (Vanden Berk et al., 2001), after normalizing individual SEDs at 0.51 μm. We fitted the composite SEDs with third-order polynomials in the UV ($< 0.3\,\mu$m) and with optical power-law plus IR blackbody combinations (Section 4.3) to obtain the overall shape information, and to compare the bolometric corrections (Section 4.4.2). The composite hot dust-poor SED in Figure 4.4 is bluer in the optical, and about 3 times fainter in the rest-frame 2.3 μm, than the composite of all SEDs.

Individual hot dust-poor SEDs overplotted with the composite in Figure 4.5 are also depicted with model fits in Figure 4.5, while their properties are summarized in Table 4.2. We find that the majority of hot dust-poor quasars

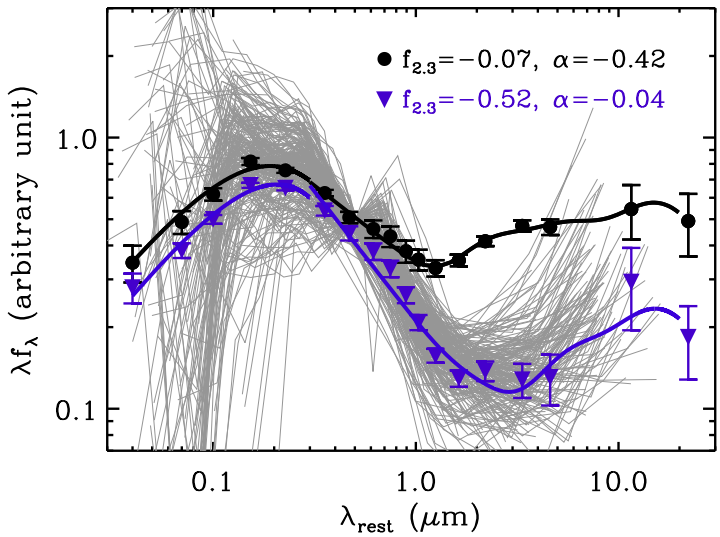

Figure 4.4: Composite SED of hot dust-poor (downward-pointing triangles) and all (circles) quasars, gridded on the rest-frame 400, 700, and 1000 Å–*GALEX*–SDSS–UKIDSS–*WISE* wavelengths. Solid lines are polynomial fits below 0.3 μm and power-law continuum plus black body dust fits above 0.3 μm. Individual hot dust-poor SEDs based on the detected data points are overplotted with thin gray lines. Note that the MIR part is generally poorer in sensitivity because of shallow W3 and W4 imaging.

exhibit warm dust emission under the detection of NIR–MIR, even if the hot dust component is negligible. Exceptions are objects for which upper limits in the rest-frame MIR do not allow us to assess whether they are lacking a warm dust component or not. Specifically, the optical–NIR spectral shapes of the upper W4 limit objects at $z > 2$ in Figure 4.5 are similar to the two dust-free quasars in J10. Nevertheless, we would like to be careful about calling these objects "dust-free", instead using the term "dust-poor" until deep MIR data are available to confirm the absence of warm dust emission. Although mostly present in warm dust emission, our hot dust-poor quasars are in general very weak in hot dust emission that would belong to a smaller subset of hot dust-poor AGNs in other studies. Our hot dust-poor quasars fall within H10's Class II, i.e., hot dust-poor quasars that are power-law shaped in the optical–NIR, or optically blue hot dust-poor quasars in M11.

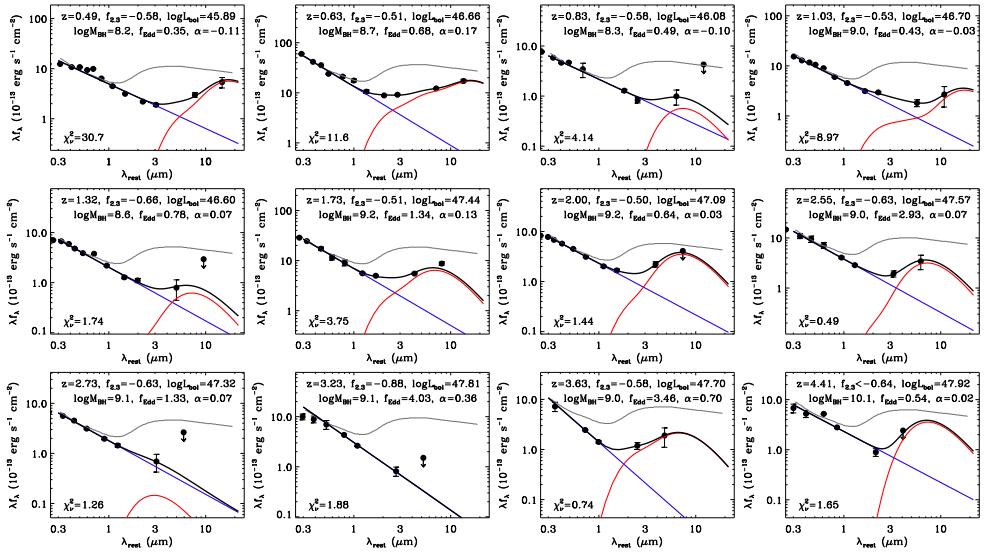

Figure 4.5: Selected list of hot dust-poor quasar SEDs, sorted by redshift. Along with the observed data points and 2σ upper limits, model fits with an accretion disk (blue) and dust components with T=1250, 500, and 200 K phases (red) are overplotted. We include the 500 and 200 K blackbodies only when the longest wavelength of each SED exceeds 3.5 and 9 μm, respectively, except for calculating upper limits in $f_{2.3}/f_{10}$. In addition, the composite SED of luminous ($L_{\rm bol} \gtrsim 10^{46}\,{\rm ergs\,s^{-1}}$) SDSS quasars (gray; Richards et al. 2006a) normalized to the data at 5100 $\mathring{A}$ are overplotted. SDSS J144706.80+212839.3, at $z = 3.23$ (bottom, second panel from left), is the quasar with the smallest NIR-to-optical flux ratio, $f_{2.3} = -0.88$, reaching down to values similar to J10's dust-free quasars.

Table 4.2. Hot dust poor quasar properties

Name (1)	z (2)	$f_{2.3}$ (3)	f_{10} (4)	$\log L_{\rm bol}$ (5)	$\log M_{\rm BH}$ (6)	$f_{\rm Edd}$ (7)
J001754.17+011123.4	1.465	-0.77 ± 0.04	99.00 ± 99.00	46.503 ± 0.020	8.47 ± 0.32	0.836 ± 0.609
J005205.56+003538.2	0.399	-0.52 ± 0.01	-0.48 ± 0.03	46.521 ± 0.004	8.43 ± 0.01	0.959 ± 0.030
J012112.14–003037.1	1.654	-0.64 ± 0.03	99.00 ± 99.00	46.594 ± 0.020	8.75 ± 0.07	0.532 ± 0.088
J013113.42–093401.1	1.149	-0.53 ± 0.08	-0.43 ± 0.18	46.759 ± 0.027	9.18 ± 0.08	0.293 ± 0.058
J014036.47+000335.9	1.636	-0.58 ± 0.02	99.00 ± 99.00	46.975 ± 0.011	10.09 ± 0.03	0.059 ± 0.005
J014049.19–083942.5	3.713	-0.76 ± 0.10	99.00 ± 99.00	48.013 ± 0.025	9.74 ± 0.18	1.431 ± 0.607
J014123.04–002422.1	2.598	-0.52 ± 0.03	99.00 ± 99.00	47.339 ± 0.015	9.05 ± 0.08	1.487 ± 0.290
J021944.34+004740.9	0.890	-0.58 ± 0.03	99.00 ± 99.00	45.832 ± 0.018	8.30 ± 0.15	0.263 ± 0.090
J022724.00–010623.5	2.177	-0.54 ± 0.17	99.00 ± 99.00	47.030 ± 0.025	9.27 ± 0.06	0.444 ± 0.065
J025247.34+005135.2	2.115	-0.57 ± 0.03	99.00 ± 99.00	46.965 ± 0.014	8.85 ± 0.07	1.007 ± 0.168
J034433.20–004411.4	2.565	-0.61 ± 0.02	99.00 ± 99.00	47.273 ± 0.017	9.40 ± 0.20	0.575 ± 0.271
J063505.18+824554.6	2.641	-0.50 ± 0.11	99.00 ± 99.00	47.322 ± 0.054	8.58 ± 0.09	4.248 ± 1.042
J064553.27+281554.8	2.339	-0.64 ± 0.02	99.00 ± 99.00	47.279 ± 0.015	9.18 ± 0.21	0.960 ± 0.474
J072534.24+431335.1	2.450	<-0.50 ± 0.02	99.00 ± 99.00	47.312 ± 0.014	9.49 ± 0.05	0.507 ± 0.055
J073346.06+421848.4	1.715	-0.53 ± 0.07	99.00 ± 99.00	47.096 ± 0.013	9.34 ± 0.07	0.443 ± 0.074
J074320.91+220945.1	2.064	<-0.67 ± 0.04	99.00 ± 99.00	47.095 ± 0.014	8.88 ± 0.20	1.254 ± 0.590
J074435.83+192342.0	1.752	-0.66 ± 0.09	99.00 ± 99.00	47.296 ± 0.019	9.53 ± 0.21	0.449 ± 0.213
J074606.78+161716.4	2.367	-0.51 ± 0.08	99.00 ± 99.00	47.422 ± 0.037	9.04 ± 0.03	1.831 ± 0.203
J075159.29+353338.4	2.232	-0.56 ± 0.02	99.00 ± 99.00	47.186 ± 0.014	9.48 ± 0.02	0.392 ± 0.026
J075352.98+315341.7	0.494	-0.58 ± 0.01	-0.36 ± 0.08	45.891 ± 0.006	8.24 ± 0.04	0.348 ± 0.033
J075627.89+273827.3	1.443	-0.57 ± 0.01	-0.01 ± 0.09	47.109 ± 0.007	8.98 ± 0.03	1.032 ± 0.076
J075846.51+461652.3	2.358	-0.75 ± 0.07	99.00 ± 99.00	47.137 ± 0.043	9.31 ± 0.03	0.510 ± 0.060
J080413.66+251633.9	2.301	-0.53 ± 0.02	99.00 ± 99.00	47.477 ± 0.012	9.64 ± 0.02	0.529 ± 0.023
J080817.89+465501.2	2.728	-0.63 ± 0.14	99.00 ± 99.00	47.320 ± 0.018	9.08 ± 0.04	1.333 ± 0.143
J081116.06+083837.7	2.065	-0.53 ± 0.26	99.00 ± 99.00	47.173 ± 0.068	8.94 ± 0.52	1.330 ± 1.616
J081148.16+572213.7	1.514	<-0.63 ± 0.18	99.00 ± 99.00	46.444 ± 0.035	9.07 ± 0.29	0.181 ± 0.123
J081415.06+412323.5	1.297	-0.52 ± 0.07	-0.26 ± 0.20	46.720 ± 0.032	9.19 ± 0.05	0.260 ± 0.034
J082754.25+333604.2	1.806	-0.55 ± 0.11	99.00 ± 99.00	46.843 ± 0.022	9.03 ± 0.18	0.500 ± 0.207
J084258.83+361444.2	2.490	-0.67 ± 0.02	99.00 ± 99.00	47.180 ± 0.020	9.05 ± 0.08	1.031 ± 0.202
J084512.58+390245.2	1.837	-0.51 ± 0.18	99.00 ± 99.00	46.667 ± 0.028	8.91 ± 0.20	0.438 ± 0.205
J084834.47+521408.3	1.821	-0.55 ± 0.02	99.00 ± 99.00	47.137 ± 0.010	9.21 ± 0.07	0.649 ± 0.102
J085437.60+031734.8	2.245	-0.52 ± 0.02	99.00 ± 99.00	47.199 ± 0.012	9.09 ± 0.06	0.992 ± 0.147
J085820.52+083151.6	1.355	-0.64 ± 0.02	<-0.22 ± 99.00	46.581 ± 0.013	8.83 ± 0.10	0.432 ± 0.100

Table 4.2 (cont'd)

Name (1)	z (2)	$f_{2.3}$ (3)	f_{10} (4)	$\log L_{\rm bol}$ (5)	$\log M_{\rm BH}$ (6)	$f_{\rm Edd}$ (7)
J090221.58+114120.2	1.289	$<-0.73 \pm 0.05$	99.00 ± 99.00	46.374 ± 0.027	8.23 ± 0.76	1.083 ± 1.906
J090342.91+593643.9	1.214	-0.56 ± 0.03	-0.15 ± 0.19	46.467 ± 0.015	8.75 ± 0.23	0.398 ± 0.212
J090349.04+254658.5	1.944	-0.58 ± 0.04	99.00 ± 99.00	46.923 ± 0.024	9.31 ± 0.28	0.314 ± 0.202
J090840.64+084539.7	1.680	$<-0.86 \pm 0.03$	99.00 ± 99.00	46.860 ± 0.014	9.09 ± 0.08	0.453 ± 0.088
J091133.46+195814.1	1.640	-0.58 ± 0.10	99.00 ± 99.00	47.132 ± 0.021	9.63 ± 0.06	0.245 ± 0.037
J091208.75+005857.3	2.187	-0.57 ± 0.02	99.00 ± 99.00	47.171 ± 0.012	8.90 ± 0.12	1.429 ± 0.388
J091420.43+065040.7	1.575	-0.65 ± 0.02	99.00 ± 99.00	46.951 ± 0.009	9.10 ± 0.18	0.547 ± 0.223
J091735.71+112414.7	1.969	-0.51 ± 0.14	99.00 ± 99.00	46.918 ± 0.019	9.18 ± 0.07	0.416 ± 0.068
J091826.08+351243.2	1.521	-0.67 ± 0.02	99.00 ± 99.00	46.918 ± 0.010	8.68 ± 0.08	1.326 ± 0.256
J092102.70+241129.2	2.202	-0.53 ± 0.13	99.00 ± 99.00	47.150 ± 0.054	8.40 ± 0.04	4.355 ± 0.672
J092251.15+074119.7	2.101	-0.54 ± 0.02	99.00 ± 99.00	47.206 ± 0.012	8.81 ± 0.06	1.919 ± 0.287
J092316.45+332116.4	2.360	$<-0.50 \pm 0.01$	99.00 ± 99.00	47.106 ± 0.018	9.17 ± 0.20	0.666 ± 0.307
J092332.32+574557.4	1.378	-0.57 ± 0.04	-0.15 ± 0.05	47.288 ± 0.015	9.67 ± 0.01	0.322 ± 0.014
J092636.24+300139.3	1.002	-0.56 ± 0.03	$<0.06 \pm 99.00$	46.109 ± 0.020	8.60 ± 0.18	0.246 ± 0.101
J092830.98+052432.3	2.413	-0.52 ± 0.02	99.00 ± 99.00	47.291 ± 0.012	9.60 ± 0.13	0.379 ± 0.118
J093142.04+182939.9	0.668	-0.55 ± 0.02	$<-0.39 \pm 99.00$	46.034 ± 0.012	9.06 ± 0.06	0.073 ± 0.011
J093212.78+274400.1	1.847	$<-0.50 \pm 0.22$	99.00 ± 99.00	46.731 ± 0.055	9.29 ± 0.25	0.214 ± 0.125
J093236.12+104117.2	1.134	-0.61 ± 0.08	$<-0.11 \pm 99.00$	46.297 ± 0.017	8.36 ± 0.13	0.665 ± 0.203
J093359.35+551550.7	1.863	-0.59 ± 0.03	99.00 ± 99.00	46.801 ± 0.019	9.02 ± 0.06	0.462 ± 0.065
J093849.99+055520.8	1.983	-0.53 ± 0.17	99.00 ± 99.00	46.911 ± 0.022	8.70 ± 0.44	1.262 ± 1.266
J093938.57–002552.9	2.748	-0.52 ± 0.28	99.00 ± 99.00	47.043 ± 0.037	8.99 ± 0.10	0.861 ± 0.210
J094032.21+112703.1	1.614	-0.63 ± 0.02	99.00 ± 99.00	46.983 ± 0.011	8.85 ± 0.55	1.043 ± 1.329
J094115.28+250722.1	3.175	-0.55 ± 0.14	99.00 ± 99.00	47.613 ± 0.052	9.13 ± 0.07	2.323 ± 0.479
J094151.20+215456.2	0.830	-0.58 ± 0.03	$<-0.31 \pm 99.00$	46.083 ± 0.017	8.28 ± 0.21	0.488 ± 0.238
J094440.43+041055.7	1.984	-0.60 ± 0.03	99.00 ± 99.00	47.002 ± 0.015	9.15 ± 0.03	0.548 ± 0.043
J095117.00+185131.1	2.267	-0.78 ± 0.07	99.00 ± 99.00	47.126 ± 0.041	8.65 ± 0.18	2.294 ± 0.980
J095314.28+141042.7	1.597	-0.50 ± 0.03	99.00 ± 99.00	46.826 ± 0.015	8.46 ± 0.12	1.779 ± 0.492
J095656.73+242856.5	2.817	$<-0.57 \pm 0.20$	99.00 ± 99.00	47.501 ± 0.035	99.00 ± 99.00	99.000 ± 99.000
J095845.40+341319.5	2.551	-0.63 ± 0.13	99.00 ± 99.00	47.573 ± 0.026	8.99 ± 0.06	2.933 ± 0.453
J100010.17+314251.3	1.976	-0.62 ± 0.16	99.00 ± 99.00	47.125 ± 0.023	9.47 ± 0.14	0.347 ± 0.113
J100504.80+191316.3	2.817	-0.74 ± 0.17	99.00 ± 99.00	47.549 ± 0.029	99.00 ± 99.00	99.000 ± 99.000
J100957.13+081704.6	0.970	-0.54 ± 0.02	$<-0.13 \pm 99.00$	46.154 ± 0.013	8.69 ± 0.14	0.222 ± 0.071
J101321.55+495209.8	1.985	-0.52 ± 0.15	99.00 ± 99.00	47.246 ± 0.038	9.75 ± 0.13	0.239 ± 0.074

Table 4.2 (cont'd)

Name (1)	z (2)	$f_{2.3}$ (3)	f_{10} (4)	$\log L_{\rm bol}$ (5)	$\log M_{\rm BH}$ (6)	$f_{\rm Edd}$ (7)
J101346.55+112231.8	3.256	-0.58 ± 0.18	99.00 ± 99.00	47.445 ± 0.025	8.97 ± 0.05	2.283 ± 0.313
J101539.35+111815.9	2.915	-0.54 ± 0.17	99.00 ± 99.00	47.334 ± 0.021	9.26 ± 0.08	0.902 ± 0.170
J101945.26+211911.0	1.839	-0.51 ± 0.08	99.00 ± 99.00	47.224 ± 0.020	9.30 ± 0.18	0.649 ± 0.277
J101956.60+274401.7	1.925	-0.52 ± 0.03	99.00 ± 99.00	48.020 ± 0.010	10.09 ± 0.04	0.660 ± 0.068
J102202.57+143445.1	1.471	-0.52 ± 0.09	99.00 ± 99.00	46.926 ± 0.024	8.88 ± 0.13	0.856 ± 0.270
J103059.75–013237.8	2.155	-0.58 ± 0.03	99.00 ± 99.00	47.031 ± 0.017	9.24 ± 0.12	0.478 ± 0.138
J103105.72+173524.7	2.498	-0.64 ± 0.02	99.00 ± 99.00	47.257 ± 0.018	9.73 ± 0.43	0.256 ± 0.254
J103124.62+291300.4	2.040	-0.53 ± 0.14	99.00 ± 99.00	47.026 ± 0.018	9.39 ± 0.12	0.335 ± 0.090
J103212.97+152729.6	0.631	-0.51 ± 0.03	-0.31 ± 0.03	46.661 ± 0.018	8.72 ± 0.09	0.679 ± 0.144
J103324.60+363443.4	1.149	-0.51 ± 0.03	-0.06 ± 0.23	46.273 ± 0.019	8.54 ± 0.20	0.416 ± 0.194
J103403.87+380248.4	3.552	-0.52 ± 0.10	99.00 ± 99.00	47.759 ± 0.040	9.29 ± 0.04	2.247 ± 0.305
J104018.76+075553.6	1.800	-0.51 ± 0.07	99.00 ± 99.00	47.157 ± 0.012	9.46 ± 0.06	0.387 ± 0.056
J104453.15+621939.5	1.870	-0.52 ± 0.14	99.00 ± 99.00	46.897 ± 0.026	9.02 ± 0.09	0.580 ± 0.125
J105150.55+522847.3	1.854	-0.63 ± 0.03	99.00 ± 99.00	47.124 ± 0.016	9.34 ± 0.08	0.473 ± 0.088
J105153.05+072122.2	1.976	-0.69 ± 0.11	99.00 ± 99.00	47.287 ± 0.013	9.63 ± 0.26	0.349 ± 0.212
J105328.46+485746.5	1.786	-0.51 ± 0.16	99.00 ± 99.00	46.765 ± 0.039	9.42 ± 0.16	0.169 ± 0.062
J105843.67+191428.5	1.877	-0.55 ± 0.18	99.00 ± 99.00	46.975 ± 0.030	9.49 ± 0.20	0.237 ± 0.112
J110103.30+233352.9	2.096	<-0.52 ± 0.23	99.00 ± 99.00	47.087 ± 0.059	9.21 ± 0.06	0.584 ± 0.110
J110152.92+275838.6	2.865	-0.50 ± 0.15	99.00 ± 99.00	47.378 ± 0.016	99.00 ± 99.00	99.000 ± 99.000
J110726.05+385158.3	2.662	-0.52 ± 0.13	99.00 ± 99.00	47.376 ± 0.036	8.82 ± 0.03	2.787 ± 0.320
J110810.87+014140.8	1.614	-0.64 ± 0.01	99.00 ± 99.00	47.163 ± 0.008	9.14 ± 0.08	0.807 ± 0.149
J111120.59+243740.9	3.188	-0.51 ± 0.10	99.00 ± 99.00	47.805 ± 0.029	9.25 ± 0.23	2.786 ± 1.463
J111252.45+152123.5	2.787	-0.53 ± 0.10	99.00 ± 99.00	47.641 ± 0.013	9.93 ± 0.06	0.400 ± 0.054
J111647.60+130533.4	2.196	-0.67 ± 0.04	99.00 ± 99.00	47.083 ± 0.016	9.22 ± 0.06	0.562 ± 0.077
J111959.49+063641.2	2.725	-0.58 ± 0.02	99.00 ± 99.00	47.292 ± 0.019	8.86 ± 0.08	2.100 ± 0.376
J112214.20+070914.4	1.773	-0.55 ± 0.11	99.00 ± 99.00	46.924 ± 0.016	9.73 ± 0.09	0.120 ± 0.024
J112409.74+264359.0	2.419	-0.54 ± 0.02	99.00 ± 99.00	47.285 ± 0.013	8.89 ± 0.08	1.905 ± 0.375
J113941.27+525233.2	1.862	<-0.83 ± 0.05	99.00 ± 99.00	46.856 ± 0.023	9.23 ± 0.22	0.322 ± 0.161
J114013.73+624156.3	3.070	-0.51 ± 0.13	99.00 ± 99.00	47.522 ± 0.032	99.00 ± 99.00	99.000 ± 99.000
J114048.04+425448.2	1.699	-0.52 ± 0.16	99.00 ± 99.00	46.596 ± 0.042	8.81 ± 0.12	0.469 ± 0.142
J114449.33+032751.8	2.098	-0.59 ± 0.01	99.00 ± 99.00	47.550 ± 0.008	9.80 ± 0.03	0.433 ± 0.028
J114455.00+543450.6	0.434	-0.53 ± 0.04	-0.59 ± 0.07	45.918 ± 0.020	8.23 ± 0.05	0.373 ± 0.046
J114553.88+522408.0	0.660	-0.57 ± 0.02	99.00 ± 99.00	45.743 ± 0.015	7.96 ± 0.46	0.468 ± 0.493

Table 4.2 (cont'd)

Name (1)	z (2)	$f_{2.3}$ (3)	f_{10} (4)	$\log L_{\rm bol}$ (5)	$\log M_{\rm BH}$ (6)	$f_{\rm Edd}$ (7)
J114851.31+104824.5	2.127	-0.55 ± 0.01	99.00 ± 99.00	47.459 ± 0.009	9.72 ± 0.02	0.423 ± 0.024
J114911.26+573202.1	0.588	-0.53 ± 0.02	-0.51 ± 0.14	45.885 ± 0.010	8.45 ± 0.08	0.210 ± 0.038
J114948.29+020505.4	2.003	-0.68 ± 0.05	99.00 ± 99.00	46.816 ± 0.024	9.32 ± 0.04	0.242 ± 0.024
J115034.66+233552.8	2.650	-0.69 ± 0.13	99.00 ± 99.00	47.505 ± 0.030	99.00 ± 99.00	99.000 ± 99.000
J115354.52+223329.1	1.712	-0.52 ± 0.04	99.00 ± 99.00	46.735 ± 0.023	9.17 ± 0.10	0.279 ± 0.066
J115723.82+661416.1	2.216	-0.63 ± 0.13	99.00 ± 99.00	47.304 ± 0.040	9.01 ± 0.23	1.512 ± 0.815
J115842.18+172452.4	1.768	-0.50 ± 0.22	99.00 ± 99.00	46.673 ± 0.040	8.75 ± 0.25	0.644 ± 0.372
J120152.64+195232.2	3.150	-0.50 ± 0.08	99.00 ± 99.00	47.779 ± 0.027	99.00 ± 99.00	99.000 ± 99.000
J120331.10–014111.6	1.832	-0.57 ± 0.09	99.00 ± 99.00	47.111 ± 0.014	9.41 ± 0.17	0.383 ± 0.147
J120703.63+092138.1	1.522	-0.56 ± 0.15	99.00 ± 99.00	46.450 ± 0.038	9.37 ± 0.26	0.092 ± 0.056
J120821.01+090130.4	2.074	-0.74 ± 0.03	99.00 ± 99.00	47.161 ± 0.013	9.22 ± 0.08	0.675 ± 0.118
J121028.93+205544.5	2.386	-0.65 ± 0.10	99.00 ± 99.00	47.439 ± 0.029	9.36 ± 0.04	0.915 ± 0.099
J121118.67+143810.5	0.580	-0.54 ± 0.03	-0.26 ± 0.10	45.852 ± 0.014	7.70 ± 0.08	1.088 ± 0.197
J121135.35+185421.4	2.030	-0.58 ± 0.05	99.00 ± 99.00	47.251 ± 0.028	9.18 ± 0.05	0.910 ± 0.117
J121440.28+142859.2	1.625	-0.60 ± 0.01	99.00 ± 99.00	47.185 ± 0.008	9.25 ± 0.21	0.665 ± 0.322
J121524.24+042952.7	1.049	<-0.52 ± 0.09	99.00 ± 99.00	46.169 ± 0.018	8.44 ± 0.29	0.412 ± 0.279
J122017.07+454941.1	3.293	-0.63 ± 0.10	99.00 ± 99.00	47.803 ± 0.033	9.49 ± 0.03	1.583 ± 0.157
J122148.57+045908.9	1.110	-0.63 ± 0.01	-0.04 ± 0.07	46.760 ± 0.007	9.11 ± 0.03	0.345 ± 0.025
J122513.94+211920.8	2.002	-0.50 ± 0.12	99.00 ± 99.00	47.091 ± 0.017	9.17 ± 0.10	0.640 ± 0.144
J122758.20+303101.9	0.641	-0.54 ± 0.04	-0.23 ± 0.11	45.839 ± 0.015	8.65 ± 0.20	0.119 ± 0.054
J122855.91+341436.9	2.139	-0.68 ± 0.18	99.00 ± 99.00	47.281 ± 0.038	9.10 ± 0.11	1.165 ± 0.316
J122918.77+650249.5	2.134	-0.56 ± 0.16	99.00 ± 99.00	47.252 ± 0.082	99.00 ± 99.00	99.000 ± 99.000
J123125.75+475013.8	1.782	-0.61 ± 0.04	99.00 ± 99.00	46.689 ± 0.022	9.11 ± 0.24	0.292 ± 0.163
J123139.13+010229.3	2.885	-0.56 ± 0.04	99.00 ± 99.00	47.445 ± 0.019	9.10 ± 0.04	1.716 ± 0.192
J123430.55+170148.0	3.199	-0.51 ± 0.14	99.00 ± 99.00	47.499 ± 0.054	9.41 ± 0.08	0.955 ± 0.207
J123530.55+522827.7	1.651	-0.60 ± 0.08	99.00 ± 99.00	47.100 ± 0.020	9.52 ± 0.10	0.294 ± 0.069
J123643.12–020421.0	1.865	-0.55 ± 0.13	99.00 ± 99.00	46.926 ± 0.016	9.38 ± 0.05	0.273 ± 0.033
J124943.76+261629.7	1.838	<-0.84 ± 0.05	99.00 ± 99.00	46.731 ± 0.021	9.10 ± 0.21	0.332 ± 0.161
J125053.08+053612.2	2.330	-0.53 ± 0.03	99.00 ± 99.00	47.185 ± 0.014	8.69 ± 0.04	2.392 ± 0.210
J125156.29+070929.3	1.032	-0.53 ± 0.03	-0.59 ± 0.18	46.697 ± 0.008	8.95 ± 0.18	0.427 ± 0.179
J125246.49+130630.1	1.698	-0.51 ± 0.11	99.00 ± 99.00	46.840 ± 0.017	9.09 ± 0.06	0.437 ± 0.067
J125757.62+315101.1	1.102	<-0.61 ± 0.09	99.00 ± 99.00	46.169 ± 0.026	8.67 ± 0.21	0.243 ± 0.116
J125905.42+063123.9	2.034	-0.54 ± 0.14	99.00 ± 99.00	47.037 ± 0.019	9.60 ± 0.28	0.213 ± 0.137

Table 4.2 (cont'd)

Name (1)	z (2)	$f_{2.3}$ (3)	f_{10} (4)	$\log L_{\rm bol}$ (5)	$\log M_{\rm BH}$ (6)	$f_{\rm Edd}$ (7)
J130059.98–030314.6	1.432	-0.84 ± 0.03	0.12 ± 0.22	46.524 ± 0.016	8.26 ± 0.87	1.410 ± 2.835
J130159.83+231914.4	1.393	-0.56 ± 0.04	-0.02 ± 0.11	46.869 ± 0.011	9.18 ± 0.04	0.374 ± 0.036
J130238.91–013732.9	2.498	-0.52 ± 0.02	99.00 ± 99.00	47.018 ± 0.023	8.94 ± 0.03	0.929 ± 0.085
J130309.58+595123.3	2.356	-0.55 ± 0.24	99.00 ± 99.00	46.986 ± 0.084	8.80 ± 0.06	1.178 ± 0.285
J130443.85+214131.0	1.804	-0.53 ± 0.03	99.00 ± 99.00	46.860 ± 0.017	9.42 ± 0.11	0.211 ± 0.052
J130452.58+023924.9	3.651	<-0.55 ± 0.03	99.00 ± 99.00	47.689 ± 0.018	9.97 ± 0.07	0.403 ± 0.067
J130853.03+135004.3	1.046	-0.55 ± 0.06	-0.21 ± 0.19	46.294 ± 0.013	8.66 ± 0.22	0.329 ± 0.164
J131144.12+330748.5	0.676	-0.50 ± 0.03	<-0.31 ± 99.00	45.848 ± 0.020	8.77 ± 0.08	0.091 ± 0.017
J131233.55+282146.5	1.318	-0.66 ± 0.02	<-0.22 ± 99.00	46.600 ± 0.011	8.59 ± 0.12	0.781 ± 0.222
J131511.60+472517.1	2.370	-0.55 ± 0.28	99.00 ± 99.00	47.049 ± 0.065	9.42 ± 0.15	0.327 ± 0.122
J131825.04+375216.2	1.934	-0.57 ± 0.15	99.00 ± 99.00	46.930 ± 0.027	9.21 ± 0.09	0.403 ± 0.091
J131915.80+391915.1	1.999	-0.64 ± 0.07	99.00 ± 99.00	47.061 ± 0.045	8.67 ± 0.29	1.898 ± 1.289
J132131.43+103039.5	2.272	-0.50 ± 0.02	99.00 ± 99.00	47.048 ± 0.013	9.61 ± 0.04	0.213 ± 0.019
J132702.13+030219.4	1.081	-0.59 ± 0.09	<-0.19 ± 99.00	46.247 ± 0.020	8.51 ± 0.39	0.422 ± 0.375
J132742.92+003532.7	1.875	-0.53 ± 0.02	99.00 ± 99.00	46.988 ± 0.011	8.96 ± 0.03	0.817 ± 0.062
J132822.92+125203.1	1.590	-0.54 ± 0.01	99.00 ± 99.00	46.903 ± 0.010	9.19 ± 0.04	0.400 ± 0.041
J133142.64+044826.5	2.317	-0.52 ± 0.02	99.00 ± 99.00	47.162 ± 0.012	8.91 ± 0.02	1.385 ± 0.079
J133150.61+333546.1	1.944	<-0.67 ± 0.27	99.00 ± 99.00	46.692 ± 0.029	8.71 ± 0.63	0.745 ± 1.076
J134211.21+133516.8	2.492	-0.57 ± 0.02	99.00 ± 99.00	47.387 ± 0.012	8.78 ± 0.12	3.090 ± 0.856
J134530.05+031208.3	2.123	-0.51 ± 0.02	99.00 ± 99.00	47.110 ± 0.011	8.88 ± 0.09	1.310 ± 0.259
J134636.52+011155.3	1.682	-0.64 ± 0.06	99.00 ± 99.00	46.436 ± 0.026	8.48 ± 0.46	0.696 ± 0.738
J135122.71+175401.9	1.525	-0.59 ± 0.23	99.00 ± 99.00	46.423 ± 0.049	8.62 ± 0.18	0.487 ± 0.210
J135247.24+080915.3	3.354	-0.58 ± 0.03	99.00 ± 99.00	47.493 ± 0.019	9.06 ± 0.05	2.087 ± 0.242
J135530.35+250853.4	2.573	-0.72 ± 0.02	99.00 ± 99.00	47.518 ± 0.011	9.02 ± 0.12	2.438 ± 0.696
J135831.87+263034.1	1.044	-0.55 ± 0.08	<-0.19 ± 99.00	46.111 ± 0.022	8.70 ± 0.10	0.197 ± 0.044
J135936.55+650931.9	1.733	-0.51 ± 0.04	99.00 ± 99.00	47.444 ± 0.013	9.19 ± 0.05	1.369 ± 0.171
J140922.50+405823.4	0.975	-0.65 ± 0.06	-0.43 ± 0.16	46.468 ± 0.025	8.91 ± 0.10	0.281 ± 0.067
J141551.75–015053.9	1.605	-0.68 ± 0.02	99.00 ± 99.00	46.837 ± 0.012	8.68 ± 0.30	1.115 ± 0.771
J141617.38+264906.1	2.301	-0.70 ± 0.03	99.00 ± 99.00	47.534 ± 0.021	9.22 ± 0.05	1.577 ± 0.207
J141744.05+044948.2	2.659	-0.54 ± 0.03	99.00 ± 99.00	47.106 ± 0.017	8.97 ± 0.05	1.042 ± 0.129
J141835.14+322932.4	0.996	-0.58 ± 0.02	-0.09 ± 0.07	46.457 ± 0.010	8.57 ± 0.41	0.596 ± 0.567
J141840.42+474721.3	1.994	-0.61 ± 0.05	99.00 ± 99.00	47.196 ± 0.031	9.13 ± 0.90	0.887 ± 1.835
J141927.43+045234.3	3.078	-0.70 ± 0.04	99.00 ± 99.00	47.319 ± 0.021	9.22 ± 0.11	0.960 ± 0.251

Table 4.2 (cont'd)

Name (1)	z (2)	$f_{2.3}$ (3)	f_{10} (4)	$\log L_{\rm bol}$ (5)	$\log M_{\rm BH}$ (6)	$f_{\rm Edd}$ (7)
J142054.14+165002.0	2.713	-0.54 ± 0.04	99.00 ± 99.00	47.542 ± 0.023	8.92 ± 0.10	3.217 ± 0.769
J142241.43+391815.5	3.505	-0.70 ± 0.15	99.00 ± 99.00	47.624 ± 0.039	9.89 ± 0.22	0.413 ± 0.211
J142906.94+221001.6	1.959	-0.66 ± 0.03	99.00 ± 99.00	46.809 ± 0.018	8.76 ± 0.24	0.861 ± 0.476
J143008.05+063914.4	2.497	-0.51 ± 0.02	99.00 ± 99.00	47.220 ± 0.015	8.79 ± 0.05	2.088 ± 0.248
J143049.70+603153.2	1.706	-0.55 ± 0.07	99.00 ± 99.00	47.056 ± 0.020	9.35 ± 0.07	0.388 ± 0.064
J143212.86+113953.2	2.990	-0.53 ± 0.06	99.00 ± 99.00	47.650 ± 0.012	9.59 ± 0.04	0.892 ± 0.087
J143310.24+311912.1	2.063	-0.50 ± 0.12	99.00 ± 99.00	47.270 ± 0.043	9.58 ± 0.03	0.373 ± 0.046
J143415.53+380624.9	1.759	-0.61 ± 0.13	99.00 ± 99.00	46.888 ± 0.024	9.03 ± 0.05	0.549 ± 0.070
J143436.52+010522.3	2.203	-0.59 ± 0.06	99.00 ± 99.00	46.628 ± 0.031	8.59 ± 0.04	0.848 ± 0.093
J143834.54+394260.0	1.567	-0.58 ± 0.03	99.00 ± 99.00	46.630 ± 0.018	9.49 ± 0.19	0.106 ± 0.045
J144144.77+472003.2	3.633	-0.58 ± 0.10	99.00 ± 99.00	47.695 ± 0.047	9.04 ± 0.08	3.455 ± 0.744
J144624.29+173128.8	2.195	-0.58 ± 0.09	99.00 ± 99.00	47.383 ± 0.031	8.59 ± 0.06	4.727 ± 0.687
J144706.80+212839.3	3.232	-0.88 ± 0.12	99.00 ± 99.00	47.813 ± 0.031	9.09 ± 0.07	4.031 ± 0.734
J145038.00+243925.4	3.102	-0.63 ± 0.15	99.00 ± 99.00	47.521 ± 0.040	99.00 ± 99.00	99.000 ± 99.000
J145049.93+000144.3	1.958	-0.52 ± 0.17	99.00 ± 99.00	46.732 ± 0.024	9.11 ± 0.12	0.325 ± 0.095
J145544.84+441049.5	1.903	-0.55 ± 0.07	99.00 ± 99.00	47.218 ± 0.016	9.43 ± 0.01	0.468 ± 0.022
J145903.26–002256.5	2.008	-0.53 ± 0.17	99.00 ± 99.00	46.863 ± 0.031	8.83 ± 0.66	0.825 ± 1.255
J150427.88+390222.5	1.842	-0.52 ± 0.15	99.00 ± 99.00	46.642 ± 0.031	8.41 ± 0.08	1.316 ± 0.269
J150800.30+582707.5	3.305	-0.59 ± 0.10	99.00 ± 99.00	47.470 ± 0.049	8.84 ± 0.08	3.309 ± 0.701
J151051.35+210151.7	2.893	-0.51 ± 0.08	99.00 ± 99.00	47.249 ± 0.048	9.09 ± 0.14	1.108 ± 0.367
J152119.68–004818.8	2.934	-0.56 ± 0.07	99.00 ± 99.00	47.682 ± 0.011	9.28 ± 0.07	1.935 ± 0.305
J152413.35+430537.4	3.929	-0.73 ± 0.12	99.00 ± 99.00	47.708 ± 0.053	9.44 ± 0.30	1.432 ± 1.004
J153024.16+481416.3	2.364	-0.73 ± 0.11	99.00 ± 99.00	47.239 ± 0.042	9.16 ± 0.16	0.930 ± 0.364
J153201.61+370002.4	3.098	-0.50 ± 0.05	99.00 ± 99.00	47.897 ± 0.015	9.49 ± 0.04	1.965 ± 0.186
J153837.02+522555.1	2.078	-0.55 ± 0.10	99.00 ± 99.00	47.216 ± 0.039	9.17 ± 0.10	0.856 ± 0.210
J154008.66–015826.9	2.167	-0.62 ± 0.04	99.00 ± 99.00	46.968 ± 0.019	8.82 ± 0.18	1.087 ± 0.455
J154340.38+341744.5	4.414	<-0.64 ± 0.06	99.00 ± 99.00	47.917 ± 0.026	10.07 ± 0.15	0.536 ± 0.188
J154416.85+140905.5	1.935	-0.61 ± 0.33	99.00 ± 99.00	46.689 ± 0.054	9.17 ± 0.18	0.253 ± 0.112
J154458.50+230810.1	0.372	-0.60 ± 0.01	-0.43 ± 0.02	46.004 ± 0.005	8.90 ± 0.52	0.097 ± 0.116
J154515.78+003235.3	1.051	<-0.57 ± 0.06	99.00 ± 99.00	46.273 ± 0.015	99.00 ± 99.00	99.000 ± 99.000
J155255.51+461614.6	1.921	-0.52 ± 0.14	99.00 ± 99.00	46.536 ± 0.040	9.12 ± 0.23	0.199 ± 0.106
J155621.31+112433.2	1.730	-0.61 ± 0.08	99.00 ± 99.00	47.244 ± 0.019	9.73 ± 0.23	0.252 ± 0.135
J155731.19+241250.2	2.371	-0.53 ± 0.14	99.00 ± 99.00	47.302 ± 0.049	9.20 ± 0.03	0.972 ± 0.124

Table 4.2 (cont'd)

Name (1)	z (2)	$f_{2.3}$ (3)	f_{10} (4)	$\log L_{\rm bol}$ (5)	$\log M_{\rm BH}$ (6)	$f_{\rm Edd}$ (7)
J155755.50+400738.5	1.119	-0.55 ± 0.07	-0.42 ± 0.15	46.502 ± 0.026	8.95 ± 0.08	0.276 ± 0.056
J160223.35+451950.2	2.807	-0.50 ± 0.11	99.00 ± 99.00	47.405 ± 0.031	8.99 ± 0.06	2.020 ± 0.322
J161013.08+452850.2	3.650	-0.71 ± 0.09	99.00 ± 99.00	47.749 ± 0.035	99.00 ± 99.00	99.000 ± 99.000
J161326.23+064958.7	1.941	-0.54 ± 0.13	99.00 ± 99.00	47.190 ± 0.022	9.20 ± 0.03	0.753 ± 0.066
J161604.32+135053.6	2.532	-0.56 ± 0.16	99.00 ± 99.00	47.461 ± 0.030	8.87 ± 0.05	2.963 ± 0.402
J161705.31+091131.0	1.925	-0.68 ± 0.22	99.00 ± 99.00	46.985 ± 0.029	9.04 ± 0.10	0.673 ± 0.161
J161742.37+250934.3	1.789	-0.50 ± 0.02	99.00 ± 99.00	47.115 ± 0.009	9.18 ± 0.03	0.670 ± 0.046
J161842.44+234131.7	2.281	-0.65 ± 0.03	99.00 ± 99.00	47.125 ± 0.015	8.81 ± 0.09	1.574 ± 0.314
J162058.52+103905.5	2.692	-0.59 ± 0.14	99.00 ± 99.00	47.354 ± 0.081	99.00 ± 99.00	99.000 ± 99.000
J162659.24+301535.1	1.577	-0.62 ± 0.01	99.00 ± 99.00	47.076 ± 0.008	9.26 ± 0.03	0.505 ± 0.037
J163004.01+414100.2	2.056	-0.64 ± 0.10	99.00 ± 99.00	47.117 ± 0.061	9.55 ± 0.10	0.282 ± 0.075
J163923.64+111333.9	2.058	<-0.54 ± 0.24	99.00 ± 99.00	46.926 ± 0.093	8.95 ± 0.14	0.733 ± 0.288
J164552.11+224450.0	2.719	-0.58 ± 0.09	99.00 ± 99.00	47.589 ± 0.026	9.83 ± 0.03	0.443 ± 0.039
J165154.07+313305.0	2.705	-0.61 ± 0.03	99.00 ± 99.00	47.235 ± 0.016	8.97 ± 0.02	1.427 ± 0.098
J165334.39+344413.6	3.236	-0.52 ± 0.13	99.00 ± 99.00	47.663 ± 0.035	9.37 ± 0.06	1.511 ± 0.228
J165748.64+255811.1	2.075	-0.58 ± 0.06	99.00 ± 99.00	47.190 ± 0.041	9.50 ± 0.06	0.374 ± 0.063
J170634.13+361508.0	0.918	-0.51 ± 0.05	-0.58 ± 0.12	46.623 ± 0.024	8.90 ± 0.08	0.407 ± 0.075
J170650.86+225745.4	2.268	-0.58 ± 0.21	99.00 ± 99.00	47.102 ± 0.055	9.44 ± 0.08	0.352 ± 0.078
J170931.01+630357.2	2.395	-0.56 ± 0.05	99.00 ± 99.00	47.647 ± 0.019	99.00 ± 99.00	99.000 ± 99.000
J171118.71+612732.7	0.994	-0.54 ± 0.07	-0.19 ± 0.05	46.386 ± 0.021	8.60 ± 0.23	0.468 ± 0.251
J171328.81+305907.8	1.213	-0.58 ± 0.16	<-0.10 ± 99.00	46.276 ± 0.044	9.85 ± 0.08	0.021 ± 0.004
J172308.15+524455.5	1.818	-0.52 ± 0.05	99.00 ± 99.00	47.301 ± 0.016	9.86 ± 0.10	0.211 ± 0.049
J205303.06–003612.7	1.249	-0.56 ± 0.01	-0.39 ± 0.21	46.927 ± 0.006	9.93 ± 0.21	0.076 ± 0.036
J210336.75+010434.8	1.954	-0.62 ± 0.22	99.00 ± 99.00	46.857 ± 0.025	9.62 ± 0.23	0.132 ± 0.069
J210926.42–073925.1	1.878	<-0.75 ± 0.05	99.00 ± 99.00	46.827 ± 0.028	8.68 ± 0.69	1.069 ± 1.708
J212345.33+112823.8	0.965	-0.51 ± 0.10	<-0.28 ± 99.00	46.293 ± 0.032	9.28 ± 0.15	0.080 ± 0.028
J213023.62+122252.3	3.272	-0.61 ± 0.10	99.00 ± 99.00	47.855 ± 0.029	9.08 ± 0.05	4.557 ± 0.566
J213138.07–002537.8	1.837	-0.67 ± 0.04	99.00 ± 99.00	46.782 ± 0.018	8.71 ± 0.03	0.912 ± 0.068
J215954.46–002150.2	1.961	-0.71 ± 0.01	99.00 ± 99.00	47.737 ± 0.006	9.68 ± 0.16	0.872 ± 0.325
J221511.94–004550.0	1.478	-0.59 ± 0.04	99.00 ± 99.00	47.467 ± 0.008	9.76 ± 0.03	0.395 ± 0.029
J224826.98–005350.6	0.594	-0.61 ± 0.04	<-0.27 ± 99.00	46.049 ± 0.011	9.04 ± 0.05	0.078 ± 0.009
J230547.37+153015.4	0.583	-0.58 ± 0.09	<-0.09 ± 99.00	45.809 ± 0.041	8.92 ± 0.48	0.060 ± 0.066
J232615.50–104748.0	1.950	-0.51 ± 0.27	99.00 ± 99.00	46.796 ± 0.040	9.30 ± 0.08	0.239 ± 0.050

Table 4.2 (cont'd)

Name (1)	z (2)	$f_{2.3}$ (3)	f_{10} (4)	$\log L_{\rm bol}$ (5)	$\log M_{\rm BH}$ (6)	$f_{\rm Edd}$ (7)
J234657.26+145735.9	2.168	$<-0.58 \pm 0.05$	99.00 ± 99.00	46.891 ± 0.021	9.54 ± 0.05	0.173 ± 0.020
J234812.39+002939.8	1.946	-0.78 ± 0.05	99.00 ± 99.00	46.679 ± 0.030	8.70 ± 1.07	0.729 ± 1.806

Note. — Catalog of hot dust-poor quasars sorted in RA. Columns (1)–(7) are SDSS coordinates, redshift, 2.3 μm-to-optical flux ratio, 10 μm-to-optical flux ratio, bolometric luminosity, black hole mass, and Eddington ratio. The units for $L_{\rm bol}$ and $M_{\rm BH}$ are erg s^{-1} and $M_{\odot}$. Empty parameters are fixed to 99.

To better understand the photometric properties of hot dust-poor quasars, we plot the luminosity correlations in Figure 4.6. The NIR versus optical luminosities in Figure 4.6(a) show that $L_{2.3}$ is in general proportional to $L_{0.51}$, meaning luminous AGNs show stronger dust emission than faint AGNs (see, e.g., Haas et al. 2003). With respect to this relation, we find that hot dust-poor quasars are the objects defining the lower $\sim 3.2\,\sigma$ envelope. Next, warm and hot dust emission strengths are compared through the 2.3 μm versus 10 μm luminosities in Figure 4.6(b), which shows a linear relation between the MIR and NIR luminosities. Interestingly, the detected hot dust-poor data points lie moderately below the relation, by 1.8σ on average, suggesting perhaps a shifted MIR–NIR luminosity relation for hot dust-poor SEDs. Nonetheless, we may find hot dust-poor quasars to stay on the warm dust-poor side, as their 10 μm luminosities are lower by 1.9σ on average than the linear relation, $\log L_{10} = (1.148 \pm 0.004) \log L_{0.51} - (6.627 \pm 0.188)$, rms $= 0.200$, derived from the entire sample with 10 μm detections. Therefore, we find it reasonable from our NIR/MIR luminosity correlation of hot dust-poor quasars, although with a possible offset, to deduce that hot dust emission is a marginally good tracer of warm dust emission in AGNs. The IR portion of the quasar SED peaking in the MIR (e.g., Richards et al. 2006a), and the acceptable correlation between MIR and far-IR (hereafter FIR) luminosities of quasars (e.g., Haas et al. 2003),

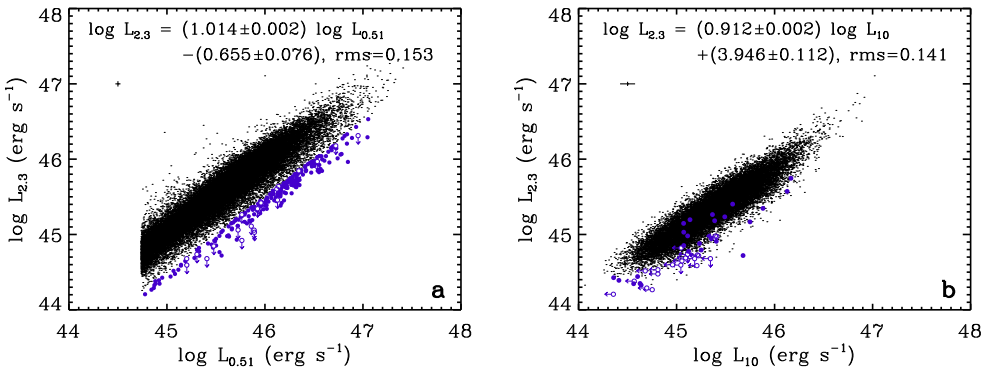

Figure 4.6: Correlations between (a) optical and NIR monochromatic luminosities and (b) MIR and NIR luminosities. The distributions of hot dust-poor quasars (purple; filled circles represent detections, and open arrows are based on *WISE* 2σ upper limits at the corresponding wavelengths) and of the rest of the sample (dots; detections only) are plotted, together with an overall median error bar at upper left in each panel. Linear fits to luminosity correlations are obtained by applying the ordinary least-squares bisector method (Isobe et al., 1990) to the entire sample with detections; the fit coefficients and rms scatter are shown.

further suggest that hot dust-poor sources stay relatively dust-poor through the entire IR. For these reasons, we choose to refer to "hot dust-poor" quasars as "dust-poor" quasars from here on.

To investigate how dust-poor quasars differ from ordinary quasars in wavelengths other than the NIR/MIR, we plot $f_{2.3}$ as a function of optical continuum slope α in Figure 4.7. The average slope and its scatter, $<\alpha> = -0.08 \pm 0.31$, from our entire sample are somewhat bluer than the -0.44 of Vanden Berk et al. (2001). This is consistent with the results of Davis et al. (2007), where more luminous quasars have bluer continuum slopes, as our sample are high-luminosity–selected SDSS quasars. We also note that differences in the fitting range or the method to measure α could further shift the values of α (see, e.g., Table 5 of Vanden Berk et al. 2001). In any case, $<\alpha> = 0.10 \pm 0.20$ for dust-poor quasars comes roughly close to the $\alpha = (1/3)$ predicted from optically thick and locally heated accretion disk models, and from polarized observations

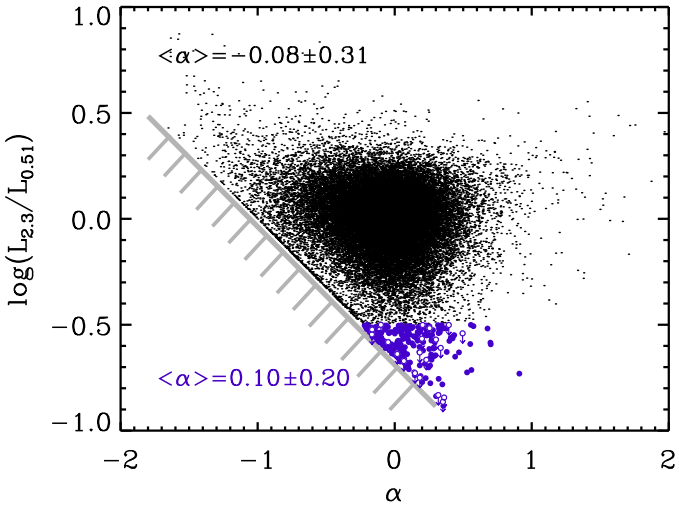

Figure 4.7: Distribution of $f_{2.3}$ with continuum slope α, following the styles in Figure 4.6. The average and standard deviation of α are displayed for both the entire and dust-poor samples. The data points forming the diagonal line just above the gray highlighted line are SEDs fitted as pure power laws in the optical–NIR, with no contribution from a hot dust component ($c_{\rm hd} = 0$). The gray shaded regions are prohibited, since they require $c_{\rm hd} < 0$.

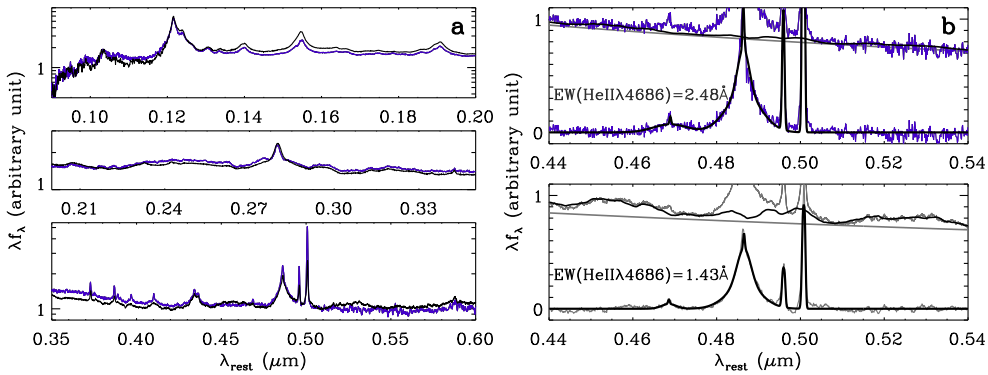

Figure 4.8: (a) Composite spectra of dust-poor quasars (purple) and of general SDSS quasars (black; from Vanden Berk et al. 2001), smoothed by 3 pixels to display the spectral features better. The numbers of spectra used to construct the composite, from top to bottom, are 163, 125, and 22 for dust-poor quasars and around 500, 1800, and 700 from Vanden Berk et al. (2001). (b) Spectral fits around the Hβ region for dust-poor (top) and ordinary (bottom) composites. The measured He$_{\rm II}\lambda$4686 equivalent widths are shown for both samples.

of quasar SEDs seen through the dust (Kishimoto et al., 2008). This indicates that the optical continua from the accretion disks of dust-poor quasars are mostly unobscured to our line of sight, consistent with the weak IR reemission observed. Meanwhile, there are points forming a diagonal line across the lower left part of α–$f_{2.3}$ space in Figure 4.7, which are optical-to-NIR SEDs best fitted by the continuum component only. Although these objects do not seem to involve a hot dust component for the SED fitting, satisfying $c_{\rm hd} = 0$ in Equation (4.2), the NIR emission could be taken over by the extrapolated optical continuum component, especially at the red end of small α. Therefore, we regard at least part of the diagonal sequence in Figure 4.7 to effectively represent lower limits in the measured α.

In addition to the optical continuum slope measurements from photometric data points, we constructed a composite UV–optical spectrum of dust-poor quasars, plotted in Figure 4.8(a), along with the composite of general SDSS quasars from Vanden Berk et al. (2001). Compared with typical quasars, dust-poor quasars have a bluer NUV–optical continuum slope. Moreover, fitting all prominent UV–optical emission lines, we find the $\rm He_{II}\lambda4686$ line emission of dust-poor quasars to be especially strong, with equivalent widths that are about 1.7 times higher than measured using the composite from Vanden Berk et al. (2001), in Figure 4.8(b). For the $\rm He_{II}$ fitting, we subtracted the continuum and broad $\rm Fe_{II}$ in a similar way as S11 but with the template of Tsuzuki et al. (2006), while a single Gaussian profile was used for both broad and narrow emission components of $\rm He_{II}$. The $\rm He_{II}$ region was simultaneously fitted with $\rm H\beta$ and $\rm [O_{III}]$ lines to better decompose the $\rm He_{II}$ line emission.

Because $\rm He_{II}\lambda4686$ line is relatively well decoupled from neighboring emission lines, and to check whether the strong $\rm He_{II}$ of the dust-poor composite spectrum is reflected in the individual spectra, we further calculated the $\rm He_{II}/H\beta$ line ratios for all $z < 0.8$ DR7 objects with spectral continuum S/N > 10 and $\rm H\beta$ line S/N > 2. The results are plotted in Figure 4.9, where $\rm He_{II}$ and $\rm H\beta$

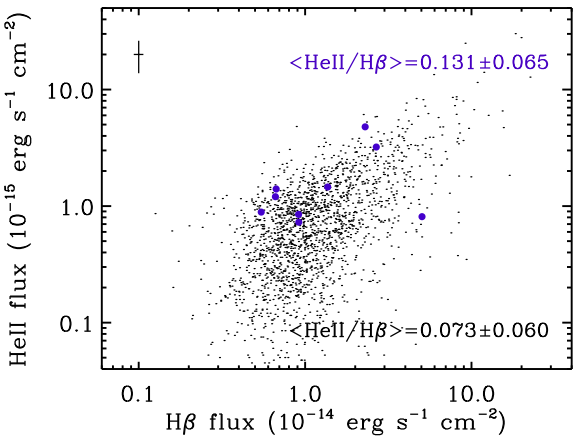

Figure 4.9: Distribution of $\mathrm{He_{II}}\lambda4686$ to Hβ broad-line fluxes, following the styles of Figure 4.6. The Hβ and $\mathrm{He_{II}}\lambda4686$ line fluxes are measured for objects at $z < 0.8$, with an overall median error bar shown at the upper left. Of 3880 continuum S/N > 10 spectra, 1899 have nondetections in Hβ or $\mathrm{He_{II}}$ or fail to meet Hβ line S/N > 2, where they are excluded from the plot. The average and standard deviation of $\mathrm{He_{II}}$/Hβ are shown for both the entire and the dust-poor samples.

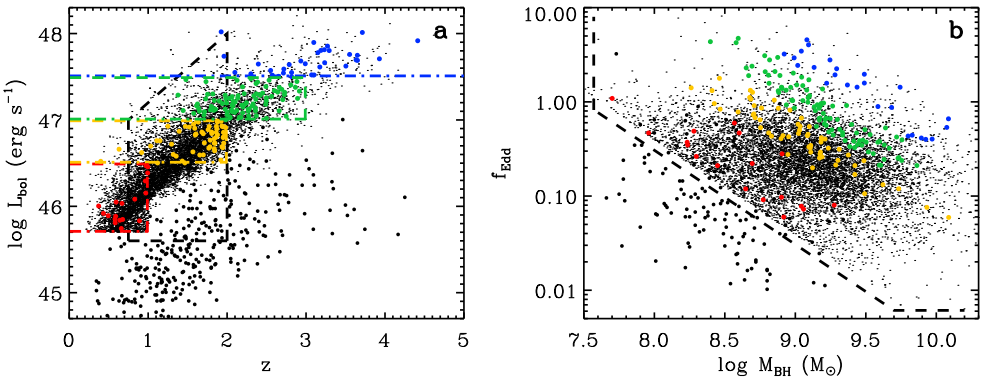

Figure 4.10: (a) Redshift–bolometric-luminosity (left) and (b) black hole mass–Eddington-ratio distributions of our sample. The range of data points from M11 is highlighted for comparison (dashed lines). Furthermore, the 361 *XMM*-COSMOS spectroscopically confirmed type 1 AGNs from Lusso et al. (2010) that are similar to the sample of H10 are overplotted (black circles). Since the full sample is large, a quarter of the sample was randomly selected and plotted (black dots) in each panel, to better resolve and compare the overall distribution with that of dust-poor objects (colored circles). We subdivide our sample into four bolometric luminosity bins (dot-dashed lines) so that the analysis will be independent of luminosity selection effects.

line fluxes of dust-poor quasars are compared with those of ordinary sources. Dust-poor quasars occupy regions with $\sim$1.8 times higher $\mathrm{He_{II}}/\mathrm{H}\beta$ line ratios compared with typical quasars, being on average 13% and 7%, respectively, consistent with the results from Figure 4.8(b). This can be understood as a result of the strong UV continuum source, as the $\mathrm{He_{II}}/\mathrm{H}\beta$ line ratio and the source spectral shape in the extreme-UV (EUV) form a relation

$$\frac{L_{\mathrm{He_{II}}\lambda 4686}}{L_{\mathrm{H}\beta}} = 1.99 \times 4^{\alpha_{\mathrm{EUV}}} \tag{4.4}$$

(Penston & Fosbury, 1978), where α_{EUV} indicates the EUV slope of the source that brings $\mathrm{H_I}$ and $\mathrm{He_{II}}$ emission. Equation (4.4) yields a bluer slope of $\alpha_{\mathrm{EUV}} \sim -2.0$ for dust-poor quasars, which hints at their broad-line regions' being more illuminated by energetic UV photons than average, consistent with the observed bluer EUV spectra in the left part of the top panel of Figure 4.8(a). This, together with the blue NUV–optical spectra of dust-poor quasars in Figure 4.8(a), suggests that high-temperature, energetic radiation sources are connected to the dust-poor property. An example of such a case would be the model prediction of an accretion disk temperature–dependent UV–optical color for AGNs (Bonning et al. 2007).

4.4.2 Parameter Space Study of Dust-poor Quasars

Figure 4.10 shows the distribution of AGNs in our sample in L_{bol} versus redshift, and f_{Edd} versus M_{BH}. Also plotted are the range of parameter space covered by other studies (H10 and M11). Here the dashed boundary for the M11 sample is determined following their selection criteria, and we mimic the distribution of the H10 sample by plotting with heavy black points objects in the sample of Lusso et al. (2010) which contains 88% of the 408 AGNs in H10. Overall, our sample is brighter than H10's in L_{bol} and less extensive in L_{bol}, but more extensive in redshift-space coverage than M11. From Figure 4.10,

we find that the $L_{\rm bol}$ and i-band limits (Section 4.2) introduce a faint-end luminosity cut that is variable with redshift. Moreover, the anticorrelation between $L_{\rm bol}$ and the hot dust covering factor $\mathrm{CF_{hd}}$ (see, e.g., M11) may act as a luminosity selection effect (Section 4.5.1) to mix up the distributions of $f_{2.3}$ or $\mathrm{CF_{hd}}$ when plotted against a parameter closely associated with $L_{\rm bol}$, such as $M_{\rm BH}$ or $f_{\rm Edd}$. To minimize any such effect, we split the whole sample into four volume-limited subsamples where 204 dust-poor quasars remain inside the dot-dashed limits in Figure 4.10(a).

Now we use the fraction of dust-poor quasars ($p_{\rm hdp}$) to visualize the global trends of dust-poor quasars in observed parameters. When the $p_{\rm hdp}$ are plotted against $L_{\rm bol}$ (Figure 4.11(a)), we find a positive correlation between the two products, in accord with the distribution of $f_{2.3}$ decreasing with $L_{\rm bol}$ in Figure 4.11(c). The first parameter to look into through $p_{\rm hdp}$ under the volume limits is the redshift, as we would like to know the evolution of the fraction of dust-poor quasars independent of luminosity selection. In Figure 4.11, we find not only a trend of lower $f_{2.3}$ at higher redshift overall (Figure 4.11(d)), but also a clear tendency of increased $p_{\rm hdp}$ at higher redshifts at given luminosity (Figure 4.11(b)), mixed with the $p_{\rm hdp}$ increasing with luminosity at a given redshift. Compiling our $p_{\rm hdp}$ with that inferred from J10, we fit the $z > 2$, $L_{\rm bol} > 10^{47}\,\mathrm{erg\,s^{-1}}$ data points in Figure 4.11(b) to model the redshift evolution of the dust-poor fraction as $p_{hdp} = (1.35 \pm 0.13) \times 10^{-3}\,(1+z)^{2.34\pm0.08}$.

Since we are dealing with a small number of special objects, some of dust-poor quasars could be misclassified normal quasars due to large photometric errors or sparse wavelength sampling in the *WISE* data points. To estimate what fraction of dust-poor quasars could have arisen from these artifacts, we selected 7834 SDSS DR7 quasars in our sample at $z < 1$ with K and W4 detections and redshifted their SEDs while adding appropriate noise to make them appear to have i=18–19.5 mag. Starting from a set of observed fluxes and errors linearly interpolated to simulated redshifts ($F_{\rm obs}, \Delta F_{\rm obs}$), we assigned flux er-

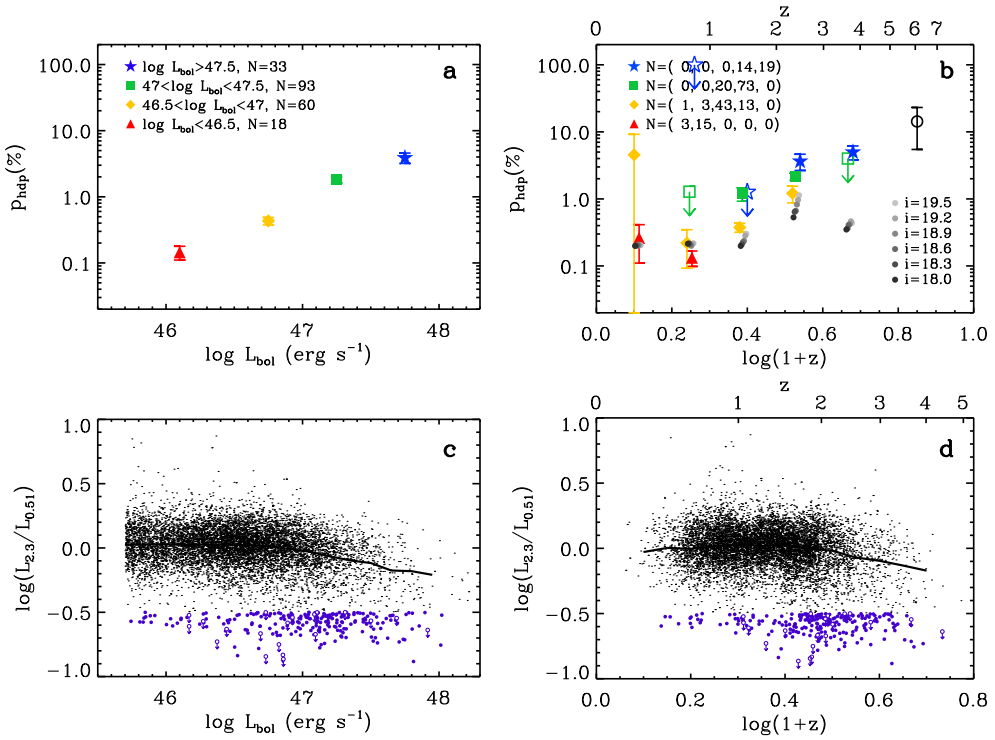

Figure 4.11: Left: (a) plot of hot dust-poor fraction ($p_{\rm hdp}$) vs. $L_{\rm bol}$. Colored filled symbols represent the fraction of quasars in each luminosity bin that are hot dust-poor. The error bars are calculated based on Poisson statistics. (c) Plot of $f_{2.3}$ vs. $L_{\rm bol}$. The individual distribution of hot dust-poor quasars (purple) is plotted with a randomly selected quarter (following Figure 4.10) of the entire sample (black). In addition, the average $f_{2.3}$ along $L_{\rm bol}$ is overplotted (solid line). Right: (b) plot of $p_{\rm hdp}$ vs. z. Colored filled symbols (slightly shifted to avoid overlap) represent the fraction of quasars in each luminosity and redshift bin that are hot dust-poor, with the number of objects per data point shown following the arrangement of the data. The open circle is the $z=6$ result of J10. Upper limits in $p_{\rm hdp}$ are calculated as $1/N_{\rm bin}$ when there are no dust-poor quasars in the bin with size $N_{\rm bin}$. The gray circles are test results for our $z<1$, K- and $W4$-detected sample SEDs, simulated for each redshift and observed i-band magnitude. (d) Plot of $f_{2.3}$ vs. z. The layout follows panel (c).

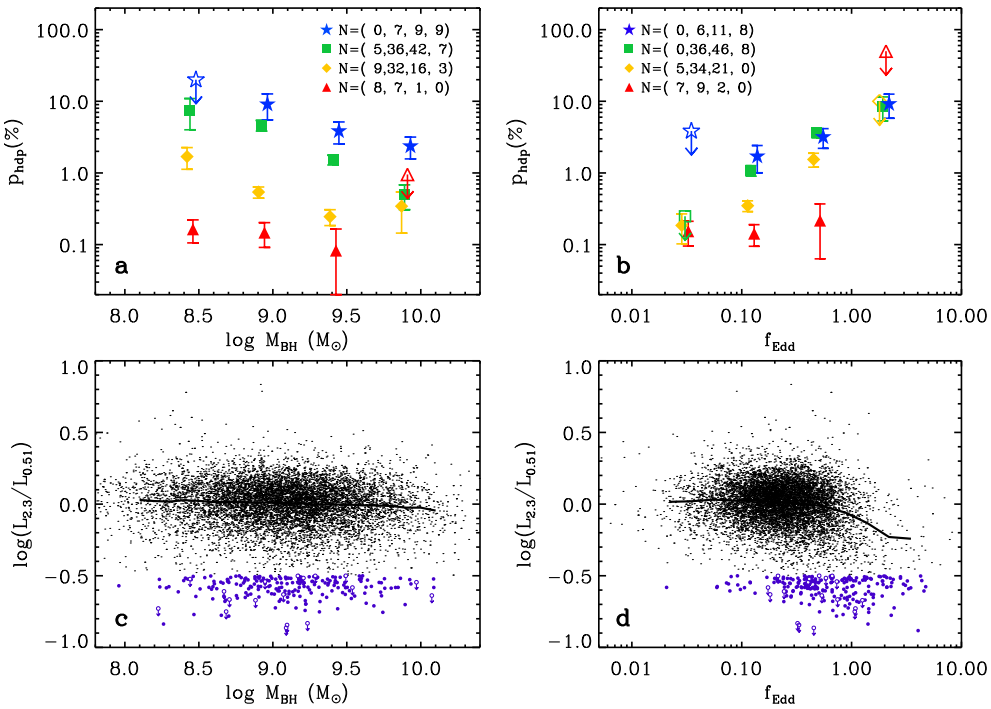

Figure 4.12: Left, $M_{\rm BH}$–$p_{\rm hdp}$ plot (top) and the $M_{\rm BH}$–$f_{2.3}$ distribution (bottom); right, $f_{\rm Edd}$–$p_{\rm hdp}$ plot (top) and the distribution of $f_{\rm Edd}$–$f_{2.3}$ (bottom). The styles are as in Figure 4.11.

rors corresponding to the simulated fluxes as $\Delta F_{\rm sim} = \Delta F_{\rm obs} 10^{0.2(m_{\rm sim}-m_{\rm obs})}$, where $m_{\rm obs}, m_{\rm sim}$ are observed and simulated magnitudes. Then we added Gaussian random noise ($\sigma_{gauss} = \Delta F_{sim}$) to the simulated fluxes, to obtain a set of fluxes and errors ($F_{\rm sim}, \Delta F_{\rm sim}$). Every object was simulated 50 times with randomly added errors, for a given simulated redshift and magnitude. Finally the redshifted, error-scaled, and noise-added set of SEDs were fitted to calculate the dust-poor fraction. The dust-poor fractions from this simulation are overplotted in Figure 4.11(b) with gray circles.

The figure indicates that the objects selected for this test are representative of general quasars at $z<1$, since the simulated $p_{\rm hdp}$ values, regardless of test magnitude, are within the errors of the observed $p_{\rm hdp}$ at $z<1$. But then, the test gives the possibility of dust-rich ($f_{2.3}>-0.5$) quasars being artificially classified as dust-poor, as the simulated $p_{\rm hdp}$ starts to increase at $z>1$. Not only does $p_{\rm hdp}$ increase for fainter simulated magnitudes, it also has a peak at $2<z<3$ where the rest-frame 2.3 μm lies between the widely separated W2/W3 bands. This indicates that the dust-poor selection becomes uncertain when the photometric data points around the peak of the hot dust radiation are sparse. Comparing the observed versus simulated $p_{\rm hdp}$ of $L_{\rm bol} = 10^{46.5}$–$10^{47}\,{\rm erg\,s^{-1}}$ sources in Figure 4.11(b), for example (yellow and gray points), we estimate that $\sim 60\%$ of the faintest objects ($i = 18.5$–19; see Figure 4.2(b)) in the dust-poor sample might be misclassified normal or borderline quasars at $2<z<3$. However, at $z>3$ only a small fraction of dust-poor quasars are possible misclassifications, suggesting that the observed $p_{\rm hdp}$ are genuinely higher at $z>3$. Furthermore, taking into account the higher possibility of identifying false dust-poor objects at $2<z<3$, the intrinsic distribution of true dust-poor quasars will show a stronger positive z–$p_{\rm hdp}$ relation at $z>2$ for any given luminosity bin. Therefore, we consider the overall trend of increased $p_{\rm hdp}$ with redshift to remain unchanged under the possible artifacts.

Next, $p_{\rm hdp}$ versus black hole mass and Eddington ratio are plotted in Fig-

ures 12(a) and (b) for four different $L_{\rm bol}$ bins. We find higher $p_{\rm hdp}$ for more luminous $L_{\rm bol}$ binned subsamples, which is consistent with Figures 11(a) and (b) and with predictions of smaller dust covering factors at brighter $L_{\rm bol}$, such as from the receding dust torus model (Lawrence, 1991). Therefore, we note the importance of controlling the range of $L_{\rm bol}$ in order to accurately trace the properties of dust-poor quasars. In addition, because our dust-poor quasars are systematically smaller in $\mathrm{CF_{hd}}$ or, equivalently, larger in NIR bolometric corrections (BC_λ=$\mathrm{BC}_{\lambda(\mu\mathrm{m})}$) than average, we would like to double-check whether the $L_{\rm bol}$–$p_{\rm hdp}$ trend is affected by systematically different BCs for dust-poor SEDs. We integrated the model fit on the composite photometric SED of all quasars (Figure 4.4) in the 0.04–20 μm range, to find $L_{0.04-20}/L_{0.51}=6.46$, or 70% of the bolometric luminosity to be bounded within the selected UV–MIR wavelengths, adopting $\mathrm{BC}_{0.51}=9.26$ from S11. Now, assuming that the SEDs of the average and dust-poor composites do not systematically vary with each other in the γ-ray/X-ray or FIR/radio (see Section 4.5.1 and Table 4.3 for the assumption to roughly hold for X-ray and radio wavelengths), $[(L_{<0.04}+L_{>20})/L_{0.51}]_{\rm hdp}=2.80=(L_{<0.04}+L_{>20})/L_{0.51}$. From our measurement of $(L_{0.04-20}/L_{0.51})_{\rm hdp}=5.04$ out of the composite dust-poor SED, we obtain $\mathrm{BC}_{0.51,\rm hdp}=7.84$, meaning that bolometric luminosities of dust-poor quasars are about 18% overestimated with respect to ordinary quasars, under the adoption of a single $\mathrm{BC}_{0.51}=9.26$.

Drawing Figures 11 and 12 again with an 18% smaller $\mathrm{BC}_{0.51}$ for dust-poor quasars, however, does not change the strength of $p_{\rm hdp}$ trends found in (z, $L_{\rm bol}$, $M_{\rm BH}$, $f_{\rm Edd}$)-spaces. Therefore, we conclude that possible systematic biases in the bolometric correction for dust-poor quasars does not artificially produce the $L_{\rm bol}$–$p_{\rm hdp}$ relation or change the observed $p_{\rm hdp}$ trends within the main observed parameters, although our test suggests caution when applying the BC to dust-poor quasars from the monochromatic luminosity alone. After all this, reading Figures 12(a) and (b) within each luminosity bin decoupled

from the $L_{\rm bol}$ dependence on $p_{\rm hdp}$, we find more dust-poor quasars with lower black hole masses and high Eddington ratios.

Finally, we plot $p_{\rm hdp}$ against other AGN observables in Figure 4.13, starting from the broad-line width and velocity offset. We used the FWHMs from S11 as broad-line widths, updated and replaced for some dust-poor quasars as in Section 4.3. Meanwhile, we took the broad-line velocity offset measurements from S11, defined as the relative shift of the broad-line center with respect to the systemic redshift. The choice of broad line for the line width and offset measurements at each redshift was identical to that when measuring $M_{\rm BH}$ (Section 4.3), except that $\rm C_{IV}$ line velocity shifts were not used, because of their overall blueshift (S11). There is a negative correlation between $p_{\rm hdp}$ and broad-line FWHM in Figure 4.13(a), consistent with the trend found for $M_{\rm BH}$, and a meaningful tendency for velocity offset toward blueshifted broad emission, in Figure 4.13(b). The implications of these results are discussed in the next section. Next, reading Figure 4.13(c), dust-poor quasars with respect to the $\rm Fe_{II}$ (2200–3090 Å)/$\rm Mg_{II}\lambda2798$ metallicity derived from S11 tend to have more iron-rich broad-line regions. Last, in Figure 4.13(d) we investigate the dependence of radio loudness on $p_{\rm hdp}$, with $R_{\rm radio} = F_{\nu,\rm 6cm}/F_{\nu,2500}$ from S11. The radio data are from the FIRST survey (Faint Images of the Radio Sky at Twenty cm; White et al. 1997), roughly coinciding with the SDSS coverage and reaching a typical 5σ sensitivity of 1 mJy. This is similar to the *WISE* W3 sensitivity when assuming a flat source SED in F_ν from MIR to radio, implying that most radio-loud/intermediate sources are radio detectable. However, the FIRST detection threshold (5σ) is higher than that of *WISE* (2σ) and misses the majority of radio-quiet sources, which results in only 10% of the final AGN sample used in this work being detected. Still, the radio loudness is roughly complete down to $R_{\rm radio} \sim 10$ within the detection limit, while the distribution of $R_{\rm radio}$ shows a trend expected to fall below $R_{\rm radio} \sim 10$ under nondetections, for both dust-poor and all AGNs. To further investigate the

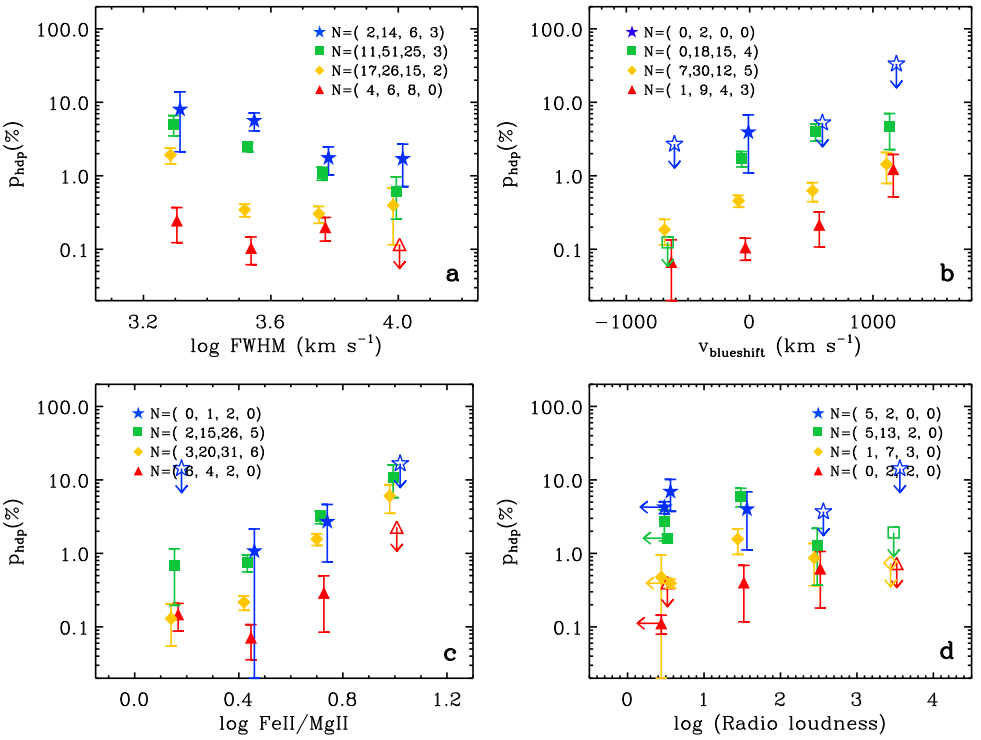

Figure 4.13: Plots of $p_{\rm hdp}$ vs. parameters related to broad emission lines and radio properties: (a) broad-line FWHM, (b) broad-line blueshift from the systemic redshift, (c) $\rm Fe_{II}$ (2200–3090 Å)/$\rm Mg_{II}\lambda2798$ metallicity, and (d) radio loudness $R_{\rm radio} = F_{\nu,6\rm cm}/F_{\nu,2500}$. The symbols are as in Figure 4.11; the left-pointing arrows in panel (d) indicate $p_{\rm hdp}$ estimated without radio detections but with a rough $R_{\rm radio} \lesssim 10$ limit.

Table 4.3. K-S test on dust-poor quasar fraction in observed parameters

$\log L_{\rm bol}$ (erg s^{-1})	45.7–46.5	46.5–47	47–47.5	>47.5	45.7–46.5	46.5–47	47–47.5	>47.5
Parameter	$p_{\rm KS}$	$p_{\rm KS}$	$p_{\rm KS}$	$p_{\rm KS}$	$N_{\rm hdp}$	$N_{\rm hdp}$	$N_{\rm hdp}$	$N_{\rm hdp}$
z	-0.09	3.1e-06	1.2e-03	0.13	18	60	93	33
$M_{\rm BH}$	-0.62	-1.1e-04	-7.7e-12	-3.4e-03	18	60	90	25
$f_{\rm Edd}$	0.43	1.8e-07	1.6e-10	1.2e-04	18	60	90	25
FWHM	-0.26	-3.8e-04	-7.3e-08	-8.9e-03	18	60	90	25
$v_{\rm blueshift}$	2.8e-03	2.9e-05	9.0e-11	...	18	60	40	3
$\rm Fe_{II}/Mg_{II}$	-0.26	3.8e-04	7.3e-08	...	16	60	50	3
$R_{\rm radio}$	0.76	0.64	0.16	-0.05	4	11	20	7

Note. — $p_{\rm KS}$ is the K–S probability for the distribution of dust-poor quasars in each parameter and luminosity bin, to be indistinguishable from that of the rest of our whole sample. The configuration of volume-limited luminosity bins follow Figure 4.10a. Positive $p_{\rm KS}$ implies dust-poor quasars to have a larger parameter value than average quasars, and vice versa for negative signs, while statistically meaningful probabilities set as $|p_{\rm KS}|$ <1%, are printed in exponential format. $N_{\rm hdp}$ is the number of dust-poor quasars used in each bin to calculate $p_{\rm KS}$, ordered by the same luminosity range as for $p_{\rm KS}$. Blank fields correspond to bins with few quasars to perform a test.

completeness of the radio data, we calculated the $p_{\rm hdp}$ in Figure 4.13(d) while adding the FIRST nondetections into the $R_{\rm radio} < 10$ bin, finding the $p_{\rm hdp}$ to be consistent within the errors, to that with the detections only. Ultimately, we find no significant preference of dust-poor quasars in the $R_{\rm radio}$–$p_{\rm hdp}$ distribution. Likewise, we tried to search for the X-ray loudness features from the *ROSAT All-Sky Survey* observed counts in Schneider et al. (2010) but failed to compile enough matches (N=7) for proper analysis.

4.5 Discussion

4.5.1 Observational Characteristics of Dust-poor Quasars

To quantify how distinct dust-poor quasars are from typical quasars in various physical properties, we performed a set of Kolmogorov–Smirnov (K-S) tests by comparing the distribution of the dust-poor sample against the average sample. The result is summarized in Table 4.3. Although it becomes uncertain

at $L_{\rm bol} < 10^{46.5}\,{\rm ergs\,s^{-1}}$, most of the K-S probabilities at $L_{\rm bol} > 10^{46.5}\,{\rm ergs\,s^{-1}}$ are smaller than 1%, indicating that dust-poor quasars are likely to be drawn from a different population than average luminous quasars. Moreover, the directions of the inequality between dust-poor and average quasar properties in Table 4.3 are consistent with Figures 11–13. To begin summarizing the main results from the table and figures, dust-poor quasars are at higher redshifts for a given luminosity, with this trend found to be secure at $z > 2$. This is consistent with J10 and H10, but not with M11, who did not find any evolution in the dust-poor fraction. Next, we find dust-poor quasars of relatively lower black hole mass, of order $10^8 M_\odot$, and high Eddington ratios indicating super-Eddington accretion, at a given luminosity, in agreement with J10 at $z > 6$ but not with H10 or M11, where dust-poor quasars are indistinguishable from the average in $M_{\rm BH}$ and $f_{\rm Edd}$. In addition to these fundamental properties, dust-poor quasars show narrower broad-line FWHMs of 2000–3000 $\rm km\,s^{-1}$, blueshifted line centers of order 10^3 km $\rm s^{-1}$, and $\rm Fe_{II}/Mg_{II}$ line ratios a few times higher than average.

Although we find some of the parameter trends summarized above to agree with previous studies, there are also debatable results. To investigate further among conflicting arguments, we first note the limitation of small number statistics. The number of our volume-limited dust-poor quasars is N=204, which is enough to precisely look for parameter trends, as we find many of the K-S probabilities in Table 4.3 to be statistically significant. Also, our study serves as a lower redshift counterpart to J10, as they miss the $z < 6$ dust-poor population, possibly because of a combination of the small parent sample size in J10 and the z–$p_{\rm hdp}$ trend found in this work, which predicts fewer dust-poor quasars at lower z. Meanwhile, although H10 selected dust-poor quasars with a relatively high fraction ($\gtrsim 10\%$), their total of N=41 dust-poor quasars is still insufficient to tell whether they are drawn from a different population or not, as the K-S probabilities lie ambiguously between 0 and 1 except with

respect to the redshift. Therefore, a larger sample size would be required to understand in detail the dust-poor quasars defined in H10. We additionally note that the X-ray selection of H10 may bring discrepancies to the dust-poor population properties based on our optically selected AGNs. However, our $f_{2.3} < -0.5$ limit is similarly met only for the Class II criterion of H10, which is merely 15% of the dust-poor population in H10. Thus, we mostly regard the high $p_{\rm hdp}$ in H10 as coming from the different definitions of being dust-poor rather than from the X-ray selection of AGNs to elevate the $p_{\rm hdp}$.

Next, we note the difference of studying $\mathrm{CF_{hd}}$ in overall distributions from previous works and under volume-limited subsampling here. For instance, the overall distribution of $\mathrm{CF_{hd}}$ is roughly independent of $M_{\rm BH}$ in J10 ($z < 6$), in M11, and in Figure 4.12(c). However, in Figure 4.12(a) we witness clearly higher $p_{\rm hdp}$ for smaller $M_{\rm BH}$ at a given luminosity of $L_{\rm bol} > 10^{46.5}\,\mathrm{ergs\,s^{-1}}$. If the sample had a wide dynamic range of $L_{\rm bol}$, there would be a higher chance of the anticorrelation between $L_{\rm bol}$ and $\mathrm{CF_{hd}}$ mixing up the distribution of $\mathrm{CF_{hd}}$ when plotted against a parameter dependent on $L_{\rm bol}$. In other words, quasars with higher $M_{\rm BH}$ are more likely to be selected as dust-poor objects, since $M_{\rm BH} \propto \sqrt{L_{\rm bol}}$ (e.g., Equation (4.3) with constant BC) and because there are more dust-poor quasars with high $L_{\rm bol}$ (Figure 4.11(a)). Revisiting Figure 4.12, this luminosity selection effect is indeed visible, where Figure 4.12(c) under a wide range of $L_{\rm bol}$ displays flatter $f_{2.3}$ with $M_{\rm BH}$, or more chance of dust-poor quasars at higher $M_{\rm BH}$, than Figure 4.12(a) under a fixed range of $L_{\rm bol}$. Therefore, we expect the disconnection between $f_{3.5}$ or $\mathrm{CF_{hd}}$ versus $M_{\rm BH}$ in the $z < 6$ population of J10 or M11 to be at least partially caused by a relatively broad range of $L_{\rm bol}$ that would smooth out the possible underlying correlation between $M_{\rm BH}$ and $f_{3.5}/\mathrm{CF_{hd}}$.

Likewise, the luminosity selection would act on the Eddington ratio as $f_{\rm Edd} \propto L_{\rm bol}/M_{\rm BH} \propto \sqrt{L_{\rm bol}}$, selecting more dust-poor quasars at higher $f_{\rm Edd}$ than when volume limited. This time, the positive $f_{\rm Edd}$–$p_{\rm hdp}$ relation of Fig-

ure 4.12(b) is consistent with the $f_{\rm Edd}$–$\rm CF_{hd}$ anticorrelation in Figure 4.12(d), which can be explained by the stronger $f_{\rm Edd}$–$\rm CF_{hd}$ anticorrelation than that of $L_{\rm bol}$–$\rm CF_{hd}$ (compare Figure 4.12(d) with Figure 4.11(c)). Furthermore, we expect the luminosity selection effect to be somewhat mixed by the redshift selection effect, as a result of the z–$p_{\rm hdp}$ trend and the luminosity distribution of our sample, such that higher luminosity sources are at higher redshift on average. We tested the redshift selection effect by drawing figures similar to Figures 12(a) and (b) in a fixed $L_{\rm bol} = 10^{47}$–$10^{47.5}\,\rm erg\,s^{-1}$ interval while comparing the $p_{\rm hdp}$ between $1 < z < 2$ and $2 < z < 3$. We find a higher normalization of $p_{\rm hdp}$ at higher redshift, but the difference in the $p_{\rm hdp}$ is smaller than when the redshift interval is fixed as one of the two above, and instead subsamples in the range of $L_{\rm bol}$ adjacent to the 10^{47} to $10^{47.5}\,\rm erg\,s^{-1}$ bin are compared. Therefore, the luminosity selection effect on $p_{\rm hdp}$ in this work is only mildly mixed with that from redshift selection.

As a way to remove this effect, M11 defined their hot dust-poor quasars as the lower outlying objects in $\rm CF_{hd}$, dependent on $L_{\rm bol}$. Therefore, the $p_{\rm hdp}$-based parameter trends of dust-poor quasars in M11 can be compared directly with the volume-limited $p_{\rm hdp}$-based trends in this work, as both studies are corrected for luminosity selection, while the sample size of M11 is as large as ours, so they do not suffer from small number statistics. The $L_{\rm bol}$–$p_{\rm hdp}$ trend would be different for the two studies, though, as the definition of dust poorness in M11 inherently leads to a flat $p_{\rm hdp}$–$L_{\rm bol}$ relation, while our result of increasing $p_{\rm hdp}$ with $L_{\rm bol}$ is free from such a selection. Apart from this exception, we expect the $p_{\rm hdp}$-related parameter trends from M11 and this work to be consistent with each other, but we still witness somewhat conflicting results in z-, $M_{\rm BH}$-, and $f_{\rm Edd}$-spaces. However, the redshift range of $0.75 < z < 2$ covered by M11 is not as wide as that of this work, which according to Figure 4.11(b), implies they could miss up to an additional order of magnitude of increase in $p_{\rm hdp}$ above $z = 2$. Next, M11 did not find the $p_{\rm hdp}$ to depend on

$M_{\rm BH}$ or $f_{\rm Edd}$, while we find negative and positive dependences on $M_{\rm BH}$ and $f_{\rm Edd}$, respectively. A caveat is that the dust-poor selection of M11 passes through $\gtrsim 16\%$ of the sample, which is much higher than the 0.6% from this work, or $\sim 1\%$ from Figure 4.11(b) within the redshift interval $0.75 < z < 2$ matched with M11. From this, we suggest that M11's method of selecting low-$\rm CF_{hd}$ sources may choose too many objects as dust-poor, making it hard to distinguish properties of dust-poor quasars from the rest of the sample. To summarize, we conclude that the differences in $p_{\rm hdp}$ trends between M11 and this work, originate from the different redshift coverage and the selection criteria for dust-poor quasars.

We note that the observational characteristics of dust-poor quasars could be different at lower AGN luminosities, as our K-S probabilities in Table 4.3 are weaker at $L_{\rm bol} < 10^{46.5}\,{\rm ergs\,s^{-1}}$. Combining our results with the study of Mor & Netzer (2012, hereafter M12) helps to constrain the properties of fainter dust-poor AGNs, since their sample are Seyfert 1 galaxies mostly covering $L_{\rm bol} = 10^{44}$–$10^{46}\,{\rm erg\,s^{-1}}$. Although their dust-poor and total sample sizes are only ~ 10 and 115, they do find low-$\rm CF_{hd}$ sources for narrow-line Seyfert 1's in low $M_{\rm BH}$ and high $f_{\rm Edd}$, consistent with our results above $10^{46.5}\,{\rm ergs\,s^{-1}}$. Since the optical luminosities of AGNs in M12 are likely to be affected by host galaxy contamination (see, e.g., S11), it would be interesting for future studies to check whether the parameter trends of intermediate-luminosity ($L_{\rm bol} \lesssim 10^{46}\,{\rm ergs\,s^{-1}}$) dust-poor AGNs, as in M12, are valid after correcting for host contamination in the optical luminosity.

Physically connecting our observational results of luminous dust-poor quasars, the $L_{\rm bol}$–$p_{\rm hdp}$ relation is well explained by the receding-torus model (Lawrence, 1991), such that more luminous quasars have smaller dust covering factors as a result of the torus's being located far from the central light source. In addition, the link between FWHM and $p_{\rm hdp}$ in Figure 4.13(a) is closely connected with the $M_{\rm BH}$–$p_{\rm hdp}$ and $f_{\rm Edd}$–$p_{\rm hdp}$ relations in Figures 12(a) and (b), since

quasars with narrow FWHM would be lower in $M_{\rm BH}$ and higher in $f_{\rm Edd}$ at a given $L_{\rm bol}$. This implies that quasars that are not only luminous but also violent in growth and small in cumulative mass, or actively growing quasars, would have a higher chance of being dust-poor. Since our dust-poor quasars, although skewed to higher z, are fairly spread within the z–$p_{\rm hdp}$ relation, we describe the dust-poor epoch of quasars as being positioned in a buildup state within individual black hole growth histories, rather than a specific global cosmic epoch (J10).

In addition to the key trends, the $v_{\rm offset}$–$p_{\rm hdp}$ relationship for dust-poor quasars preferring blueshifted broad emission could be related to radiative outflows affecting the broad-line emission (e.g., Richards et al. 2011), which are necessary for radiative quasar feedback or QSO dust production through the expansion of broad-line clouds (Section 4.5.2). Alternatively, the blueshifts could be explained as recoiling black holes separated from the dusty torus (Guedes et al., 2011), but the predicted probabilities of detecting kinematically offset AGNs are still lower by several orders of magnitude than the fraction of our dust-poor quasars with large blueshifts. Meanwhile, the high $\rm Fe_{II}/Mg_{II}$ of dust-poor quasars could be a sign of metal seeds where QSO dust can grow (Section 4.5.2; Pipino et al. 2011), although it is difficult to arrive at a clear interpretation from observed metallicities alone.

4.5.2 The Origin of Dust-poor Quasars

We now consider possible scenarios for the origin of dust-poor quasars. First, we would like to list the explanations for the occurrence of dust-poor objects being dependent on the geometry of the surrounding dusty structure. One of the descriptions is the receding-torus model (Lawrence, 1991), which predicts smaller dust covering factors at higher luminosities, for the obscuring structure to be located more outward. Our study provides further constraints for this model, as our dust-poor quasars are not only more luminous but also less

massive and high in Eddington ratio. To fit our observational results, the viewing angle of dust-poor quasars could be considered as being observed from a face-on direction, because the unified model predicts obscuration from the dusty torus when observed through an inclined angle. Assuming that the broad-line region follows the inclination of the torus (Gaskell et al., 2007), and adopting a simplified planar geometry for these AGN substructures, the observed line widths would satisfy $\mathrm{FWHM_{obs}} = \mathrm{FWHM} \sin i$, where i is the inclination angle. Therefore, we may expect the broad FWHMs of dust-poor quasars to be systematically narrower merely because of the projected $\sin i$ factor for a planar geometry.

While this orientation-based approach is capable of explaining many parameter-space features (FWHM, M_{BH}, f_{Edd}) of dust-poor quasars, the problem is that it cannot describe the redshift dependence of p_{hdp} unless higher redshift quasars are systematically biased to lower inclination angle objects at given luminosity. Moreover, when a dusty torus is observed face-on, the unified model suggests more chance of being directly illuminated by radio jets (see, e.g., Figure 3 of Antonucci 1993), whereas in Table 4.3 we do not find dust-poor quasars to be radio-louder, although the number statistics may not be secure. Several other geometric explanations of the origin of dust-poor quasars include low-level misalignment of the torus with respect to the accretion disk (Kawaguchi & Mori, 2011) and mildly misaligned disks even without the torus structure (Lawrence & Elvis, 2010). At this time, where our observations are not able to strictly validate each geometric scenario, we leave it as an open question to explain dust-poor quasars in a geometric sense, although we do stress the need for future models to be able to further explain our observational features (Section 4.5.1).

Second, in terms of the physical origin of dust-poor AGNs, that is, for intrinsic lack of dust emission under the dust blowout process, we would like to suggest in which stage dust-poor quasars would lie if they followed ex-

isting AGN evolutionary scenarios. With regard to the triggering of quasar activity, we follow Treister et al. (2012) and apply their result that within the luminosity limit of our study ($L_{\rm bol} > 10^{45.7}\,{\rm ergs\,s^{-1}}$), more than 50% of quasars are triggered by major mergers. Merger-triggered quasar activity is often observationally interpreted to begin from the stage of luminous infrared galaxies, showing strong signatures of dense gas and dust out to kiloparsec scales (e.g., Sanders et al. 1988; Surace et al. 1998). Therefore, for the majority of luminous dust-poor quasars to originate from galaxy merging, not only are the host galaxies expected to have been dusty during the merging stage, but the obscured host galaxies also require feedback mechanisms that blow out the surrounding material to become more transparent to the quasar radiation like normal quasar systems. This step is predicted in the merger-driven AGN model of Hopkins et al. (2008) as the blowout stage, where the gas and dust surrounding the quasar host galaxy are expelled.

Depending on the extent of merger-driven quasar feedback, red quasars are thought to be in the blowout stage when the surrounding dust has not yet been removed (e.g., Figure 5(e) in Hopkins et al. 2008; Urrutia et al. 2008), while we may now place dust-poor quasars at the end of the blowout stage for the dust to have sufficiently been dispersed. Our study further helps to observationally constrain the evolutionary boundary of dust-poor quasars as we find it to agree with the blowout-phase predictions of rapidly growing black holes (low $M_{\rm BH}$, high $f_{\rm Edd}$) and intense feedback (high $L_{\rm bol}$ and blue UV continuum) from Hopkins et al. (2008), and with observations of high-$f_{\rm Edd}$ objects within the red quasar sample of Urrutia et al. (2012). At the same time, however, dust-poor quasars are closer to normal quasar phases, as their accretion-disk-dominated SEDs indicate that the nucleus is less obscured from its surroundings, compared with red quasars. Therefore, we consider it most plausible to assign dust-poor quasars in between the blowout and traditional quasar phases, where dust-poor quasars can be explained as having

just become unobscured as they went through intense feedback during the rapid black hole growth but are still relatively low in $M_{\rm BH}$ and high in $f_{\rm Edd}$ on their way to becoming normal quasars. When our dust-poor fraction of 0.6 % is translated into the visible dust-poor timescale, it becomes $\sim$0.1–1 Myr from the visible timescale of quasar activity (Martini 2004; Hopkins et al. 2005). Therefore, the short visible timescale may imply either that dust can form efficiently after the short/intense dust-dispersing part of the blowout phase, or that it is difficult for typical quasars to clear off the surrounding dust to a sufficient extent.

This approach to clarify the evolutionary state of dust-poor quasars from the key parameter trends would be strengthened if the redshift evolution of $p_{\rm hdp}$ from this work were further explained. At high redshift, the amount of dust observed in quasars or gamma-ray bursts can be explained by dust-producing sources, mainly supernovae and the most massive asymptotic giant branch (AGB) stars, whereas QSO dust[4] or contributions from less massive AGB stars are relatively limited (see, e.g., Pipino et al. 2011; Jang et al. 2011). The restricted dust production routes within the short age of high-redshift quasar systems, therefore, could be the cause of the z–$p_{\rm hdp}$ relation of dust-poor quasars as their progenitors may not have enriched enough dust to survive under the presence of AGN feedback, observed to be in action up to the early universe (e.g., Maiolino et al. 2012). Hence, the increased fraction of dust-poor quasars at higher redshift is consistent with current dust formation model predictions and with observations of bluer UV continuum slopes of inactive galaxies at high redshift (e.g., Bouwens et al. 2009).

Stemming from the evolutionary model for dust-poor quasars, the fact that we find BAL quasars in our dust-poor sample has interesting implications for the dust origin of BAL quasars. Utilizing the BAL flag in S11 based on the

[4]We use the term QSO dust for the dust production originating from the quasar activity and to distinguish from stellar-related sources.

criterion from Gibson et al. (2009), we find a BAL fraction of $4.3\% \pm 1.5\%$ from the dust-poor sample, similar to or only slightly higher than $3.2\% \pm 0.1\%$ from the entire sample. As stated earlier, dust-poor quasars have a strong blue UV–optical continuum. If the BAL is caused by an orientation toward absorption (e.g., Elvis 2000), BAL quasars would not be included in the dust-poor sample since the dusty structure would obscure the UV–optical light too. The evolutionary model for dust-poor quasars seems to provide a natural explanation for the dust in BAL quasars, supporting an evolutionary model of the BAL phase that lies in between luminous infrared galaxies and normal quasars (e.g., Briggs et al. 1984; Lípari & Terlevich 2006).

4.5.3 The Future of Dust-poor Quasars

Having considered dust-poor quasars to possibly be explained by geometric or evolutionary models, to be observed by an unobscured orientation or to have undergone a duration of strong feedback, we would finally like to comment on their near future by comparing with average optically selected quasars. If dust-poor quasars have a geometric explanation, we may expect the covering factor to become larger at later quasar phases when they become quieter in luminosity or Eddington ratio, as the covering factors are anticorrelated with $L_{\rm bol}$ and $f_{\rm Edd}$ (Lawrence 1991; Kawaguchi & Mori 2011).

On the other hand, assuming an evolutionary origin for dust-poor quasars, we need to consider dust formation mechanisms during the AGN evolution. Although our observational explanation of dust-poor quasars as rapidly growing (Section 4.5.1) supports their being younger than ordinary quasars, the evolutionary models predict the other way round, for quasars to become more dust-poor along the duration of their activity. This is due to the solely destructive nature of AGN feedback, to blow out the surrounding dust (e.g., Haas et al. 2003; Hopkins et al. 2008). Thus, assuming that the evolutionary paths for dust-poor and ordinary quasars are aligned—in other words, consid-

ering the dust-poor phase to be general within the lifetime of optically selected quasars—the only way to reconcile with observations is to add to the models constructive feedback from the AGN activity itself, which is to say, a dust formation mechanism at the center of quasars. This idea makes sense in that it satisfies the temporal causality to enrich the dusty tori as the system accumulates its black hole mass. Our rapid-growth scenario therefore naturally supports the model production of QSO dust, possibly during the free expansion of broad-line clouds (Elvis et al., 2002), which is in fact likely to be the dominant source of dust formation in the inner galaxy once AGN feedback becomes effective (Pipino et al., 2011). To summarize, revising the evolutionary model for luminous quasars passing the dust-poor phase, dust blowout in the inner kiloparsecs of the galaxy is followed by dust formation from the central parsecs of the AGN.

Still, in the cases of powerful AGN feedback, one could imagine the intense radiation not only removing the galaxy-scale dust, but destroying the freshly formed QSO dust at the center of active galaxies such that dust-poor quasars remain dust-poor. This may not be the case for $L_{\rm bol} < 2 \times 10^{47}\,{\rm erg\,s^{-1}}$ quasars, though, since the radiative flux density illuminating the QSO dust-forming region is weaker than that around giant stars (Elvis et al., 2002). Considering that 75% of our dust-poor quasars are less luminous than this limit, the extreme case of continued dust destruction can mostly be rejected as the fate of dust-poor quasars. Therefore, provided that the dust production is effectively working, we suggest the near future of dust-poor quasars is to be richer in dust, including the contributions from QSO dust, which is contrary observation-based scenarios in which ordinary quasars become dust-poor objects (Haas et al. 2003; Hao et al. 2012, although for a fainter luminosity range) but supports dust enrichment within the torus (Elvis et al. 2002; J10) or circumnuclear regions (e.g., Simões Lopes et al. 2007) of active galaxies during its activity.

But what if dust-poor quasars are not causally related to ordinary quasars? It could be the case that dust-poor quasars are indeed rare objects within AGN evolution, to be placed in intrinsically dust-poor environments within their host galaxies and/or with weak QSO dust formation, such that they do not become as dust-rich as ordinary quasars during the quasar phase. This idea may be supported by observations of early-type AGN host galaxies, where the ratio of dust mass to 4.5 μm luminosity, representing the stellar mass (e.g., Jun & Im 2008), ranges widely at given 4.5 μm luminosity (Martini et al., 2013). Within this framework, the relative lifetimes of each AGN evolutionary stage based on obscuration could be scattered as a result of the variety of dust content within each host environment. For example, although AGN evolutionary models predict obscured AGNs to be younger than the unobscured, under an especially low dust-to-stellar mass ratio environment of the host, AGNs would quickly become optically luminous without a typically long duration of being obscured (e.g., Hopkins et al. 2005). Thus, even if dust-poor quasars may be explained as lying in a rare dust-poor environment, this shifts the visible dust-poor lifetime to the relatively earlier growing state of the black hole, still consistent with our rapid-growth explanation (Section 4.5.1).

4.6 Conclusion

Out of a large-area, multiwavelength sample of luminous quasars, we identified 233 (0.6%) objects that satisfy a hot dust-poor criterion analogous to that of Jiang et al. (2010). The selected dust-poor quasars are weak in both NIR- and MIR-to-optical flux ratios and show a blue continuum with mean slope of $\alpha \sim 0.1$ from the UV through the NIR. We calculated the fraction of dust-poor quasars in four bolometric luminosity bins and find statistical preferences of dust-poor quasars to be more abundant in higher redshift, and to have lower black hole mass, higher Eddington ratio, blueshifted and narrower broad lines,

and higher Fe_{II}/Mg_{II} ratio, at a given luminosity. The results show that dust-poor quasars are a population that is rapidly growing in terms of M_{BH} and f_{Edd}, while the rapid growth of black holes and the dust-poorness should be linked closely to the evolution of quasars as a function of redshift.

To explain the observational characteristics of dust-poor quasars, we suggest a scenario in which dust-poor quasars are transient phenomena during an evolutionary process, when they became unobscured by merger-driven AGN feedback. Luminous quasars are often triggered by violent major merging (Treister et al., 2012), involving large extinctions from their host galaxies (e.g., Sanders et al. 1988). From the onset of strong AGN activity, radiative feedback blows out (Hopkins et al., 2008) the surrounding galactic dust to produce dust-poor quasars, for a very short period if they produce QSO dust (Elvis et al. 2002; Pipino et al. 2011), or for longer if they are in an especially dust-poor environment. The redshift evolution of the dust-poor fraction is an indication of the dust content at different redshifts, where the dust-poor phase is more easily identified and lasts longer at higher redshift, since the elements that make up dust grains are scarce in the early universe. An alternative scenario would be to explain dust-poor quasars as a distinct population with small covering factors due to the geometry or orientation of the obscuring material. Such models (Lawrence 1991; Lawrence & Elvis 2010; Kawaguchi & Mori 2011) are consistent with most of the observed properties, but not with the redshift evolution of the dust-poor fraction.

We find the short timescale from the rare population of dust-poor quasars to provide meaningful evolutionary predictions. Deep and resolved imaging of the AGN hosts will tell us whether these dust-poor quasars are closely linked to the evolutionary phase, as the merging features would be clearer at earlier times than the rapid fading of tidal features (Hopkins et al., 2008). Besides, extrapolating the rough relation $p_{hdp} \propto (1+z)^{2.34}$ (Section 4.4.2) up to the early universe, we expect $p_{hdp} = 18\%$ and $p_{hdp} = 37\%$ or more for luminous

quasars at $z = 7$ and $z = 10$, respectively. Therefore, discovery of the highest-redshift quasars will help us learn whether the higher incidence of dust-poor quasars, blue in UV continuum, boost the quasar contribution in reionizing the universe (e.g., Fan et al. 2006b) or if they are born in extremely dust-poor galaxies, as hinted at by the UV slopes of low-luminosity galaxies at $z \sim 7$ (e.g., Bouwens et al. 2010). Future deep multiwavelength studies of dust-poor AGNs should place better constraints on the multitemperature dust emission of the AGN host system and the redshift evolution of these objects.

Chapter 5

The Mid-Infrared Fundamental Plane of Early-Type Galaxies

5.1 Introduction

In the search for correlations among physical parameters of early-type galaxies, it has been recognized that the effective radius (r_e), the effective mean surface brightness ($\langle I \rangle_e$), and the central velocity dispersion (σ_0) form a planar relation (in logarithmic space) known as the fundamental plane (hereafter FP; Dressler et al. 1987; Djorgovski & Davis 1987), in the form of $r_e \propto \sigma_0^a \langle I \rangle_e^b$ where a and b are found to be $(a, b) \simeq (1.2\text{–}1.5, -0.8)$ at visible wavelengths (Jørgensen et al. 1996; Bernardi et al. 2003). Under the assumption of structural homology and a constant mass-to-light ratio, the virial theorem implies that the FP coefficients should be $(a, b)=(2, -1)$–the so-called virial expectation. The observed discrepancy, or tilt of the FP with respect to the virial expectation has prompted many discussions to explain its origin (see D'Onofrio et al. 2006 for a review of this field).

One of the ideas is that the tilt is caused by the systematic variation in the stellar population as a function of physical parameters such as galaxy luminosity. Pahre et al. (1998b) investigated this effect by constructing the FP in K band, which is supposedly a good tracer of the stellar mass less affected by age and dust. Meanwhile, Scodeggio et al. (1998) examined the wavelength dependence of the FP coefficients, and concluded that some of the tilt is caused by the stellar population manifested by the color-magnitude relation. These studies found that the stellar population effect exists, but it can only partially explain the tilt of the FP.

More recent investigations tackle the FP tilt problem using new methods such as gravitational lensing (Treu et al. 2006; Bolton et al. 2007) or dynamical modeling (Padmanabhan et al. 2004; Cappellari et al. 2006). Such studies suggest that the FP tilt nearly disappears when the FP is constructed in the mass domain. Their conclusion is that the tilt must arise from the variation in the central mass-to-light ratio (Robertson et al. 2006), but it is not clear whether the variation is dominated by dark matter or by stars (Bolton et al., 2007).

In this chapter, we extend the FP analysis to wavelengths beyond K band to further investigate the effect of stellar population on the tilt. By doing so we aim to provide the FP that possibly better represents stellar mass (see Section 5.4), and to improve the constraints on different scenarios for the FP tilt.

5.2 The sample

Early-type galaxies were chosen from the sample of Pahre (1999), which was used to study the FP of nearby early-type galaxies in visible and near-infrared (hereafter NIR) passbands. The sample has the velocity dispersion information necessary for constructing the FP. We then searched for mid-infrared

(hereafter MIR)[1] archival images for galaxies in the Pahre (1999) sample. For the MIR data, we used the *Spitzer Space Telescope*, Infrared Array Camera (hereafter IRAC; Fazio et al. 2004) images, covering four wavelength channels at 3.6, 4.5, 5.8, and 8.0 μm. The flux-calibrated, mosaicked IRAC images were retrieved from the *Spitzer* archive for these objects.

The surface brightness fitting was performed for these matched galaxies, and the objects satisfying $r_e > 2''$ for three or more IRAC-bands were retained for the FP analysis. We imposed this size limit in order to work with a sample with reliable r_e values (see Section 5.3.1). After removing a few galaxies (NGC1275, NGC4824, NGC4478, and NGC6166) that show peculiar light profiles (multiple source, close to a bright galaxy or stars), we finally identified 56 galaxies with IRAC data in five clusters (A0426, A1656, A2199, A2634, and Virgo) satisfying our selection criteria. We present a brief summary of the photometric information in Table 5.1. The exposure times for the IRAC data range from 72 to 1000 s.

The above selection of the sample may introduce a bias in the derived FP coefficients (Scodeggio et al. 1998). However, such a bias would not affect our derivation of the wavelength dependence of the FP coefficients, since the multi-wavelength FP coefficients will be derived from the same galaxies for which the same bias would apply.

5.3 Analysis of the data

5.3.1 Surface Brightness Fitting

IRAF ELLIPSE was used to obtain surface brightness profiles of our IRAC sample galaxies. We restricted the fitting region to $a > 2$ pixels (along the semi-major axis) and discarded regions with $\mathrm{S}/N_{\mathrm{rms}} < 1$. During the fit, we held the center and fixed the ellipticities and the position angles of isophotes to

[1] We designate these wavelengths MIR to distinguish them from the K band.

Table 5.1. Photometric parameters of the sample

λ (μm)	$r_{e,min}$ ($''$)	$r_{e,avg}$ ($''$)	$r_{e,max}$ ($''$)	M_{min} (mag)	M_{avg} (mag)	M_{max} (mag)
0.55	2.1	20.1	81.1	−23.4	−21.4	−19.4
2.2	2.3	14.8	104.0	−26.7	−24.5	−22.6
3.6	2.0	14.3	65.3	−25.8	−23.6	−21.8
4.5	2.2	14.7	80.5	−25.1	−23.0	−21.2
5.8	1.2	15.2	90.0	−25.1	−22.7	−21.0
8.0	1.1	13.6	86.8	−24.2	−22.3	−20.5

Note. — Effective radii and absolute magnitudes from Pahre 1999 (V and K bands) and our *Spitzer* IRAC analysis (3.6–8.0 μm) are presented in minimum, average, and maximum values.

those at the effective radius in the 3.6 μm band. In addition, 3 σ clipping was applied to reject outliers such as foreground stars. To subtract the background, we used the values determined from SExtractor (Bertin & Arnouts, 1996). The adaptive background mesh sizes were varied between 16 and 96 pixels, and the best mesh was chosen to be the one which flattened the growth curve at the largest isophote ($a \sim 3$–$6\, a_e$).

After the ELLIPSE photometry, we used the de Vaucouleurs $r^{1/4}$ law to fit the observed surface brightness profiles measured along the semi-major axis[2]. The fitting procedure yields the effective radius (in arcseconds) $r_e = \sqrt{(b/a)_e}\, a_e$ where a_e is the effective semi major axis and $(b/a)_e$ is the axis ratio of the isophote at this position. We tested the reliability of our fitting procedure using the simulated, PSF-convolved galaxies, and found that the

[2]We also tried the Sersic $r^{1/n}$ law but found no difference in the FP coefficients; we therefore kept the $r^{1/4}$ methodology.

surface brightness fitting gives unbiased, reliable results when $r_e > 2''$. At the same time, we get the mean surface brightness within r_e (in AB magnitudes) $\langle\mu\rangle_e = m_{1/2} + 2.5\log(\pi r_e^2) - 10\log(1+z) - A_\lambda - K(z)$ where $m_{1/2}$ is the magnitude of the total flux within the effective isophote defined by a_e and b_e, while cosmological dimming, Galactic extinction (A_λ, using the formula of Laureijs et al. 1994, and the extinction curve of Fitzpatrick & Massa 2007), and K-correction are taken into account. The K-correction is computed using the spectral energy distribution of a 13 Gyr age, solar metallicity, and 0.1 Gyr burst model from Bruzual & Charlot (2003), assuming the Salpeter initial mass function. The last observable, σ_0, is a kinematic parameter and is not expected to vary as a function of wavelength; we consequently use the same data used for the visible and NIR bands (Pahre, 1999).

In our analysis, angular sizes were converted into physical length units for the FP construction by setting the distance to A1656 as 98.1 Mpc and calibrating the distances to individual clusters, utilizing the NIR FP (Pahre et al., 1998a) as a distance ladder.

5.3.2 Fitting of FP Coefficients

We fitted the FP coefficients of the multi-waveband sample in the following manner using a variety of methods:

$$\log r_e = a\log\sigma_0 + b\log\langle I\rangle_e + c, \tag{5.1}$$

where $\langle\mu\rangle_e$ and $\langle I\rangle_e$ are related as $\langle\mu\rangle_e \propto -2.5\log\langle I\rangle_e$. For the input r_e and $\langle I\rangle_e$, we use our SB-fit results for MIR (Section 5.3.1), and those listed in Pahre (1999) for V and K bands. We tried five different fitting methods: standard least-squares fit, the inverse least-squares fit, the bisector of the two, the least-squares fit to the orthogonal plane, and the least absolute deviation fit to the orthogonal plane. These methods are outlined below.

It is natural to think of doing the standard least-squares fit of log r_e (hereafter LSQ; Guzmán et al. 1993; Bernardi et al. 2003), but early FP work mainly took log σ_0 at the ordinate (Dressler et al. 1987; Djorgovski & Davis 1987; hereafter inverse LSQ) for their purposes. More recent work prefers the least-squares fitting of log r_e by minimizing the variance orthogonal to the FP plane (hereafter orthogonal least-squares fit, or OLSQ; Bernardi et al. 2003) or the least absolute deviations orthogonal to the plane (hereafter orthogonal least absolute deviation fit, or OLAD; Jørgensen et al. 1996; Pahre et al. 1998a). The orthogonal fitting has an advantage over other methods, reducing the systematic error by treating the variables symmetrically (Isobe et al., 1990). However, the orthogonal methods yield larger measurement errors than the LSQ methods, especially for small samples (Isobe et al., 1990).

Therefore, we also estimated the FP coefficients by taking the bisector, or the plane equidistant from the planes obtained through the standard LSQ and inverse LSQ (hereafter the LSQ bisector). We performed 1000 Monte Carlo samplings of subsets of early-type galaxies from Bernardi et al. (2003) to derive the FP coefficient errors on a sample of 50 early types to justify our approach. Through the sampling, we found the errors of the FP coefficients to be $(\sigma_a, \sigma_b) = (0.14, 0.06)$, best reproduced with the LSQ bisector method, while the other orthogonal methods gave overestimated errors ($\gtrsim$50% for the coefficient a). Aside from the error estimates, all three symmetrized methods reproduce the FP coefficient a of Bernardi et al. (2003) and the K band early-type galaxy sample of Pahre et al. (1998a) within 5% agreement. On the other hand, the standard and inverse LSQ methods are found to have about minus and plus 20% systematic biases in the coefficient a estimates respectively in comparison to the symmetrized methods. Given these results, we adopted the FP coefficients with the LSQ bisector method as our base result.

Table 5.2. Constructed Fundamental Planes at visible through MIR

$\lambda(\mu\mathrm{m})$ (1)	a (2)	b (3)	c (4)	r (5)
0.55	1.23 ± 0.10	-0.86 ± 0.04	-9.16 ± 0.40	0.96
2.2	1.42 ± 0.11	-0.81 ± 0.05	-8.20 ± 0.41	0.95
3.6	1.55 ± 0.11	-0.89 ± 0.04	-9.89 ± 0.39	0.96
4.5	1.47 ± 0.11	-0.92 ± 0.04	-10.16 ± 0.41	0.96
5.8	1.57 ± 0.13	-0.92 ± 0.05	-10.55 ± 0.50	0.95
8.0	1.55 ± 0.14	-0.75 ± 0.05	-9.30 ± 0.60	0.93

Note. — Fundamental planes for the sample of 56 galaxies with the $r_e > 2''$ cut using the LSQ bisector method. Col. (1): wavelength in μm. Cols. (2)–(4): Plane coefficients a, b, and c with associated uncertainties. Col. (5): Linear correlation coefficient.

5.4 Results

In Table 5.2, we list the FP coefficients with errors from 1000 bootstrap resamplings (unless obtained directly from known error estimates, e.g., LSQ methods) derived from the LSQ bisector method, for wavelengths of 0.55–8.0 μm. We further plot the result of the FP fit in Figure 5.1, overlayed on the data points. We caution readers to focus less on the absolute values of (a, b) and more on the trend of the values with wavelengths or methods (see discussion at the end of this section and Section 5.2). Gathering the outcomes, we are led to the wavelength-dependent nature of the FP coefficients, with (a, b) values getting close to the virial expectation of $(2, -1)$ as the wavelength increases. Such a tendency has been noted before (Pahre et al. 1998b; Scodeggio et al. 1998), but our result indicates that it extends to 3.6 μm, and possibly beyond. When each cluster was analyzed separately, we also find the trend.

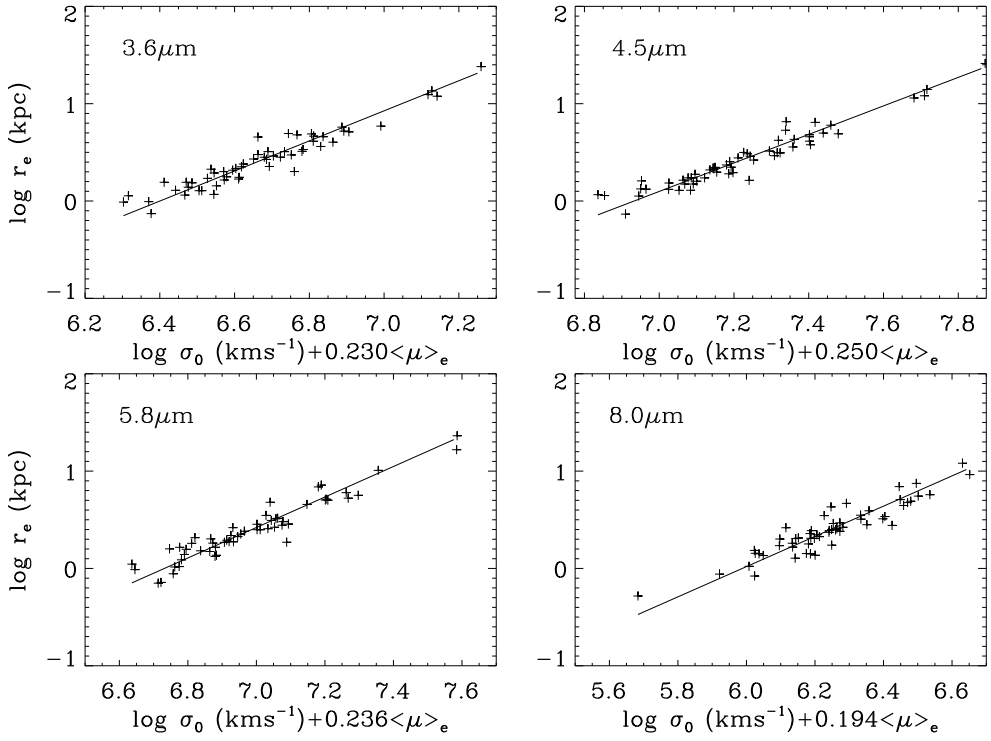

Figure 5.1: Constructed fundamental planes projected in the direction of smallest scatter at 3.6, 4.5, 5.8, and 8.0 μm, respectively.

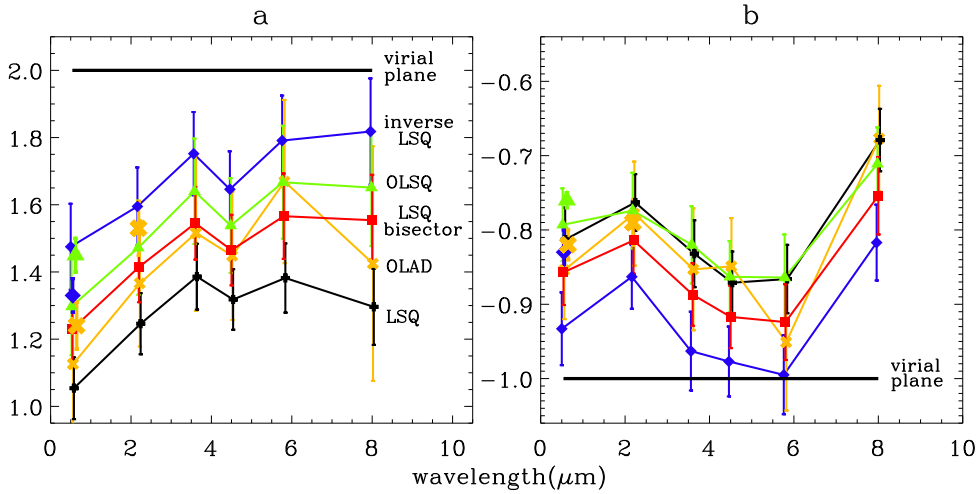

Figure 5.2: Wavelength dependence of coefficients a and b; diamond, triangle, square, cross, and plus sign symbols correspond to methodologies of inverse LSQ, OLSQ, LSQ bisector, OLAD, and ordinary LSQ respectively. Connected lines with spacing for identification are from our catalog, while solitary symbols are from other literature (Dressler et al. 1987; Jørgensen et al. 1996; Pahre et al. 1998a; Bernardi et al. 2003) of nearby samples with N $\gtrsim$ 100. Virial plane values assuming constant M/L are (a, b)=$(2, -1)$.

The wavelength dependence of the FP coefficients is further presented in Figure 5.2, where they are plotted using five different fitting methods (Section 5.3.2). The tilt of the FP is maximally reduced toward the virial expectation at IRAC-bands, and the thickness of the FP is maintained thin for all but beyond 5.8 μm. In terms of the methodology, we confirm the analysis of Section 5.3.2– the three symmetrized fittings give coefficient a values that are fairly consistent with each other (considering the sample size).

To quantify the wavelength dependence, we model the change of coefficient a as a linear function of wavelength by simultaneously fitting the OLSQ, OLAD, and the LSQ bisector results as follows:

$$da/d\lambda = 0.11 \pm 0.04\,\mu m^{-1}, \tag{5.2}$$

from the visible to 3.6 μm (coefficient a behavior is flat afterward). This relation nicely explains the difference in coefficient a of 0.05 in the SDSS g*- to z*-bands (Bernardi et al., 2003). Meanwhile, for b, the tendency is not as linear as that for a, but has a local maximum near the K band, approaches closest to -1 at the IRAC 3.6–5.8 μm bands, and increases again at 8.0 μm. We attribute this behavior at 8.0 μm to the lower S/N, as well as the complexity in the 8.0 μm emission which can be dominated by the dust emission in some cases (Bressan et al. 2006; Ko & Im 2007). Indeed, the 8.0 μm FP has the largest scatter among IRAC bands. The above result, together with the tendency of coefficient b from Table 5.2, implies that the increases in coefficients a and b are $(\Delta a, \Delta b) \simeq (0.34, \text{-}0.03)$ from V-band to 3.6 μm, and $(\Delta a, \Delta b) \simeq (0.15, \text{-}0.08)$ from K band to 3.6 μm. If we use the FP coefficients from the references in Figure 5.2 as the base values on which to apply equation (5.2), we obtain $(a, b) \simeq (1.6\text{–}1.8, -0.9)$ at 3.6 μm, which is quite close to the virial expectation. The implication of this result is discussed in the next section.

Note that our coefficient a in K band, derived from a subsample of 56 early

types from Pahre et al. (1998a) is smaller than the value derived from their full sample of 251 early types by $\Delta a = -0.11$. The discrepancy should be mostly due to the limited sample size. More than half of our MIR galaxies belong to the Coma Cluster (29 objects), and the Coma Cluster galaxies in Pahre et al. (1998a) show coefficient a in the K band ($a = 1.33$) smaller than the total sample result by $\Delta a = -0.20$, consistent with the results of Mobasher et al. (1999). Apart from the wavelength dependence, our results seem to be skewed toward the FP of the Coma Cluster.

5.5 Implications on the origin of the FP tilt

Recent studies suggest that the FP tilt originates mostly from a systematic variation in the mass-to-light ratio (Cappellari et al. 2006; Bolton et al. 2007). However, the cause for the mass-to-light ratio variation is uncertain: it could be due to the stellar population, or the central dark matter fraction (Bolton et al., 2007). Also, some studies suggest that the tilt is mostly explained by the non-homology related to the variation in the Sersic index n among early-type galaxies (Trujillo et al., 2004). Here, we discuss the implication of our result on these issues.

First, we investigated which one of the parameters–size or luminosity–dominates the observed change in the FP coefficients with increasing wavelength. This was done by deriving the FP coefficients from the MIR sample by replacing (1) r_e value or (2) $\langle I \rangle_e$ values with those from the shorter wavelength data (in our case the K band). The result is presented in Figure 5.3 ($left$), showing that the luminosity effect is the dominant factor up to 5.8 μm. Interpretation at 8.0 μm is difficult due to low S/N and dust emission. Our result suggests that the stellar population effect is significant going from K band to IRAC bands.

Next, we examined to what extent the stellar population plays a role in

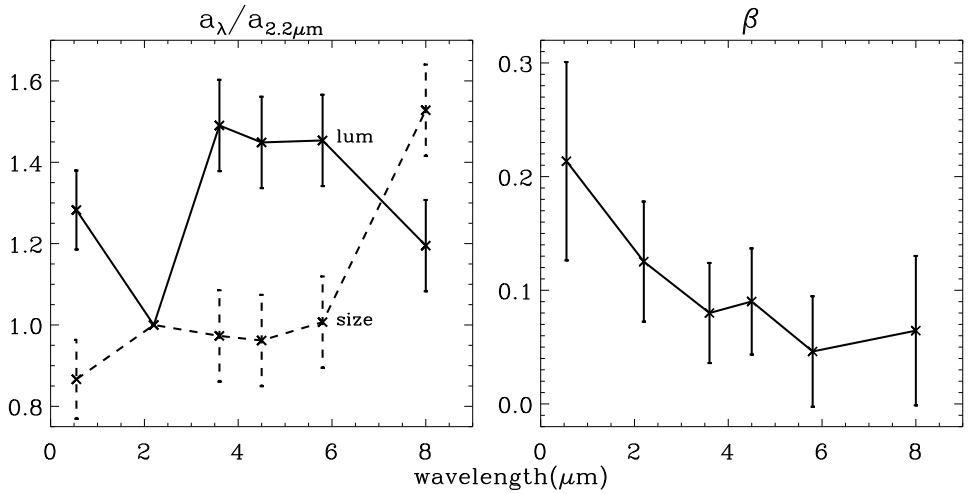

Figure 5.3: *Left*: Size vs luminosity test on the FP coefficient a. The solid line (labeled "lum") is for the set of coefficients computed by exchanging the $\langle I \rangle_e$ data of each wavelength with that from the K band, while the dashed line (labeled "size") is the similar result by exchanging the r_e data. *Right*: The wavelength dependence of $M_{\rm dyn}/L$ on L as represented by the parameter β of $M_{\rm dyn}/L \propto L^\beta$ (see Section 5.4).

the FP tilt through the dynamical mass-to-light ratio $M_{\rm dyn}/L \propto r_e\sigma_0^2/L \propto \sigma_0^2/(r_e\langle I \rangle_e)$ (e.g., Bernardi et al. 2003) variation calculated from the FP coefficients. If $M_{\rm dyn}/L \propto L^\beta$, then $r_e \propto \sigma_0^{2/(1+2\beta)}\,\langle I \rangle_e^{-(1+\beta)/(1+2\beta)}$. The study of Trujillo et al. (2004) suggests $\beta \simeq 0.27$ based on the visible FP. Our result is that the FP coefficient reaches $a \simeq 1.6$–1.8 at $3.6\,\mu$m (Section 5.3.2). In such a case, this relation gives $\beta \simeq 0.06$–0.13, which enables us to explain more than half of the tilt in the visible FP. Moreover, the reduced tilt in the mass plane ($a_{MP} - a_{FP} = 0.27$: Bolton et al. 2007) is consistent with our $\Delta a = 0.30 \pm 0.11$ from the I-band to the $3.6\,\mu$m in equation (5.2), advocating that the $M_{\rm dyn}/L$ variation is reduced by the regular light distributions in the MIR. As for the origin of the FP tilt, these results add another piece of evidence against the significance of non-homology (Padmanabhan et al. 2004; Cappellari et al. 2006; Bolton et al. 2007), which predicts no change in the tilt with wavelength.

We also derived the β parameter by directly fitting the $M_{\rm dyn}/L$ ratio. Fig-

ure 5.3 (right) demonstrates that the observed dependence of $M_{\rm dyn}/L$ on L decreases and becomes flatter at IRAC bands, just like the changes in β derived from the FP coefficients. Combined with the fact that the change in the FP tilt with wavelength is dominated by the luminosity change, our $M_{\rm dyn}/L$-fit result suggests that the rest-frame MIR luminosities at 3.6–5.8 μm better represent the stellar mass than the shorter wavelengths, somewhat in agreement with Temi et al. (2008), but not so with Lacey et al. (2008). Among many possibilities, a proper combination of the metallicity and the age variation can possibly reproduce the observed trend, and we plan to investigate as future work, the physical origin of the $M_{\rm dyn}/L$ - L relation as a function of wavelength.

5.6 Summary

We studied the MIR fundamental plane relation of 56 early-type galaxies and derived the wavelength dependence of the FP coefficients. When the FP is expressed as $r_e \propto \sigma_0^a \langle I \rangle_e^b$, we found that the exponent on σ_0, a, increases as a function of wavelength as $da/d\lambda = 0.11 \pm 0.04\,\mu m^{-1}$, while b reaches closest to -1 without systematic variation with wavelength. When the FP coefficients of previous studies are adopted as the starting point to calculate the MIR FP coefficients, we found that $(a, b) \simeq (1.6\text{–}1.8, -0.9)$ which is closer to the virial expectation, and that the change is dominated by the luminosity change. Together with the reduced dependence of the $M_{\rm dyn}/L$ ratio on L at MIR wavelengths, our outcomes suggest that the variation in the stellar population is responsible for a significant portion of the FP tilt, and that the rest-frame MIR better probes the stellar mass of low redshift early-type galaxies than the shorter wavelengths.

Chapter 6

Summary

In this thesis, we studied the observable fundamental properties of massive BHs in their active phase, and their quiescent host galaxies. The main objectives of our study were to better constrain and understand the massive limit of $M_{\rm BH}$ up to the distant universe, connect the physical properties of a large sample of luminous dust-poor quasars to a geometric or evolutionary explanation, and to investigate the change of tilt in the fundamental plane relation of early-type galaxies from the optical to mid-infrared wavelengths. In this section, we summarize our findings as follows.

In Chapter 2, we measured the $M_{\rm BH}$ of the most massive active galactic nuclei (AGNs). In order to double check whether the most massive AGNs are likely to reach $10^{10} M_{\odot}$, we observed 27 SDSS quasars at $0.7 < z < 2.5$ from IRTF rest-optical spectroscopy. We find that the Hα AGN mass estimations yield $10^{10} M_{\odot}$ consistent with the Mg II masses but with a large scatter between the C IV masses, in accord with previous work (e.g., Shen & Liu 2012). The $> 10^{10} M_{\odot}$ BHs however, are partially shown as disk emitters from their Hα spectra, which places caution to $M_{\rm BH}$ of AGNs beyond $10^{10} M_{\odot}$. We also checked for biases in the mass estimation recipes to calculate the possible amount of overestimation in single epoch $M_{\rm BH}$, which may reduce the upper

envelope of $M_{\rm BH}$'s excluding the disk emitters down to $10^{9.8-10.0} M_{\odot}$. Therefore, we suggest that the most massive quasars in the intermediate redshift universe are likely to reach $10^{10} M_{\odot}$ unless they have additional features on the spectra, or are extreme outliers in the mass estimating recipes. It hints that the most massive BHs are fully grown at at $z = 1$–2, as they match the $M_{\rm BH}$ of the most massive local BHs (e.g., McConnell et al. 2011).

In Chapter 3, we presented the rest-frame optical spectral properties of luminous and distant AGNs from *AKARI* observations. We collected the redshifted Hα line luminosity, rest-frame UV–optical continuum luminosity and line widths of 155 quasars at $3 \lesssim z \lesssim 6$, to estimate the $M_{\rm BH}$ of 43 objects. Not only the L_{5100}–$L_{\rm H\alpha}$ relation holds up to the most luminous quasars ($L_{5100} \sim 10^{47}\,{\rm ergs\,s^{-1}}$) with a single slope unchanging up to $z \sim 6$, similar behavior are found in the relations between rest-optical and UV continuum luminosities or FWHMs. This, together with predictions of an extended optical R–L relation to the highest luminosities, enables calibration of $M_{\rm BH}$ estimators to be generally applied for AGNs, including our distant, luminous quasars. Despite the overall agreement of rest-optical and UV $M_{\rm BH}$, the scatter are not negligible especially for the C IV estimation, consistent with previous studies at intermediate redshifts (Netzer et al. 2007; Shen & Liu 2012). We suggest that Balmer, or Mg II line based BH masses to be more reliable in studying the mass evolution of distant AGNs. Using these masses, the massive end envelope of $M_{\rm BH}$ up to the current data steeply increases with time at $z > 5$. This supports that the most massive and distant AGNs are in a rapidly growing state from given seed masses, but since the current number of massive AGNs is limited at high redshift we expect clearer constraints on BH growth from future discoveries and compilation of $M_{\rm BH}$'s.

In Chapter 4, we studied the evolution of the AGN hot–warm dusty structure through spectral energy distribution fitting and identification of luminous dust-poor quasars from the large SDSS data set. To follow-up the search for

dust-poor quasars initially found only at $z > 6$ (Jiang et al., 2010), we fit the rest-frame UV-to-IR spectral energy distribution (SED) of 41,000 optically selected type 1 quasars at $z = 0$–5 with $L_{\rm bol} > 10^{45.7}\,{\rm ergs\,s^{-1}}$, to find 0.6% of the sample to be hot dust-poor, with rest-frame 2.3 μm-to-0.51 μm flux density ratios of -0.5 dex or less. The less obscured, dust-poor SEDs were indeed blue in the UV–optical, while their mid-IR emission were weak, suggesting that the hot dust emission traces that of warm dust down to the dust-poor regime. At a given bolometric luminosity, we found that dust-poor quasars are lower in black hole mass, higher in Eddington ratio, and higher in redshift than general luminous quasars, suggesting that they are in a rapidly growing evolutionary state in which the dust-poor phase appears as a short or rare phenomenon. The redshift evolutionary trend at $z > 5$ was further extended by Leipski et al. (2014) to show a good agreement with our expectation of higher fraction of luminous dust-poor quasars at high redshift. Thus, we suggest that the dusty structures in rapidly growing distant quasars may be under an enrichment stage, although we note that we cannot fully reject other scenarios such as a geometric origin to the dust-poor phenomenon.

In Chapter 5, we constructed the mid-infrared fundamental plane (FP) of local early-type galaxies. To investigate the stellar population effect to the tilt of the FP, we performed surface photometry of 56 local early-type galaxies from *Spitzer* MIR imaging, and derived the wavelength dependence of the FP coefficients. We found that the FP coefficients come closer to the virial expectation than shorter wavelengths, and that the wavelength trend is dominated by the luminosity change. Together with the reduced dependence of the $M_{\rm dyn}/L$ ratio on L at MIR wavelengths, our results suggest that the variation in the stellar population is responsible for a significant portion of the FP tilt, such that the rest-frame MIR better probes the dynamical mass, and perhaps the stellar mass of early-type galaxies than the shorter wavelengths. Our study was somewhat supported by Hyde & Bernardi (2009), where they substituted

the luminosity with the stellar mass to find a reduced tilt to the optical FP, by Jeong et al. (2009) where the stellar population effect is mostly responsible for the UV FP tilt, and by Sani et al. (2011), where our MIR relation holds to a wider dynamic range. However, our results were criticized by numerous studies that the sample size was too small, and we expect future work with larger surveys to better disentangle the scenarios of the origin of FP tilt, including the structural non-homology or varying dark matter fraction with mass.

Overall, we make a concluding remark as follows. Through the study of the rest-frame optical spectra of high redshift AGNs, we find that the governing physics in AGNs appear to be similar between $z = 0$ through $z = 6$, and provide further support for the existence of $M_{\rm BH} \sim 10^{10} M_{\odot}$ AGNs at $z = 1$ through $z = 5$. These EMBHs appear at $z = 5$ with a vigorous growth happening at $z = 6$ possibly involving a dust-poor phase. EMBHs finally settles in at quiescent, massive galaxies today. The host galaxies possess the infrared fundamental plane relation slightly off from a simple virial expectation suggesting dark matter content is less prominent than galaxies hosting less massive BHs, or the most massive galaxies belong to a structurally non-homologous group of ellipticals.

Bibliography

Ahn, C. P., Alexandroff, R., Allende Prieto, C., et al. 2012, ApJS, 203, 21

Ahn, C. P., Alexandroff, R., Allende Prieto, C., et al. 2014, ApJS, 211, 17

Akritas, M. G., & Bershady, M. A. 1996, ApJ, 470, 706

Antonucci, R. 1993, ARA&A, 31, 473

Assef, R. J., Denney, K. D., Kochanek, C. S., et al. 2011, ApJ, 742, 93

Bañados, E., Venemans, B. P., Morganson, E., et al. 2014, arXiv:1405.3986

Barvainis, R. 1987, ApJ, 320, 537

Baskin, A., & Laor, A. 2005, MNRAS, 356, 1029

Begelman, M. C., Volonteri, M., & Rees, M. J. 2006, MNRAS, 370, 289

Bell, E. F., & de Jong, R. S. 2001, ApJ, 550, 212

Bellovary, J., Volonteri, M., Governato, F., et al. 2011, ApJ, 742, L13

Bennert, V. N., Treu, T., Woo, J.-H., et al. 2010, ApJ, 708, 1507

Bentz, M. C., Denney, K. D., Grier, C. J., et al. 2013, ApJ, 767, 149

Bentz, M. C., Peterson, B. M., Pogge, R. W., Vestergaard, M., & Onken, C. A. 2006, ApJ, 644, 133

Bernardi, M., et al. 2003, AJ, 125, 1866

Bertin, E., & Arnouts, S. 1996, A&AS, 117, 393

Blandford, R. D., & Payne, D. G. 1982, MNRAS, 199, 883

Bolton, A. S., Burles, S., Treu, T., Koopmans, L. V. E., & Moustakas, L. A. 2007, ApJ, 665, L105

Bonifacio, P., Monai, S., & Beers, T. C. 2000, AJ, 120, 2065

Bonning, E. W., Cheng, L., Shields, G. A., Salviander, S., & Gebhardt, K. 2007, ApJ, 659, 211

Boroson, T. A., & Green, R. F. 1992, ApJS, 80, 109

Bouwens, R. J., Illingworth, G. D., Franx, M., et al. 2009, ApJ, 705, 936

Bouwens, R. J., Illingworth, G. D., Oesch, P. A., et al. 2010, ApJ, 708, L69

Boyle, B. J., Shanks, T., Croom, S. M., et al. 2000, MNRAS, 317, 1014

Bressan, A., et al. 2006, ApJ, 639, L55

Briggs, F. H., Turnshek, D. A., & Wolfe, A. M. 1984, ApJ, 287, 549

Bromm, V., & Loeb, A., 2003, ApJ, 596, L34

Bruns, L. R., Wyithe, J. S. B., Bland-Hawthorn, J., & Dijkstra, M. 2012, MNRAS, 421, 2543

Bruzual, G., & Charlot, S. 2003, MNRAS, 344, 1000

Cappellari, M., et al. 2006, MNRAS, 366, 1126

Casali, M., Adamson, A., Alves de Oliveira, C., et al. 2007, A&A, 467, 777

Chelouche, D., Daniel, E., & Kaspi, S. 2012, ApJ, 750, L43

Chen, K., & Halpern, J. P. 1989, ApJ, 344, 115

Collin, S., Kawaguchi, T., Peterson, B. M., & Vestergaard, M. 2006, A&A, 456, 75

Cool, R. J., Kochanek, C. S., Eisenstein, D. J., et al. 2006, AJ, 132, 823

Cushing, M. C., Vacca, W. D., & Rayner, J. T. 2004, PASP, 116, 362

Davis, S. W., Woo, J.-H., & Blaes, O. M. 2007, ApJ, 668, 682

Denney, K. D., Peterson, B. M., Dietrich, M., Vestergaard, M., & Bentz, M. C. 2009, ApJ, 692, 246

Denney, K. D. 2012, ApJ, 759, 44

De Rosa, G., Decarli, R., Walter, F., et al. 2011, ApJ, 739, 56

De Rosa, G., Venemans, B. P., Decarli, R., et al. 2013, arXiv:1311.3260

Djorgovski, S., & Davis, M. 1987, ApJ, 313, 59

Dunlop, J. S., & Peacock, J. A. 1990, MNRAS, 247, 19

Diamond-Stanic, A. M., Fan, X., Brandt, W. N., et al. 2009, ApJ, 699, 782

Dietrich, M., Mathur, S., Grupe, D., & Komossa, S. 2009, ApJ, 696, 1998

D'Onofrio, M., Valentinuzzi, T., Secco, L., Caimmi, R., & Bindoni, D. 2006, New Astronomy Review, 50, 447

Dressler, A., Lynden-Bell, D., Burstein, D., Davies, R. L., Faber, S. M., Terlevich, R. J., & Wegner, G. 1987, ApJ, 313, 42

Elvis, M. 2000, ApJ, 545, 63

Elvis, M., Marengo, M., & Karovska, M. 2002, ApJ, 567, L107

Emsellem, E. 2013, MNRAS, 433, 1862

Eracleous, M., & Halpern, J. P. 1994, ApJS, 90, 1

Fan, X., Hennawi, J. F., Richards, G. T., et al. 2004, AJ, 128, 515

Fan, X., Narayanan, V. K., Lupton, R. H., et al. 2001, AJ, 122, 2833

Fan, X., Strauss, M. A., Gunn, J. E., et al. 1999, ApJ, 526, L57

Fan, X., Strauss, M. A., Becker, R. H., et al. 2006, AJ, 132, 117

Fan, X., Strauss, M. A., Richards, G. T., et al. 2006, AJ, 131, 1203

Fan, X., Strauss, M. A., Schneider, D. P., et al. 2003, AJ, 125, 1649

Fan, X., White, R. L., Davis, M., et al. 2000, AJ, 120, 1167

Fazio, G. G., et al. 2004, ApJS, 154, 10

Ferrarese, L., & Merritt, D. 2000, ApJ, 539, L9

Fitzpatrick, E. L., & Massa, D. 2007, ApJ, 663, 320

Gaskell, C. M., Klimek, E. S., & Nazarova, L. S. 2007, arXiv:0711.1025

Gebhardt, K., Bender, R., Bower, G., et al. 2000, ApJ, 539, L13

Gibson, R. R., Jiang, L., Brandt, W. N., et al. 2009, ApJ, 692, 758

Glikman, E., Helfand, D. J., & White, R. L. 2006, ApJ, 640, 579

Goto, T. 2006, MNRAS, 371, 769

Greene, J. E., & Ho, L. C. 2005, ApJ, 630, 122

Greene, J. E., Peng, C. Y., & Ludwig, R. R. 2010, ApJ, 709, 937

Guedes, J., Madau, P., Mayer, L., & Callegari, S. 2011, ApJ, 729, 125

Guzmán, R., Lucey, J. R., & Bower, R. G. 1993, MNRAS, 265, 731

Haas, M., Klaas, U., Müller, S. A. H., et al. 2003, A&A, 402, 87

Hambly, N. C., Collins, R. S., Cross, N. J. G., et al. 2008, MNRAS, 384, 637

Hao, H., Elvis, M., Civano, F., et al. 2010, ApJ, 724, L59

Hao, H., Elvis, M., Civano, F., & Lawrence, A. 2011, ApJ, 733, 108

Hao, H., Elvis, M., Bongiorno, A., et al. 2013, MNRAS, 434, 3104

Hao, L., Spoon, H. W. W., Sloan, G. C., et al. 2005, ApJ, 625, L75

Hewett, P. C., Foltz, C. B., & Chaffee, F. H. 1995, AJ, 109, 1498

Hewett, P. C., Warren, S. J., Leggett, S. K., & Hodgkin, S. T. 2006, MNRAS, 367, 454

Ho, L. C., Goldoni, P., Dong, X.-B., Greene, J. E., & Ponti, G. 2012, ApJ, 754, 11

Hodgkin, S. T., Irwin, M. J., Hewett, P. C., & Warren, S. J. 2009, MNRAS, 394, 675

Hopkins, P. F., Hernquist, L., Cox, T. J., & Kereš, D. 2008, ApJS, 175, 356

Hopkins, P. F., Hernquist, L., Martini, P., et al. 2005, ApJ, 625, L71

Hyde, J. B., & Bernardi, M. 2009, MNRAS, 396, 1171

Im, M., Lee, I., Cho, Y., et al. 2007, ApJ, 664, 64

Im, M. 2010, IAU Symposium, 267, 40

Isobe, T., Feigelson, E. D., Akritas, M. G., & Babu, G. J. 1990, ApJ, 364, 104

Jahnke, K., & Macciò, A. V. 2011, ApJ, 734, 92

Jang, M., Im, M., Lee, I., et al. 2011, ApJ, 741, L20

Jeong, H., Yi, S. K., Bureau, M., et al. 2009, MNRAS, 398, 2028

Jiang, L., Fan, X., Brandt, W. N., et al. 2010, Nature, 464, 380

Jiang, L., Fan, X., Hines, D. C., et al. 2006, AJ, 132, 2127

Jiang, L., Fan, X., Vestergaard, M., et al. 2007, AJ, 134, 1150

Jørgensen, I., Franx, M., & Kjærgaard, P. 1996, MNRAS, 280, 167

Jun, H. D., & Im, M. 2008, ApJ, 678, L97

Jun, H. D., Im, M., Lee, H. M., & AKARI QSONG Team 2012, Publication of Korean Astronomical Society, 27, 361

Jun, H. D., & Im, M. 2013, ApJ, 779, 104

Kaspi, S., Brandt, W. N., Maoz, D., et al. 2007, ApJ, 659, 997

Kaspi, S., Maoz, D., Netzer, H., et al. 2005, ApJ, 629, 61

Kaspi, S., Smith, P. S., Netzer, H., et al. 2000, ApJ, 533, 631

Kawaguchi, T., & Mori, M. 2011, ApJ, 737, 105

Kelly, B. C., Vestergaard, M., & Fan, X. 2009, ApJ, 692, 1388

Kennefick, J. D., Djorgovski, S. G., & de Carvalho, R. R. 1995, AJ, 110, 2553

Kishimoto, M., Antonucci, R., Blaes, O., et al. 2008, Nature, 454, 492

Ko, J., & Im, M. 2007, BAAS, 211, 9603

Kormendy, J., & Richstone, D. 1995, ARA&A, 33, 581

Krolik, J. H., & Begelman, M. C. 1988, ApJ, 329, 702

Kurk, J. D., Walter, F., Fan, X., et al. 2007, ApJ, 669, 32

Lacey, C. G., Baugh, C. M., Frenk, C. S., et al. 2008, MNRAS, 385, 1155

Laor, A., Bahcall, J. N., Jannuzi, B. T., et al. 1994, ApJ, 420, 110

Laureijs, R. J., Helou, G., & Clark, F. O. 1994, in ASP Conf. Proc. 58, The First Symp. on the Infrared Cirrus and Diffuse Interstellar Clouds, ed. R. M. Cutri & W. B. Latter (San Francisco: ASP), 133

Lawrence, A. 1991, MNRAS, 252, 586

Lawrence, A., & Elvis, M. 2010, ApJ, 714, 561

Lawrence, A., Warren, S. J., Almaini, O., et al. 2007, MNRAS, 379, 1599

Leipski, C., Meisenheimer, K., Walter, F., et al. 2014, ApJ, 785, 154

Lípari, S. L., & Terlevich, R. J. 2006, MNRAS, 368, 1001

Lodato, G. & Natarajan, P. 2006, MNRAS, 371, 1813

Lusso, E., Comastri, A., Vignali, C., et al. 2010, A&A, 512, A34

Ma, X.-C., & Wang, T.-G. 2013, MNRAS, 817

Madau, P., Haardt, F., & Dotti, M. 2014, ApJ, 784, L38

Maiolino, R., Gallerani, S., Neri, R., et al. 2012, MNRAS, 425, L66

Marconi, A., Risaliti, G., Gilli, R., et al. 2004, MNRAS, 351, 169

Martin, D. C., Fanson, J., Schiminovich, D., et al. 2005, ApJ, 619, L1

Martini, P. 2004, in Coevolution of Black Holes and Galaxies, ed. L. C. Ho (Cambridge: Cambridge Univ. Press), 169

Martini, P., Dicken, D., & Storchi-Bergmann, T. 2013, ApJ, 766, 121

Matsuoka, K., Silverman, J. D., Schramm, M., et al. 2013, ApJ, 771, 64

McConnell, N. J., & Ma, C.-P. 2013, ApJ, 764, 184

McConnell, N. J., Ma, C.-P., Gebhardt, K., et al. 2011, Nature, 480, 215

McGill, K. L., Woo, J.-H., Treu, T., & Malkan, M. A. 2008, ApJ, 673, 703

McGreer, I. D., Jiang, L., Fan, X., et al. 2013, ApJ, 768, 105

McLure, R. J., & Dunlop, J. S. 2004, MNRAS, 352, 1390

McLure, R. J., & Jarvis, M. J. 2002, MNRAS, 337, 109

Mobasher, B., Guzman, R., Aragon-Salamanca, A., & Zepf, S. 1999, MNRAS, 304, 225

Mor, R., & Netzer, H. 2012, MNRAS, 420, 526

Mor, R., & Trakhtenbrot, B. 2011, ApJ, 737, L36

Mortlock, D. J., Warren, S. J., Venemans, B. P., et al. 2011, Nature, 474, 616

Murakami, H., Baba, H., Barthel, P., et al. 2007, PASJ, 59, 369

Natarajan, P. 2014, General Relativity and Gravitation, 46, 1702

Netzer, H. 1990, in Active Galactic Nuclei, ed. T. J.-L. Courvoisier and M. Major (Berlin: Springer), 57

Netzer, H., Lira, P., Trakhtenbrot, B., Shemmer, O., & Cury, I. 2007, ApJ, 671, 1256

Ohyama, Y., Onaka, T., Matsuhara, H., et al. 2007, PASJ, 59, 411

Onaka, T., Matsuhara, H., Wada, T., et al. 2007, PASJ, 59, 401

Osterbrock, D. E. 1989, Astrophysics of Gaseous Nebulae and Active Galactic Nuclei (Research supported by the University of California, John Simon Guggenheim Memorial Foundation, University of Minnesota, et al.; Mill Valley, CA: University Science Books), 422

Oyabu, S., Wada, T., Ohyama, Y., et al. 2007, PASJ, 59, 497

Oyabu, S., Kawara, K., Tsuzuki, Y., et al. 2009, ApJ, 697, 452

Padmanabhan, N., et al. 2004, New Astronomy Review, 9, 329

Pahre, M. A. 1999, ApJS, 124, 127

Pahre, M. A., Djorgovski, S. G., & de Carvalho, R. R. 1998a, AJ, 116, 1591

Pahre, M. A., de Carvalho, R. R., & Djorgovski, S. G. 1998b, AJ, 116, 1606

Park, D., Woo, J.-H., Denney, K. D., & Shin, J. 2013, ApJ, 770, 87

Pâris, I., Petitjean, P., Aubourg, É., et al. 2012, A&A, 548, A66

Peng, C. Y., Impey, C. D., Rix, H.-W., et al. 2006, ApJ, 649, 616

Penston, M. V., & Fosbury, R. A. E. 1978, MNRAS, 183, 479

Péroux, C., Storrie-Lombardi, L. J., McMahon, R. G., Irwin, M., & Hook, I. M. 2001, AJ, 121, 1799

Peterson, B. M. 1993, PASP, 105, 247

Peterson, B. M., Ferrarese, L., Gilbert, K. M., et al. 2004, ApJ, 613, 682

Pipino, A., Fan, X. L., Matteucci, F., et al. 2011, A&A, 525, A61

Planck Collaboration, Ade, P. A. R., Aghanim, N., et al. 2013, arXiv:1303.5076

Rayner, J. T., Toomey, D. W., Onaka, P. M., et al. 2003, PASP, 115, 362

Richards, G. T., Fan, X., Newberg, H. J., et al. 2002, AJ, 123, 2945

Richards, G. T., Lacy, M., Storrie-Lombardi, L. J., et al. 2006a, ApJS, 166, 470

Richards, G. T., Strauss, M. A., Fan, X., et al. 2006b, AJ, 131, 2766

Richards, G. T., Kruczek, N. E., Gallagher, S. C., et al. 2011, AJ, 141, 167

Robertson, B., Cox, T. J., Hernquist, L., Franx, M., Hopkins, P. F., Martini, P., & Springel, V. 2006, ApJ, 641, 21

Sanders, D. B., Soifer, B. T., Elias, J. H., et al. 1988, ApJ, 325, 74

Sani, E., Marconi, A., Hunt, L. K., & Risaliti, G. 2011, MNRAS, 413, 1479

Schlegel, D. J., Finkbeiner, D. P., & Davis, M. 1998, ApJ, 500, 525

Schmidt, M., & Green, R. F. 1983, ApJ, 269, 352

Schmidt, M., Schneider, D. P., & Gunn, J. E. 1995, AJ, 110, 68

Schneider, D. P., Schmidt, M., & Gunn, J. E. 1989, AJ, 98, 1507

Schneider, D. P., Hall, P. B., Richards, G. T., et al. 2007, AJ, 134, 102

Schneider, D. P., Richards, G. T., Hall, P. B., et al. 2010, AJ, 139, 2360

Scodeggio, M., Gavazzi, G., Belsole, E., Pierini, D., & Boselli, A. 1998, MNRAS, 301, 1001

Sedgwick, C., Serjeant, S., Pearson, C., et al. 2013, MNRAS, 436, 395

Shang, Z., Wills, B. J., Wills, D., & Brotherton, M. S. 2007, AJ, 134, 294

Shemmer, O., Netzer, H., Maiolino, R., et al. 2004, ApJ, 614, 547

Shen, J., Vanden Berk, D. E., Schneider, D. P., & Hall, P. B. 2008, AJ, 135, 928

Shen, Y., Greene, J. E., Strauss, M. A., Richards, G. T., & Schneider, D. P. 2008, ApJ, 680, 169

Shen, Y., Richards, G. T., Strauss, M. A., et al. 2011, ApJS, 194, 45

Shen, Y., & Liu, X. 2012, ApJ, 753, 125

Simões Lopes, R. D., Storchi-Bergmann, T., de Fátima Saraiva, M., & Martini, P. 2007, ApJ, 655, 718

Skrutskie, M. F., Cutri, R. M., Stiening, R., et al. 2006, AJ, 131, 1163

Sluse, D., Schmidt, R., Courbin, F., et al. 2011, A&A, 528, A100

Soltan, A. 1982, MNRAS, 200, 115

Stern, D., Kirkpatrick, J. D., Allen, L. E., et al. 2007, ApJ, 663, 677

Storrie-Lombardi, L. J., McMahon, R. G., Irwin, M. J., & Hazard, C. 1996, ApJ, 468, 121

Storrie-Lombardi, L. J., Irwin, M. J., McMahon, R. G., & Hook, I. M. 2001, MNRAS, 322, 933

Sulentic, J. W., Bachev, R., Marziani, P., Negrete, C. A., & Dultzin, D. 2007, ApJ, 666, 757

Surace, J. A., Sanders, D. B., Vacca, W. D., Veilleux, S., & Mazzarella, J. M. 1998, ApJ, 492, 116

Temi, P., Brighenti, F., & Mathews, W. G. 2008, ApJ, 672, 244

Trakhtenbrot, B., Netzer, H., Lira, P., & Shemmer, O. 2011, ApJ, 730, 7

Treister, E., Schawinski, K., Urry, C. M., & Simmons, B. D. 2012, ApJ, 758, L39

Treu, T., Koopmans, L. V. E., Bolton, A. S., Burles, S., & Moustakas, L. A. 2006a, ApJ, 640, 662

Trujillo, I., Burkert, A., & Bell, E. F. 2004, ApJ, 600, L39

Tsuzuki, Y., Kawara, K., Yoshii, Y., et al. 2006, ApJ, 650, 57

Urrutia, T., Lacy, M., & Becker, R. H. 2008, ApJ, 674, 80

Urrutia, T., Lacy, M., Spoon, H., et al. 2012, ApJ, 757, 125

Urry, C., & Padovani, P. 1995, PASP, 107, 803

Vacca, W. D., Cushing, M. C., & Rayner, J. T. 2003, PASP, 115, 389

van den Bosch, R. C. E., Gebhardt, K., Gültekin, K., et al. 2012, Nature, 491, 729

van Dokkum, P. G. 2001, PASP, 113, 1420

Vanden Berk, D. E., Richards, G. T., Bauer, A., et al. 2001, AJ, 122, 549

Venemans, B. P., Findlay, J. R., Sutherland, W. J., et al. 2013, ApJ, 779, 24

Véron-Cetty, M.-P., & Véron, P. 2010, A&A, 518, A10

Vestergaard, M. 2004, ApJ, 601, 676

Vestergaard, M., & Peterson, B. M. 2006, ApJ, 641, 689

Vestergaard, M., & Wilkes, B. J. 2001, ApJS, 134, 1

Vestergaard, M., Fan, X., Tremonti, C. A., Osmer, P. S., & Richards, G. T. 2008, ApJ, 674, L1

Volonteri, M., Lodato, G., & Natarajan, P. 2008, MNRAS, 383, 1079

Volonteri, M., & Rees, M. J. 2005, ApJ, 633, 624

Volonteri, M., & Ciotti, L. 2013, ApJ, 768, 29

Wang, J.-G., Dong, X.-B., Wang, T.-G., et al. 2009, ApJ, 707, 1334

Warren, S. J., Hewett, P. C., & Osmer, P. S. 1994, ApJ, 421, 412

Whit3e, R. L., Becker, R. H., Helfand, D. J., & Gregg, M. D. 1997, ApJ, 475, 479

Willott, C. J., Delorme, P., Omont, A., et al. 2007, AJ, 134, 2435

Willott, C. J., Albert, L., Arzoumanian, D., et al. 2010, AJ, 140, 546

Willott, C. J., Delorme, P., Reylé, C., et al. 2010, AJ, 139, 906

Woo, J.-H., Treu, T., Malkan, M. A., & Blandford, R. D. 2008, ApJ, 681, 925

Woo, J.-H., Schulze, A., Park, D., et al. 2013, ApJ, 772, 49

Wright, E. L., Eisenhardt, P. R. M., Mainzer, A. K., et al. 2010, AJ, 140, 1868

Wu, X.-B., Jia, Z.-D., Chen, Z.-Y., et al. 2010, Research in Astronomy and Astrophysics, 10, 745

Wyithe, J. S. B., & Loeb, A. 2012, MNRAS, 425, 2892

York, D. G., Adelman, J., Anderson, J. E., Jr., et al. 2000, AJ, 120, 1579

Yu, Q., & Tremaine, S. 2002, MNRAS, 335, 965

Appendix

We present the spectra and the fit to the rest-frame Hα region of all 155 objects (including 5 with both NG/NP coverage) used in Chapter 3.

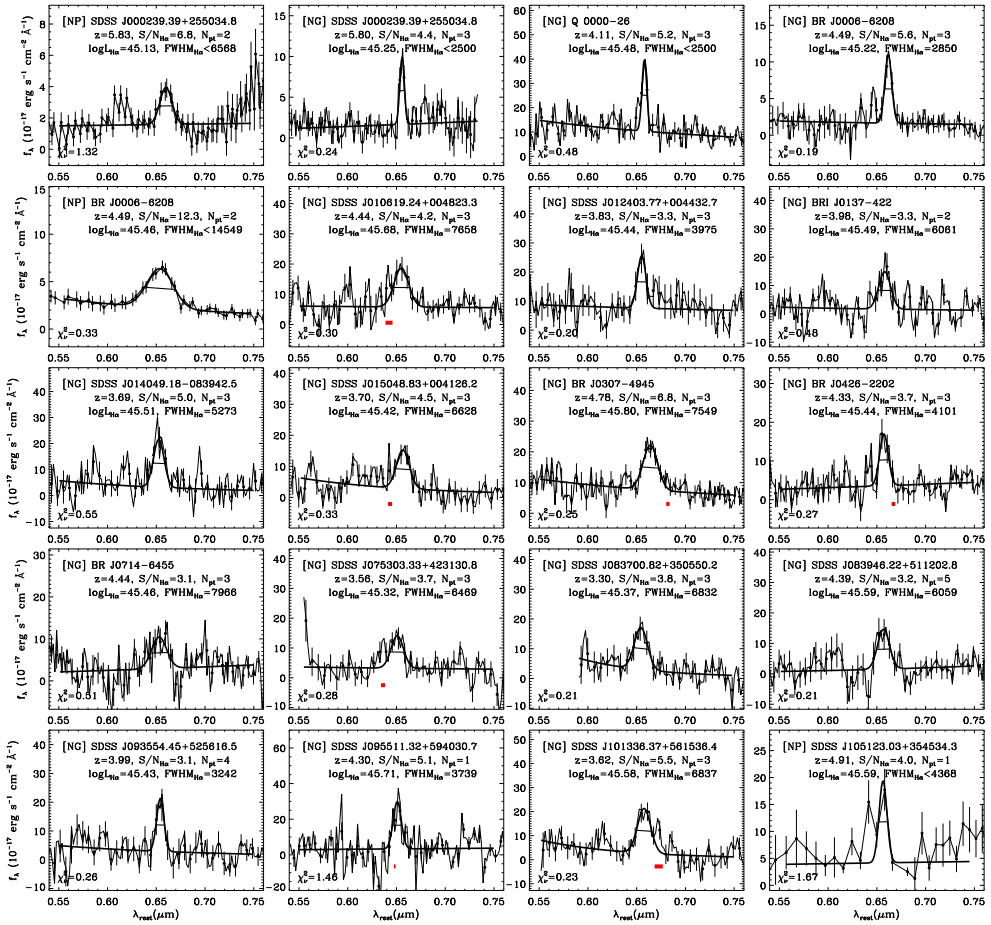

Figure 6.1: Rest-frame Hα spectral fitting of 45 objects with S/N$_{H\alpha} > 3$, sorted in ascending right ascension, used in the study of Chapter 3. The data point symbols and colors follow the meaning of Figure 3.4. When there were contaminations to the Hα emission, we masked out the region (red rectangle).

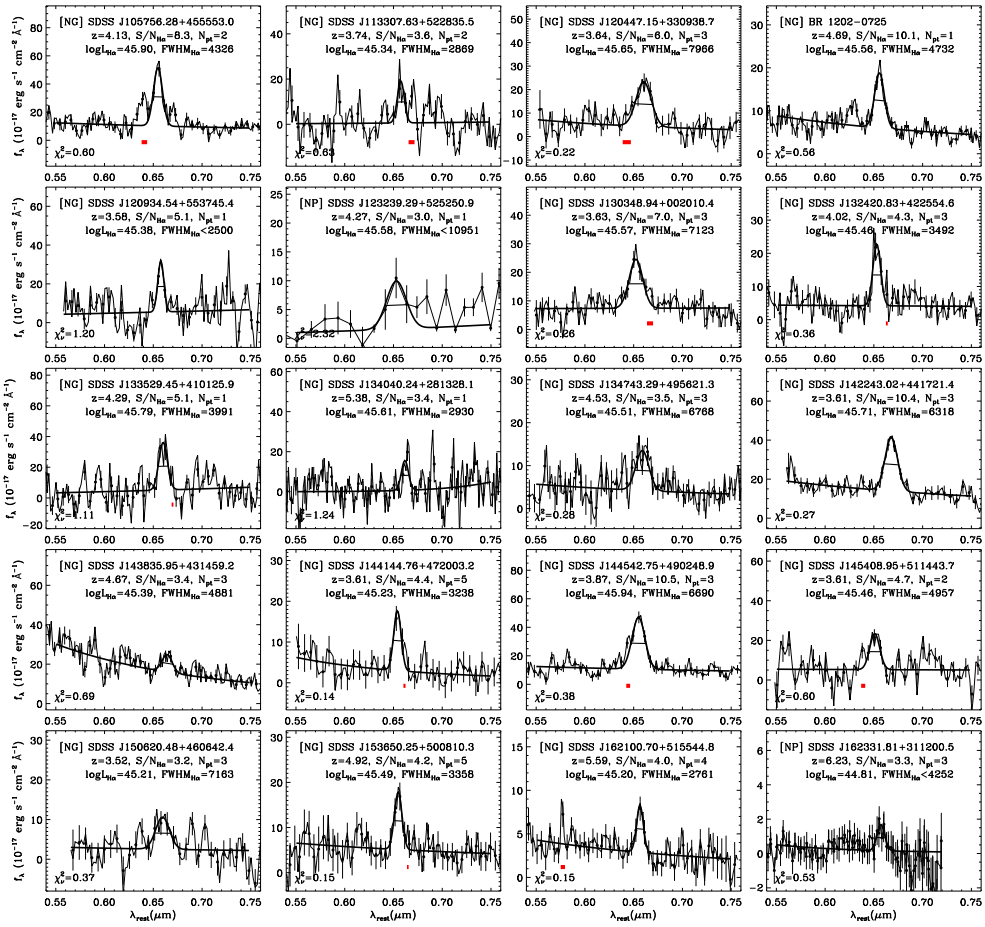
[NG] SDSS J105756.28+455553.0
z=4.13, S/N$_{Ha}$=8.3, N$_{pt}$=2
logL$_{Ha}$=45.90, FWHM$_{Ha}$=4326
[NG] SDSS J113307.63+522835.5
z=3.74, S/N$_{Ha}$=3.6, N$_{pt}$=2
logL$_{Ha}$=45.34, FWHM$_{Ha}$=2869
[NG] SDSS J120447.15+330938.7
z=3.64, S/N$_{Ha}$=6.0, N$_{pt}$=3
logL$_{Ha}$=45.65, FWHM$_{Ha}$=7966
[NG] BR 1202−0725
z=4.69, S/N$_{Ha}$=10.1, N$_{pt}$=1
logL$_{Ha}$=45.56, FWHM$_{Ha}$=4732
[NG] SDSS J120934.54+553745.4
z=3.58, S/N$_{Ha}$=5.1, N$_{pt}$=1
logL$_{Ha}$=45.38, FWHM$_{Ha}$<2500
[NP] SDSS J123239.29+525250.9
z=4.27, S/N$_{Ha}$=3.0, N$_{pt}$=1
logL$_{Ha}$=45.58, FWHM$_{Ha}$<10951
[NG] SDSS J130348.94+002010.4
z=3.63, S/N$_{Ha}$=7.0, N$_{pt}$=3
logL$_{Ha}$=45.57, FWHM$_{Ha}$=7123
[NG] SDSS J132420.83+422554.6
z=4.02, S/N$_{Ha}$=4.3, N$_{pt}$=3
logL$_{Ha}$=45.46, FWHM$_{Ha}$=3492
[NG] SDSS J133529.45+410125.9
z=4.29, S/N$_{Ha}$=5.1, N$_{pt}$=1
logL$_{Ha}$=45.79, FWHM$_{Ha}$=3991
[NG] SDSS J134040.24+281328.1
z=5.38, S/N$_{Ha}$=3.4, N$_{pt}$=1
logL$_{Ha}$=45.61, FWHM$_{Ha}$=2930
[NG] SDSS J134743.29+495621.3
z=4.53, S/N$_{Ha}$=3.5, N$_{pt}$=3
logL$_{Ha}$=45.51, FWHM$_{Ha}$=6768
[NG] SDSS J142243.02+441721.4
z=3.61, S/N$_{Ha}$=10.4, N$_{pt}$=3
logL$_{Ha}$=45.71, FWHM$_{Ha}$=6318
[NG] SDSS J143835.95+431459.2
z=4.67, S/N$_{Ha}$=3.4, N$_{pt}$=3
logL$_{Ha}$=45.39, FWHM$_{Ha}$=4881
[NG] SDSS J144144.76+472003.2
z=3.61, S/N$_{Ha}$=4.4, N$_{pt}$=5
logL$_{Ha}$=45.23, FWHM$_{Ha}$=3238
[NG] SDSS J144542.75+490248.9
z=3.87, S/N$_{Ha}$=10.5, N$_{pt}$=3
logL$_{Ha}$=45.94, FWHM$_{Ha}$=6690
[NG] SDSS J145408.95+511443.7
z=3.61, S/N$_{Ha}$=4.7, N$_{pt}$=2
logL$_{Ha}$=45.46, FWHM$_{Ha}$=4957
[NG] SDSS J150620.48+460642.4
z=3.52, S/N$_{Ha}$=3.2, N$_{pt}$=3
logL$_{Ha}$=45.21, FWHM$_{Ha}$=7163
[NG] SDSS J153650.25+500810.3
z=4.92, S/N$_{Ha}$=4.2, N$_{pt}$=5
logL$_{Ha}$=45.49, FWHM$_{Ha}$=3358
[NG] SDSS J162100.70+515544.8
z=5.59, S/N$_{Ha}$=4.0, N$_{pt}$=4
logL$_{Ha}$=45.20, FWHM$_{Ha}$=2761
[NP] SDSS J162331.81+311200.5
z=6.23, S/N$_{Ha}$=3.3, N$_{pt}$=3
logL$_{Ha}$=44.81, FWHM$_{Ha}$<4252
f$_\lambda$ (10^{-17} erg s^{-1} cm^{-2} Å^{-1})
λ$_{rest}$(μm)

Figure 6.1

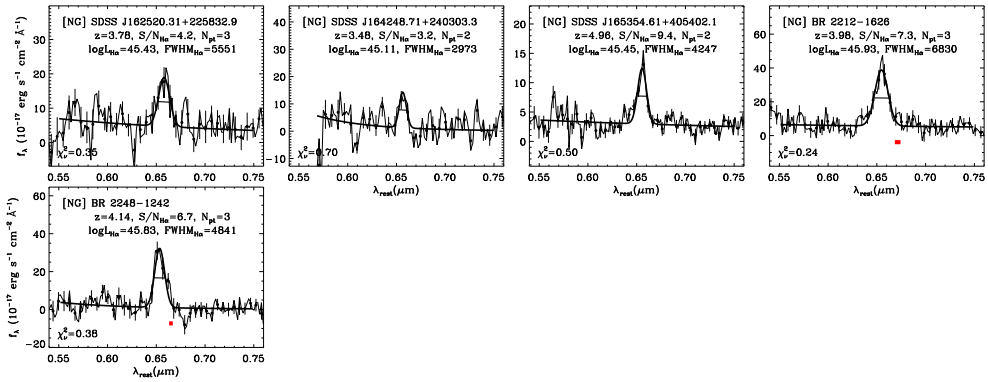
[NG] SDSS J162520.31+225832.9
z=3.78, S/N$_{Hα}$=4.2, N$_{pt}$=3
logL$_{Hα}$=45.43, FWHM$_{Hα}$=5551
[NG] SDSS J164248.71+240303.3
z=3.48, S/N$_{Hα}$=3.2, N$_{pt}$=2
logL$_{Hα}$=45.11, FWHM$_{Hα}$=2973
[NG] SDSS J165354.61+405402.1
z=4.96, S/N$_{Hα}$=9.4, N$_{pt}$=2
logL$_{Hα}$=45.45, FWHM$_{Hα}$=4247
[NG] BR 2212−1626
z=3.98, S/N$_{Hα}$=7.3, N$_{pt}$=3
logL$_{Hα}$=45.93, FWHM$_{Hα}$=6830
[NG] BR 2248−1242
z=4.14, S/N$_{Hα}$=6.7, N$_{pt}$=3
logL$_{Hα}$=45.83, FWHM$_{Hα}$=4841
f$_λ$ (10^{-17} erg s^{-1} cm^{-2} Å^{-1})
λ$_{rest}$(μm)

Figure 6.1

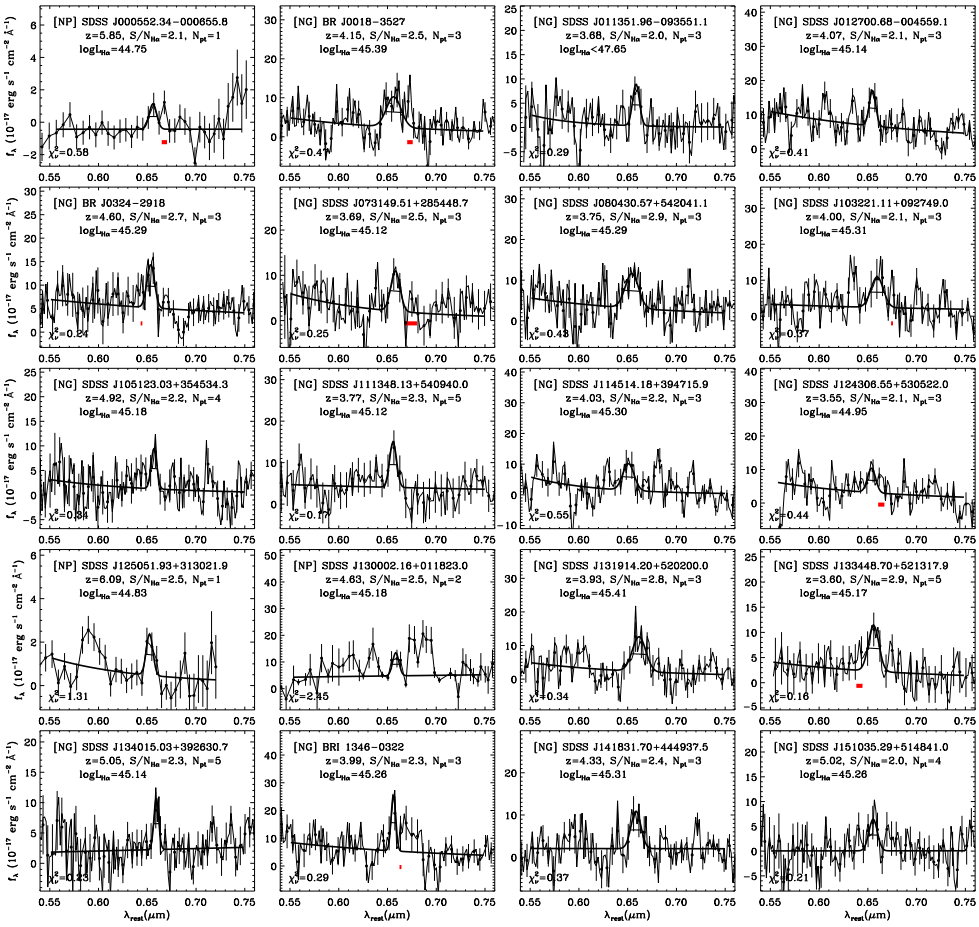

Figure 6.2: Continued from Figure 6.1, for 27 objects with $2 < \mathrm{S/N_{H\alpha}} < 3$.

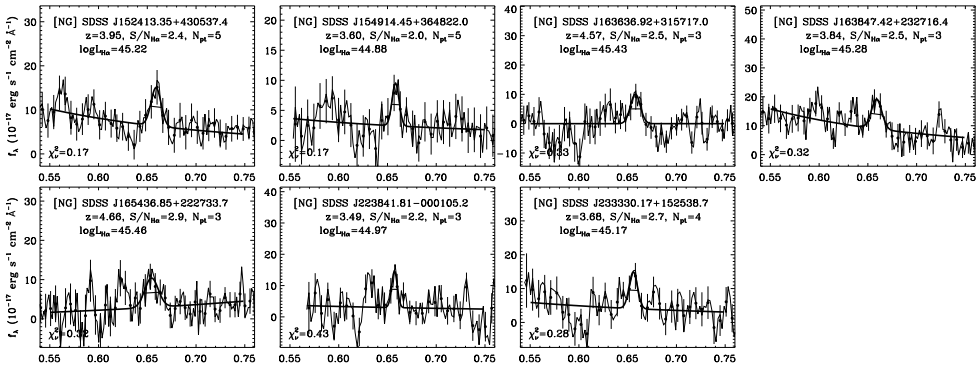
[NG] SDSS J152413.35+430537.4
z=3.95, S/N$_{Ha}$=2.4, N$_{pt}$=5
logL$_{Ha}$=45.22
χ^2_c=0.17
[NG] SDSS J154914.45+364822.0
z=3.60, S/N$_{Ha}$=2.0, N$_{pt}$=5
logL$_{Ha}$=44.88
χ^2_c=0.17
[NG] SDSS J163636.92+315717.0
z=4.57, S/N$_{Ha}$=2.5, N$_{pt}$=3
logL$_{Ha}$=45.43
χ^2_c=0.33
[NG] SDSS J163847.42+232716.4
z=3.84, S/N$_{Ha}$=2.5, N$_{pt}$=3
logL$_{Ha}$=45.28
χ^2_c=0.32
[NG] SDSS J165436.85+222733.7
z=4.66, S/N$_{Ha}$=2.9, N$_{pt}$=3
logL$_{Ha}$=45.46
χ^2_c=0.26
[NG] SDSS J223841.81−000105.2
z=3.49, S/N$_{Ha}$=2.2, N$_{pt}$=3
logL$_{Ha}$=44.97
χ^2_c=0.43
[NG] SDSS J233330.17+152538.7
z=3.68, S/N$_{Ha}$=2.7, N$_{pt}$=4
logL$_{Ha}$=45.17
χ^2_c=0.26
f$_\lambda$ (10^{-17} erg s^{-1} cm^{-2} Å^{-1})

Figure 6.2

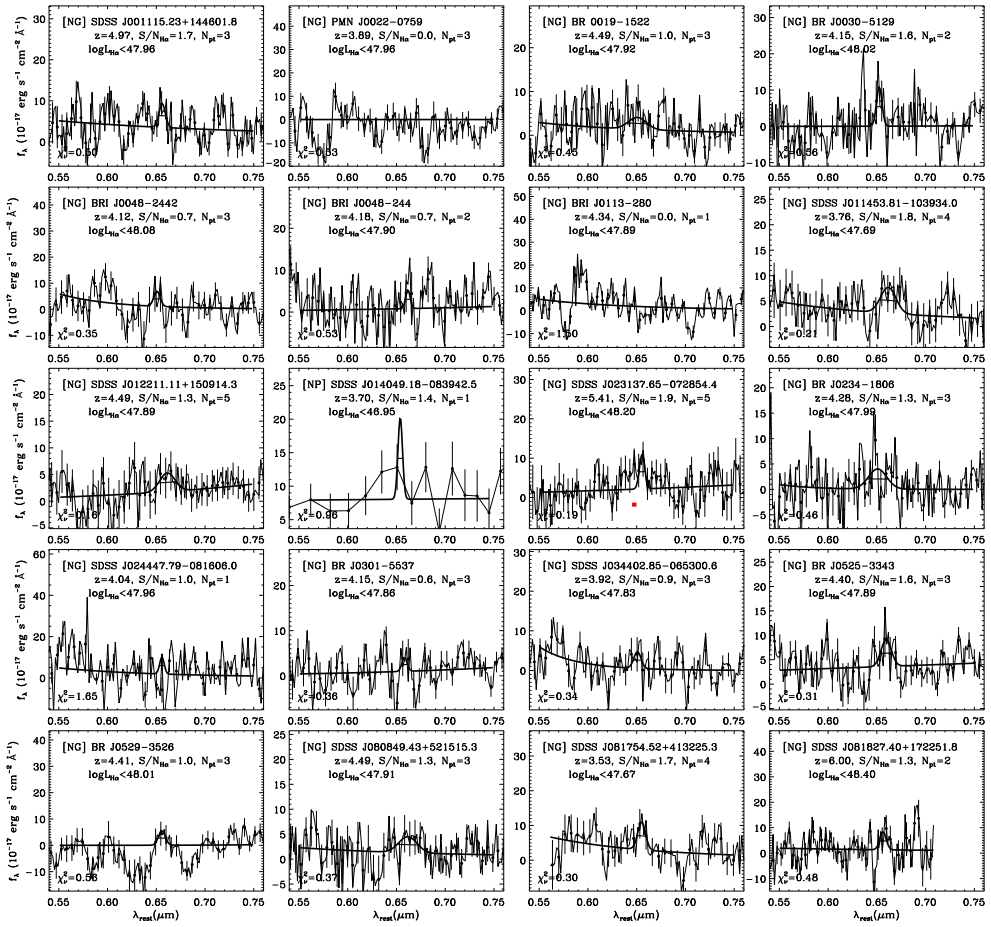

Figure 6.3: Continued from Figure 6.1, for 88 objects with $\mathrm{S/N_{H\alpha}} < 2$.

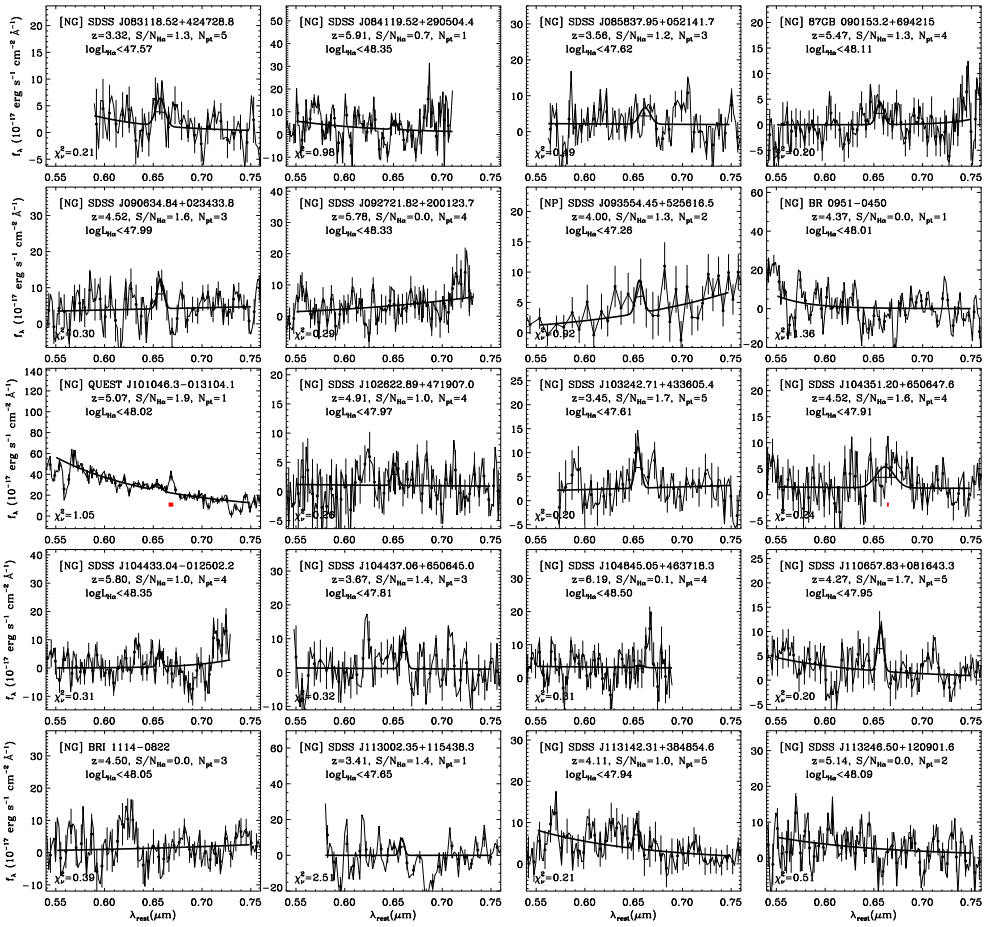
[NG] SDSS J083118.52+424728.8
z=3.32, S/N_Hα=1.3, N_pt=5
logL_Hα<47.57
χ²_ν=0.21
[NG] SDSS J084119.52+290504.4
z=5.91, S/N_Hα=0.7, N_pt=1
logL_Hα<48.35
χ²_ν=0.98
[NG] SDSS J085837.95+052141.7
z=3.56, S/N_Hα=1.2, N_pt=3
logL_Hα<47.62
χ²_ν=0.49
[NG] B7GB 090153.2+694215
z=5.47, S/N_Hα=1.3, N_pt=4
logL_Hα<48.11
χ²_ν=0.20
[NG] SDSS J090634.84+023433.8
z=4.52, S/N_Hα=1.6, N_pt=3
logL_Hα<47.99
χ²_ν=0.30
[NG] SDSS J092721.82+200123.7
z=5.78, S/N_Hα=0.0, N_pt=4
logL_Hα<48.33
χ²_ν=0.29
[NP] SDSS J093554.45+525616.5
z=4.00, S/N_Hα=1.3, N_pt=2
logL_Hα<47.26
χ²_ν=0.92
[NG] BR 0951−0450
z=4.37, S/N_Hα=0.0, N_pt=1
logL_Hα<48.01
χ²_ν=1.36
[NG] QUEST J101046.3−013104.1
z=5.07, S/N_Hα=1.9, N_pt=1
logL_Hα<48.02
χ²_ν=1.05
[NG] SDSS J102622.89+471907.0
z=4.91, S/N_Hα=1.0, N_pt=4
logL_Hα<47.97
χ²_ν=0.29
[NG] SDSS J103242.71+433605.4
z=3.45, S/N_Hα=1.7, N_pt=5
logL_Hα<47.61
χ²_ν=0.20
[NG] SDSS J104351.20+650647.6
z=4.52, S/N_Hα=1.6, N_pt=4
logL_Hα<47.91
χ²_ν=0.24
[NG] SDSS J104433.04−012502.2
z=5.80, S/N_Hα=1.0, N_pt=4
logL_Hα<48.35
χ²_ν=0.31
[NG] SDSS J104437.06+650645.0
z=3.67, S/N_Hα=1.4, N_pt=3
logL_Hα<47.81
χ²_ν=0.32
[NG] SDSS J104845.05+463718.3
z=6.19, S/N_Hα=0.1, N_pt=4
logL_Hα<48.50
χ²_ν=0.31
[NG] SDSS J110657.83+081643.3
z=4.27, S/N_Hα=1.7, N_pt=5
logL_Hα<47.95
χ²_ν=0.20
[NG] BRI 1114−0822
z=4.50, S/N_Hα=0.0, N_pt=3
logL_Hα<48.05
χ²_ν=0.39
[NG] SDSS J113002.35+115438.3
z=3.41, S/N_Hα=1.4, N_pt=1
logL_Hα<47.65
χ²_ν=2.51
[NG] SDSS J113142.31+384854.6
z=4.11, S/N_Hα=1.0, N_pt=5
logL_Hα<47.94
χ²_ν=0.21
[NG] SDSS J113246.50+120901.6
z=5.14, S/N_Hα=0.0, N_pt=2
logL_Hα<48.09
χ²_ν=0.51
f_λ (10⁻¹⁷ erg s⁻¹ cm⁻² Å⁻¹)
λ_rest(μm)

Figure 6.3

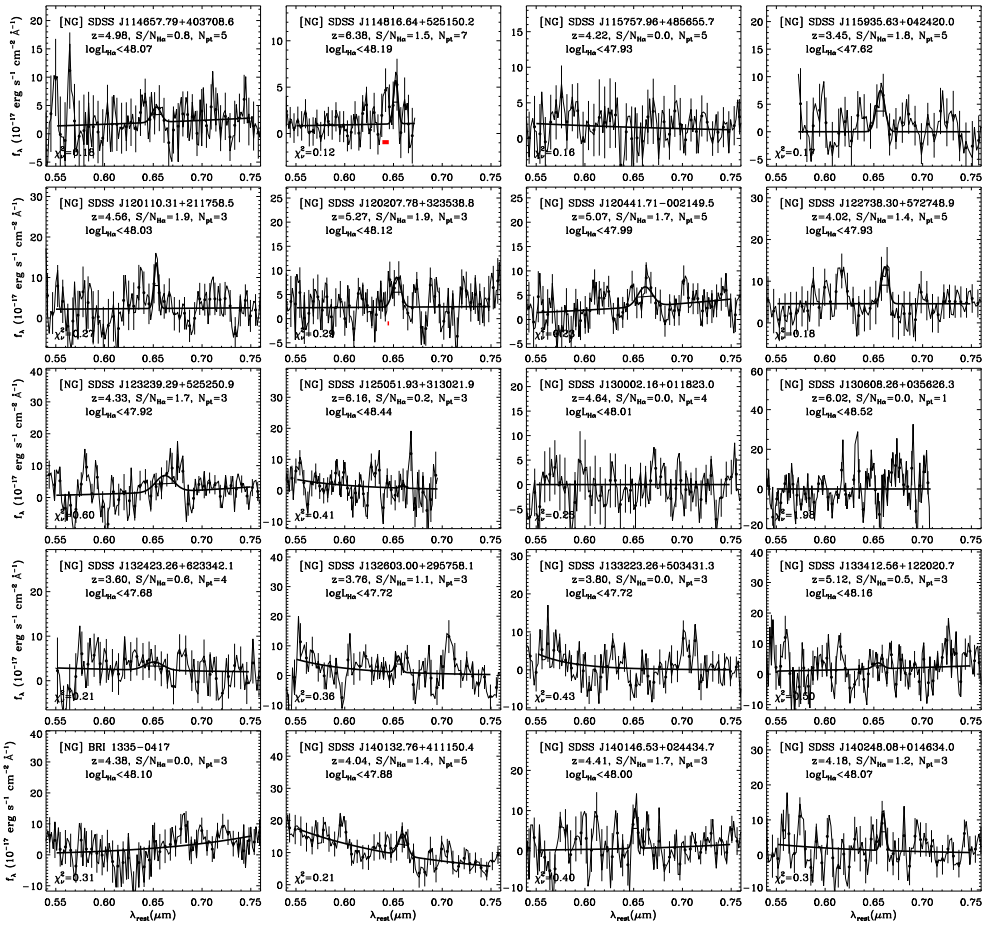
[NG] SDSS J114657.79+403708.6
z=4.98, S/N_Hα=0.8, N_pt=5
logL_Hα<48.07
[NG] SDSS J114816.64+525150.2
z=6.38, S/N_Hα=1.5, N_pt=7
logL_Hα<48.19
[NG] SDSS J115757.96+485655.7
z=4.22, S/N_Hα=0.0, N_pt=5
logL_Hα<47.93
[NG] SDSS J115935.63+042420.0
z=3.45, S/N_Hα=1.8, N_pt=5
logL_Hα<47.62
[NG] SDSS J120110.31+211758.5
z=4.56, S/N_Hα=1.9, N_pt=3
logL_Hα<48.03
[NG] SDSS J120207.78+323538.8
z=5.27, S/N_Hα=1.9, N_pt=3
logL_Hα<48.12
[NG] SDSS J120441.71−002149.5
z=5.07, S/N_Hα=1.7, N_pt=5
logL_Hα<47.99
[NG] SDSS J122738.30+572748.9
z=4.02, S/N_Hα=1.4, N_pt=5
logL_Hα<47.93
[NG] SDSS J123239.29+525250.9
z=4.33, S/N_Hα=1.7, N_pt=3
logL_Hα<47.92
[NG] SDSS J125051.93+313021.9
z=6.16, S/N_Hα=0.2, N_pt=3
logL_Hα<48.44
[NG] SDSS J130002.16+011823.0
z=4.64, S/N_Hα=0.0, N_pt=4
logL_Hα<48.01
[NG] SDSS J130608.26+035626.3
z=6.02, S/N_Hα=0.0, N_pt=1
logL_Hα<48.52
[NG] SDSS J132423.26+623342.1
z=3.60, S/N_Hα=0.6, N_pt=4
logL_Hα<47.68
[NG] SDSS J132603.00+295758.1
z=3.76, S/N_Hα=1.1, N_pt=3
logL_Hα<47.72
[NG] SDSS J133223.26+503431.3
z=3.80, S/N_Hα=0.0, N_pt=3
logL_Hα<47.72
[NG] SDSS J133412.56+122020.7
z=5.12, S/N_Hα=0.5, N_pt=3
logL_Hα<48.16
[NG] BRI 1335−0417
z=4.38, S/N_Hα=0.0, N_pt=3
logL_Hα<48.10
[NG] SDSS J140132.76+411150.4
z=4.04, S/N_Hα=1.4, N_pt=5
logL_Hα<47.88
[NG] SDSS J140146.53+024434.7
z=4.41, S/N_Hα=1.7, N_pt=3
logL_Hα<48.00
[NG] SDSS J140248.08+014634.0
z=4.18, S/N_Hα=1.2, N_pt=3
logL_Hα<48.07
f_λ (10^−17 erg s^−1 cm^−2 Å^−1)
λ_rest(μm)

Figure 6.3

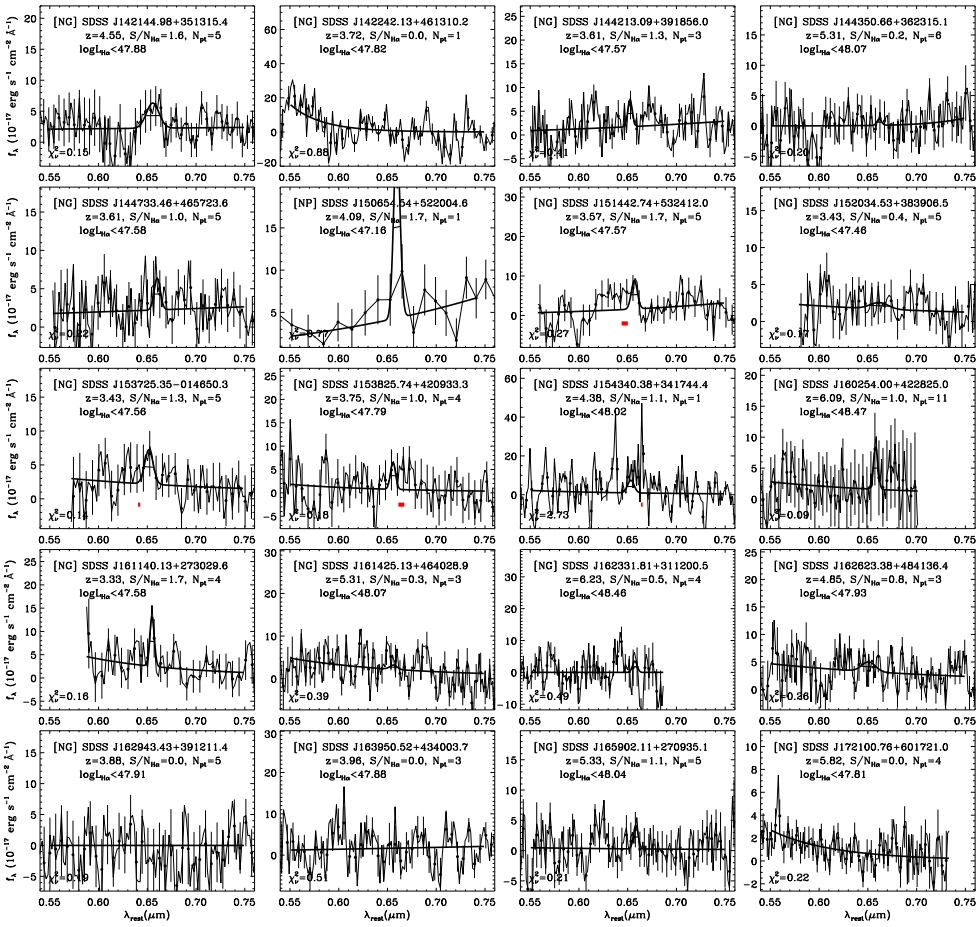
[NG] SDSS J142144.98+351315.4
z=4.55, S/N_Hα=1.6, N_pt=5
logL_Hα<47.88
[NG] SDSS J142242.13+461310.2
z=3.72, S/N_Hα=0.0, N_pt=1
logL_Hα<47.82
[NG] SDSS J144213.09+391856.0
z=3.61, S/N_Hα=1.3, N_pt=3
logL_Hα<47.57
[NG] SDSS J144350.66+362315.1
z=5.31, S/N_Hα=0.2, N_pt=6
logL_Hα<48.07
[NG] SDSS J144733.46+465723.6
z=3.61, S/N_Hα=1.0, N_pt=5
logL_Hα<47.58
[NP] SDSS J150654.54+522004.6
z=4.09, S/N_Hα=1.7, N_pt=1
logL_Hα<47.16
[NG] SDSS J151442.74+532412.0
z=3.57, S/N_Hα=1.7, N_pt=5
logL_Hα<47.57
[NG] SDSS J152034.53+383906.5
z=3.43, S/N_Hα=0.4, N_pt=5
logL_Hα<47.46
[NG] SDSS J153725.35−014650.3
z=3.43, S/N_Hα=1.3, N_pt=5
logL_Hα<47.56
[NG] SDSS J153825.74+420933.3
z=3.75, S/N_Hα=1.0, N_pt=4
logL_Hα<47.79
[NG] SDSS J154340.38+341744.4
z=4.38, S/N_Hα=1.1, N_pt=1
logL_Hα<48.02
[NG] SDSS J160254.00+422825.0
z=6.09, S/N_Hα=1.0, N_pt=11
logL_Hα<48.47
[NG] SDSS J161140.13+273029.6
z=3.33, S/N_Hα=1.7, N_pt=4
logL_Hα<47.58
[NG] SDSS J161425.13+464028.9
z=5.31, S/N_Hα=0.3, N_pt=3
logL_Hα<48.07
[NG] SDSS J162331.81+311200.5
z=6.23, S/N_Hα=0.5, N_pt=4
logL_Hα<48.46
[NG] SDSS J162623.38+484136.4
z=4.65, S/N_Hα=0.8, N_pt=3
logL_Hα<47.93
[NG] SDSS J162943.43+391211.4
z=3.88, S/N_Hα=0.0, N_pt=5
logL_Hα<47.91
[NG] SDSS J163950.52+434003.7
z=3.96, S/N_Hα=0.0, N_pt=3
logL_Hα<47.88
[NG] SDSS J165902.11+270935.1
z=5.33, S/N_Hα=1.1, N_pt=5
logL_Hα<48.04
[NG] SDSS J172100.76+601721.0
z=5.82, S/N_Hα=0.0, N_pt=4
logL_Hα<47.81
f_λ (10^-17 erg s^-1 cm^-2 Å^-1)
λ_rest(μm)

Figure 6.3

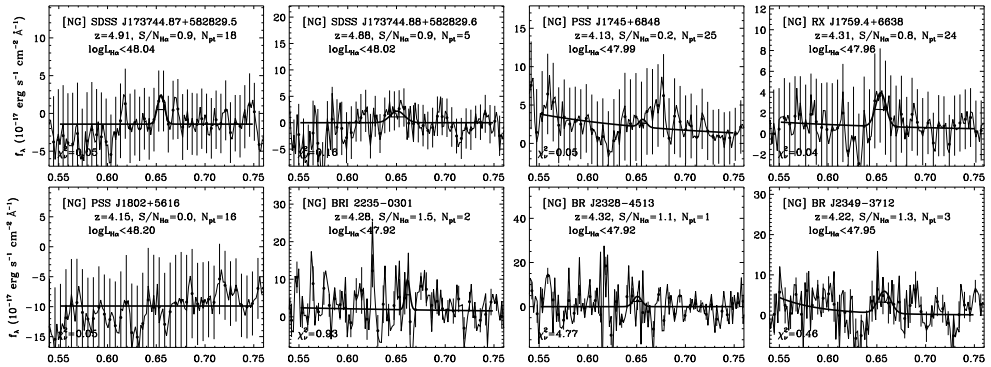
[NG] SDSS J173744.87+582829.5
z=4.91, S/N_Hα=0.9, N_pt=18
logL_Hα<48.04
[NG] SDSS J173744.88+582829.6
z=4.88, S/N_Hα=0.9, N_pt=5
logL_Hα<48.02
[NG] PSS J1745+6848
z=4.13, S/N_Hα=0.2, N_pt=25
logL_Hα<47.99
[NG] RX J1759.4+6638
z=4.31, S/N_Hα=0.8, N_pt=24
logL_Hα<47.96
[NG] PSS J1802+5616
z=4.15, S/N_Hα=0.0, N_pt=16
logL_Hα<48.20
[NG] BRI 2235−0301
z=4.28, S/N_Hα=1.5, N_pt=2
logL_Hα<47.92
[NG] BR J2328−4513
z=4.32, S/N_Hα=1.1, N_pt=1
logL_Hα<47.92
[NG] BR J2349−3712
z=4.22, S/N_Hα=1.3, N_pt=3
logL_Hα<47.95
f_λ (10^-17 erg s^-1 cm^-2 Å^-1)

Figure 6.3

List of Publications

1. "*Rest-frame Optical Black Hole Masses of Extremely Massive 1<z<2 Quasars*"
Jun, H. D. et al., 2014, ApJ, in preparation

2. "*Rest-frame Optical Spectra and Black Hole Masses of 3<z<6 Quasars*"
Jun, H. D. et al., 2014, ApJ, to be submitted

3. "*Physical Properties of Luminous Dust-poor Quasars*"
Jun, H. D. & Im, M., 2013, ApJ, 779, 104

4. "*The Mid-Infrared Fundamental Plane of Early-Type Galaxies*"
Jun, H. D. & Im, M., 2008, ApJL, 678, 97

요 약

은하의 팽대부에서 주로 발견되는 거대 블랙홀은 활동성 은하핵(AGN) 단계를 거쳐 질량이 커지는 것으로 알려져 있다. 현재 활동이 잦아진 무거운 은하들에서 발견되는 가장 무거운 거대 블랙홀은 그 질량이 태양의 10억 배로 측정된다. 대단히 무거운 블랙홀(태양 질량의 1억 배 이상)의 물리적 진화를 살펴보기 위해 블랙홀 질량의 상한치, 대단히 무거운 블랙홀 질량의 시간 변화, AGN의 먼지 구조의 진화, 그리고 무거운 블랙홀의 모은하들의 적외선 물리량 사이의 관계를 관측적인 방법으로 살펴보기로 한다.

먼저, 가장 무거운 AGN의 블랙홀 질량 측정의 신뢰도를 점검하기 위해 적색편이 0.7에서 2.5 사이에 있는 27개의 AGN에 대하여 가시광 측정식을 사용하여 블랙홀 질량을 재고, 자외선 측정식으로 그 질량이 10억 태양 질량인 AGN의 블랙홀 질량과 비교하였다. 수소 발머선으로 잰 질량이 Mg II 질량과 전반적으로 일치하는 것을 확인하였다. 반면, 10억 태양 질량보다 무거운 AGN의 일부 스펙트럼에서는 넓은 Hα 방출선 외에 강착 원반 방출 모양이 나타나며, 넓은 자외선 방출선 주위에는 추가적인 방출 모양이 거의 드러나지 않는 것으로 나타났다. 한편, C IV 질량은 Hα 질량에 대해 큰 편차를 보이며 C IV 질량이 10억 태양 질량 이상인 8개의 천체 중 4개에서 Hα 질량이 10억 태양 질량 이하인 것으로 나타난다. 이에 따라 기존에 10억 태양 질량 이상으로 측정된 자외선 기반의 블랙홀 질량 측정값은 조심스레 받아들여야 할 것으로 보인다. AGN의 블랙홀 질량 측정식의 계통 오차로 인해 블랙홀 질량은 실제보다 크게 측정될 수 있으나, 오차를 감안하여도 질량이 여전히 10억 태양 질량에 가까울 것으로 보인다.

둘째로, 아카리 우주 망원경을 통해 적색편이 3.3에서 6.4 사이에 있는 155개의 밝은 퀘이사의 정지 가시광 스펙트럼을 얻었다. 기존의 AGN의 5100 $\AA$ 및 Hα 광도 관계를 간단한 선형 식으로 높은 광도, 높은 적색편이 영역까지 확장하였다. 이는 광도 사이의 관계를 이루는 근본 물리 현상들이 십만 배의 광도 범위 ($10^{43} < L_{\rm bol} < 10^{48}\,{\rm ergs\,s^{-1}}$)에서 적색편이 0–6사이에 진화하지 않음을 시사한다. 비슷한 광도 및 선폭 관계가 가시광선 및 자외선 파장대 사이에서 성립함을 확인하였다. 이러한 물리량 간 관계를 Hβ 블랙홀 질량 추정식에 대입함으로 Hα, Mg II, C IV 방출선을 이용한 블랙홀 질량 추정식을 추출하였으며, 자외선 기반의

질량이 발머선 기반의 질량과 전반적으로 일치하나, C IV 질량은 발머선 질량에 대해 크게 흩어져 있음을 확인하였다. 우리가 구한 Hα 블랙홀 질량 추정값은 약 10억, 1억 태양 질량의 블랙홀이 각각 적색편이 5, 6까지 존재할 수 있음을 지지하며, 초기 우주에 급속한 블랙홀의 성장이 있었다는 기존 연구를 더욱 든든히 뒷받침한다.

다음으로는, 대단히 무거운 블랙홀이 되어 가는 도중 AGN의 구조적 형성 및 진화를 가늠할 수 있는 방법으로, 기존에 적색편이 6 이상에서 발견된 것과 측광학적으로 비슷한 적색편이 5 이하의 먼지가 적은 퀘이사를 수집하고 그 특성을 분석하였다. 가시광에서 발견한 $L_{\rm bol} > 10^{45.7}\,{\rm ergs\,s^{-1}}$인 41,000개의 1형 퀘이사의 정지 자외선으로부터 적외선까지 아우르는 분광 에너지 분포를 맞춘 결과, 샘플의 0.6%가 0.51 μm 대비 2.3 μm가 -0.5 dex보다 약한, 뜨거운 먼지가 적은 퀘이사로 분류되었다. 먼지가 적은 퀘이사의 분광 에너지 분포는 자외선 및 가시광에서 푸른 색을 띄며 중적외선에서 약한 복사를 내는 것으로 보아, 이들 퀘이사의 강착 원반 복사가 상대적으로 먼지에 덜 흡수되었으며 뜨거운 먼지로부터의 복사가 따듯한 먼지가 내는 복사의 세기를, 먼지가 약한 영역에까지 잘 따른다고 생각된다. 먼지가 적은 퀘이사는 일반적인 퀘이사에 대해 일정한 복사광도에서 블랙홀 질량이 작고 에딩턴 비율이 높으며 적색편이가 높아, 블랙홀이 급속도로 자라나는, 짧거나 드문 진화 단계에 있는 것으로 해석할 수 있다.

마지막으로, 무거운 블랙홀이 활동을 멈추고 어두워졌을 현재 우주에서 조기형 은하들의 중적외선 근본 평면 관계를 연구하였다. 조기형 은하의 크기, 표면밝기 및 속도 분산이 이루는 평면은 간단한 비리얼 평면의 예상으로부터 기울어져 있어, 그 이유가 종종 논란에 싸이고는 했다. 근본 평면 관계가 기울어지는 요인 중 항성 종족의 효과를 살펴보기 위해 가시광, 근적외선, 및 중적외선(*Spitzer* IRAC) 자료가 있는 56개의 조기형 은하들을 이용하였다. 계산된 중적외선 근본 평면의 기울기로부터 항성 종족 효과가, 기울기의 예측으로부터 벗어나는 정도의 절반 이상을 설명할 수 있음을 제시하였는데, 이는 중적외선 광도가 더 짧은 파장에 비해 질량을 더 잘 따르는 것을 암시한다.

멀리 있는 AGN의 정지 가시광 스펙트럼 연구로부터, 우리는 AGN의 물리적 기작이 적색편이 0부터 6까지 변하지 않음을 살펴보았고, 가장 무거운 AGN

의 블랙홀 질량이 적색편이 6에서부터 먼지가 적은 단계를 거쳐 적색편이 5까지 급속히 자라나는 경우를 뒷받침하였다. 가장 무거운 블랙홀이 조용하고 무거운 오늘날의 은하 안에 정착하였을 때, 모은하들의 적외선 근본평면 관계식은 중적외선을 그 질량으로 대신하였을 때 비리얼 평면 예측에 근접한다.

주요어: 은하: 활동성 — 은하: 진화 — 은하: 본질적 변수 — 적외선: 은하

학 번: 2006 – 22963